Modelling of physical and chemical processes in the small intestine

by

AJAY THARAKAN

A thesis submitted to
The University of Birmingham
for the degree of
DOCTOR OF ENGINEERING

Centre for Formulation Engineering
Department of Chemical Engineering
University of Birmingham
September 2008

ABSTRACT

Chemical and physical processing in the small intestine is an important step for food digestion and absorption. Having reviewed the literature, a relevant model has been developed which enabled investigation into the fluid flow, mixing mechanisms and delivery of nutrients to the wall of the model small intestine.

Designing, developing and using the Small Intestinal Model (SIM), a physical model of a section of the small intestine, mimicking the physiological contractions, allowed mass transfer to be measured using different process conditions and ingredients. Experiments were carried out using the SIM to study mass transfer, starch digestion and flow visualisation. While simulating the small intestinal flow profile, experiments have shown that the functional ingredient guar gum reduces the mass transfer coefficient of the model nutrient riboflavin. This together with computational modelling suggests an explanation for the observed functionality of guar gum to reduce the peak increase in blood glucose levels after ingestion of test meals.

Industrial implications are to give a scientific and engineered design methodology for novel food formulations by understanding the food product behaviour in the SIM. Optimisation of formulation candidates going to the human trial stage and improvement of speed to market of new product introductions is intended.

DEDICATION

To the shoulders that I stand on

ACKNOWLEDGMENTS

Many thanks to my academic and industrial supervisors Peter Fryer, Ian Norton and Pip Rayment for setting up the project and inviting me to work on it. Their support throughout the project has been invaluable and is greatly appreciated. The pastoral care provide by Richard Greenwood has also been greatly appreciated.

I would like to thank the people who have helped me from The University of Birmingham in particular Serafim Bakalis and also those from Unilever Colworth. I am sorry not to name them all individually but I hope they know who they are.

I would like to thank The University of Birmingham, Unilever and the EPSRC for their engagement and funding of this EngD.

Finally thank you to wife Amy for her relentless support during the EngD and to my Family.

CONTENTS PAGE

Chapter 1 – Introduction

Chapter 2 – Literature Review

LIST OF FIGURES

Chapter 2 – Literature Review

Chapter 3 – Materials and Methods

Chapter 4 – FRAP and Diffusion Cell

Chapter 5 – Mass Transfer Studies Using the Small Intestinal Model

Chapter 6 – Experimental Fluid Dynamics Techniques Applied to the SIM

LIST OF TABLES

Chapter 2 – Literature Review

Chapter 3 – Materials and Methods

Chapter 4 – FRAP and Diffusion Cell

Chapter 5 – Mass Transfer Studies Using the Small Intestinal Model

Chapter 6 – Experimental Fluid Dynamics Techniques Applied to the SIM

ABBREVIATIONS

BAMPA	Bio-mimetic Artificial Membrane Permeation Assay
CAGR	Compound Annual Growth Rate
CAT	Compartmental Absorption and Transit model
CFD	Computational Fluid Dynamics
CMC	Carboxymethyl Cellulose sodium salt
EPSRC	Engineering and Physical Sciences Research Council
FDA	Food and Drugs Administration
FRAP	Fluorescence Recovery After Photobleaching
GI Tract	Gastrointestinal Tract
MRI	Magnetic Resonance Imaging
PAMPA	Parallel Artificial Membrane Permeation Assay
PLIF	Planar Laser Induced Fluorescence
PIV	Particle Image Velocimetry
SIM	Small Intestinal Model

CHAPTER 1 - INTRODUCTION

1.1 Overview

The subject of this thesis is the modelling of physical and chemical processes in the small intestine. The physical and chemical processing of food in the small intestine is an important step in the digestion and absorption of food. To exploit the opportunities of producing foods with health advantages due to their behaviour in the human digestive system, it is necessary to understand and predict the digestion and subsequent absorption of structured functional foods.

The purpose of this project was to investigate and understand how the structuring of foods can influence the delivery of nutrients to the wall of the small intestine. By simulating intestinal flow profiles it is possible to carry out investigations into the effect food formulation has on nutrient delivery to the wall of the intestine and thus aid in the design of novel foods.

Much of the research into new foods is currently in the field of ‘Functional Foods’. The International Food Information Council (2008) defines ‘Functional Foods’ as foods or dietary components that may provide a health benefit beyond basic nutrition. Examples can include fruits and vegetables, whole grains, fortified or enhanced foods and beverages, and some dietary supplements. Biologically active components in functional foods may impart health benefits or desirable physiological effects. Functional attributes of many traditional foods are being discovered, while new food products are being developed with beneficial components.

Currently food product development uses mainly qualitative approaches to structure-function relationships that lead to cycles of prototyping and testing to develop the final product (Norton *et al*., 2006). As products become more sophisticated and require greater degrees of proof of function, for example by clinical trials (Gibson *et al*., 2002), the cost and time of development begins to escalate. The final and much over looked stage of food processing is the human digestive system and in particular the gastrointestinal tract (GI tract). The processing that the food undergoes in the human GI tract takes place in the mouth, stomach, small and large intestine. By (i) understanding the chemical and physical processes that the food goes through in the GI tract and (ii) being able to model them appropriately, food product development time and cost may be reduced.

The Engineering Doctorate is a four year research programme that combines academic research expertise with applied industrial research. The industrial host was Unilever Research & Development and the academic host was Birmingham University's Centre for Formulation Engineering. The work was funded by the Engineering and Physical Sciences Research Council (EPSRC) and Unilever.

1.2 Functional Foods Market

The design and development of functional foods is the commercial stimulus for this work. Functional foods may help prevent disease, reduce the risk of developing disease, or enhance health (Gibson 2002, Arnoldi 2004). In recent years there has been an increase in consumer awareness about the influence of diet and nutrition on health and general wellbeing. The increase in incidence of medical conditions such as coronary heart disease,

diabetes and obesity, has made the incorporation of nutritious and healthy ingredients into the normal daily diet more important.

Examples of functional foods are cholesterol lowering spreads containing either plant sterols (Flora pro.activ) or plant stanol ester (Benecol), typically at levels of 8g per 100g. Flora pro.activ is marketed by Unilever and has the endorsement of the FDA (Food and Drugs Administration) in the USA and in Europe it has been cleared under the EU Novel Foods Regulations (Flora Professional). The Flora pro.activ cholesterol lowering spread helps lower cholesterol while following a healthy diet and lifestyle. The spread contains plant sterols, an active ingredient that is clinically proven to dramatically lower bad cholesterol (LDL) as part of a healthy diet. This helps to maintain a healthy heart. Plant sterols can lower LDL by 10-15% in just three weeks, when moving to a healthy diet and lifestyle (Flora Professional).

Datamonitor analysts estimate that the combined US, Western European and Asia Pacific functional food and drink market is worth $72.3 billion in 2008 and forecasts that this market will grow at a compound annual growth rate (CAGR) of 5.7% between 2007 and 2012 (Food Business Review, 2008).

An example of the food industry's response to the functional food market is that in 2002 Nestlé assigned scientists to study weight gain and diabetes, which led to the development of a cereal bar for diabetics. The cereal bar is currently sold only in Asia under the brand name Nutren Balance. It contains beta-glucan, a fibre occurring naturally in oats and barley that slows the body's absorption of starches and thus reduces the risk of blood sugar surges

that are dangerous for diabetics. Nestlé developed a patented method (Patent WO/2003/055331) to triple the level of beta-glucan in oats, while altering the fibre so it becomes more viscous in the stomach (Businessweek, June 2006).

Another example is Unilever who developed a process to alter the molecular structure of fat-containing emulsions so the intestine absorbs fat more slowly, thereby delaying the onset of hunger (Patent US 2006/0105093). These new emulsions have been used in Unilever's Slim-Fast Optima diet shakes since early 2006 (Businessweek, June 2006).

Major food manufacturers and other food companies are patenting technologies that alter naturally occurring fats and fibres. In conjunction with this they are carrying out medically supervised tests on humans, in much the same way pharmaceutical companies conduct drug trials. The goal is to develop new products that change the way food is digested, leading to more desirable levels of nutrient in the blood and/or increased levels of satiety (Businessweek, June 2006).

Further challenges are the identification and screening of functional ingredients and final formulations for development. Assessing the technological and commercial feasibility of new product concepts will require formalisation. Appropriate systems for validating product safety and functional benefits are needed, for example through *in vitro* models and clinical human trials (Gibson and Williams, 2002).

1.3 Unilever

Unilever is one of the world's leading suppliers of fast moving consumer goods across the 'Foods' and 'Home and Personal Care' categories with a turnover in 2006 of £27 billion (Unilever Annual Report, 2006). Unilever's food offerings have a broad product range that falls into two main food groups: (i) savoury, dressings and spreads: (ii) ice cream and beverages.

The savoury, dressings and spreads group includes sales of soups, bouillons, sauces, snacks, mayonnaise, salad dressings, olive oil, margarines, spreads and cooking products such as liquid margarines and some frozen foods businesses. Among the leading brands are *Knorr*, *Hellmann's*, *Calvé*, *Wish-Bone*, *Amora*, *Bertolli*, healthy heart *Becel* and *Flora* ranges, and brands including *Rama*, *Blue Band* and *Country Crock*.

The ice cream and beverages group includes sales of ice cream under the international *Heart* brand, including *Cornetto*, *Magnum*, *Carte d'Or* and *Solero*, and also *Ben & Jerry's*, *Breyers*, *Klondike* and *Popsicle*. It also includes sales of tea, where brands include *Lipton* and *Brooke Bond*, weight management products (principally *Slim Fast*), and nutritionally enhanced staples sold in developing markets, including *Annapurna* and *AdeS* ranges.

The personal care group has six global brands that are the core of the business in the deodorants, skin cleansing, daily hair care and mass-market skin care categories – *Axe*, *Dove*, *Lux*, *Pond's*, *Rexona* and *Sunsilk*. Other important brands include *Suave*, *Clear*, *Lifebuoy* and *Vaseline*, together with *Signal* and *Close Up* in oral care. The home care group is a series of laundry products, including tablets as well as traditional powders and

liquids for washing by hand or machine and tailored products including soap bars. Brands include *Comfort*, *Omo*, *Radiant*, *Skip*, *Snuggle* and *Surf* and the household care products are led by *Cif* and *Domestos* brands (Unilever Annual Report, 2006).

Unilever's mission is "To add vitality to life, meeting everyday needs for nutrition, hygiene and personal care with brands that help people feel good, look good and get more out of life" (Unilever Annual Report, 2006). Therefore the area of functional foods has a clear place under this objective.

1.4 Engineering in the Small Intestine

The understanding of the fluid flow in the small intestine is required to achieve good *in vitro-in vivo* correlation (from experimental model as compared to in the body) for assessing the impact that food formulation has on nutrient absorption profiles. In situations where the delivery and movement of molecules to the wall of the intestine, surface renewal or enzyme substrate interactions are a rate controlling step for absorption then the fluid dynamics will influence absorption. Therefore, the fluid dynamics of digesta (digesting food material) in the small intestine can influence absorption profiles, a consequence of both the fluid properties and the pumping mechanism.

Designing an *in vitro* apparatus that can simulate the *in vivo* process with the ability to operate in the shear stresses and Reynolds numbers (Re) relevant for the human small intestine under fed conditions has been a major section of this work. This apparatus, named the small intestinal model (SIM), has allowed investigation into the effect that food formulation has on the delivery of nutrients or actives to the intestinal wall. *In vitro*

experiments into molecular delivery and fluid dynamics, along with computer simulation, help to quantify the effect of changing digesta rheology on nutrient delivery.

1.5 Overview of the Thesis

Chapter 2 is a review both on modelling of the small intestine and of controlled nutrient delivery food formulations. The chapter describes the process of food digestion, the small intestine (anatomy and physiology), absorption in the small intestine and the effect of intestinal motion on nutrient absorption profiles. The review then looks at food formulation and controlled nutrient delivery, specifically on the effects of guar gum on glucose absorption. Existing models are then discussed and related to the context of this work.

The materials and methods used as part of this work are described in Chapter 3 along with their preparation and characterisation. A description of the experimental apparatus and procedures, diffusion cell design, method of use and starch hydrolysis experiments is presented. This chapter also describes other techniques used in later chapters; consisting of fluorescence recovery after photobleaching (FRAP), particle image velocimetry (PIV) and planar laser induced fluorescence (PLIF), as well as the use of computational fluid dynamics (CFD) methods. The design of the small intestinal model (SIM) in also described in Chapter 3.

Diffusion of the nutrient riboflavin through a range of guar gum solutions has been studied using fluorescence recovery after photobleaching (FRAP) and this is described in Chapter 4. Investigations into the delivery of riboflavin to the surface of a membrane were

undertaken using the diffusion cell and a range of guar gum solutions were studied under different processing conditions (Chapter 4).

To simulate the process conditions found in the small intestine the SIM was used for the experiments described in Chapter 5. Several experiments into the delivery of riboflavin to the membrane surface of the model with guar gum solutions were carried out, as were starch hydrolysis experiments.

Using the SIM and model food formulations the fluid dynamics of the system were investigated using the experimental fluid dynamics techniques particle image velocimetry (PIV) and planar laser induced fluorescence (PLIF). Using the PIV technique the velocity profiles, peak flow rates, shear rates and Reynolds numbers have been established for model foods with different properties. The effectiveness of mixing has also been studied using PLIF while varying the physical properties of model foods and this is also described in Chapter 6.

Using computational fluid dynamics (CFD) methods it has been possible to create a model of the segmentation motion seen in the human small intestine and in the small intestinal model. This has allowed the theoretical fluid flow for the complex fluids to be simulated and compared with those from the experimental fluid dynamics work which is also described in Chapter 6.

Chapter 7 is a summary of the key developments and findings from the work into modelling of chemical and physical processes in the small intestine. The limitations of the work are discussed as are the conclusions and recommendations for future work.

Some of the work as part of this thesis has been published and presented externally to Birmingham University and to Unilever, as shown below.

Publication

Tharakan A., Rayment P., Fryer P.J. and Norton I.T. (2007) Modelling of physical and chemical processes in the small intestine, *Proceedings of European Congress of Chemical Engineering (ECCE-6)*, Copenhagen, 16-20 September 2007.

Presentations

Tharakan A., Rayment P., Norton I.T., and Fryer P.J. (2006) Modelling of physical processes in the small intestine, 7th *UK Particle Technology Forum 2007,* Imperial College, London.

Tharakan A. (2005) Investigation of physical & chemical processing in the small intestine using an *in vitro* model to aid design of novel food formulations, *Reception and Competition at the House of Commons.*

Bakalis S., Tharakan A., Norton I.T. and Fryer P.J. (2007) Modelling of physical processes in the small intestine, *The Journal of the Federation of American Societies for Experimental Biology*, 21: lb524.

Bakalis S., Tharakan A., Norton I.T. and Fryer P.J. (2008) Modelling of physical processes in the small intestine, *International Congress of Engineering and Food 10.*

CHAPTER 2 - LITERATURE REVIEW

2.1 Introduction

Understanding the fluid flow, mixing and diffusion of nutrients through structured foods in the small intestine is required to achieve good *in vitro-in vivo* correlations of the effects that changing structured food formulations have on the delivery of nutrients or actives to the intestinal wall. This chapter gives an overview of the various scientific and engineering aspects of the project combined with the necessity for the models that have been developed and the research work carried out as part of this body of work. The gastrointestinal tract is described in Section 2.2, food design is discussed in Section 2.3, chemical engineering processes occurring in the small intestine are described in Section 2.4 and existing intestinal models are discussed in Section 2.5.

The delivery of a nutrient or actives to the intestinal wall is a result of convective mixing of the intestinal contents known as digesta (a mixture of consumed foods and secretions from the body) and their diffusion through the digesta. The nutrient uptake has been shown to be influenced by the physical properties of the intestinal contents. An example of this is the work of Blackburn *et al*. (1984) who showed that the presence of 14.5 grams of guar gum in a 250 ml glucose solution reduced the peak increase in blood glucose level by 50%. The processing of digesta within the intestine has been shown experimentally to affect absorption. Macagno *et al.* (1982) showed that the motions of modelled intestinal wall caused an increase of 30-35% of absorption. Therefore, the rheology and mixing of digesta in the small intestine is important as it could influence absorption profiles. This work investigates the behaviour of model foods and the delivery of nutrients to the wall, as a function of both the fluid properties and the fluid dynamics of the digesta.

The behaviour of the food material in the small intestine and the subsequent absorption into the body is an area of scientific interest, as well as being of practical value to the food and pharmaceutical industries. The scientific fields of chemical engineering science, food science, human nutrition and physiology are integrated in this work.

A number of models and techniques that aim to predict the intestinal absorption of molecules in humans have been developed and are described later in this chapter (Section 2.5). These models vary greatly in their complexity and type, as each has been developed for different individual applications. The application of specific models has led to the range of models seen today, encompassing chemical, physical and biological models. Each model has the common purpose of reducing the experimental time, costs or risks that can arise at the human studies stage of investigation, by understanding how the food will behave in the body. The models allow individual parameters to be controlled and varied, leading to better understanding of the chemical, physical or biological process of interest, specific to the model. However, as will be shown, no model exists that specifically addresses the effect of food formulation on nutrient delivery to the wall of the small intestine while mimicking the segmentation motion. The models developed as part of this body of work have been developed ultimately for this purpose.

2.2 The Gastrointestinal Tract

2.2.1 Overview of the Gastrointestinal Tract

Figure 2.1 shows a diagrammatic representation of the human digestive system which consists of the mouth (and salivary glands), the stomach, the small intestine (duodenum, jejunum, ileum), the liver, the gallbladder and the large intestine (cecum, colon and

rectum) (Guyton, 1996). The digestive tract and process is the system by which nutrients from food and beverages gain access to the circulatory system and the body. Prior to passage into the blood, nutrients within any food or beverage must be reduced to very simple molecules (such as sugars, amino acids, fatty acids) by a combination of mechanical and enzymatic degradation (Guyton, 1996). These simple molecules can then be transported across the epithelium lining of the small intestine into blood (Guyton, 1996).

The mouth is used for the mechanical breakdown of food and the mixing of the food with enzymes. It also contains taste sensors and permits partition of flavour molecules into the vapour phase of the gas filled spaces in the mouth and nose. The stomach serves the function of mechanical processing (churning) mixing with hydrolytic enzymes, pH change and digestion. The small intestine serves the following purposes:

- bulk transit of digesta from the stomach to the large intestine;
- digestive reactions such as the breaking down of starch by pancreatic α-amylase (Table 2.2);
- convection and diffusion of nutrients, fats, enzymes and biosurfactants; and
- absorption of water across the wall of the small intestine and movement of water into the small intestine. Water moves into or out of the intestine until the osmotic pressure of the intestinal contents equals that of the plasma (Ganong, 2005).

The large intestine's (colon) function is to absorb remaining water from the by-then indigestible food matter, the microbial fermentation of undigested food, the storage of this unusable food matter (wastes) and then elimination the wastes from the body.

Table 2.1 gives details on the dimensions and approximate residence times of various parts of the gastrointestinal tract.

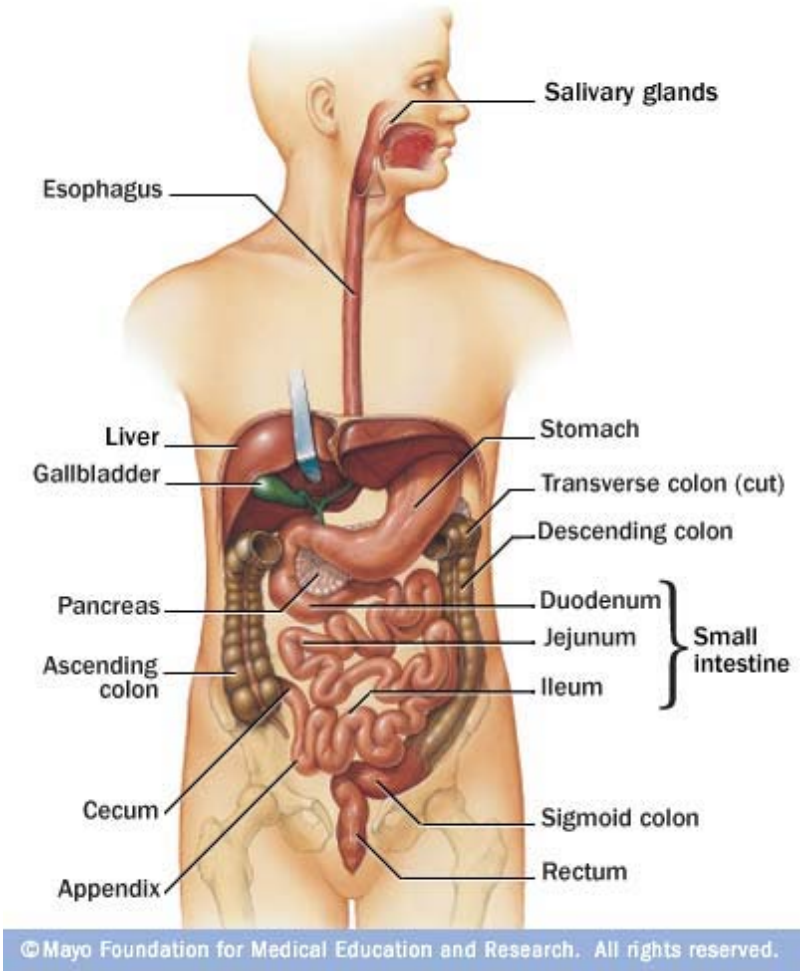

Figure 2.1 An illustration of the gastrointestinal tract (Riversideonline, 2008)

Section of GI Tract	Dimensions	Approximate Residence Time
Mouth	-	A few seconds to a few minutes (Dean et al, 2007)
Stomach	Can expand to contain a volume of upto 4 litres (Kong *et al.,* 2008)	A solid dose can vary from 15 minutes to about 2 hours (Banker, 2002)
Small intestine	~ 285 cm in length, diameter varies from 5 cm (start) to ~ 2 cm (end) (Ganong, 2005)	Transit time is 2.5 hours +/- 78 min (Yu *et al.* 1996)
Large intestine	~ 100 cm in length (Ganong, 2005) 7.5 cm in diameter (Gray, 1918)	Takes 12 to 25 hours to finish up the remaining processes of the digestive system (Maton, 1993)

Table 2.1 Table of the dimensions and approximate residence time of food within various parts of the gastrointestinal tract.

The digestive and absorptive functions of the gastrointestinal system involve a variety of mechanisms that soften the food, propel it through the gastrointestinal tract and then mix it both with bile (stored in the gallbladder) and digestive enzymes secreted by salivary glands and pancreas (Ganong, 2005).

The digestion process is made up of several processes as required:

- mechanical digestion (food break down in the mouth, mechanical processing in the stomach and small intestine);
- enzymatic digestion (enzyme addition to food in the mouth, stomach and small intestine);
- hormone production/release such as gastrin secreted in from the mucosa of the stomach which increases gastric motility and secritin in the small intestine which increases the rate of bile secretion from cell in the liver;
- pH (the hydrogen ion concentration varies at different stages of the intestine); and
- transit time (the time that food material is in a particular section of the intestine).
- fermentation of undigested food by gut microflora in the large intestine.
- enterohepatic circulation of bilary acid from the liver to the small intestine where they aid in lipid digestion and are then returned back to the liver.

Several parameters need to be studied to define and model the events involved in gastrointestinal tract absorption of nutrients and non-nutrients. These include anatomical and physiological features of the gastrointestinal tract such as surface area, vascularity, transit time/motility and enterohepatic circulation (DeSesso and Jacobson, 2001). There are also the physicochemical properties of the digesta and the functional ingredients of interest in it such as lipophilicity, chemical and/or enzymatic stability, solubility, particle size, density, diffusivity, pK_a and crystal form. Other factors are the type of membrane transport mechanism (described in Section 2.2.4.1), pH and stomach emptying (Idkaidek and Abdel-Jabbar, 2001).

By defining the role that one of the parameters has in the absorption of a particular food, a quantitative description of the absorption process should be possible. However, in many cases, the data necessary to evaluate the importance of these parameters is not available, and experiments must be carried out to measure their effect on absorption. Only by doing so can the kinetics of ingested compounds be effectively understood and accurately modelled (DeSesso and Jacobson, 2001).

This work has focussed on the fluid flow, mixing and molecular delivery of nutrients to intestinal wall in the small intestine and the methods to model this.

2.2.2 The Mouth

The mouth is the oral cavity that is enclosed by the apposition of the lips within which are the tongue, teeth and glands. A diagram of the mouth is shown in Figure 2.2.

The mouth is the point of entry for foods and liquids to the human body and carries out several functions. It is responsible for mastication (chewing) which involves mechanically breaking down food by fracturing or tearing the material between the teeth to form smaller pieces that can be swallowed. Mastication also mixes food with the secretions from the salivary glands. The wetting and homogenisation action aids swallowing and subsequent digestion. The mouth also exposes the food to sensors that perform the function of taste which is a complicated sensory perception that uses taste buds on the tongue (Taylor, 1996). The mouth lubricates the food by the secretion of saliva into the mouth from the salivary glands. The chemical digestion begins in the mouth with the mixing of food or

beverages with enzymes from the saliva. The mouth also serves a protective function from harmful substances with the use of taste and also from feel (Guyton, 1996).

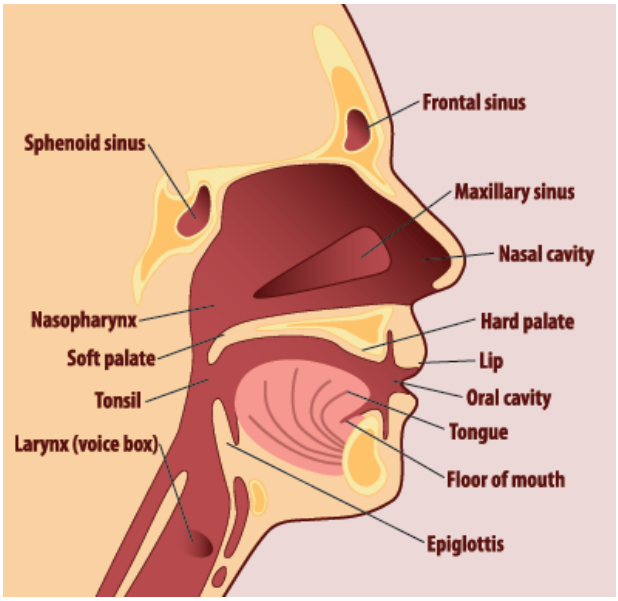

Figure 2.2 Diagram of the side view of the structures of the mouth and throat (RT Answers, 2008)

Saliva is secreted from three glands in the mouth and is a watery secretion that contains alpha-amylase (starch digestion enzyme), lingual lipase, mucin (a glycoprotein that lubricates food, binds bacteria and protects the oral mucosa) and ions (Na^+, K^+, Cl^+). The saliva has a pH of around 7 and performs the functions of facilitating swallowing, keeping the mouth moist, acting as a solvent for molecules that stimulate the taste buds and keeping the mouth and teeth clean. About 1500 ml of saliva is secreted per day (Ganong, 2005).

When the food entering the mouth has been broken down in size via mastication, it is mixed with saliva to form a bolus (a soft wet ball of food made after the mouth has chewed and moistened it) which is a size that can be swallowed. The optimal number of chews depends on the food, but usually ranges from 20 to 25 (Ganong, 2005).

2.2.2.1 Food Flavour and the Mouth

Flavour has been defined as the combined perception of mouthfeel, texture, taste and aroma (British Standards Institute, 1975). The impact that varying these factors has on food quality is of significant importance to the food industry in the formulation of foods that are acceptable to the consumer. In addition to food flavour, the other factors that contribute to the perceived quality of food are appearance and nutritional benefit. Appearance is determined by the colour, shape, size and gloss of the food and the perceived optically. Nutritionally, foods are comprised of major nutrients (carbohydrates, fat, protein) and minor nutrients (minerals, vitamins, fibre and others) (Henry, 2002). However, although humans are effective at sensing taste/flavour, humans are not effective in sensing nutritional quality.

The taste of food is perceived by sensors on the tongue, whilst aroma is perceived in the olfactory centre in the nose. These senses are triggered in response to receptors in the oral and nasal cavities to chemical stimuli. The mouth plays a major part in food flavour perception, as does the nasal cavity once molecules are released from the food into the headspace of the mouth and delivered to receptors in the nose (Taylor *et al.*, 1996). Both taste and smell (aroma) receptors are chemoreceptors that are stimulated by molecules in solution both in mucus in the nose and in saliva in the mouth. Aroma molecules are delivered to the chemoreceptors in the nasal cavity in the gas phase. The source of the gas is either via the orthonasal route (from in front of the nasal cavity {see Figure 2.2}) or via a retronasal route (from behind the nasal cavity, from the mouth).

Flavour molecules perceived at the olfactory epithelium need to be volatilized from the food matrix to reach the olfactory receptors by either the retro- or ortho-nasal route. For example the release of volatiles from the drink tea into the surrounding air, produces the initial, orthonasal aroma (Wright *et al*., 2007). This release process is governed by the mass transfer properties of the tea volatiles, first from the tea leaf into the liquid phase and then from the liquid into the gas phase (the headspace) above the infused tea (Wright *et al*., 2007). As for the retronasal pathway of flavour delivery, the in-mouth release of flavour molecules is of importance as the released quantity of a volatile determines, among other variables, the intensity of aroma sensation (Rabe *et al*., 2004).

The factors that affect retronasal flavour delivery during the eating/drinking process include the muscle actions in the mouth and throat during chewing and swallowing, the tidal airflow into and out of the lungs with the continuous exchange of air from and into the mouth, combined with portioning of flavour molecules from the food matrix into the gas phase (Buettner *et al.*, 2001). The delivery of flavour is also affected by volatiles released from residuals of the food matrix adhering to the throat and the pharyngeal part of the tongue after swallowing (Taylor, 1996; Buettner *et al.*, 2001).

2.2.3 The Stomach

Food enters the stomach from the mouth in the form of a food bolus (a soft wet ball of food made after the mouth has chewed and moistened it). The stomach then acts as a short-term storage reservoir to allow large meals to be consumed quickly and then processed over a period of time. The stomach performs the function of mixing and grinding the digesting food with gastric secretions, resulting in a food form suitable to be presented to the small

intestine. During time in the stomach food undergoes significant chemical and enzymatic digestion and in particular protein digestion. A diagrammatic picture of the stomach is shown in Figure 2.3.

The stomach has three main parts: the top which is called the fundus; the middle which is called the body of the stomach; and the bottom which is called the antrum or pylorus. At each end of the stomach is there is a valve or sphincter. The valve located between the oesophagus and the top of the stomach is called the cardiac sphincter. The valve located between the bottom of the stomach and the duodenum is called the pyloric sphincter (Cancer Research UK website, 2008).

The fundus and body act as a reservoir for undigested material, responsible for the emptying of liquids into the small intestine, whereas the antrum grinds, mixes and sieves solid food and acts as a pump for gastric emptying of solids by propelling actions (Urbain *et al*., 1989). The reservoir function of the stomach is achieved through the flexible volume of the stomach, which can expand to accommodate food up to a volume of approximately 4 litres. The mixing and homogenizing function is achieved through the secretion of gastric juice and stomach contraction, that produces grinding and crushing of foods (Kong *et al.,* 2008). Gastric juice is secreted from glands lining the stomach and contains hydrochloric acid (pH approximately 1.0) and digestive enzymes (Ganong, 2005). The gastric juices penetrate and dilute the food bolus.

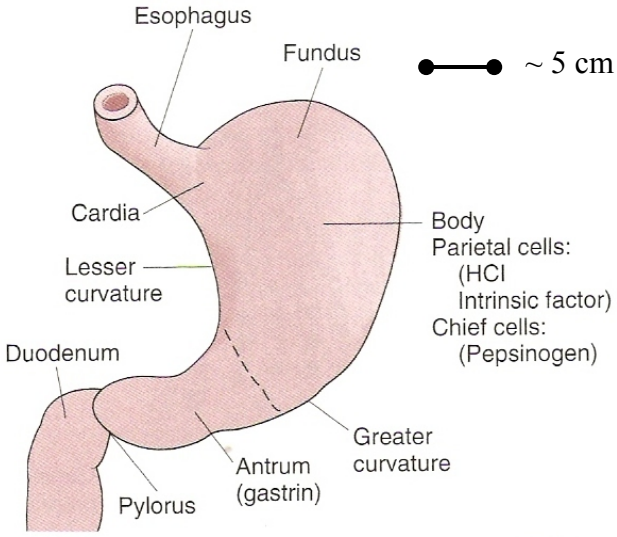

Figure 2.3 Diagrammatic representation of the anatomy of the stomach, mucus is secreted in all parts of the stomach and the dashed line marks the border between the body and the antrum (Ganong, 2005).

Peristaltic waves originate from the stomach wall and spread toward the antrum, mixing and forcing the antral contents toward the pylorus. The pylorus contracts to slow gastric emptying and results in further mixing of gastric contents (Kong *et al,*. 2008). During this time, the stomach transforms its contents into a multiphase slurry called chyme. The chyme is a combination of separate phases of aqueous solutions, fats, and solids. More intense peristaltic waves promote antral emptying, which allows gastric contents, mainly fluid mixed with small particles, to pass through the pylorus and enter the duodenum in the small intestine. The particle size of the food emptied through the pylorus is less than 1 to 2 mm during the fed state (Thomas, 2006). The typical gastric contents in the stomach have a viscosity roughly in the range 0.01 to 2 Pa.s and a density close to that of water (Marciani *et al*., 2000; Abrahamsson *et al*., 2005).

Food structure and texture have been found to affect stomach emptying. For example, studies have shown that the addition of acid-unstable emulsions to pre-processed foods led to accelerated gastric emptying, whereas ingestion of acid-stable emulsions delayed gastric emptying and reduced the amount of food consumed (Marciani *et al*., 2007).

Recent research indicates that gastric emptying is controlled so that about 2 to 4 kcal/min (8.4 to 16.8 kJ/min) caloric content is delivered to the duodenum through a negative feedback mechanism mediated by the duodenal receptors. Meals with similar energy content are emptied from the stomach at similar rates which has been shown using magnetic resonance imaging studies (Faas *et al*., 2002; Gentilcore *et al*., 2006).

Stomach physiology has not yet been fully understood; the stomach wall movement, rheological properties of gastric content, the flow state of gastric fluid, and hydrodynamic/mechanical forces acting on foods require further clarification (Kong *et al.,* 2008).

2.2.4 The Small Intestine

The small intestine was chosen as the area of focus for this study, initially as it is responsible for virtually all nutrient absorption that enters the GI tract within the food and from secretions within the GI tract (Smith and Morton, 2001). The stomach is also important as this provides the input fluid (chyme) of a certain composition and rate into the small intestine, as described in Section 2.2.3.

The small intestine is shown in diagrammatic form in Figure 2.4 and more detail of the internal structure is shown on Figure 2.5. The small intestine is a multi functional organ that simultaneously pumps the intestinal contents, maintains a mixed state of the digesting chyme with enzymes, hosts reactions between enzymes and substrates and facilitates the absorption of nutrients. Wall motion in the small intestine is complex as it appears to vary randomly both in space and time (Christensen *et al.*, 1978).

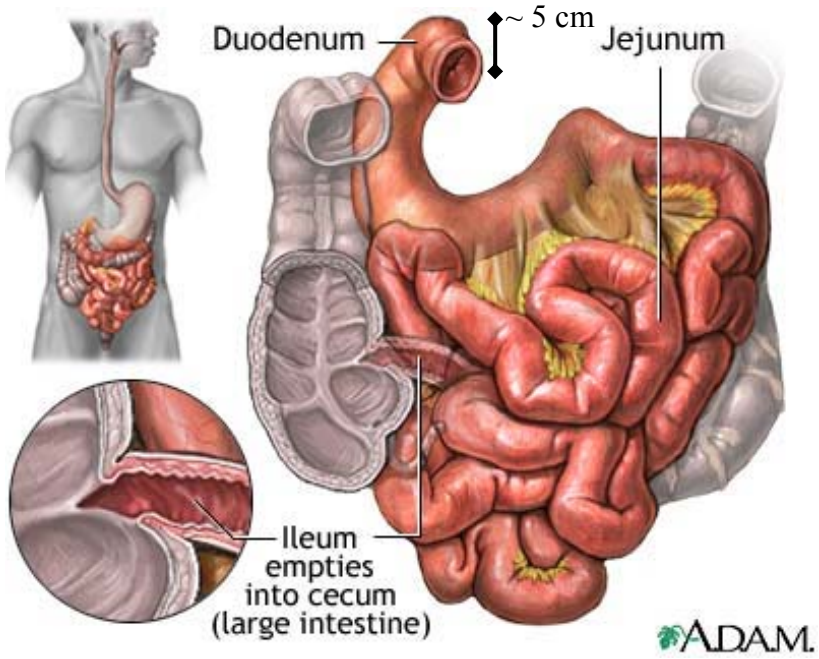

Figure 2.4 Diagrammatic representation of the small intestine (U.S. National Library of Medicine, 2008)

The small intestine is loosely divided up into three parts and the mean total length is said to be 285 cm. The mean length of the duodenum is approximately 25 cm and the jejunum and ileum combined are approximately 260 cm (Ganong, 2005). The average length of the human small intestine will vary depending on sex, height, weight and method of measurement (Ganong, 2005). The transition from the duodenum to the jejunum occurs at point where there is a ligament known as the ligament of Treitz. Arbitrarily, the upper 40%

of the small intestine below the duodenum is known as the jejunum and the lower 60 % the ileum, although there is no sharp anatomical boundary between the two. The ileocecal valve marks the point where the ileum ends by passage into the colon (Ganong, 2005).

The average diameter of the small intestine is approximately 2.5 cm, but it varies from 5 cm in the upper portions of the duodenum to less than 2 cm in the end of the ileum. The various anatomical features of the small intestine are characterised by four distinct length scales that are shown in Figure 2.5:

(a) mesoscale ~10cm (over which there is longitudinal muscle, circular muscle and circular folds on the inside of the small intestine);

(b) submesoscale ~1cm (this scale shows the *villi* - projections which increase the surface area, and the mucosa and submucosa);

(c) microscale ~1mm (this scale shows individual *villus* and crypts); and

(d) submicroscale ~10μm (this scale shows epithelial cells).

The wall of the small intestine is folded and covered with projections called *villi* which increase the surface area. The villi are also covered with *microvilli*. The total exposed intestinal surface area is about 200 m^2 (Ganong, 2005) due to the large increase in area that the villi and microvilli provide.

Bile is made in the liver and stored in the gall bladder and is secreted into the duodenum. It contains bile salts (sodium and potassium salts of bile acids which are synthesised from cholesterol) that emulsify dietary fat into small droplets to increase surface area for lipase activity (Ganong, 2005). Re-absorption of most of the secreted bile salts occurs in the ileum for re-use. The acidic intestinal contents entering from the stomach are neutralised

by a bicarbonate secretion from the pancreas that enters the duodenum to obtain the appropriate pH for small intestinal enzymes (Minekus *et al*., 1995). Pancreatic juice is also secreted into the duodenum and contains a complex mixture of enzymes described in Table 2.2. The pancreatic juice is alkaline and neutralises the gastric acid, raising the pH of the duodenal contents to 6.0 – 7.0. The powerful protein-splitting enzymes of the pancreatic juice (see Table 2.2) are secreted into the small intestine (Ganong, 2005). Approximately 1500 ml of pancreatic juice and 500 ml of bile is secreted per day.

Enzyme	**Activator**	**Substrate**	**Catalytic Function or Products**
Trypsin (trypsinogen)	Enteropeptidase	Proteins and polypeptides	Cleave peptide bonds on carboxyl side of basic amino acids
Chymotrypsins (chymotrypsinogens)	Trypsin	Proteins and polypeptides	Cleave peptide bonds on carboxyl side of aromatic amino acids
Elastase (proelastase)	Trypsin	Elasin, some other proteins	Cleave carboxyl terminal amino acids that have aromatic or branched aliphatic side chains
Carboxypeptidase A (procarboxypeptidase A)	Trypsin	Proteins and polypeptides	Cleave carboxyl terminal amino acids that have aromatic or branched aliphatic side chains
Carboxypeptidase B (procarboxypeptidase B)	Trypsin	Proteins and polypeptides	Cleave carboxyl terminal amino acids that have aromatic or branched aliphatic side chains
Colipase (procolipase)	Trypsin	Fat droplets	Facilitates exposure of active site of pancreatic lipase
Pancreatic lipase	…	Triglycerides	Monoglycerides and fatty acids
Bile salt-acid lipase	…	Cholesteryl esters	Cholesterol
Cholesteryl ester hydrolase	…	Cholesteryl esters	Cholesterol
Pancreatic α-amylase	Cl^-	Starch	Hydolyses 1:4 α linkages, producing α-limit dextrins, maltotriose, and maltose
Ribonuclease	…	RNA	Nucleotides
Deoxyribonuclease	…	DNA	Nucleotides
Phospholipase A_2 (prophospholipase A_2)	Trypsin	Phospholipids	Fatty acids, lysophospholipids

Table 2.2 Digestive enzymes secreted from the exocrine pancreas (Ganong, 2005)

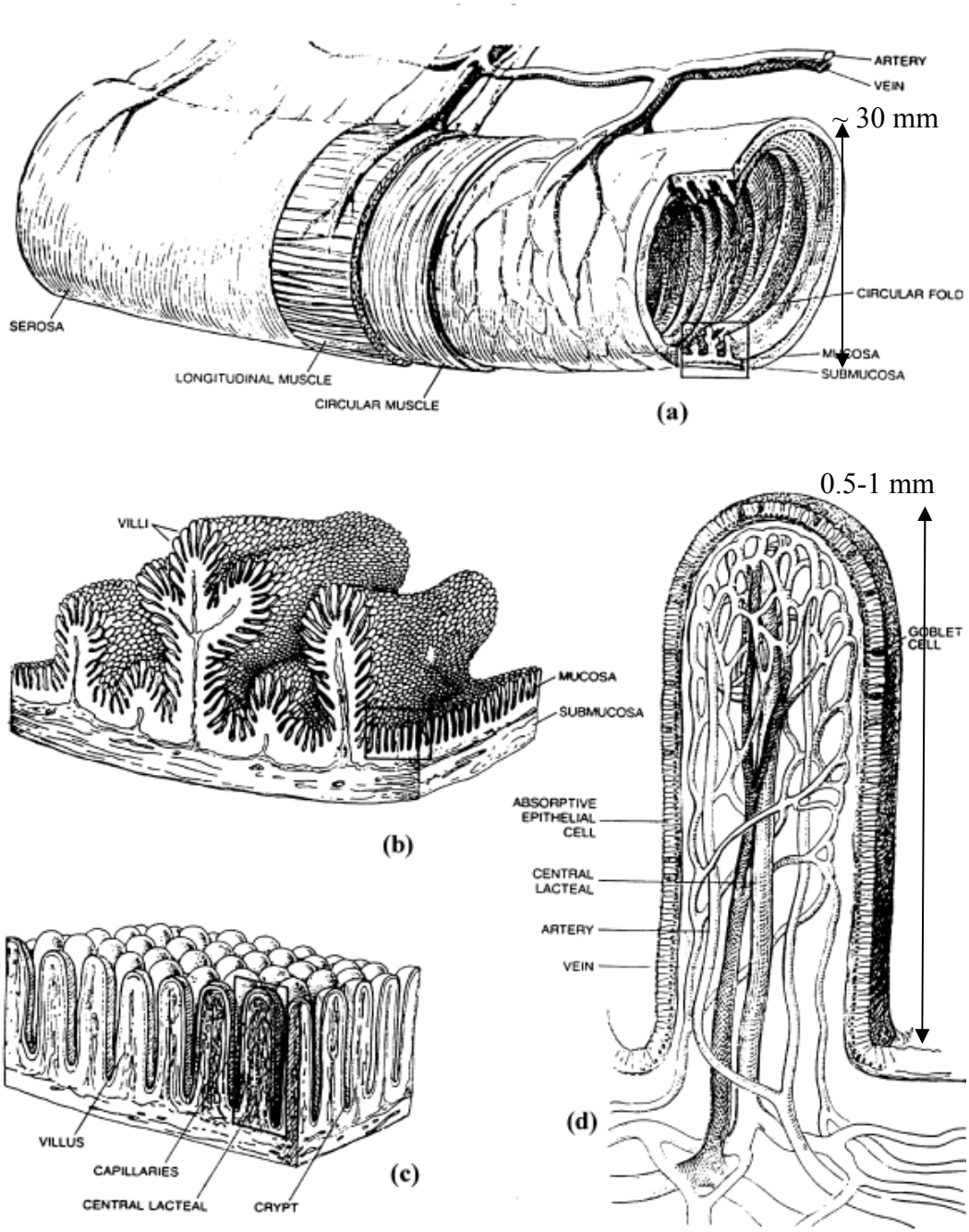

Figure 2.5 The small intestine at varying length scales. (a) mesoscale ~10cm; (b) submesoscale, shows villi (20-40 per mm^2) ; (c) microscale, shows individual villus 0.5-1 mm long; (d) submicroscale (Figure adapted by Stoll *et al.*, 2000 from Moog, 1981)

2.2.4.1 The Cell Membrane of Intestinal Cells

The cell membrane varies between cells but the common features are that it is semi-permeable and generally around 7.5 nm thick (Ganong, 2005). The membrane consists of protein and lipids (mainly phospholipids with a nonpolar hydrophobic tail and a polar hydrophilic head) as shown in Figure 2.6. Each cell is surrounded by a membrane and an example of one of the cells is shown in Figure 2.5.d that shows a goblet cell (the function of which is to secrete mucus). Mucus provides a protective function from the digestive enzymes found in the small intestine and also lubricates the digesting food (Ganong, 2005). Mucus is not shown in Figure 2.6 as it does not form part of the cell membrane.

To be absorbed into the body, nutrient must pass through the epithelium which is a layer of cells that lines the wall of the small intestine and is connected by tight junctions. The wall of epithelium cells is made of a cell membrane which is a lipid bi-layer containing phospholipids, steroids and proteins. The mechanisms of transfer through the membrane are shown in Figure 2.7.

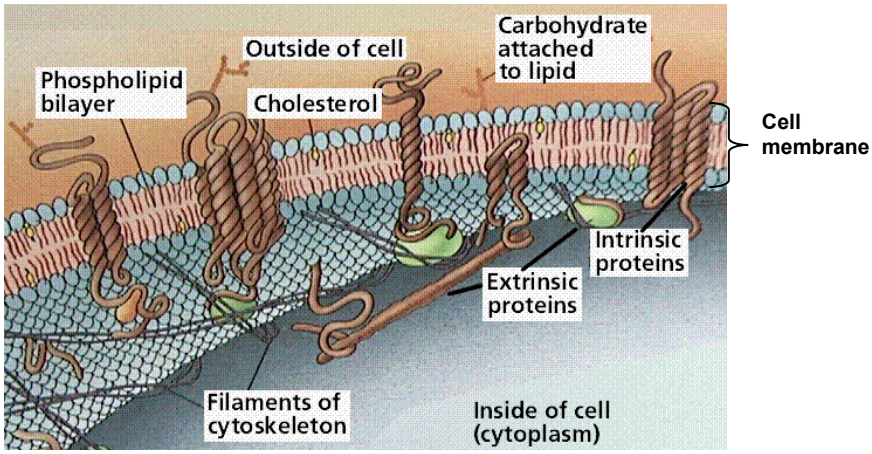

Figure 2.6 Diagram of a cell membrane (Purves, 1998).

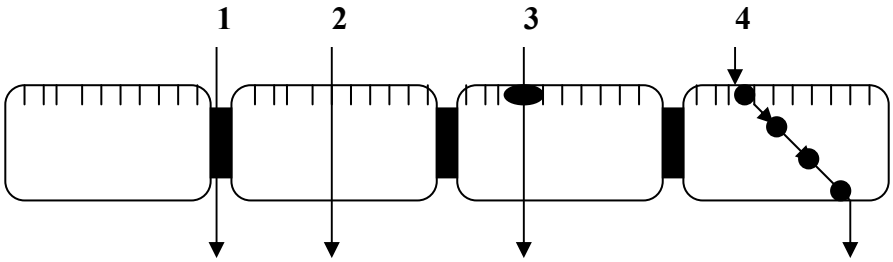

Figure 2.7 Mechanisms of transport across intestinal mucosa

1. *Paracellular transport* is the passage through the tight junctions between intestinal cells. The purpose of the tight junctions are to prevent the passage of molecules and ions through the space between cells.

2. *Passive diffusion* of the compound through the cellular membrane. Examples include the diffusion of oxygen and carbon dioxide, movement of water.

3. *Active transport* using a specific transport protein present in the membrane that recognises the molecule for transport. Active transport requires some form of energy for this process. Examples include the movement of amino acids, iron and glucose.

4. *Transcytosis* is where the molecule causes the cell membrane to bulge inward, forming a vesicle and the vesicle is transported to the other side of the cell and then released. Examples include the transport of insulin and cholesterol into animal cells (Martini, 2006).

Water-soluble nutrients leave the GI tract in the blood (vein in Figure 2.5.d) and travel via the portal vein, first to the liver where some nutrient metabolism occurs (chemical reaction to break down or build the chemicals) and then to the heart. Fat-soluble nutrients enter the lymphatic system (central lacteal in Figure 2.5.d). Unlike blood, the lymphatic system has no pump for fat-soluble nutrients and instead these nutrients eventually enter the vascular system, though they bypass the activity of the liver (Insel, 2004).

2.2.4.2 Movement of the Walls and Chyme in the Small Intestine

Small intestinal motility participates in several ways to facilitate the digestion and absorption of food. Material passing from the stomach to the small intestine is first mixed with digestive enzymes from the pancreas and bile salts from the biliary system by the movements of the small intestinal walls.

Digestion and absorption in the intestine require constant mixing and propulsion of the intestinal contents and also diffusion to and across the absorbing surface of the epithelium (Gregersen, 2002). The movements of the small intestinal walls are responsible for the fluid dynamics of the contents and can be divided into *segmentation contractions* and *propulsive contractions* (Guyton, 1996).

Segmentation contractions occur when a portion of the small intestine becomes filled with digesta (the food and intestinal secretions in the small intestine) and the stretching of the muscle causes one localised concentric contraction in that area (Guyton, 1996).

Propulsive contractions are responsible for propelling the digesta through the small intestine and are known as *peristalsis*, in contrast to the segmentation motion responsible for mixing. Peristalsis is also a reflex response that is initiated when the gut wall is stretched by the contents of the lumen (Ganong, 2005). Peristalsis waves move at a velocity of 0.5 to 2.0 cm/sec and are normally very weak contractions which die out after 3 to 5 centimetres (Guyton, 1996). Figure 2.8 gives a diagrammatic representation of the segmentation and peristalsis movements.

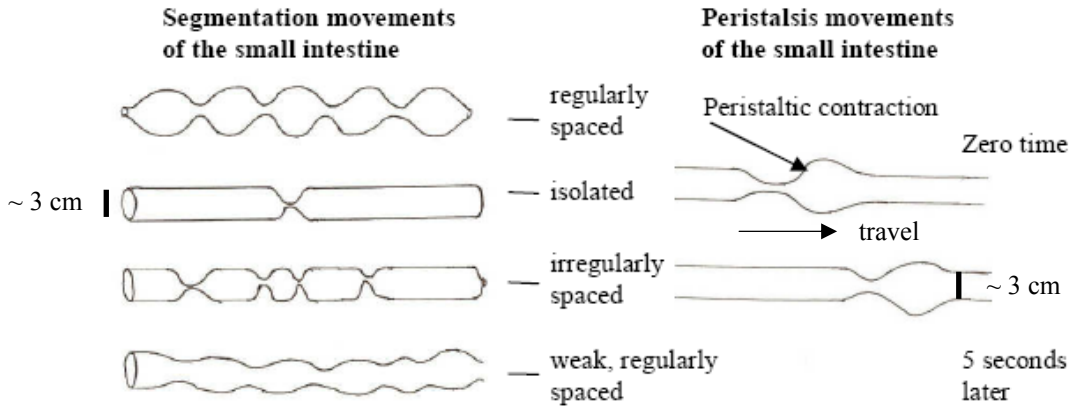

Figure 2.8 A schematic of the segmentation and peristalsis contractions found in the small intestine (adapted from Guyton, 1996). Scale is shown by bars representing ~ 3 cm.

Molecules within the intestinal lumen (the inside of the tube) are transported by diffusion or by convection set up by intestinal contractions which are responsible for the flow of the luminal contents. The movement of the intestinal wall is responsible for the mixing of substrate with enzymes and also the movement of nutrients close to the absorptive epithelium (Macagno *et al.*, 1982).

Macagno *et al.,* (1980) investigated the frequency of the segmentation motion in the small intestine. A bundle of four polyvinyl tubes (1 mm inside diameter and 2 mm outside diameter) were passed through the mouth into the duodenum of fasting human subjects. Pressure transducers were connected at the other ends of the tubes and the pressure variations within the closed tube recorded on magnetic tape. Records were made for several hours after the subject had ingested a glass of skimmed milk. The time between any two successive contractions was then recorded and the results are shown in Figure 2.9. Figure 2.9 shows the frequency of a particular time between any two contractions; the most frequent time between contractions was 5-6 seconds (approximately 8.5 % of the contractions).

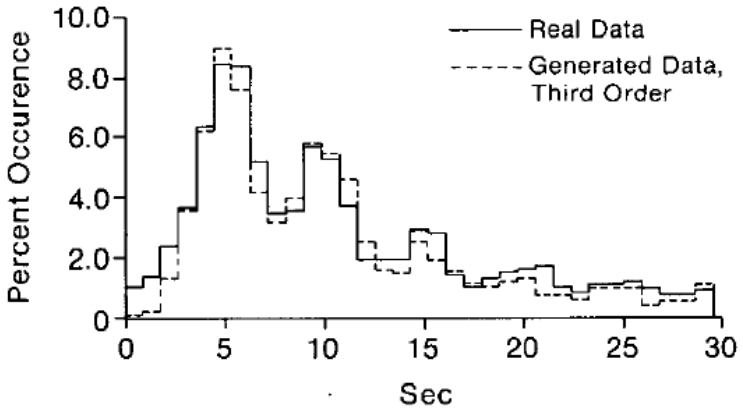

Figure 2.9 Frequency distribution of intercontractile times in the human duodenum (taken from Macagno *et al*., 1980)

The data was further analysed to determine the frequency distribution of contractions one after another at the same location in the human duodenum. The results from this (as shown in Figure 2.10) show the frequency distribution of the time between sequential contractions at a given location. Figure 2.10 shows that almost 70 % of the contractions are isolated events. This information is necessary in attempting a description of the flow induced by contractions. Macagno *et al*., (1980) showed that two successive contractions happen at a given segment only 20 % of the time and for greater numbers of contractions at the same locations the percentage occurrence is less (Macagno *et al*., 1980).

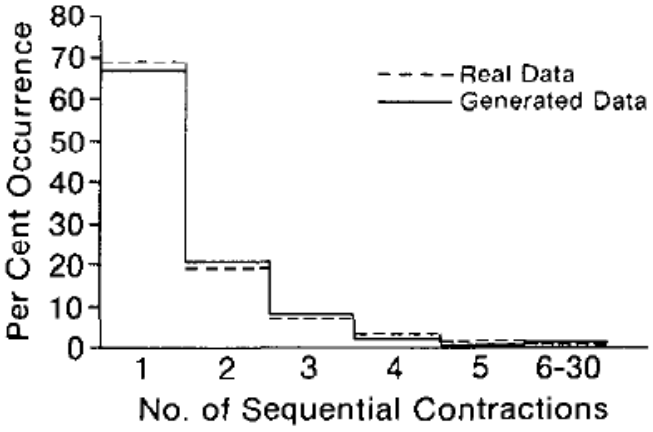

Figure 2.10 Frequency distribution of sequential contractions in the human duodenum (taken from Macagno *et al*., 1980).

2.2.5 The Large Intestine

The large intestine is the portion of the digestive system most responsible for absorption of water from the indigestible residue of food and the fermentation of indigestible food by gut microflora . Figure 2.11 shows the anatomical structure of the large intestine.

The ileocecal valve of the ileum (small intestine) passes material into the large intestine at the cecum. The proportion of the ileum containing the ileocecal valve projects slightly into the cecum. Increases in colonic pressure squeeze the valve shut, whereas increases in ileal pressure open it, therefore effectively preventing reflux of colonic contents into ileum (Ganong, 2005). Material passes through the ascending, transverse, descending and sigmoid portions of the colon and finally enters into the rectum. From the rectum, the waste is expelled from the body (U.S. National Library of Medicine, 2008). The large intestine removes about 90% of the fluid, it converts 1000-2000 ml of isotonic chyme that enters it each day from the ileum, to about 200-250 ml of semisolid faeces.

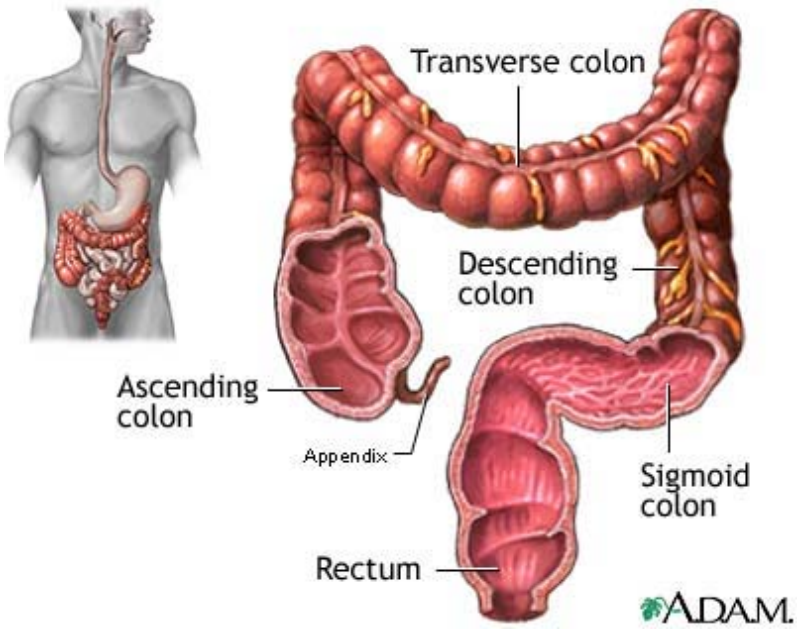

Figure 2.11 Diagrammatic representation of the large intestine (U.S. National Library of Medicine, 2008)

The diameter of the colon is greater than that of the small intestine. Its length is approximately 100 cm and there are no villi on the mucosa. The movements of the colon include segmentation contractions and peristaltic waves similar to those occurring in the small intestine. The segmentation motion mixes the contents of the colon and, by exposing more of the contents to the mucosa, facilitates absorption. Peristaltic waves propel the contents forward towards the rectum.

2.2.6 Conclusion

The small intestine was chosen for this project as the important area of focus from the gastrointestinal tract. The aspects of the small intestine that were intended to be addressed were molecular diffusion and convection from the bulk fluid to the absorptive wall of the small intestine under physiological flow conditions and the overall effect that food formulation had on this. The parameters from the anatomy and physiology of the gastrointestinal tract that were taken forward for use in the design of the small intestinal model are as follows:

(i) the diameter of the model small intestinal section should be approximately 3 cm on the basis that the diameter varies from 5 cm in the upper portion to less than 2 cm in the end of the ileum (Ganong, 2005);

(ii) the intercontractile time between each contraction has been chosen to be 6 seconds (based on the work done by Macagno *et al*. 1980, shown in Figure 2.9), as this is the peak frequency of intercontractile time; and

(iii) segmentation is to be carried out at two separate locations, based on the work done by Macagno *et al*. 1980. Figure 2.10 shows that approximately 70% of contractions occur once and are not succeeded by a sequential contraction.

2.3 Food Design

2.3.1 Introduction

In most industrialised countries, cardiovascular disease and cancer are ranked as the top two leading causes of death. The causes of both diseases have been linked to lifestyle choices and one of the most important is diet. It has been estimated that a healthy diet could prevent approximately 30% of all cancers (Doll *et al.*, 1981; Willet *et al.*, 1995). High cholesterol and obesity are greatly influenced by diet and lifestyle and are costing the United States billions of dollars in health related expenses (Boyer *et al.*, 2004). In 1998, obesity, a risk factor for cardiovascular disease, cancer and diabetes, has been estimated to cost the United States over 92 billion dollars per year (Finkelstein *et al.,* 2003). These diet-related problems could change eating habits, processing technologies and products (Parada *et al*., 2007).

The U.S. Food and Drug Administration (FDA, 2002) has defined *bioavailability* as the rate and extent to which the active substances or therapeutics contained in a drug are absorbed into the blood and become available at the site of action. This definition of bioavailability also applies to nutrients such amino acids, minerals and vitamins available from foods. Bioavailability is different to another term, *bioaccessibility*, which is the total amount of an ingested nutrient available for absorption in the intestine after digestion (Hedren *et al.*, 2002). Faulks and Southon (2005) stated that although all of a nutrient is potentially bioaccessible, in reality very few nutrients are totally converted during digestion into a potentially absorbable form.

Parada *et al*. (2007) stated that food processing such as grinding, fermentation, and/or mild heating may improve bioavailability of certain nutrients, most likely as a result of disruption of the cell walls of plant tissues, dissociation of the nutrient-matrix complexes, or transformation into more active molecular structures. Parada *et al*. (2007) described the case seen in Figure 2.12 where (i) the total amount of a nutrient decreases in the food chain due to chemical degradation during storage and physical losses in processing, while at the same time (ii) the bioavailability may increase as the nutrient becomes more available for absorption.

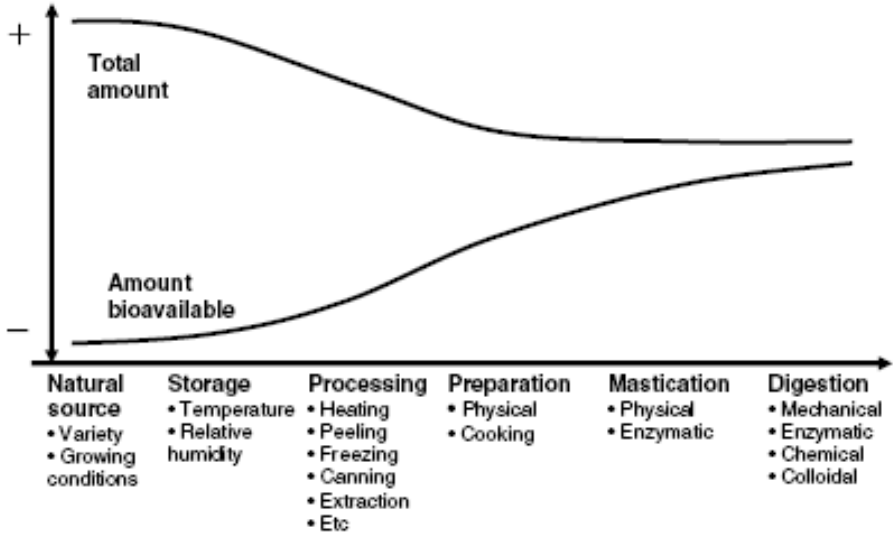

Figure 2.12 Example of a food where the total amount of a nutrient diminishes with time, but the amount bioavailable increases due to suppression of food matrix effects. Taken from Parada *et al*. (2007).

Experiments undertaken by Livny *et al*.(2003), showed that significantly more of the *β*-carotene was absorbed from cooked and pureed carrots (65.1% ± 7.4%) than from the raw vegetable (41.4% ± 7.4%). The release of carotenoids from plant foods occurs only when the cells in the food matrix are disrupted, as is usually the case during food preparation, processing, and/or mastication (Parada *et al*., 2007).

Lycopene, a carotenoid responsible for the red colour of ripe tomatoes, is usually located within cell membranes and its release is a determinant on the bioavailability. Epidemiological studies have suggested that consumption of lycopene may protect against cardiovascular disease and reduce the risk of several types of cancer, most notably those of the prostate, breast, lung, and digestive tract (Omoni *et al.*, 2005). Food processing, such as cooking, or heating may improve lycopene bioavailability by breaking down cell walls, which weakens the bonding forces between lycopene and the tissue matrix, making it more accessible (Parada *et al*., 2007). The result is that lycopene is 2.5 times more bioavailable in humans when present in tomato paste than in fresh tomatoes (Omoni *et al*., 2005).

As described by Parada *et al*. (2007), 'natural' food structures can be classified into four broad categories:

1. fibrous structures assembled hierarchically from macromolecules into tissues for specific functionality (e.g. muscles);
2. fleshy materials from plants which are hierarchal composites of hydrated cell walls (e.g. tubers, fruits and vegetables);
3. encapsulated embryos of plants that contain a dispersion of starch, protein and lipids, assembled into discrete packets (e.g. grains and pulses); and
4. complex fluids such as milk intended for nutrition of young mammals with several nutrients in a state of dispersion.

Many natural foods such as fruits, vegetables, meat and fish are consumed after small amounts of processing and therefore their microstructure is largely dictated by nature.

Parada *et al.* (2007) also describes processed foods (for example, baked and confectionary products, dried pasta, processed meats and others) as being multicomponent structured matrices, where the individual components (such as proteins, fats, carbohydrates) have

been reassembled as colloidal dispersions, emulsions, amorphous or crystalline phases, or gel networks by heating and/or cooling and the application of shear.

The physical properties of the food itself are dictated by the microstructure of the food (Barbosa-Cánovas, 2000). A typical structured food such as margarine or ice cream has a dispersed phase-length scale of the order of 10 μm, composed of liquid or crystalline particulates which exist within a continuous phase. This may be of complex rheology and further structured by polymer or particulate networks (Norton *et al*., 2006).

As described by Norton *et al.* (2006), there are a range of opportunities to structure food for the benefit of the consumer by:

- Controlling the rate of release of macronutrient. An example of this is described by Spiller *et al.* (1984) who suggested that, if fat passes from the stomach into the ileum without being digested, then the body responds by sending signals to the brain slowing the rate of stomach emptying and slowing digestion, the so-called ileal break effect. Norton *et al*. (2006) suggest that emulsions/mixed emulsions could be designed in the future to give all the eating pleasures and performance of present products but with this new functionality;

- The ability to have self-assembled structures inside people. By choosing hydrocolloids that are acid sensitive, e.g. alginate (extracted from kelp) and gel, within microseconds and below pH 2.5, liquid products can be designed to self-structure inside the GI tract (Norton *et al*., 2006). As the liquid alginate solution reaches the stomach, the acidity causes spontaneous gelation. With the use of the appropriate alginate, the stomach content will form a gel, slowing both digestive processes and stomach emptying. This type of product could potentially have a major impact on the obesity problem (Norton *et al*., 2006);

- Encapsulation and targeted release of functional ingredients. An example of a category of functional ingredients are functional peptides that can bind to receptors in the GI tract and influence the feeling of satiety (Wildman, 2001). As described by Norton *et al.* (2006) most of these materials are unpleasant to eat and are often chemically unstable in storage or in use. There is therefore an opportunity for the food manufacturer to encapsulate these materials to allow release at the desired place and rate in the GI tract; and

- The ability to get more functionality from macronutrients. While eating certain types of foods products are required to coat the surfaces of the oral cavity and the throat resulting in the physical feeling of fat and delivering pleasant aftertastes (Appelqvist *et al*., 2002). Appelqvist *et al*. (2002) stated that low-fat emulsions with as little as 5% fat can give the feeling of fat as they break in the thin film between the hard palate and the tongue. Norton *et al.* (2006) stated that to reduce fat significantly, food manufacturers would need to extend the functionality of any fat used in the product. For instance by building smart structures, such as stable duplex emulsions with a thin coat of fat around a structured water phase with an inner core of fat acting as a flavour sink. Another example of obtaining more functionality from macronutrients is to increase the efficiency of sugars in the product by designing microstructures to interact with the receptors for longer and to deliver a larger proportion of the sugar present to the receptor. This thereby gives the perception of sweetness from a low sugar product (Norton *et al*., 2006). The use of sugar is also structural, for instance, the retention of water in cakes and biscuits, to impart succulence on chewing, or for controlling ice formation and ice content in ice cream and frozen desserts (Norton *et al*., 2006).

Norton *et al.* (2006) also noted that convenient foods and snacking are increasingly part of normal behaviour and a result of this is the proportion of digestible carbohydrate has increased at the expense of fibre. The significance of guar gum as a dietary fibre and functional ingredient is described in Section 2.3.2.

2.3.2 Guar Gum as a Dietary Fibre and Functional Ingredient

2.3.2.1 Introduction

Dietary fibre has been defined by the Institute of Food Science and Technology in 2001 as a food material, particularly a plant material that is not hydrolysed by enzymes secreted by the human digestive tract such as those secreted into the small intestine (described in Table 2.2), but that may be digested by microflora in the gut. The types of plant material that are included within the definitions of dietary fibre may be divided into two forms, based on their water solubility. Insoluble dietary fibre includes cellulose, some hemicelluloses and lignin. The other is soluble dietary fibre which includes beta-glucans, pectins, gums, mucilages and some hemicelluloses (Parada *et al*., 2007).

Dietary fibre encompasses very diverse macromolecules exhibiting a large variety of physico-chemical properties. They can be naturally present in food (e.g. in cell walls of vegetables and fruits) or introduced into the food to improve their nutritional properties (e.g. bran in bread products). The properties that are nutritionally relevant are mainly the particle size, the surface area characteristics, the hydration and rheological properties, and the adsorption or entrapment of minerals and organic molecules (Guillon *et al.,* 2000). Among these properties, the viscosity and ion exchange capacity are said to be the main contributors to glucose and lipid metabolic effects (Guillon *et al.,* 2000).

Two physicochemical properties of fibre, viscosity and fermentability, have been recognised as producing beneficial physiological responses (Dikeman *et al*., 2006). Fermentability is mostly associated with the function of the large intestine which is described in Section 2.2.5. The significance of dietary fibre to this project is that certain soluble dietary fibres form viscous solutions. These solutions are formed to create a biopolymer network through the fluid to reduce the rise in postprandial (after eating) glucose and insulin levels in man (Jenkins *et al.*, 1978). The exact mechanisms behind the reduction form part of this study. The dietary fibre of interest as part of this project was guar gum and this is covered in more detail in the following section.

2.3.2.2 Guar Gum and Glucose Absorption

In the 1970s Jenkins *et al.* (1978) investigated the dietary fibres with the greatest potential use in diabetic treatment. Subjects were given glucose solutions with or without the addition of different dietary fibres (guar gum, pectin, gum tragacanth, methylcellulose, wheat bran). The subjects had venous blood samples taken at time of fasting and 15, 30,

45, 60, 90, and 120 minutes after the start of the meal, for analysis of glucose and insulin. The results from this work showed that guar gum was the only substance that significantly decreased the percentage maximum rise in blood glucose (by 50 $^{+}$/. 6 %; P <0.01).

During the first hour the area under the blood glucose curve was significantly reduced by guar (68 %; P <0.05), tragacanth (34 %; P <0.01) and methylcellulose (29 %; P <0.05). There was positive correlation between the viscosity of the individual substances and the mean percentage reduction of the maximum rise in blood glucose concentration (r=0.926; n=6; P <0.01). This can be seen in results shown in Figure 2.13 below. The differences in the serum insulin response with the different fibres followed the same pattern as the blood glucose concentrations. Jenkins *et al.* (1978) concluded that viscosity is the most identifiable property of dietary fibre that is related to its action in reducing postprandial glycaemia, but offered no conclusive explanation.

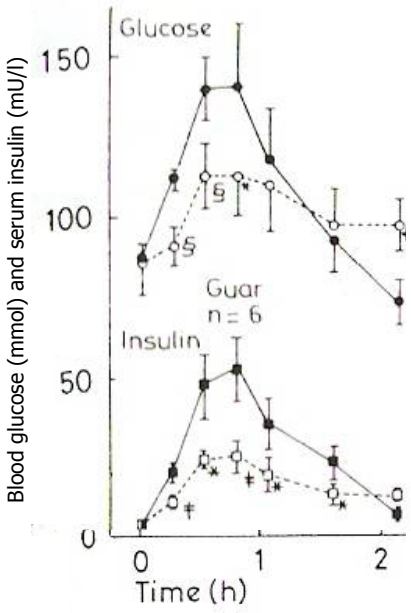

Figure 2.13 Mean blood glucose and serum insulin concentrations of volunteers after taking control and guar gum containing test meals (taken from Jenkins *et al*., 1978)

Studies by Blackburn *et al.* (1984) began to investigate the mechanisms responsible for the lowering effect of guar gum on postprandial hyperglycemia in diabetic humans, although they stated that the mechanisms responsible for this effect remained controversial. Possible mechanisms considered by Blackburn *et al*. (1984) were (i) that viscous polysaccharides act by delaying gastric emptying and thus slowing delivery to the small intestine; and (ii) viscous polysaccharides improve glucose tolerance by reducing the rate at which glucose is absorbed from the intestine (Blackburn *et al*., 1981 and Johnson *et al*., 1981). A possible mechanism for the reduction in absorption rate is that the viscosity impairs mixing, which would have an effect on molecular convection and also change enzyme/substrate interaction if reactions are involved. It is also possible that there is a binding between the absorptive molecules and the guar, or binding with the enzyme where reactions are involved.

Blackburn *et al.* (1984) carried out experiments on four main areas and summaries of the experiment methods and results are described below:

1. Measurement of gastric emptying and glucose tolerance. Human subject ingested a 250 ml drink containing 50 g of glucose and 50 μmCi of ^{99m}Tc-lableled sulphur colloid, with or without 14.5 g of guar gum. The rate of gastric emptying was determined by monitoring the decline in radioactivity over the fundus of the stomach with a gamma camera. Venous samples were taken at 10 minute intervals over the 2 hour period and analysed for glucose and total insulin.

   It was found that addition of guar gum to the glucose-containing drink, resulted in mean glucose concentrations significantly lower at 10, 20, 30, 40, 50 and 60 minutes after the drink was taken. This is shown in Figure 2.14. Studies showed no apparent correlation between the change in half time for gastric emptying and the change in blood glucose induced by guar gum (Blackburn *et al.*, 1984).

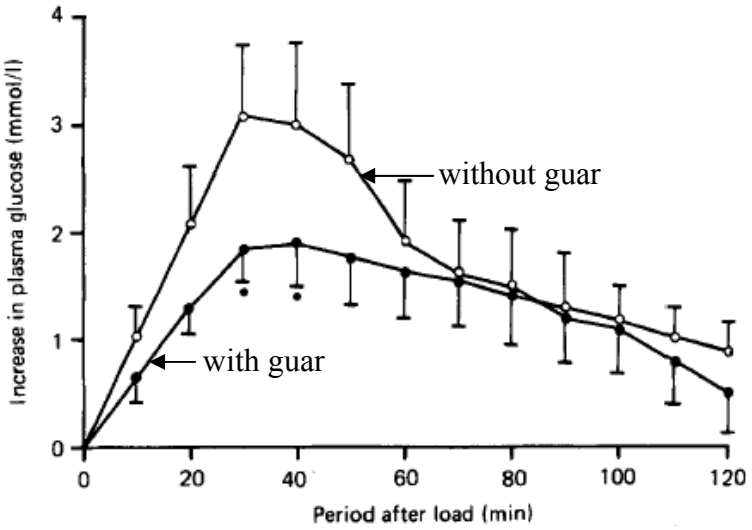

Figure 2.14 Blood glucose levels of human subjects following ingestion of 50g glucose in 250ml orange drink, with (●) or without (○) 9g guar gum. Results are expressed as a mean with the standard errors of six observations. Figure taken from Blackburn *et al.,* 1984.

2. Measurement of intestinal absorption of glucose, fluid and electrolytes. Intestinal absorption was measured by steady state perfusion technique using five lumen intestinal tubes. A solution containing glucose, NaCl and a non absorbable marker was continually infused. Samples were aspired back from a point 25 cm downstream of the infusion point. A 45 minute equilibrium period was given followed by a control study period of 1 hour. A further 30 minute equilibrium period was given and then a 1 hour test period was carried out where a control solution containing 6 g of guar per litre was infused. Finally the control solution was infused for a further 30 minutes equilibrium and then 1 hour study period. Samples of the infusate were analysed for glucose, sodium, chloride and the non absorbable marker. Absorption rates were calculated from this.

   Results showed that the addition of guar gum to the perfusates containing glucose significantly reduced the rate of glucose absorption from the small intestine compared with the initial control period. In the final control period, glucose absorption rates returned to the initial, pre-guar levels in most subjects. This is shown in Figure 2.15 (Blackburn *et al*, 1984).

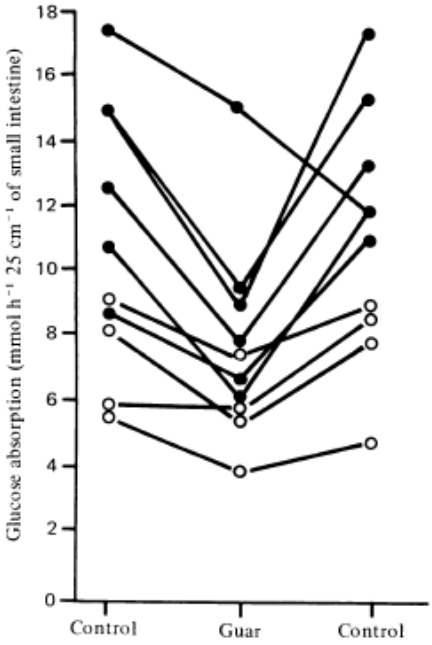

Figure 2.15 Effect of guar (6g/l) on glucose absorption from the jejunum in 10 normal volunteers: (●), infusate containing glucose at 30 mmol/l; (○) infusate containing glucose at 15 mmol/l (Blackburn *et al.*, 1984).

3. Unstirred water layer measurement. Experiments were carried to investigate the effect of guar gum on the thickness of the unstirred water layer and kinetics of glucose absorption in the jejunum and were carried out using an electrical method. 50 ml of solution with and without guar gum was infused over a 30 minute period into the duodenum. The potential difference across the wall of the small intestine was recorded. The measurement of the half-time for the attainment of the diffusion potential was used to estimate the thickness of the unstirred layer.

   Results showed that solutions containing guar did not produce any significant changes in unstirred layer thickness (Blackburn *et al.*, 1984).

4. Effect of different concentrations of guar on the diffusion of glucose from guar/glucose mixture. Dialysis bags were filled with 2 ml of a glucose solution containing various amounts of guar gum (0, 2.5, 5, 7.5, 10 and 15 g/litre). The dialysis bags were placed in a beaker containing water that was stirred. Samples were withdrawn from the beaker at 10 minute intervals for up to 3 hours and analysed for glucose. The half time for glucose to equilibrate with the external solution were determined (Blackburn *et al.*, 1984).

   Results showed that increasing the concentration of guar in the dialysis bags reduced the rate at which glucose attained equilibrium with the external media, as seen in Figure 2.16. However at concentrations of above 7.5 g/l , further increases in guar concentration had no further effect on glucose diffusion (Blackburn *et al.*, 1984).

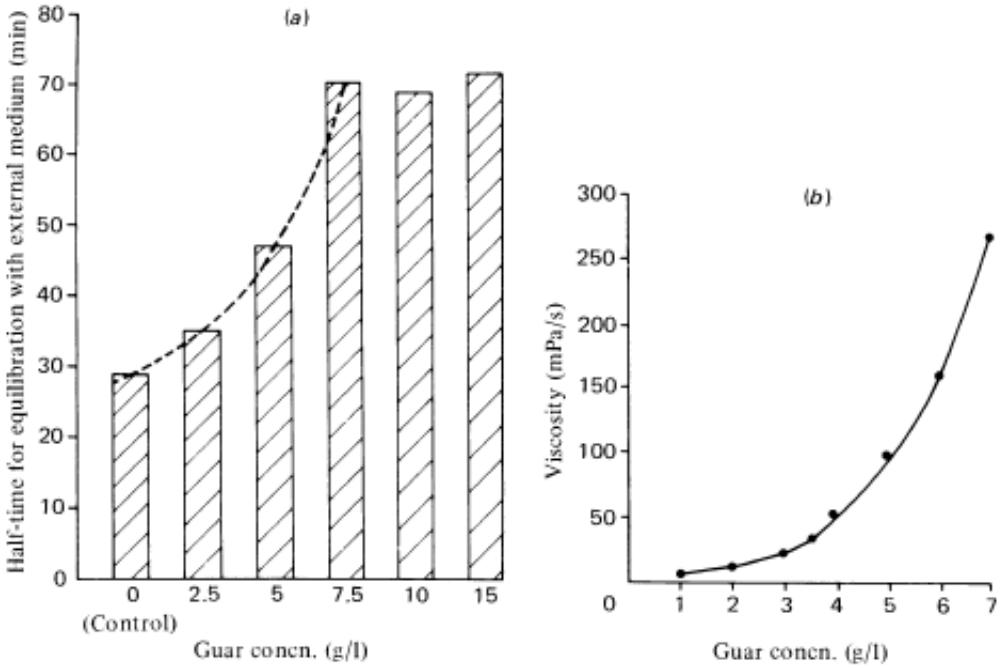

Figure 2.16 Effect of guar gum on glucose diffusion: (a) shows the time for the solution in the dialysis bag to equilibrate with the outside solution; (b) relates the viscosity produced by the guar gum as function of guar concentration. Courtesy of Blackburn *et al.,* (1984).

Blackburn *et al*. (1984) proposed that when guar/glucose mixtures are present in the intestine, viscosity-related reductions in convective solute movement occur throughout the lumen and are responsible for the inhibitory effect of guar on glucose absorption. They also hypothesised that these effects are likely to be more important when the luminal contents are non-homogeneous, as in the case of partially digested food mixtures, since access of pancreatic enzymes to their substrates may also be restricted, with possible decrease in rates of digestion (Blackburn *et al.*, 1984).

Edwards *et al*. (1988) investigated the mechanism by which the inclusion of guar gum into carbohydrate meals reduces the postprandial blood glucose levels in human subjects. They

describe the two mechanisms that bring nutrients into contact with the absorptive epithelium:

i) intestinal contractions create fluid movement and convection currents, which mix the luminal contents, bringing material from the centre of the lumen close to the epithelium; and
ii) nutrients have to diffuse across the thin relatively unstirred layer of fluid lying adjacent to the epithelium.

The aim of the experiments carried out by Edwards *et al.* (1988) was to determine the relative importance of these two mechanisms using simple *in vitro* models. The effect of guar gum on diffusion was assessed by measuring the electrical conductivity of unstirred saline solutions containing increasing concentrations of guar gum. Results showed that incorporating guar in 0.45 % and 0.9 % saline solutions in concentrations of up to 1 % w/v, had no significant effects on the conductivity. The effect of guar gum concentration on the time taken for two saline solutions to mix was investigated, by bringing two saline solutions of different saline concentrations (0.45 % and 0.9 %) but the same guar concentration (either 0, 0.5, 0.75 or 1 % w/v) into contact and mixing. The conductivity was monitored for 10 minutes and the time taken for conductivity to reach a stable value was used as a measure of mixing time. The time taken for complete mixing to occur was directly correlated with viscosity of the solutions.

Edwards *et al.* (1988) also investigated the effect of guar gum on the movement of glucose from a section of dialysis tube under different conditions of mixing. This was carried out using a simple *in vitro* model that mimicked intestinal contractions. The dialysis tubing (12

cm x 1.5 cm) was part filled with the sample fluid (15 ml) and tied at each end and anchored in a trough containing 175 ml of water. Intestinal contractions were simulated by using two pairs of cylindrical paddles at each end of the tubing where one swept the fluid forward and the other swept it backwards. The model could be set to give 36 to 72 contractions per minute. The appearance of glucose in the external solution was monitored every 15 minutes and each experiment lasted 90 minutes. Results showed that the appearance of glucose in the external fluid was significantly reduced by the presence of guar gum of both 36 and 72 contractions per minute. Doubling the rate of contraction significantly increased the appearance of glucose in the external fluid in the absence of guar ($P < 0.05$), but had no significant effect on glucose appearance in the presence of guar (as seen in Figure 2.17).

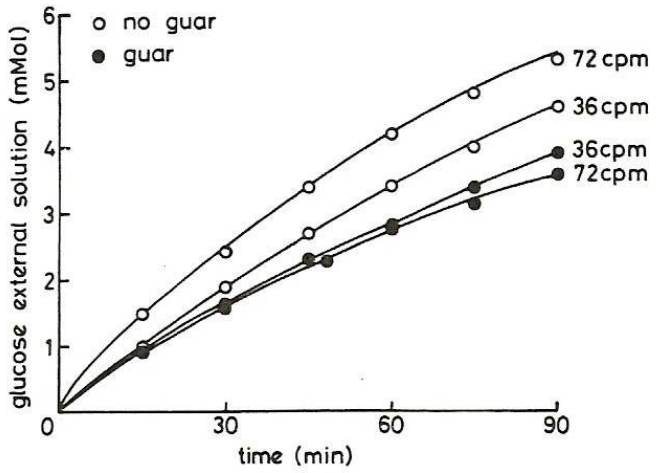

Figure 2.17 Effect of 1 % guar gum on the movement out of a dialysis tube under different mixing conditions (36 and 72 contractions per minute); (○) control, (●) 1 % guar gum (Edwards *et al*., 1988).

Ellis *et al.,* (2000) stated that there is little doubt that the injection of guar gum mixed into a drink or solid food significantly modifies digesta properties at sites along the GI tract. One important feature is the well-characterised behaviour of guar gum for producing a highly viscous network in an aqueous solution at relatively low concentrations. Jenkins *et*

al., (1978), Blackburn *et al*., (1984) and Edwards *et al*., (1988), made observations from solutions containing glucose and polymer alone. The degree of complexity increases when guar gum is ingested with other nutrients or as part of a real food (Ellis *et al.,* 2000). In these systems there is unlikely to be one unifying mechanism to explain precisely the physiological effects of guar gum in the human gut; the physicochemical mechanisms of importance may depend on the type of guar gum and the food that it is ingested in. Ellis *et al.* (2000) also concluded that much of the data seems to indicate that guar gum decreases the rate of absorption of glucose into the hepatic portal vein, mainly by inhibiting the processes associated with digestion and absorption of carbohydrates (gastric function, intestinal transit and mixing, α-amylase-starch interactions, and the movement of the hydrolysed products of starch).

There is contradictory evidence for the effect that guar gum has on gastric function. Gastric emptying studies by Blackburn *et al*. (1984) indicate that guar gum reduces the rate of emptying of a meal from the stomach into the small intestine and this is supported by several other studies such as those by Leclere *et al.,* (1994) and Torsdottir *et al.,* (1989) in experimental animals and human volunteers. However, other studies have shown that gastric emptying is unaltered or even accelerated by the presence of guar gum (Ellis *et al,* 2000). More importantly some of the early experiments did not indicate an association between gastric emptying rate and postprandial hyperglycaemia in humans (Blackburn *et al*., 1984). In contrast Torsdottir *et al*., (1989) demonstrated strong positive correlation between the slowing of the gastric emptying rate and the lowering of the rise in blood glucose. Ellis *et al.,*(2000) stated that contradictory results from the gastric-emptying experiments are probably due to differences in the types and mode of administration of

guar gum being tested, the proportion of solids and liquids in the meals consumed, and the techniques used for measuring gastric emptying. They also describe the difficulties in evaluating the pattern of gastric emptying of solid and liquid phases of digesta into the duodenum, especially when guar gum is added to the test meal.

The intestinal transit time and mixing has been shown to be affected by the presence of guar gum. Ellis *et al.* (2000) described that an inhibition of the rate of flow of digesta within the small intestine will inhibit the physical mixing of nutrients and enzymes (e.g. pancreatic amylase). This reduces not only the rate of digestion, but also the movement of nutrients from the lumen to the mucosal epithelium. Ellis *et al.* (2000) also stated that the effect of guar gum on mixing behaviour of digesta at different sites of the GI tract has yet to be investigated, but was likely to be extremely complex. It has been suggested that an increase in viscosity of digesta produces laminar or 'streamline' flow rather than turbulent or disordered flow, which is characteristic of less viscous fluids and facilitates efficient mixing of digesta in the GI tract (Macagno *et al*., 1982). Ellis *et al.* (2000) speculated that laminar-type mixing under viscous conditions from the presence of guar gum would probably reduce the rate at which nutrients are presented to the epithelial surface in comparison to without guar gum.

2.3.2.3 Viscosity of the Intestinal Contents

Evaluating the viscosity of fluid digesta from the stomach and small intestine of monogastric animals, is complex and difficult. Shear rates in the GI tract have not been determined adequately and they are thought to vary considerably with location and motility

within the GI tract. Therefore, defining of viscosity characteristics is difficult (Dikeman *et al*., 2006).

Many researchers have measured viscosity of digesta from experimental animals at only one shear rate, making comparison difficult. For example, in twelve separate studies conducted to measure digesta viscosity in hamsters, rats, chicks, salmon, humans and pigs, different shear rates were used, ranging from 0.005 to 90 s^{-1} (Dikeman *et al.*, 2006). As shear rates of digesta within the GI tract are not known, it is difficult to interpret viscosity values where they are often dependant on shear (Dikeman *et al*., 2006).

Ellis *et al.* (1995) measured the viscosity of digesta removed from the intestine of a pig. The animals were fitted with cannulas located in the mid-jejunum region, about 2.0 m downstream from the exit of the stomach, to collect digesta. The viscosity was then measured at five shear rates and estimates of the zero-shear viscosity was made. The results of the feeding trial showed that guar gum at concentrations of 2 and 4 g per 100g diet, incorporated into either liquid semi-purified (SP) diet, substantially increased the apparent zero-shear viscosity in the mid-jejunum (Figure 2.18) (Ellis *et al.*, 1996).

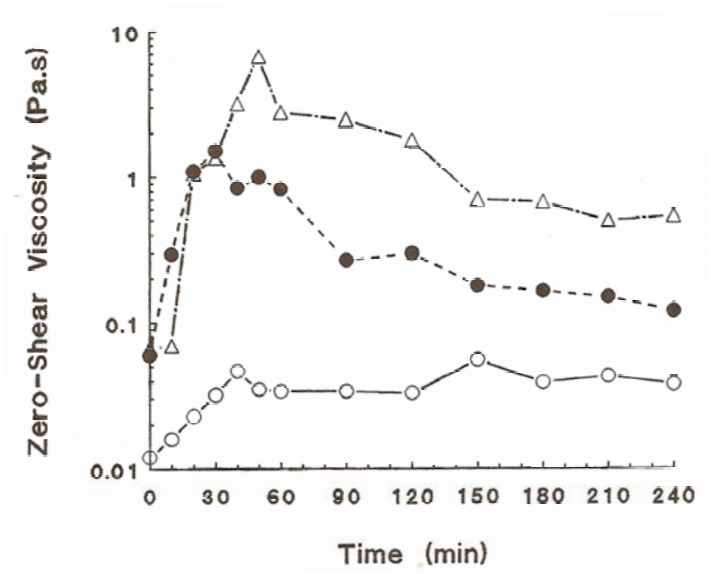

Figure 2.18 Zero-shear viscosity of jejunal digesta in pigs fed control semi-purified (SP) diet supplemented with 2 g guar gum/100 g of diet (-- ●--); and SP diet supplemented with 4 g guar gum/ 100 g of diet (- Δ-). Viscosity measurements taken at fasting and 12 postprandial time intervals after start of consumption of experimental diets. Values are means for four pigs. (Data taken from Ellis *et al*., 1996).

2.3.2.4 Enzyme-Substrate Interactions

Guar gum is likely to influence the hydrolytic action of pancreatic amylase on starch in the gut lumen in a number of ways. Ellis *et al.* (1996) found that an increase in viscosity produced by the guar gum inhibited mixing and movement of dissolved components (nutrient and enzymes) and particulate material (food particles and starch granules) in the gut lumen, thereby minimising interactions between enzyme and substrate. Early studies of amylase-starch interactions, often using pure samples of substrate, demonstrated that guar gum can inhibit the activity of pancreatic amylase and other enzymes (Flourie, 1992). The precise mechanism by which guar gum influences the action of pancreatic amylase on starch is still unknown. Detailed kinetic studies are required to facilitate the understanding of this (Ellis *et al.*, 1996).

2.3.2.5 Lipid Absorption

A major risk factor for development of atherosclerosis (hardening of an artery) and coronary heart disease is prolonged elevation of blood lipids (Behall, 1997). Over 30 years ago, the work of Farenbach *et al.* (1965) (cited in Ellis, 2000) demonstrated for the first time that guar gum elicited a plasma-lowering of cholesterol effect in human subjects, a result that has been repeated several times subsequently (Ellis *et al.*, 2000). Results from animal studies suggest that the viscosity in the gut is an important determinant of the hypercholesterolemic effect of guar gum (Gallaher *et al*.,1995).

2.3.2.6 Summary - Guar Gum as a Dietary Fibre and Functional Ingredient

In relation to this study, the effect of guar gum on the viscosity, the mixing of intestinal contents, the delivery of nutrients to the intestinal wall and on nutrient diffusion, have been identified for further investigation. The rate limiting step controlling nutrient absorption rates has been shown (see Figure 2.14) to be affected by dietary fibre that has reduced the peak in plasma glucose after consuming a glucose drink. The mechanism of this is unclear. There has been debate on this issue as viscous polysaccharides can affect several processes within the small intestine, many of which would have an impact on absorption. Understanding the exact relation between viscosity and the delivery of nutrient to the intestinal wall using an *in vitro* model of the process conditions in the small intestine is of key importance and has been addressed here (see Chapters 5 and 6).

2.4 Chemical Engineering in the Small Intestine

2.4.1 Introduction

Intestinal motility in the small intestine must affect the fluid flow profiles of the digesta. However, the digesta is subject to widely different shear rates and other deformation modes such as the squeezing of the digesta at different sites of the gut and at different times (Ellis *et al.*, 1996). The transport phenomena in the small intestine are non-Newtonian fluid flow, convective mixing and diffusion of nutrients. In addition, enzymatic digestion of complex nutrients takes place, as discussed in Section 2.2.4, that breaks them into more simple nutrients that can be absorbed by the body.

Digestion and absorption in the intestine require the mixing of the intestinal content and diffusion to the absorbing surface of the epithelium (Gregersen *et al.*, 2002). To influence these processes it is important to understand the fluid properties of the chyme in the small intestine for the shear rates and flow profiles encountered in the GI tract.

Shear rates and flow profiles have not been well established for the human small intestine, although there is some information from other animal models. However, this has been collated by observing small intestinal wall movements, combining on videotape the luminal pressures, outflow and wall movements of isolated segments of guinea pig ileum, followed by modelling the expected flow profiles numerically (Jeffrey *et al.*, 2003).

Saline solutions were used and modelled for the work done by Jeffrey *et al.*, (2003). These are Newtonian and therefore do not exhibit the larger and shear dependant viscosity of the guar gum formulations used in the work of Blackburn *et al*. (1984). The numerical findings

of Jeffrey *et al.* (2003) showed downstream and reverse flow (shown in Figure 2.19) and vortical flow patterns that redistributed particles and mixed liquids. They also found that contractions generated pressures and shear stresses (maximum magnitude of 1.2 Pa), in particular along the moving section of the wall.

The fluid dynamics and molecular delivery in the small intestine are described here. The section is divided into three parts: (i) fluid flow, (ii) mixing and (iii) molecular delivery. It is the intention to describe the fundamentals of these processes in relation to the digestion and absorption of food in the small intestine.

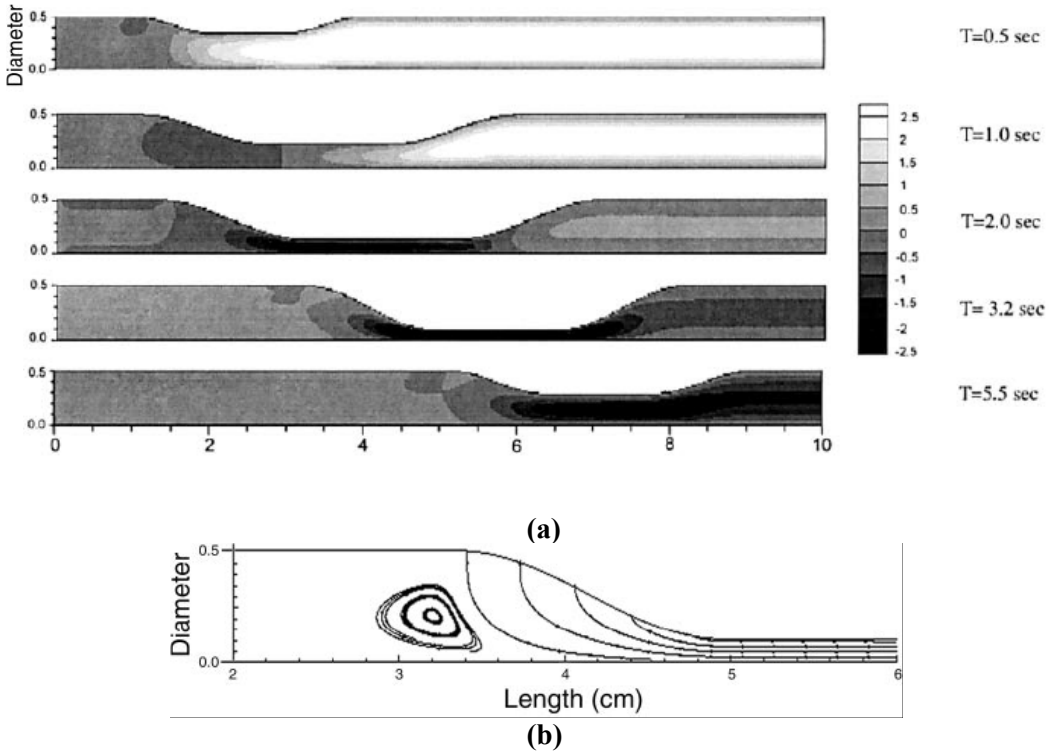

(a)

(b)

Figure 2.19 Data of Jeffery *et al*., (2003) for simulations of water flow in a model gut segment. Images are of radial sections of the gut.

(a) Axial velocity profiles. In the first second, the contraction produces primarily downstream flow. Between 2.0 and 3.2 s, flow reverses in the coapting segment, presumably because the propagation velocity of the contraction exceeds the outflow velocity. At 5.5 s, backflow occurs as fluid pooled in the receiving segment and the outflow cannula redistributes into the remainder of the segment as the contraction waves. Flow in both the receiving (downstream) and the contracting segment is mostly laminar, with high flow rates at the core and low flow rates at the periphery. Perturbations of this flow pattern and turbulences occur, particularly in the trail of the upstream shoulder of the contraction. This is shown in greater detail in Figure 2.19 b. (White contour corresponds to maximum forward velocity, whereas black contour represents maximum reverse velocity. Velocity is in cm/s, according to the greyscale bar on the *right*).

(b) Vortical flow pattern during occlusive contraction. As the contraction propagates, it generates reverse flow. Separation of the reverse flow from the upstream end of the contraction sets up vertical flow patterns that enhance luminal mixing. The analysis given here applies to the height of the contraction at 3.2 s; more vortical flow is expected to occur as the contraction wanes, provided there is adequate fluid for backflow to occur.

2.4.2 Fluid Flow

The study of the flow of fluid is based on physical principles, such as the conservation of energy and momentum and on good physical models of the fluid itself (Fryer, 1997). The complex movements of fluids in the human body and specifically the small intestine, for this work, requires the application of these principles of fluid dynamics.

It is possible to divide flows into two types: laminar and turbulent, as seen in Figure 2.20. Laminar flow occurs when a fluid flows in parallel layers without disruption between the layers. In turbulent flow the fluid undergoes irregular fluctuations and circulating vortices result in transference of fluid on a larger scale, with cyclic fluctuations in the flowrate, although the time-averaged rate remains the same. The type of flow is dependant on the velocity, physical properties of the fluid and the geometry of the surface (Coulson and Richardson, 1998).

Engineers frequently use the Reynolds number (Re) to describe the nature of fluid flow. The Reynolds number gives the relation between inertia forces and viscosity forces; for high Re numbers inertia is greater than viscous forces and the flow is turbulent, while when the Reynolds number is low viscous forces are greater and the flow is laminar. Re can be calculated using Equation 2.1. For pipe flow, laminar flow occurs when Re < 2100, while turbulent flow occurs when Re > 10,000.

$$\mathrm{Re} = \frac{\rho v D}{\mu} \qquad \text{Equation 2.1}$$

Where v is velocity (m/s), D is a characteristic dimension such as pipe diameter (m), ρ is density (kg/m^3) and μ is viscosity (Pa s). Study of fluid flow is integral to this work and

theory is detailed further in Chapter 6 on the application of experimental Fluid Dynamic techniques to understand small intestinal flow and mixing, and also in Chapter 6 where computational fluid dynamics (CFD) is used to model the flow profiles expected in the small intestine.

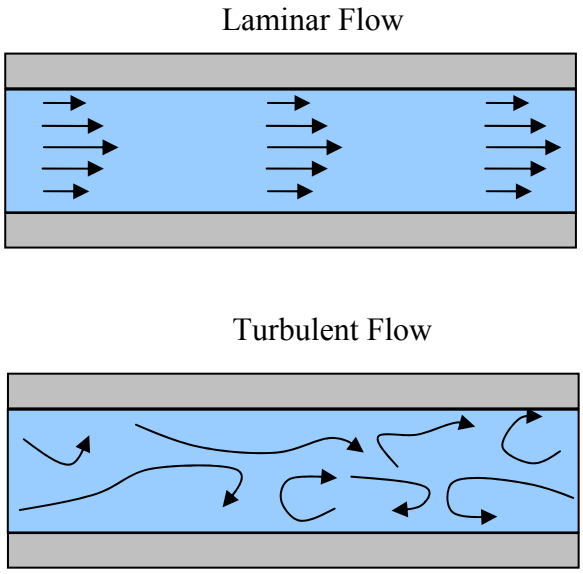

Figure 2.20 A diagram of laminar flow (Re < 2100) and Turbulent flow in a pipe (Re > 10000)

2.4.3 Fluid Mixing

Often, the complexity of both the fluids and the flow type adds sufficient complication that mixing problems are approached on an individual basis. Ottino (1990) gave a generic overview of mixing and chaotic advection, shown in Figure 2.21. The red star in Figure 2.21 specifies the estimated area of interest for this study which is in the region of the small intestine. The rationale for the estimate is that (i) the length scale of interest in the small intestine is a combination of the ranges seen in physiology and chemical engineering (10^{-6} – 0.1 m); (ii) the characteristic Reynolds numbers of the overall flow in the small intestine are in the order of $1x10^{-3}$ – 10, from fluid viscosities of 0.001 for water and up to

6 Pa.s for digesta (given by Roberts *et al.* 1990, shown in Figure 2.18), a flow velocity of 1 cm/min given by Guyton (1996) and diameter of ~ 3 cm given by Ganong (2005).

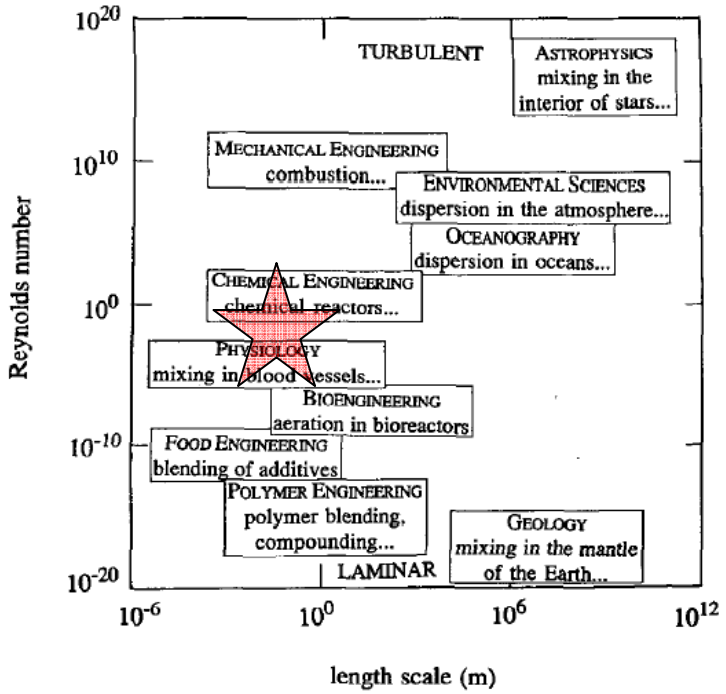

Figure 2.21 A generalised spectrum of problems studied in various disciplines where mixing is important. The red star represents the region relevant to the small intestine. Reproduced from Ottino. (1990).

These low Reynolds numbers would not generate good mixing in a static tube. However flow profiles in the small intestine are generated by segmentation and peristalsis and it is thought that segmentation is significant in mixing (Section 2.2.4.2), as shown in the fluid flow in Figure 2.19. It is necessary to consider the effect of these processes on the flow pattern.

2.4.3.1 Chaotic Mixing

Howes *et al.,* (1991) note there has been considerable work showing that many simple two-dimensional unsteady flows are extremely complex when studied from a Lagrangian view-

point (which summarises the dynamics of the system). Most of their work carried out to study this complexity, termed *chaotic advection*, concentrated on simple flow regimes in simple geometries.

A detailed study of chaotic mixing has been published by Ottino (1989), who adopted a view that from a kinematical perspective (space-time relationship of a given motion without considering the origins of forces), mixing is the efficient stretching and folding of material lines and surfaces. An exact description of mixing is given by the location of the interfaces as a function of space and time. However, this level of description is rare because the velocity fields usually found in mixing processes are complex (Ottino, 1990).

Howes *et al.*, (1991) noted that a method for efficient mixing in tubes is to apply an oscillatory flow to tubes containing a series of periodical baffles. The oscillatory flow promotes chaotic mixing in the tube, in which radial velocity components are significant. Mackley *et al*., (1995) state that an advantage of this system is that mixing effects are decoupled from the mean flow velocity, since mixing is determined by the superposition of the fluid oscillations which can be precisely controlled by varying the frequency or amplitude of oscillation.

Heat transfer enhancement due to oscillatory flow was investigated by Mackley *et al.* (1990). This was carried out by superimposing fluid oscillations on a steady net flow on the tube side of a shell-and-tube heat exchanger, in which periodically spaced orifice-type baffles were inserted. A sevenfold increase in tube-side Nusselt number was achieved (relative to steady, unbaffled flow) in a tube subjected to a low Reynolds number, bulk flow (Re < 200). The Nusselt number is a dimensionless measure of heat transfer

efficiency representing the ratio of convective to conductive heat transfer represented by Equation 2.2.

$$Nu = \frac{h_t D}{k} \qquad \text{Equation 2.2}$$

Where Nu is the Nusselt number, D is the tube inner diameter, k is the thermal conductivity of the fluid, and h_t, is the (tube side) heat transfer coefficient.

Howes *et al*, (1991) state that in steady flow through a periodically obstructed channel, regions of recirculating fluid form in the cavities and there is a strong division between the slow moving fluid in the cavities and the flow of the main stream past the cavities. Several studies have shown that by employing unsteady flow it is possible to induce interaction between the cavity fluid and the main stream, with bulk transport of fluid out of the cavity region and into the main flow stream (Howes *et al*, 1991). This increase in transport of fluid from slow moving regions is the most likely explanation of the enhanced heat transfer seen by Mackley *et al.* (1990). It would be interesting to see if such processes occur in the GI tract.

2.4.4 Molecular Delivery

Molecular delivery, which can be defined as the delivery of a molecule to a specific location at a given time, is usually a combination of diffusion and convection for a dynamic system. Diffusion of a solute though a solvent occurs in all solutions and is a result of localised concentration gradients of solute and solvent.

The rate of movement of material by diffusion is described mathematically by Fick's two laws. Fick's first law is described by Equation 2.3, which relates the diffusion flux $\boldsymbol{J_o}$ (i.e. the flux of material per unit area) to the gradient of the change in concentration (dC_0 / dx), where $\boldsymbol{C_o}$ is the solute concentration. $\boldsymbol{D_o}$ is the diffusion coefficient and x is the length. The negative sign indicates that flow is down the concentration gradient (from high to low concentration).

$$J_0 = -D_0\left(\frac{\partial C_0}{\partial x}\right) \qquad \text{Equation 2.3}$$

Fick's second law (Equation 2.4) describes how concentration changes as a function of time. The rate of change of the concentration as a function of time, is a function of the change in concentration gradient (Cussler, 1997).

$$\frac{\partial C_0}{\partial t} = D_0\left(\frac{\partial^2 C_0}{\partial x^2}\right) \qquad \text{Equation 2.4}$$

A common basis for estimating diffusion coefficients for solutes in solvents (D_0) is the Stokes-Einstein (S-E) equation, which gives diffusion coefficients that are accurate to 20%:

$$D_0 = \frac{k_B T}{6\pi\mu R_0} \qquad \text{Equation 2.5}$$

Where $k_{B,}$ is Boltzmann's constant, μ is the solvent viscosity, R_0 is the solute radius and T is the absolute temperature (Cussler, 1997).

2.4.4.1 Convection

For the systems being investigated as part of this thesis, the flow is 'forced convection', which results from deliberately induced flow, as opposed to 'natural convection' which describes the flow generated by small thermal and density differences.

2.4.4.2 Mass Transfer Coefficient

Often in engineering mass flows are expressed in terms of mass transfer coefficients. While analysing diffusion processes using this approach, it is often assumed that changes in concentration are limited to the small part of the system near the boundaries. For the transfer of mass from an interface into a well-mixed solution, the amount transferred can be modelled as being proportional to the concentration difference between that at the interface and the well-mixed solution:

$$N_1 = K\left(c_{1i} - c_1\right) \qquad \text{Equation 2.6}$$

where the proportionality K is the mass transfer coefficient (m/s). The flux $\boldsymbol{N_1}$ (mol/m^2 s) includes both diffusion and convection. The concentration $\mathbf{c_{1i}}$ (mol/m^3) is that at the interface in Figure 2.22 and the bulk concentration is $\mathbf{c_1}$ (mol/m^3) (Cussler, 1997).

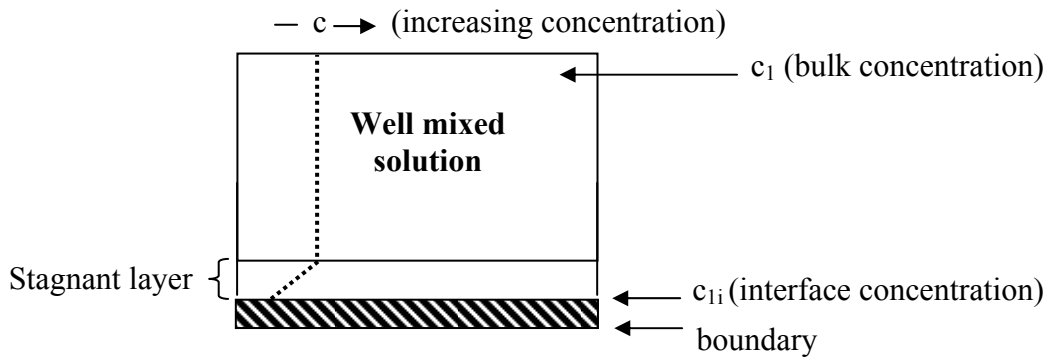

Figure 2.22 A diagram to show the concentration difference in a solution.

Figure 2.23 illustrates how the concentration and hydrodynamic profiles are thought to change at the interface of a system such as the intestine, for the biopolymer fluid. In the case of the mass transfer occurring in the small intestine; a nutrient present in the bulk fluid at the bulk concentration will diffuse towards the membrane (the membrane is assumed to be a representation of the intestinal epithelium and mucous layer, only in that it separates the two compartments and does not attempt to be a physical representation of membrane or mucous layer). The delivery of molecules from the bulk fluid to the surface of the membrane only, as within the body is the parameter that can be modelled physically by the models developed in this thesis, once the nutrient reaches the membrane active biological processes may occur. When modelling the delivery of a nutrient to the membrane wall, the concentration on the recipient side must be used as means of measuring the molecular delivery to the membrane on the food side.

It is appropriate to consider the process of transfer of material from a fluid A on one side of a membrane to another fluid (B) on the other side (as shown in Figure 2.23). There a number of consecutive processes that occur:

- transport from fluid A to the edge of the stagnant layer;
- transfer through the stagnant layer, described by a mass transfer coefficient, k_A (m/s);
- transport through the membrane controlled by diffusion, with the diffusion coefficient D (m^2/s); and
- transfer out through the stagnant layer in fluid B, described by mass transfer coefficient, k_B (m/s).

Therefore the mass flux is (in relation to Figure 2.23) calculated as follows:

$$N_1 = k_A\left(c_A^{bulk} - c_A^{int}\right)$$

$$= D\left(\frac{c_A^{int} - c_B^{int}}{x}\right) \qquad \text{Equation 2.7}$$

$$= k_B\left(c_B^{int} - c_B^{bulk}\right)$$

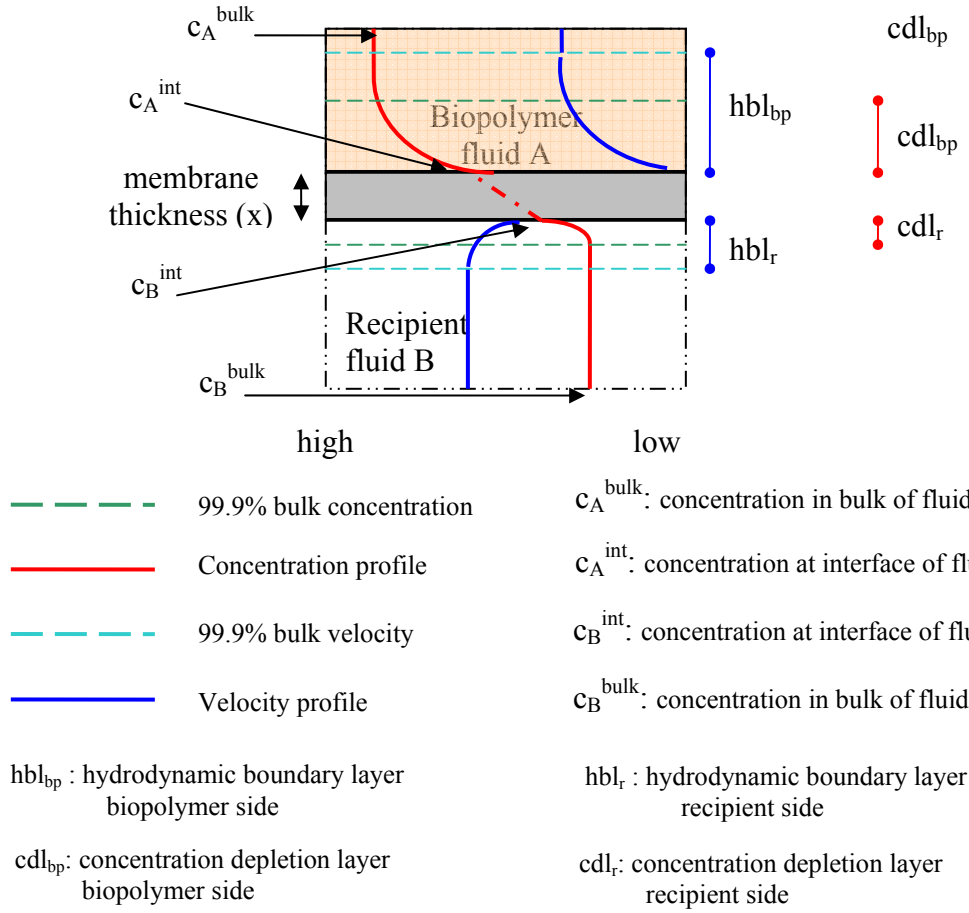

Figure 2.23 Diagram of the hydrodynamic and concentration boundary layers on each side of a membrane.

Which allows an overall mass transfer coefficient:

$$N_1 = K\left(c_A^{bulk} - c_B^{bulk}\right) \qquad \text{Equation 2.8}$$

Which can also be represented by Equation 2.9:

$$\frac{1}{K} = \frac{1}{k_B} + \frac{x}{D} + \frac{1}{k_A} \qquad \text{Equation 2.9}$$

Where K is the overall mass transfer coefficient, k_A is the fluid A side mass transfer coefficient, k_B is the fluid B side mass transfer coefficient, D is the diffusion coefficient through the membrane and x is the thickness of the membrane.

The mass transfer coefficient through fluid A can be described by Equation 2.10:

$$k_A = \frac{D_A}{x_A} \qquad \text{Equation 2.10}$$

Where k_A is the fluid A side mass transfer coefficient, D_A is the diffusion coefficient of the nutrient through the fluid A concentration depletion layer (c.d.l) (taken as that of through water) and x_A is the thickness of the c.d.l on the recipient side (Cussler, 1997).

Mass transfer coefficient on the side of fluid B is described by Equation 2.11:

$$k_B = \frac{D_B}{x_B} \qquad \text{Equation 2.11}$$

Where k_B is the mass transfer coefficient on the side of fluid B, D_B is the diffusion coefficient of the nutrient through the fluid B and x_B is the thickness of the concentration depletion layer.

For mass transfer a similar dimensionless number to the Nusselt number for heat transfer exists. This number is know as the Sherwood number (Sh) and is used in mass-transfer operations to represent the ratio of convective to diffusive mass transport. The Sherwood number is represented by Equation 2.12.

$$Sh = \frac{kL}{D} \qquad \text{Equation 2.12}$$

Where k is the mass transfer coefficient (m/s), L is the characteristic length scale (m) and D is the diffusion coefficient (m^2/s).

The convective mixing of intestinal contents is one of the functions of intestinal motility. In practice little is known about the quantitative nature of this mixing. Mass transfer experiments, visualisation and modelling of the flow, induced mixing by the wall movements, will achieve an insight into the transport and mixing of digesta and how food formulations can affect this.

2.5 Intestinal Models

2.5.1 Introduction

Methods that simulate the gastrointestinal digestion process under laboratory conditions are known as gastrointestinal models (GIMs). They are used as a suitable alternative to *in vivo* assays to determine bioavailability. GIMs aim to reproduce the physiological conditions in the mouth, stomach and small intestine during mastication, digestion and absorption (Parada *et al*., 2007). In general, GIMs fall into two broad categories: *static models*, where the products of digestion remain largely immobile and do not mimic physical processes such as shear, mixing, hydration, and so on, and *dynamic models* which try to include physical and mechanical processes and temporal changes in luminal conditions to mimic conditions *in vivo* (Parada *et al*., 2007). The latter are particularly useful where the physical condition of the digesta changes over time (for example, particle size and viscosity) and take into account some temporal effects not considered otherwise (mixing, diffusion, formation of colloidal phases) (Parada *et al*., 2007).

In this section on intestinal models, *in-vitro* models, computational models and *in vivo* models will be reviewed.

2.5.2 *In-vitro* Models

In-vitro models are a useful tool for modelling the processes and conditions in the GI tract. There are a range of types of model that have been developed and studied to assess the rate, extent and mechanism of intestinal absorption. The types of information that can be obtained from them, together with the advantages and limitations of each method are discussed below. The techniques start at the small scale and progressively become larger.

2.5.2.1 Artificial Membranes

This is a non-biological method that uses artificial membranes to study the transport of molecules across a barrier that is a physiochemical model of the membrane. Two types exist, Parallel Artificial Membrane Permeation Assay (PAMPA) and Bio-mimetic Artificial Membrane Permeation Assay (BAMPA), both of which can only be used to simulate passive absorption of molecules across this membrane. PAMPA uses two compartments separated by a filter impregnated in phospholipids. PAMPA is completely artificial, without pores and active transport systems. BAMPA is similar to the PAMPA model although it uses a mix of lipids that mimic the composition of the cellular membrane of the intestinal cells (0.8% phosphatidylcholine, 0.8% phosphatidylethanolamine, 0.2% phosphatidylserine, 0.2% phosphatidylinositol and 1% cholesterol in 1,7-octadiene). The BAMPA method allows for good prediction of human absorption from passive diffusion. The limitation is that it does not model compounds that are transported by active transport mechanism or that have paracellular transport mechanisms (Suano *et al*., 2002).

2.5.2.2 Cultured Cells

The use of cells in continuous culture as a working model for intestinal absorption has been popular for some time. Three human intestinal adenocarcinoma cell lines, Caco-2, HT29 and T84 cells have gained prominence primarily due to their capability to differentiate in culture. The three types of cell have been used as transport models with T84 to a lesser extent (Dias *et al.*, 1994). Caco-2 is a homogenous cell population derived from the colon. It spontaneously differentiates in culture to resemble cells of the small intestine (see Figure 2.7). For compounds that are transported by a carrier-mediated process, careful characterisation of the cell line is necessary.

The utility of an intestinal absorption model is based on the robustness of correlation between parameters, such as permeability, determined with the model and those parameters obtained *in vivo*. Where Caco-2 cell monolayers are grown on permeable filter supports, with drug appearance being monitored in the receiver compartment of a side-by-side diffusion apparatus, a number of laboratories have correlated permeability with fraction absorbed (Artursson *et al.*, 1991; Stewart *et al.*, 1995). A diagrammatic representation of the use of an *in vitro* method to determine bioavailability involving a digestion/absorption step using a Caco-2 cell culture is shown in Figure 2.24. The disadvantage of the Caco-2 cell line is that they do not produce mucus which could affect the results compared to *in-vivo*.

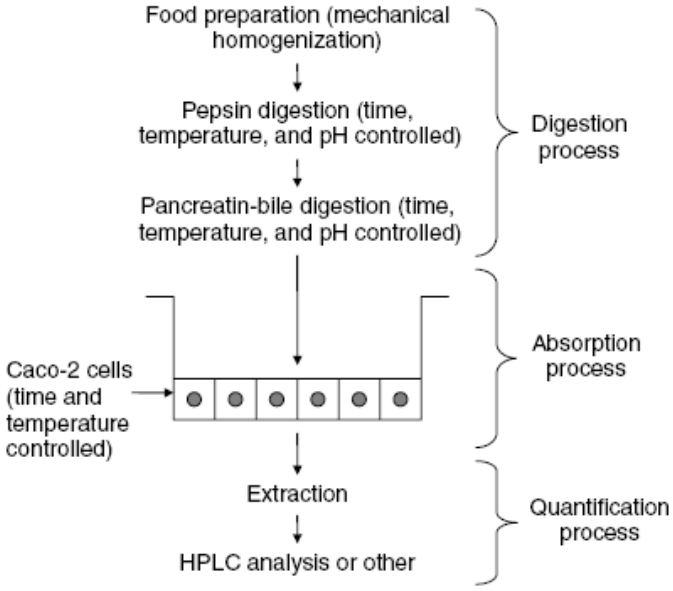

Figure 2.24 Diagram of an *in vitro* method to determine bioavailability involving a digestion/absorption step using a Caco-2 cell culture. Taken from Parada *et al*., (2007).

For the work being carried out here, the movement and delivery of molecules to the intestinal wall and the influence that food formulation can have on this was the area of focus. The movement across the wall of the intestine was considered beyond the scope of the project although an appreciation of the use and application of these methods was required. These techniques (BAMPA, PAMPA and Caco-2) were not easily adaptable to investigate the influence of the material properties and processing on molecular delivery. They are however an important technique to model the whole of the transport across the cell membrane.

2.5.2.3 Large *in vitro* models

At a larger scale, the Netherlands Organisation for Applied Scientific Research (TNO) have developed a Gastro-Intestinal Tract Model (TIM) which is a dynamic computer-controlled *in-vitro* system that mimics the human physiological conditions in the stomach

and small intestine. The TIM comprises of four compartments that represent the stomach, duodenum, jejunum and ileum. Each compartment consists of a glass jacket with a flexible wall inside. The jejunal and ileal compartments are connected with hollow fibre devices containing semi-permeable membranes. Dialysis fluid is pumped through the hollow fibres while the digesta is flowing around the fibres. Digestion products smaller than 500 Da will diffuse through the lumen to the dialysate (Blanquet *et al.*, 2001).

Physiological parameters such as pH, temperature, peristaltic movements, secretion of digestion enzymes, bile and pancreatic juices, and absorption of digested material are simulated. Studies indicate that the TIM shows promise as a useful tool for various research purposes dealing with the availability for absorption of mutagenic, as well as antimutagenic, components in food (Krul *et al.*, 2000).

A schematic of the TIM model is shown in Figure 2.25 and the TIM model is patented in Europe (number, 0642382) and in the USA (number 5525305). When reference is made to the term ‘availability’ it is referring to the concentration within the fluid that is available for absorption. Although a very effective model of the GI tract, the limitation of the model is that it is not capable of measuring the availability for absorption at the absorptive surface of the small intestine and thus does not take into consideration molecular delivery. Another limitation of the model is that the segmentation motion is not simulated which may lead to flow and mixing conditions in the small intestine not being fully reproduced.

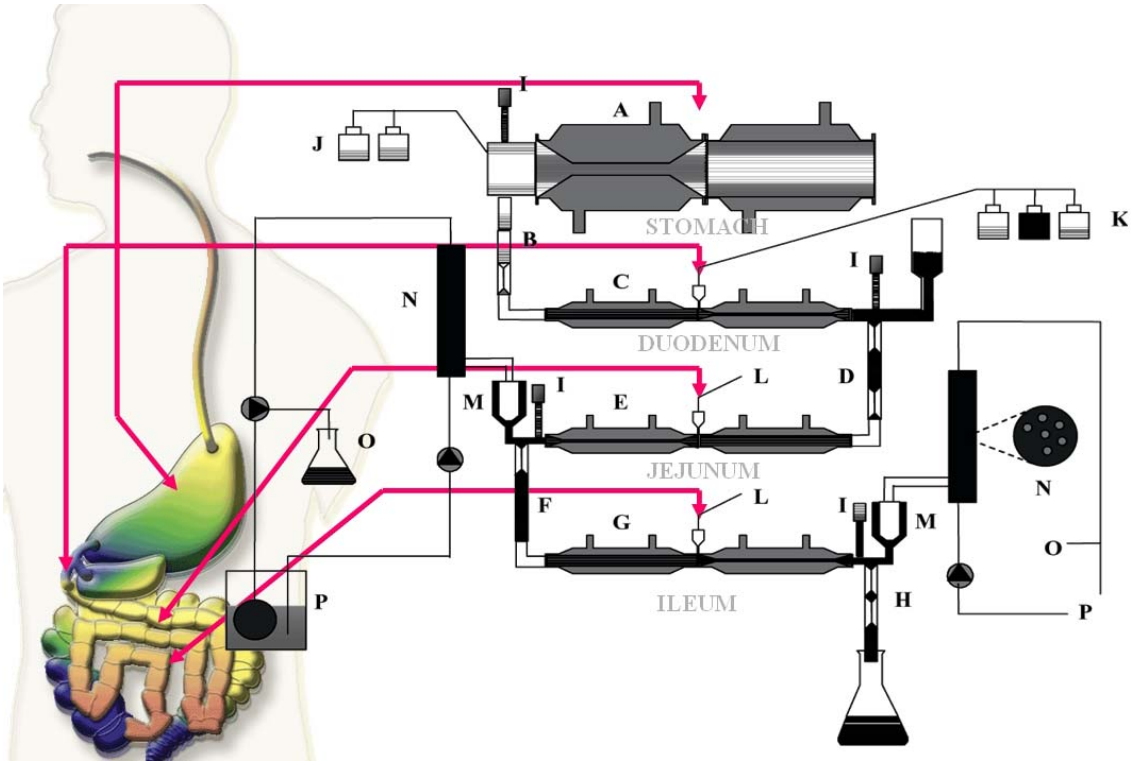

Figure 2.25 Schematic diagram of the dynamic, multi-compartmental model of the stomach and small intestine (TIM-1): A. gastric compartment; B. pyloric sphincter; C. duodenal compartment; D. peristaltic valve; E. jejunal compartment; F. peristaltic valve; G. ileal compartment; H. ileo-caecal valve; I. pH electrodes; J. gastric secretion bottles with acid and enzymes; K. duodenal secretion bottles with bile, pancreatin, bicarbonate; L. secretion of bicarbonate to control the intestinal pH; M. pre-filter system; N. hollow fibre semi-permeable membrane system; O. water absorption system; P. closed dialysing system. Taken from National Enzyme Company Literature (© National Enzyme Company, 2004).

The Institute of Food Research (Norwich, UK) has developed a model of the stomach that simulates human digestion using a flexible walled vessel and a cylinder that processes the food at representative shear rates. During the digestion, simulation acid and enzymes are added appropriately to the food in the model stomach. The first stage of developing the model stomach was to use Echo Planar Magnetic Resonance Imaging (EPI) data from a collaboration with the Sir Peter Mansfield Magnetic Resonance Centre at Nottingham University (Marciani *et al*., 2001). Non-invasive measurements of gastric processing of complex meals in human volunteers provided essential data on the digestion of multiphase

meals and the influence of structure, hydration, mixing, shear, transport and delivery within the stomach. Parallel studies on the biochemistry of digestion established the protocols for enzyme and bile addition (Wickham *et al.,* 2006).

The model stomach is built on a module design of three stages and a photo of the model is in Figure 2.26. The first module simulates the main body of the stomach and mimics the dynamics of mixing, diffusion profiles of both acid and enzymes, and emptying cycles measured within the main body of the human stomach. This is followed by an emptying routine into the second module which simulates the antrum (the lower part of the stomach). In this stage the digesta is subjected to high shear (measured using the EPI, Marciani *et al*., (2001)), forcing mechanical breakdown of the food structure. The final stage models the first part of the small intestine by the addition of the bicarbonate, phospholipids, bile and digestive enzymes (Wickham *et al.,* 2006).

Kong *et al*., (2008.a) described how the knowledge of the disintegration of solid foods in human stomach is essential to assess the bioavailability of nutrients in the gastrointestinal (GI) tract. They presented a comprehensive review of food gastric digestion, focusing on disintegration of solid foods. Kong *et al*., (2008.a) identified future research in this area to increase fundamental understanding of the food digestion process in the stomach as related to the food composition, material properties such as texture and microstructure, and chemical characteristics. They stated that this information is necessary to develop new guidelines for seeking innovative processing methods to manufacture foods specifically targeted for health. Kong *et al*., (2008.b) also described their model stomach system to investigate disintegration kinetics of solid foods during digestion. The model stomach

consisted mainly of a turntable and a jacketed glass chamber containing simulated gastric juice in which plastic beads were added to simulate food particulates as well as to provide a suitable mechanical destructive force on food samples (Kong *et al*., 2008.b). Their paper reported that a good match was observed between the kinetics of food disintegration and *in vivo* stomach emptying.

To investigate the fluid dynamics within the small intestine, the first *in-vitro* model describing the effect of intestinal wall movements on absorption was described by Macagno *et al*. (1982). Wall motions modelling that of the intestine were induced using a series of off-centred cams to squeeze dialysis tubing that was filled with a salt solution by gravity from an overhead tank. The decrease in salt concentration from the inner side was monitored with variations in the wall motion. An analytical model was also developed that contained equations representing wall motions, flow and mass transfer. Assumptions consisted of: axisymetric ring contractions, low Reynolds number, conserved fluid volume, no-slip conditions at luminal surface and internal flow being negligible. The finding from their experiments and modelling was that the wall motions caused a 30-35% increase in absorption (Macagno *et al.*, 1982).

In the model developed by Macagno *et al*. (1982), the fluid used and modelled for the studies was saline solution, a simple Newtonian fluid that does not exhibit the shear dependant viscosity of the guar gum formulations. Another limitation of this *in-vitro* model was that it did not have an annular constriction similar to that found in the small intestine.

Figure 2.26 Picture of the Institute of Food Research (Norwich, UK) model stomach. Taken from BBC website (2006).

Spratt *et al*. (2005) described the design and development of a new continuous culture system for the modelling of the human large intestine. The model comprised of a three stage membrane based fermenter, used in conjunction with an aqueous polyethylene glycol solution for water and metabolite removal and pH control of the fermentation media. The model was capable of removing 64% of incoming media across the membranes, the majority of which was assumed to be water. The model provided a good representation of the degree of water removal that occurs in the human colon itself (Spratt *et al*., 2005). A schematic of one of the experimental set ups used as part of the work done by Spratt *et al.* (2005) is shown in Figure 2.27.

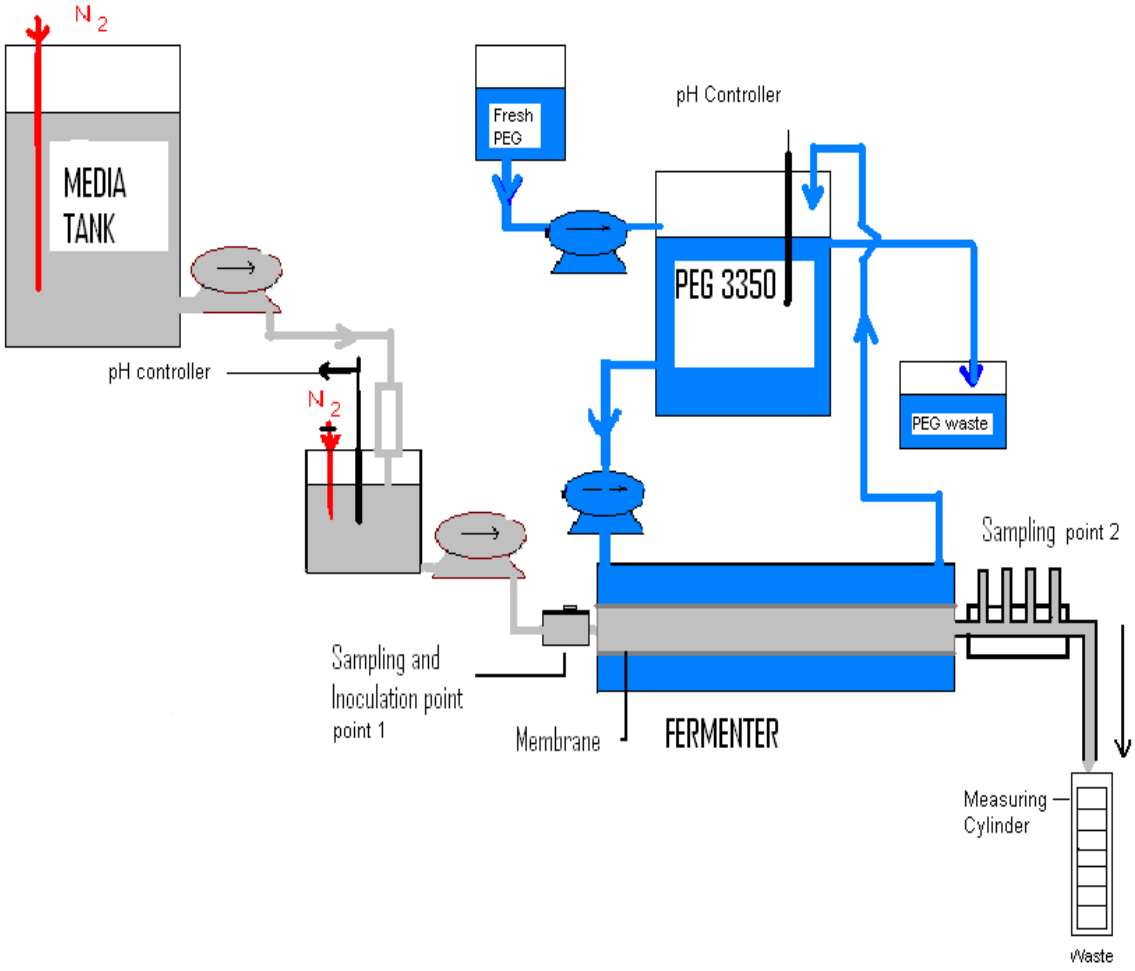

Figure 2.27 Schematic of the model developed by Spratt (reproduced from Spratt PhD Thesis, 2003).

2.5.3 Computational Models

Computational modelling of the GI tract falls into two categories: (i) numerical models such as CFD models of fluid flow and (ii) analytical models that represent the parts of the intestine using equations that can be solved analytically.

2.5.3.1 Computational Modelling

The modelling of biological processes is becoming increasingly important. Much of the early work began with the modelling of the fluid flow in the arteries due to its importance in atherosclerosis (hardening of an artery). The modelling of the lungs and of renal

processes is also being carried out. Initially these processes were modelled from a physiological perspective to study their fluid dynamics. This gives an understanding of the processes under normal conditions and can cast light upon abnormal functioning. An example of work undertaken on the circulatory system is that of McQueen *et al.* (2000) on 3D modelling of the human heart.

An example of computational modelling being applied to the intestine is the gastric flow and mixing studied by Pal *et al*. (2004) using the lattice-Bolzmann numerical method. This model used anatomical data from magnetic resonance imaging (MRI) movies of a healthy human stomach filled with 330ml of a nutrient meal. The stomach was modelled in 2D and using the MRI movie, the timing and location of gastric motility events were parameterised. The purpose of the model was to understand drug dissolution and break up in the stomach and also the intragastric fluid motions, pressure and mixing with computer simulation. Figure 2.28 shows the MRI images used to determine the movement of the stomach for modelling and Figure 2.29 shows an example of an output from the model. The simulations predicted two basic fluid motions: (i) retrograde 'jets' through contraction waves and (ii) circulatory flow between wave motions, both of which contribute to mixing (Pal *et al*., 2004).

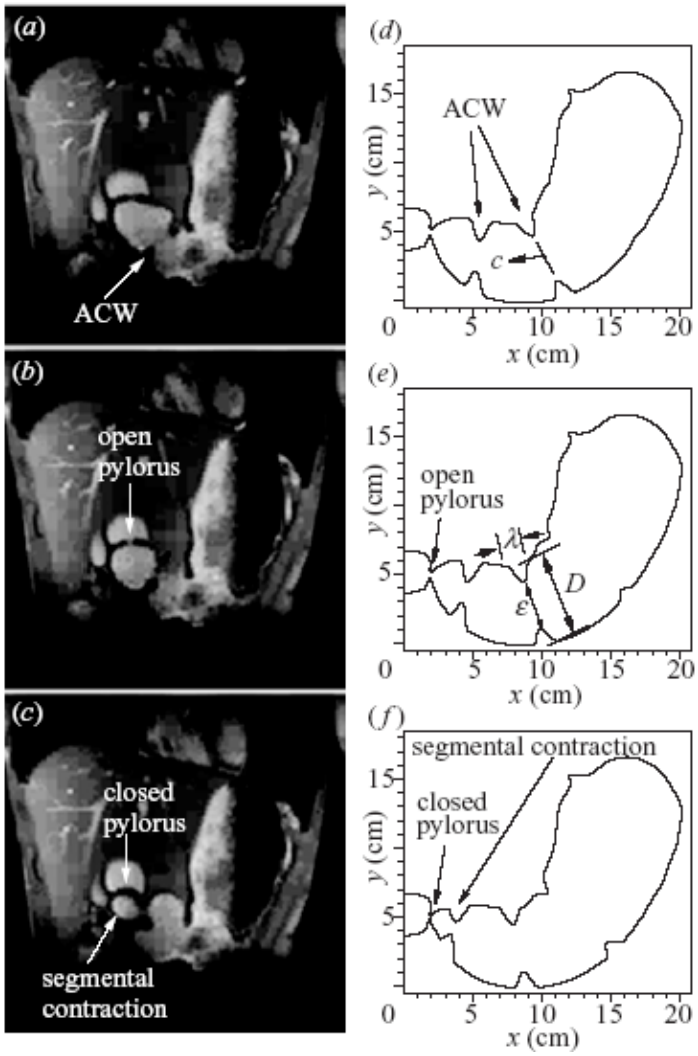

Figure 2.28 (a-c) MRI images from a movie sequence of the human stomach at 4 s intervals, (d-f) stomach geometry model at the same 4 s intervals (Pal *et al.,* 2004).

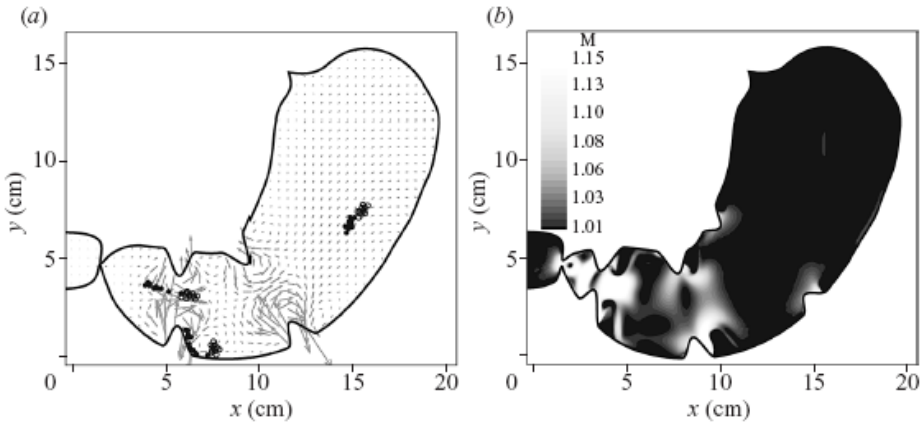

Figure 2.29 (a) mixing in the stomach illustrated by the spreading of three groups of particles released in different gastric regions from initial locations (open circles) to locations after 10s (closed circles). (b) greyscale isocontour plot of mixing parameter M (calculated over 1s) (Pal *et al.,* 2004).

A mathematical model of peristaltic flow and absorption in the small intestine was developed by Lager (2005) to model the way Newtonian fluids flow under the action of peristalsis. Lager (2005) mathematically modelled the peristaltic flow of fluid flowing in a vibrating peristaltic axisymmetric domain. This was done by deriving an asymptotic expression for the peristaltic velocity profile from Stokes flow equations which they solved with the use of a perturbation expansion in the small wave curvature. Using this method they modelled the complex flow patterns of peristalsis.

The mathematical models allow understanding into the processes and products of interest to be developed and also for rapid in-expensive variations into the modelled scenario to be carried out, albeit from a theoretical study.

2.5.3.2 Analytical Modelling

Yu *et al*. (1999) developed the "compartmental absorption and transit" (CAT) model to estimate the fraction of dose absorbed and the rate of molecular absorption for passively transported molecules, shown in Figure 2.30. The flow of solute in the small intestine is viewed as being similar to that of the flow through a series of connected, well mixed compartments. The rate of transfer of the drug from compartment (n) to the next (n+1) is proportional to the amount of drug present in (n). The number of compartments is determined by comparing modelled data with experimental results. Yu *et al*. (1999) determined the optimal number of compartments to be seven.

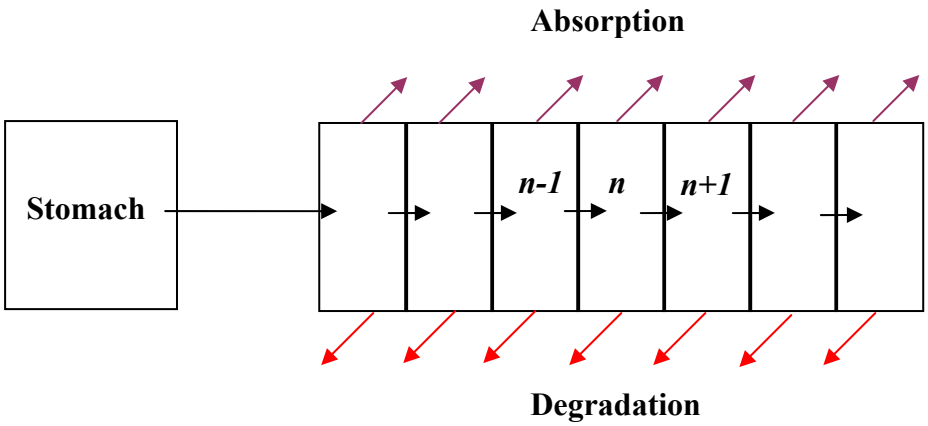

Figure 2.30 Diagram of the compartmental absorption and transit (CAT) model.

Equation 2.13 describes the concentration of the dose of drug in the stomach Y_s where the drug leaves the stomach compartment in a 1st order fashion with gastric emptying constant K_s.

$$\frac{dY_s}{dt} = -K_s Y_s \qquad \text{Equation 2.13}$$

Then the fraction dose Y_n in compartment n (shown in Figure 2.30) by C_n for intestinal compartment (n) for n = 1,2,..7 is described by Equation 2.14.

$$\frac{dY_n}{dt} = -K_t Y_{n-1} - K_t Y_n - K_{an} Y_n - K_{dn} Y_n \qquad \text{Equation 2.14}$$

i.e. flux from compartment (n-1), flux to compartment (n+1), and two terms that depend on Y_n; absorption to the wall, with rate constant K_{an} and degradation, assumed first order with rate constant K_{dn} (Yu *et al.,* 1999).

Summing the rate of absorption in each compartment yields the total rate of absorption from the intestine:

$$\frac{dY_a}{dt} = \sum_{n=1}^{7} K_{an} Y_n \qquad \text{Equation 2.15}$$

In a similar approach, the rate of degradation over the small intestine is the sum of degradation over the seven compartments:

$$\frac{dY_d}{dt} = \sum_{n=1}^{7} K_{dn} Y_n \qquad \text{Equation 2.16}$$

This leads to the fraction of the dose of the drug absorbed by the intestine as time tends to infinity to be given by:

$$F_a = \frac{Y_a}{100} = \int_0^{\infty} \sum_{n=1}^{7} \frac{K_{an} Y_{an}}{100} dt \qquad \text{Equation 2.17}$$

The CAT model is defined by a set of first order ordinary differential equations that describe plug flow through the intestine, where experimental data is used to reasonably estimate transfer and absorption rate parameters (Yu *et al*., 1999). This approach is very useful for pharmacokinetic applications and has been developed into a commercially available piece of software known as Gastroplus™. GastroPlus™ is a computer programme that simulates the absorption, pharmacokinetics and pharmacodynamics for drugs administered orally or intravenously. The underlying model is the Advanced Compartmental Absorption and Transit (ACAT) model, a development of the CAT model by Amidon and Yu. GastroPlus™ is used by more pharmaceutical researchers than any other oral absorption/pharmacokinetic software. This includes nearly all of the top 20 pharmaceutical companies in the world (Simulations-plus, 2008). This approach is unsuitable for the mechanistic understanding of the influence of bulk fluid properties on the delivery of nutrients to the intestinal wall as the properties of the fluid and fluid dynamics are not addressed as part of the GastroPlus™ model which is required as part of this work.

Stoll *et al.* (2000) describe a numerical model of the absorption of pharmaceutical therapeutics and include the idea of 'convective dispersion' from Poiseuille flow, responsible for the mixing of solutes in the small intestine. Stoll *et al.* (2000) assume a 1D asymptotic dispersion equation to describe the motion and absorption of solute in the intestine. Therapeutic molecules are assumed to be introduced in the form of a bolus into the duodenum which subsequently move by convection and diffuse through the duodenum, jejunum and ileum. Absorption into the systemic circulation across the epithelial barrier, as well as possible degradation or aggregation in the lumen or at the apical epithelial membrane, contribute to the disappearance of the therapeutic molecules as the bolus travels through the lumen in an oral to anal direction. The inputs to the model are primarily anatomical or physicochemical characteristics that are either known or can be measured for a given therapeutic and animal model. Comparisons with published experimental systemic concentrations are made for molecules ranging from small lipophilic substances, such as ibuprofen, to polypeptides, such as calcitonin, and proteins, such as insulin. The authors suggested that the model may be useful as a numerical simulation tool for predicting estimates of oral dose response relationships in animals and humans given relatively limited *in vivo* data. The viscosity of the fluid flowing through the intestine is not addressed a parameter of the mathematical model.

The assumptions being made in some of the existent models simplify the product and process description in space and time, which could affect absorption profiles of functional food ingredients being absorbed. For example, the assumption that there is a negligible radial concentration gradient in the lumen would potentially affect absorption profiles.

2.5.4 *In-Vivo* Models

This section covers work and techniques that are *in-vivo* and are used to understand how food or actives behaves in the GI tract. Animal models are used to predict the effect and responses in humans. Rats have been used extensively for studies relating to the GI tract, however it is preferred to use animals closer to humans in certain aspects, for example dogs, pigs and primates (Wickham *et al.*, 2006).

Ultimately the ideal *in-vivo* model for the human is the human body itself. Human studies normally involve a feeding study with the acquisition of serial samples of digesta from the stomach and upper small intestine, the rest of the small intestine being inaccessible. The next sample point is the terminal ileum (in ileostomy volunteers) or faeces (Wickham *et al.*, 2006). Human trials tend to be time consuming and expensive and there is considerable variation between individuals which influences the results. The consequence of this variation is that advanced statistical techniques are required to extract the subject variation from the data to give meaningful results.

As described by Wickham *et al.* (2006), studies of the complex multistage process of digestion are ethically and technically difficult, expensive to perform and so large numbers of studies are impractical. This is the basis for work on the development and implementation of *in vitro* models that replicate the conditions and processes that occur *in vivo*. The models should be sufficiently refined for the process of digestion to be followed in some detail and to be validated against *in vivo* data (Wickham *et al.,* 2006).

MRI techniques have been used to obtain valuable information on processing foods in the stomach (enabling design of the IFR Model Gut). These developments are beginning to be applied to the small intestine (Hoad *et al*., 2007). Development of imaging in the small intestine will open up the modelling of processes computationally as carried out by Pal *et al.* (2004) (Section 2.5.3) and also with *in vitro* models such as the IFR model.

The area of *in-vivo* testing is of great importance to the field of novel food development. Investigations here have utilised *in-vitro* models due to the limitations of *in-vivo* models described above. As the understanding and application of *in-vitro* models develops they will require validation with the use of advanced *in-vivo* techniques. The information for the validation would come directly from studies for this purpose and/or from validated data published in the literature.

2.6 Summary

By understanding the fluid flow, mixing and diffusion of nutrients through structured foods in the small intestine, the effects that changing structured food formulations could have on the delivery of nutrients or actives to the intestinal wall may be predicted. This is of particular benefit to the food industry as they endeavour to develop functional foods that require expensive and time consuming human trial for proof of function. The understanding of the mode of action that these functional ingredients have would lead to more systematic design of food products and away from a trial and error methodology. This would lead to benefits in product development time and costs in an industry where first to market and time to market are particularly important.

The food design section gives background on dietary fibre and describes the research findings on guar gum in particular. The reasons for using guar gum as a functional ingredient have been explained in the context of its ability to reduce the peak increase in blood glucose levels after ingestion of test meals. The plasma-lowering of cholesterol in human subjects by guar was also described (although in lesser detail) to its effect on glucose absorption. The reason for this is that the effect on glucose absorption was identified as the function of interest for guar gum within the context of the research as part of this work.

This literature review sets the context for the first mechanical model designed to simulate transport phenomena in the small intestine by mimicking the dynamic flow and mixing motions of the small intestine. The rational for the small intestine being the area of focus in the GI tract was that the small intestine is responsible for virtually all nutrient absorption and more than 95% of water absorption that enters the GI tract within the food and from secretions within the GI tract (Smith and Morton, 2001). Since one of the objectives of this work was to understand the delivery of nutrients and actives to their sites of absorption, the small intestine was chosen.

This literature review describes the GI tract, food design, chemical engineering in the small intestine and intestinal models. Further Chapters present the design, development and the results from the experimental and computational investigations into understanding the effects of structuring foods on molecular delivery and fluid flow within the small intestine using this novel approach.

CHAPTER 3 - MATERIALS AND METHODS

3.1 Introduction

As discussed in Chapters 1 and 2 the purpose of modelling the physical and chemical processes in the small intestine was to aid in the design and development of formulated foods, where molecular delivery to the intestinal wall is important.

The aim of the experiments and computational modelling was to understand how the structuring of model food formulations affects molecular delivery to the intestinal wall. This chapter contains a description of the materials and methods used as part of the investigations as follows:

- *Ingredients;* guar gum (Section 3.2.1), carboxymethyl cellulose sodium salt (CMC) (Section 3.2.3), riboflavin (Section 3.2.2) and starch (Section 3.2.4), used as model food formulations;

  Carboxymethyl cellulose (CMC) was used as a substitute for guar gum in flow visualisation experiments, as CMC forms transparent liquids through which particle positions (Section 3.8 for PIV) and dye fluorescence (Section 3.9 for PLIF) can be measured.

  Starch was used in the form of a solution for digestion experiments within the small intestine model (Chapter 5, Section 5.3). The product of the digestion of starch is glucose which was monitored on the food side of the SIM and on the recipient side of the membrane (Section 3.3.5).

  Riboflavin (Vitamin B_2) was used in the model food formulations as the model nutrient. Riboflavin was used for its fluorescent properties from which solution concentrations are easily determined using a fluorescence spectrophotometer (Section 3.3.1). The other reason for the use of riboflavin was for its low molecular weight of 376.

- *Material characterisation* using rheometry (section 3.3.3);

- *Fluorescence* measurement to determine solution concentrations (Section 3.3.2);

- *Fluorescence recovery after photobleaching* (FRAP) to determine diffusion coefficients through solutions (Section 3.5);

FRAP has been used to measure the diffusion coefficient of riboflavin through various guar gum solutions. The diffusion coefficient was measured to quantify the diffusive component of the molecular delivery (diffusion and convection) for experiments in the SIM.

- *Small Intestinal Model (SIM) and the Diffusion Cell* design and development;

  The diffusion cell (Section 3.6) was designed and used for this work in order to measure the mass transfer coefficient of molecules to a membrane, across the membrane and on the recipient side, for varying fluids and process conditions. The SIM (Section 3.7) was designed as a model of the small intestine.

- *Flow visualisation techniques*, particle image velocimetery (PIV) (Section 3.8) and planar laser induced fluorescence (PLIF) (Section 3.9) to the fluid flow within the SIM;

- *Computational fluid dynamics (CFD)* (Section 3.10) was used to develop a theoretical model of the fluid flow within the small intestine.

A brief description of the rationale for the above ingredients and techniques, is provided with in this chapter.

The epithelium is not being covered as part of this work since the factors affecting the transport across the epithelium of molecules are very specific to properties of the molecule, as described in Section 2.2.4.1. Experiments can however be conducted using Caco-2 cell lines to mimic the biological transport across the epithelium as described in Section 2.5.2.2 on cultured cells. This study is interested in the delivery of the molecule to the intestinal epithelium rather than across it. This work focuses on the small intestine and therefore other parts of the GI tract are not included such as the mouth, the liver and pancreas, the stomach and large intestine. The overall hypothesis of this work is that better understanding of the physical and chemical processing in the small intestine will help explain some of the effects of changing food composition discussed in Chapter 2.

The SIM was designed and used to model the mechanical processing of the digesta in the human small intestine. The measurements of interest to be obtained were the delivery of nutrient to the wall, the fluid dynamics and mixing profiles. These parameters were measured whilst changing the properties of the food formulation (model digesta). Using the model, it was possible to measure the influence that the variation of food formulation has on the delivery of nutrient to the wall. The fluid dynamics and mixing profiles were also determined using experimental fluid dynamics techniques PIV and PLIF. To verify the experimental results and to enable rapid evaluation of formulation prototypes, the technique of CFD was used to create a computational model of the process seen in the SIM.

3.2 Materials

This section gives a description of the materials used for the investigations undertaken as part of this work: guar gum, riboflavin, carboxymethyl cellulose sodium salt (CMC) and starch. The material properties from material characterisation are also provided.

3.2.1 Guar Gum

Guar gum is a biopolymer that is extracted from leguminous seeds. It is a high molecular weight hydrocolloid polysaccharide made from galactan and mannan units linked with glycosidic bonds, chemically described as galactomannan. Guar gum was chosen for its observed properties in reducing the blood glucose peak values after the consumption of model foods containing glucose and guar gum (Blackburn *et al*. (1984), Edwards *et al*. (1998), Ellis *et al*. (1995), Jenkins *et al*. (1978). The molecular structure is shown in Figure 3.1.

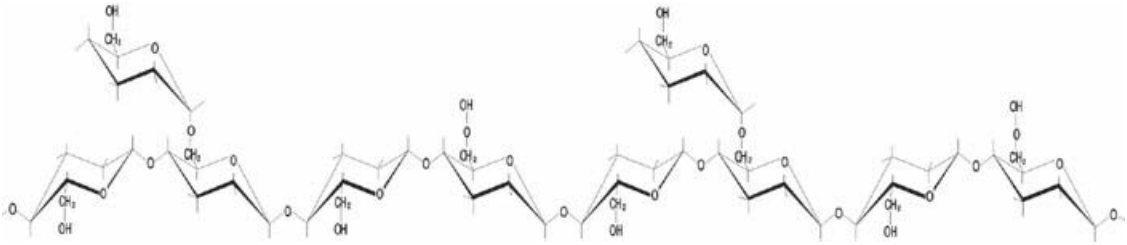

Figure 3.1 The molecular structure of guar gum (Unipektin, 2008)

To prepare the guar gum solution, a known weight by volume (w/v) of the guar powder was slowly added to the riboflavin solution in a beaker being stirred using a magnetic stirrer. Once the guar had been added the container was weighed and the solution heated to 80^{o}C and kept at 80^{o}C for 10 minutes. Stirring then continued at room temperature and the fluid allowed to cool down while stirring continued for a further 12 hours to ensure complete hydration of the guar gum. The final concentration was established after correcting for the solvent weight loss through evaporation. Samples of concentrations up to 2% were prepared by this method. The formulations were used within 24 hours of preparation as microbial growth after this time changes the properties of the formulation.

One of the samples of guar gum used was purchased from Willy Benecke, Germany (referred to subsequently as WB guar) and a range of guar samples were donated from Unipektin, Switzerland. The Unipektin samples are known as the Vidocrem range, consisting of Vidocrem A-G, each giving a different range of final viscosities (discussed in Section 3.4.1). All guar samples were cream coloured powders.

Since the focus of this work is the understanding of mixing and molecular delivery processes in the small intestine and as the guar gum used in the model digesta is non-ionic

it is therefore not affected by ionic strength or pH (Chaplin M, 2008). Therefore the physiological pH and ionic strength has not been modelled here.

3.2.2 Riboflavin

Riboflavin (Vitamin B_2) was used as the model nutrient (i) due to its fluorescent properties that allow solution concentrations to be easily determined using a fluorescence spectrophotometer (Section 3.3.1) and (ii) because of its low molecular weight of 376 which was of a similar order of magnitude to glucose of 180 which was of interest. The riboflavin was supplied from Sigma-Aldrich (Poole, UK). For all experiments using riboflavin solutions, the concentration of the riboflavin solution was 0.1 mM. This was prepared by dissolving the correct mass of riboflavin into filtered water while stirring at room temperature. The containers used to store and prepare the riboflavin solutions were covered in foil to prevent light induced degradation of riboflavin.

3.2.3 Sodium Salt of Carboxymethyl Cellulose (CMC)

The sodium salt of carboxymethyl cellulose (CMC) is derived from cellulose and has carboxymethyl groups (-CH2-COOH) bound to some of the hydroxyl groups of the glucopyranose monomers of the cellulose backbone (Phillips, 2000). As with other modified celluloses, the solution viscosity depends on the average chain length or degree of polymerisation of the cellulose molecules. The CMC was used for the particle image velocimetry experiments described in Chapter 6. CMC was used because the solutions are transparent and so well suited for optical flow visualisation and their rheological properties can be matched to that of the guar gum.

CMC powder from Sigma-Aldrich (Poole, UK) was weighed out and the correct amount of the powder was sprinkled into the water in a vessel that was being stirred using a magnetic stirrer. The solution was then further stirred for a period of two hours at room temperature.

3.2.4 Starch

Starch is an important polysaccharide in most diets and is made up of amylase and amylopectin. The starch was donated from Remy Industries (Remyline XS-DR-P; Remy Industries, Belgium) and was the pre-cooked (using a hydrothermal process) rice starch variety, to ensure that the experiments were independent of the hydration of the starch. Hydration, when brought about by cooking, produces an irreversible change in the structure of the starch granule whereby the starch–starch interactions are 'unzipped' and replaced by starch–water interactions (Phillips, 2000). By using the pre-cooked starch the rate of digestion measured would not be affected by the rate of hydration. The starch solutions were used in digestion experiments within the Small Intestine Model (Chapter 5), while the production of the digestion product (glucose) was monitored on the food side of the Small Intestine Model and on the other side of the membrane.

3.3 Methods

3.3.1 Fluorescence Spectroscopy

This technique is based on fluorescence and in particular that of riboflavin, for this work. At room temperature most molecules occupy the lowest vibrational level of the ground electronic state and on absorption of light they are elevated to produce excited states. The simplified diagram in Figure 3.2 shows absorption by molecules to produce either the first (S1) or second (S2), excited state.

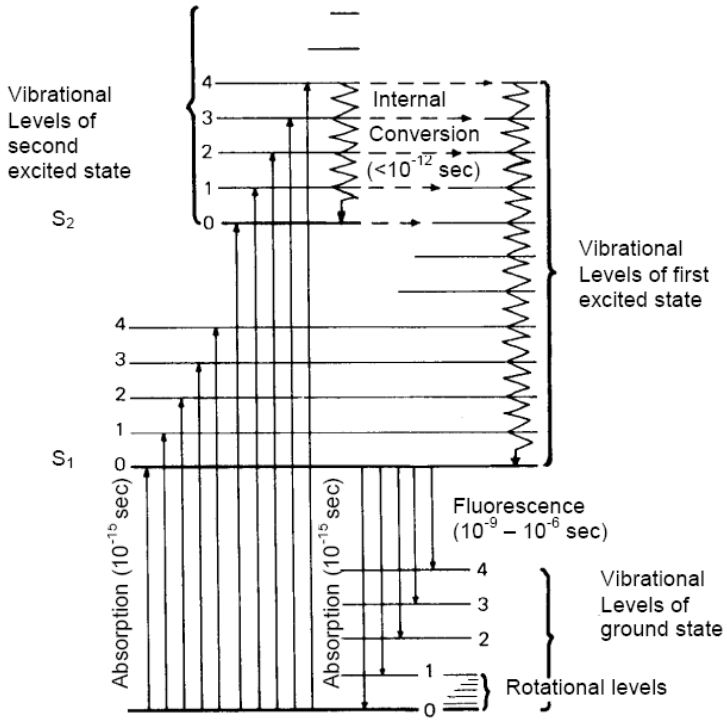

Figure 3.2 Transitions giving rise to absorption and fluorescence emission spectra (Perkin Elmer, 2006).

Excitation can result in the molecule reaching any of the vibrational sub-levels associated with each electronic state. Since the energy is absorbed as discrete amounts, this should result in a series of distinct absorption bands.

Having absorbed energy and reached one of the higher vibrational levels of an excited state, the molecule rapidly loses its excess of vibrational energy by collision and falls to the lowest vibrational level of the excited state. From this level, the molecule can return to any of the vibrational levels of the ground state, emitting its energy in the form of fluorescence (Perkin Elmer, 2006).

3.3.1.1 Equipment

All fluorescence instruments contain three basic items: a source of light, a sample holder and a detector (see Figure 3.3). In addition, to be of analytical use, the wavelength of incident radiation needs to be selectable and the detector signal capable of precise manipulation and presentation. In simple filter fluorimeters, the wavelengths of excited and emitted light are selected by filters which allow measurements to be made at any pair of fixed wavelengths. Simple fluorescence spectrometers can analyse the spectral distribution of the light emitted from the sample (the fluorescence emission spectrum) either by a continuously variable interference filter or a monochromator. In more sophisticated instruments, monochromators are provided for both the selection of exciting light and the analysis of sample emission. Such instruments are also capable of measuring the variation of emission intensity with exciting wavelength, the fluorescence excitation spectrum (Perkin Elmer, 2006).

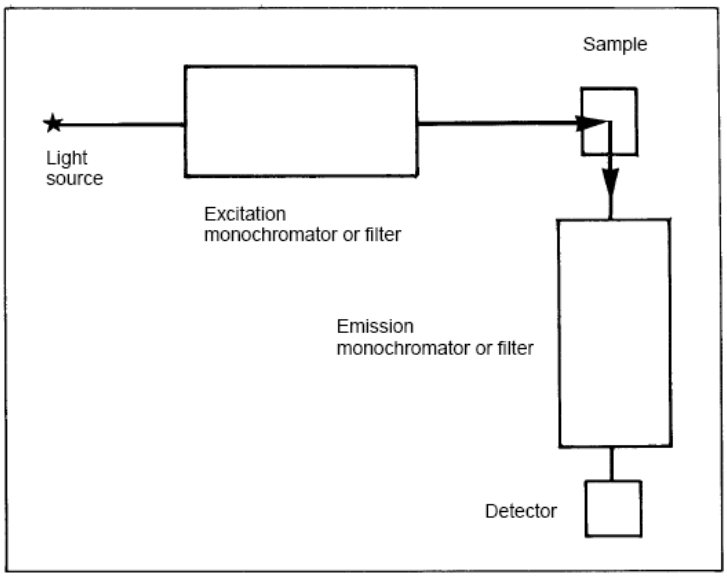

Figure 3.3 Essential components of a fluorescence spectrometer (Perkin Elmer, 2006).

3.3.2 Riboflavin Concentration Measurement

The concentration of riboflavin was measured using a Perkin-Elmer Fluorimeter (LS 50B Fluorescence Spectrometer). Initially the riboflavin was scanned for excitation and emission spectra to give Figure 3.4. The excitation and emission profile shown below was generated using MATLAB 7.1.

The parameters for the fluorescence spectrophotometer were determined by running a scan of the excitation and emission spectra to give Figure 3.4. The values to be used were determined as 488 nm for excitation and 522 nm for emission, at 2.5 nm slit widths (as this provided a good intensity for measurement).

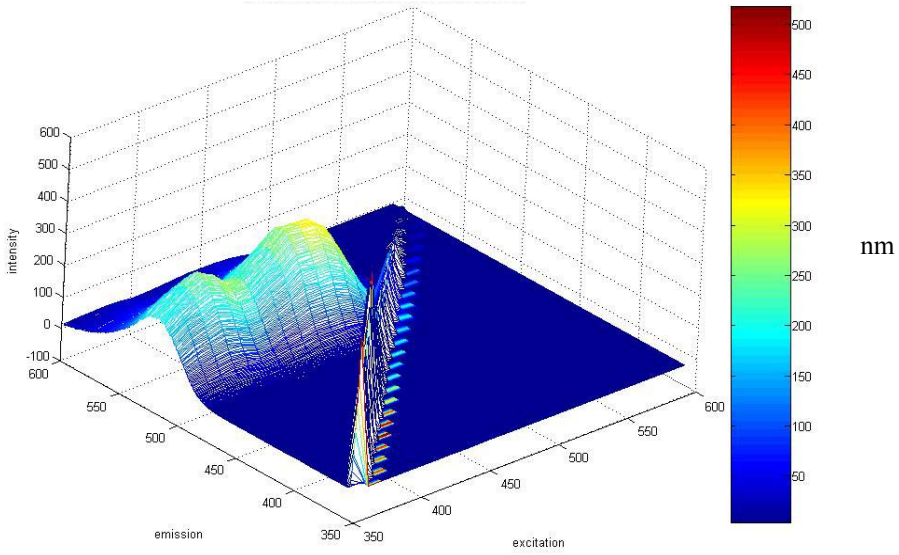

Figure 3.4 A 3D plot of the intensity versus excitation and emission spectra for riboflavin.

There were two types of measurement of riboflavin concentration: (i) as on-line measurements where a volume of fluid was continuously pumped into the fluorimeter using a peristaltic pump and the intensity read, then the fluid was pumped back into the

reservoir; (ii) as an off-line sample where 4ml of sample was placed in a cuvette and the intensity measured using the fluorimeter and then the sample returned. Using known concentrations of solution it was possible to calibrate the measurement of the intensity to the concentration and this is shown in Figure 3.5.

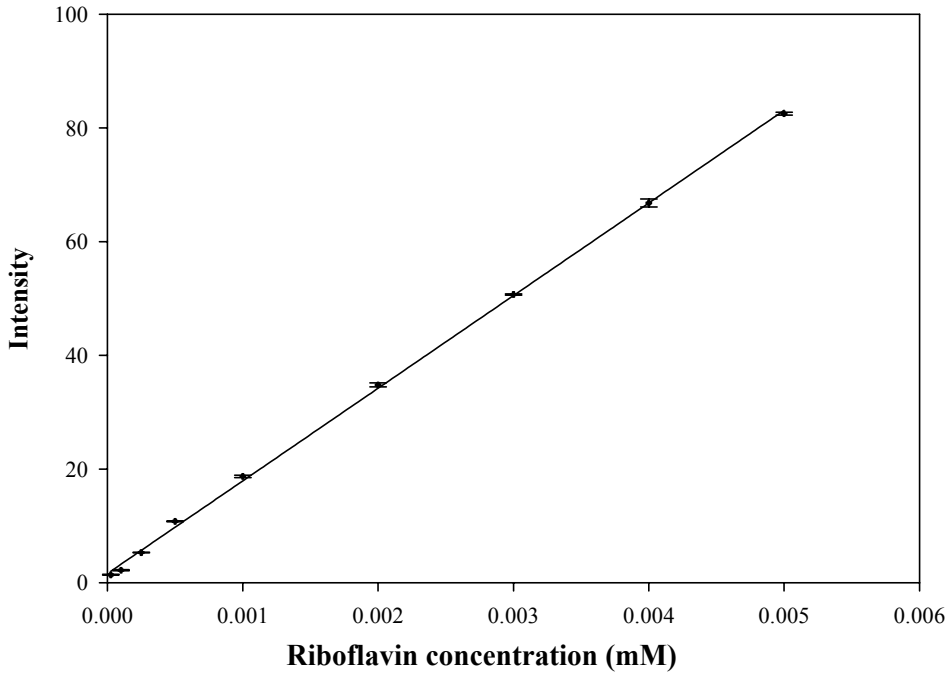

Figure 3.5 Calibration line of the intensity reading versus the known concentration for riboflavin at 488nm excitation, 522nm emission and 2.5nm excitation slit, 2.5nm emission slit and 5 seconds integration time. A linear regression of intensity ($y = mx + c$) concentration, gave m to be 16294, c to be 1.6 and R^2 is 0.99. Error bars represent 1 standard deviation from the mean of 5 measurements.

3.3.3 Rheological Measurements

Rheology is the study of the deformation and flow of matter under the influence of an applied stress and strain. Rheological measurements investigate the relationship between the two physical quantities of stress and strain. Stress is the force applied per unit area upon or within a material and strain is the amount of deformation that is induced by the stress. The rheology of a substance can be described by two components, the *viscosity* and

the *elasticity*. The viscosity is the measure of the resistance of a fluid to deform under shear stress. The elasticity of a material refers to the deformation under stress that then returns to its original state when the stress is removed. The amount of deformation is the strain.

There are two main types of deformation: (i) tensile (or normal) deformation and (ii) shear deformation, and these are displayed in Figure 3.6. The tensile or normal stress (σ) is defined by Equation 3.1:

$$\sigma = \frac{F}{A} \qquad \text{Equation 3.1}$$

where F is the force acting perpendicular to a cross sectional area A. The tensile (or normal strain (ε) from the stress is defined by:

$$\varepsilon = \frac{\Delta l}{l} \qquad \text{Equation 3.2}$$

where l is the length of sample and Δl is the change in length.

From Figure 3.6 (b) the shear stress (τ) is defined by:

$$\tau = \frac{F}{A} \qquad \text{Equation 3.3}$$

where F is the force per unit area and A is the area, and the shear rate ($\dot{\gamma}$) is defined by:

$$\dot{\gamma} = \frac{U}{d} \qquad \text{Equation 3.4}$$

where U is the relative velocity of one plane to the other and d is the distance between the planes.

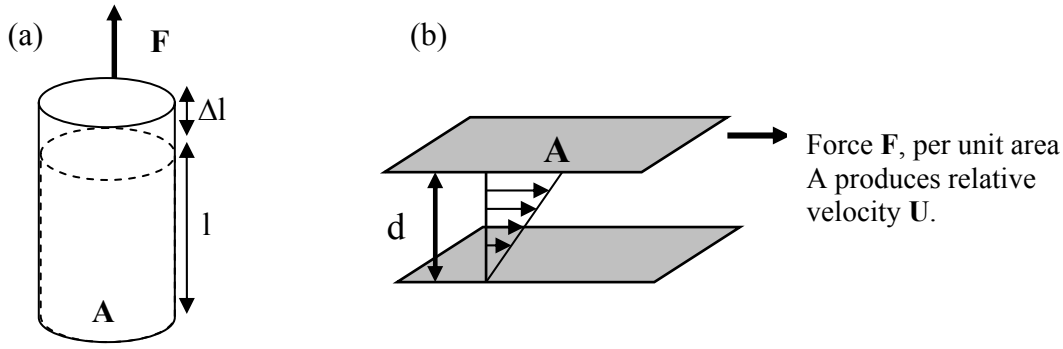

Figure 3.6 (a) the tensile (normal stress) deformation of a sample (b) shear flow under an applied shearing force. The grey rectangles represent two layers of fluid that are separated by a distance d, which are moving with a velocity U relative to one another under the applied force F.

Newton's law describes an ideal liquid as one for which the shear stress is proportional to the shear rate, so that the viscosity can be defined by:

$$\eta = \frac{\tau}{\dot{\gamma}} \qquad \text{Equation 3.5}$$

where η is the viscosity (N s m^{-2}), τ is shear stress (Nm^{-2}) and $\dot{\gamma}$ is the shear rate (s^{-1}). Many fluids are non-Newtonian; a simple empirical model frequently used for describing the non-Newtonian flow of a fluid is the 'power-law' model:

$$\tau = k\dot{\gamma}^{n} \qquad \text{Equation 3.6}$$

where *k* is the consistency index and *n* an exponent.

3.3.4 Viscosity Measurements

Viscosity measurements of the guar gum, starch and CMC solutions were performed using the Physica UDS 200 rheometer (Anton Paar, Germany). For higher viscosity solutions, the cone and plate geometry was used (Figure 3.7). For low viscosity samples a double gap cylinder geometry was used, where the sample fills the gap between the two cylinders and the inner cylinder is steadily rotated.

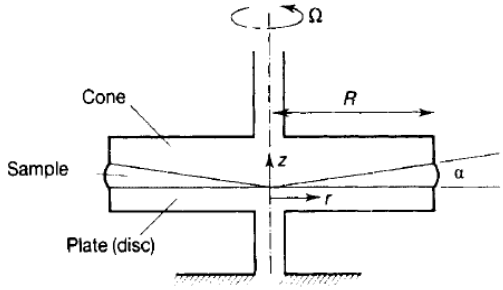

Ω is in radians per second
R is the radius of the plate (disc)
r is the radial position
z is the vertical position
α is the angle of the gap in radians

Figure 3.7 Cone and plate viscometer (Holland, 1995).

3.3.5 Starch Digestion and Glucose Measurement

The starch digestion was carried out by adding the required amount of starch (w/v) with water and then adding 20 ml of diluted amylase (Sigma-Aldrich A6255 from porcine pancreas; 1370 U/mg protein [one unit will liberate 1.0 mg of maltose from starch in 3 minutes at pH 6.9 at 20C]; diluted $^{1}/_{100,000}$ [10 µl made up to 10 ml]) per litre of starch solution and 10 ml amyloglucosidase (Sigma Aldrich S9144; Reconstituted with 20 ml de-ionised water, when reconstituted with 20 ml of water, contains 50 units/ml from *Aspergillus niger* and buffer salts) per litre of starch solution. The amyloglucosidase was simply added in excess to prevent any build-up of maltose in the reaction which is a product inhibitor and therefore to push the reaction to completion. The rational behind setting the enzyme/substrate ratio was to ensure sufficient glucose was released and transferred to the recipient side without depleting the source starch to less that 75% of the original amount. The concentration of amylase was set to give a concentration of 11.9 nM, i.e. within the range of concentrations suggested by Slaughter *et al*., (2001) of 5 – 15 nM.

The digestion assay was first mixed into a 50 ml volume of the starch solution at which point the time was noted, this mixing took place in a beaker with an overhead stirrer for 1

minute. The remained of the 1 litre starch solution was slowly added while the overhead stirrer was mixing over a 4 minute period.

The glucose concentration was measured at time intervals with the use of the blood glucose meter Accu-chek Aviva (Roche) and the Accu-chek test strips. The measuring range was 0.6 to 33.3 ($^{+}$/. 0.83) mmol/L. The enzyme on the test strip, glucose dehydrogenase, converts the glucose in the sample to gluconolactone in the presence of the coenzyme (PQQ). This reaction creates a DC electrical current that the meter converts into the glucose concentration.

3.4 Characterisation of Materials

3.4.1 Guar Gum

The guar gum samples were characterised for viscosity versus shear rate using the Physica UDS 200 rheometer (Anton Paar) with the use of the cone and plate (see Figure 3.7) and coaxial cylinder geometries. The WB guar was used for viscosity measurements at a range of concentrations. WB guar gum was used in the experiments described in Chapters 4 and 5, and for the properties from characterisation of the fluid used in computational modelling in Chapter 6.

The shear thinning properties of the guar gum solutions can be seen in the viscosity versus shear rate plot at different concentrations shown in Figure 3.8. Figure 3.9 shows a shear stress versus shear rate plot for a range of WB guar gum concentrations. The power law model (Equation 3.6) was applied to the shear stress versus shear rate data and the parameters found tabulated in Table 3.1. The power law model gives a good description of

the non-linear viscosity behaviour in-between μ_o and μ_{inf} (where μ_o is the "zero" shear rate viscosity and μ_{inf} is "infinitely large" shear rate viscosiy) and was used as a model of the viscosity over a large shear rate range, as the range of shear rates expected in the small intestine was unknown (as described in Section 2.3.2.3). The power law model shows (Table 3.1) that as the concentration of guar gum increases the solution becomes increasingly shear thinning, i.e. 'n' becomes smaller.

The peak shear rates measured in the SIM give an indication of the shear rates expected in the actual human small intestine and were found to increase from 31 to 117 s^{-1} as the concentration of CMC was increased from 0 to 0.5% CMC. From Figure 3.13 for CMC shows that the shear rates 31 to 117 s^{-1} fall within the bounds of what would be the "zero" shear rate viscosity and μ_{inf} is "infinitely large" shear rate viscosity.

Conc %	***k***	**n**	**r^2**
1	4.04	0.31	1.00
0.75	2.39	0.36	1.00
0.5	0.67	0.47	1.00
0.25	0.07	0.67	1.00
0.1	0.006	0.90	1.00
0.05	0.002	0.94	1.00

Table 3.1 A table of parameter fit of the measured shear stress versus shear rate to the power law model (Equation 3.6).

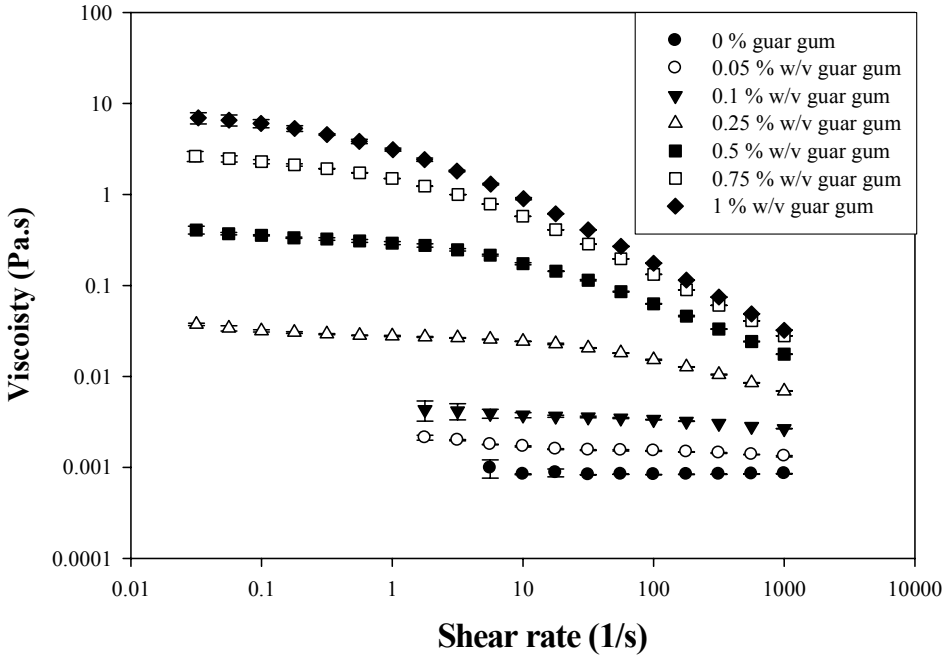

Figure 3.8 Viscosity, shear rate profile for a range of WB guar gum concentrations. Each data point is the average of three measurements and one standard deviation is shown as the error bar.

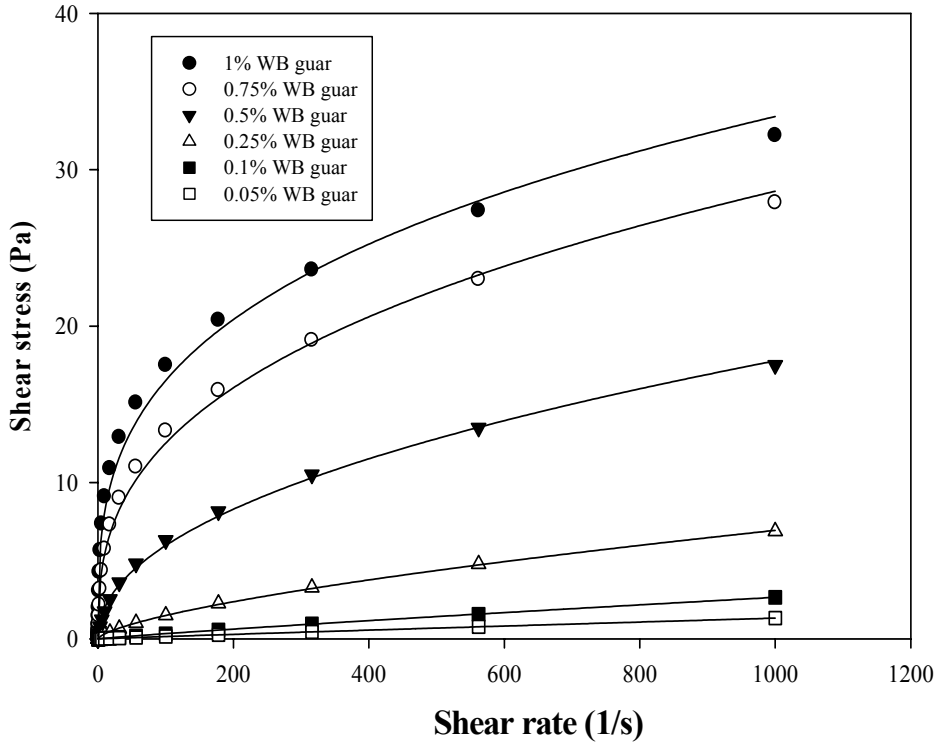

Figure 3.9 Shear stress versus shear rate plot for a range of WB guar gum solutions measured using the Physica UDS 200 rheometer. The individual points are measured values and the solid lines are the regression to a power law model where $y=a*x^b$ and the R^2 values were found.

3.4.1.1 Biopolymer Concentration

A dilute biopolymer solution can be regarded as one in which each flexible biopolymer chain occupies an individual domain within the solution (see Figure 3.10 (a)). As the solution concentration of biopolymer increases a critical concentration is reached, known as C^*, which marks the onset of significant coil overlap (see Figure 3.10 (b)) and interpenetration (Morris *et al*, 1981; Ross-Murphy, 1984). This is characterised by a significant increase in how the viscosity increases with increasing concentration. At concentrations above C^* biopolymer molecules interpenetrate with other molecules to form an entangled network (see Figure 3.10 (c)).

(a) (b) (c)

Figure 3.10 A representative diagram of three concentrations of biopolymer solution (a) dilute solution, (b) molecules are beginning to overlap ~ C^*, (c) a concentration higher than overlap concentration where there is a greater density in the entangled network.

The specific viscosity, η_{sp} is defined by Equation 3.7:

$$\eta_{sp} = \frac{\eta - \eta_{sol}}{\eta_{sol}} \qquad \text{Equation 3.7}$$

Where η is the sample viscosity and η_{sol} is the viscosity of the solvent. The sample viscosity used was determined from evaluation of the viscosity at the lowest shear rates

and by looking for a constant maximum at the so called zero-shear rate viscosity (η_0) (Ellis *et al*., 2000) or low shear rate limiting viscosity.

Figure 3.11 shows the specific viscosity - concentration relationship for WB guar gum; the entanglement concentration (C^*) can be seen as 0.1% w/v. Table 3.2 gives the specific viscosity versus concentration of WB guar gum. The viscosifying effect of commercial guar gum preparation can vary enormously depending on the molecular weight of the galactomannan (Ellis *et al*., 2000), therefore it is difficult to compare this value to literature values as molecular sizes and distributions of commercial guar gums are different depending on the viscosifying effect required (as seen in Figure 3.12).

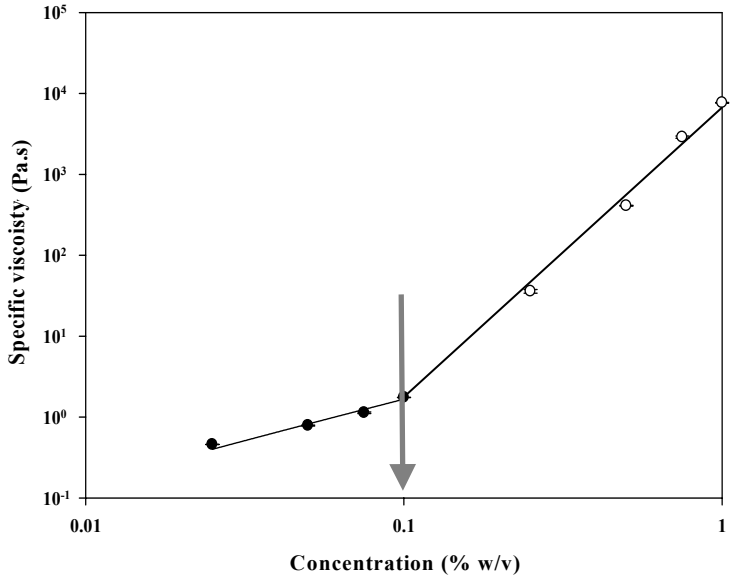

Figure 3.11 The specific viscosity versus the concentration for WB guar gum. The point at which the two lines cross gives the concentration at which entanglement between the polymer chains begins (0.1 % w/v). The error bars signify the standard deviation from three experiments.

Conc %	Specific viscosity Pa.s	standard deviation
0.025	0.5	0.003
0.05	0.8	0.01
0.075	1.1	0.03
0.1	1.8	0.002
0.25	35.9	1.9
0.5	408.3	4.6
0.75	2879.7	90.4
1	7660.8	68.5

Table 3.2 A table showing the specific viscosity of the guar gum solutions at various concentrations and the standard deviation from three measurements.

3.4.1.2 Vidocrem Guars

The vidocrem guar gums from Unipektin (Switzerland) are a range of guar powders that produce different viscosity solutions for the same concentration of guar gum. Vidocrem A, B, C, D, E, F and G give increasingly zero shear viscosities (described in Section 3.4.1.1 and shown on Figure 3.12) for a 1% w/v solution. The vidocrem solution viscosity is controlled by changing the average hydrocolloid polysaccharide molecular weight.

Vidocrem guar solutions were prepared using the method described in Section 3.2.1. Using the range of vidocrem guar gums A – G, it has been possible to investigate the effect of viscosity by using solutions of guar gum (all at 1% concentration) with different low shear rate limiting viscosities. Three measurements were taken with the Physica UDS 200 using the cone and plate geometry. The zero shear rate viscosities for the 1% w/v vidocrem solutions are shown in Figure 3.12; there is an increase in the zero shear viscosities as the sample letter increases.

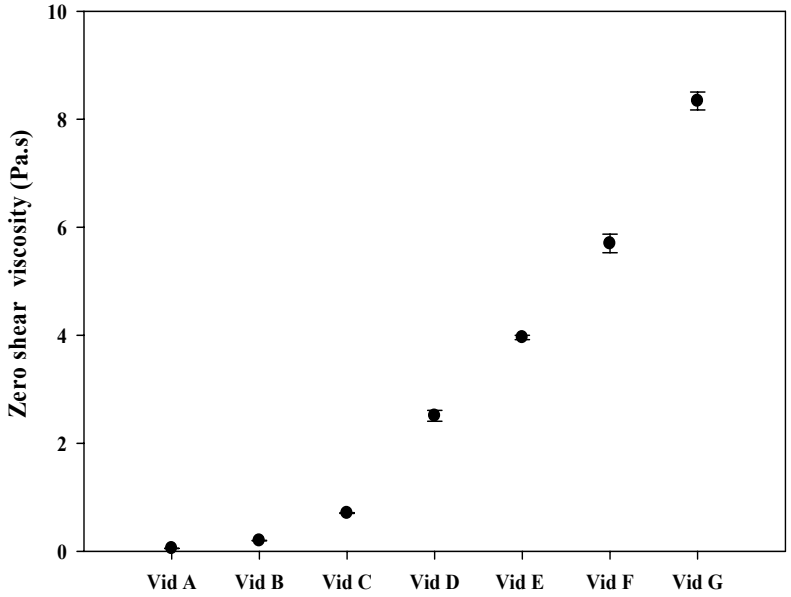

Figure 3.12 The zero shear viscosity of Vidocrem A-G samples at a concentration of 1% w/v. The error bars show one standard deviation from the mean of three measurements.

3.4.2 Sodium Salt of Carboxymethyl Cellulose

The requirement for CMC solutions to be used arose because the guar gum solutions were opaque and were therefore not well suited for optical flow visualisation (PIV and PLIF techniques), CMC was therefore used as a model polymer to the guar gum. The rheological properties of the CMC are similar to that of the guar gum in that they are both shear thinning fluids with guar gum having a '*k'* valve of 4.04 and CMC of 4.28 at 1% w/w and CMC having a *'n'* valve of 0.31 and CMC of 0.46 at 1% w/w. Although not the same the fluid were shown to have similar rheological properties.

Characterisation of the CMC solution was carried out using the Physica UDS 200. The viscosity versus shear rate profile can be seen in Figure 3.13 and the shear stress versus shear rate for a range of CMC concentrations have been plotted in Figure 3.14. The data was used to establish the power law model (Equation 3.6) and calculate the power law

model parameters found in Table 3.3. The concentration at which the entanglement (C^*) of the CMC begins is shown on Figure 3.15 and is 0.25% w/v.

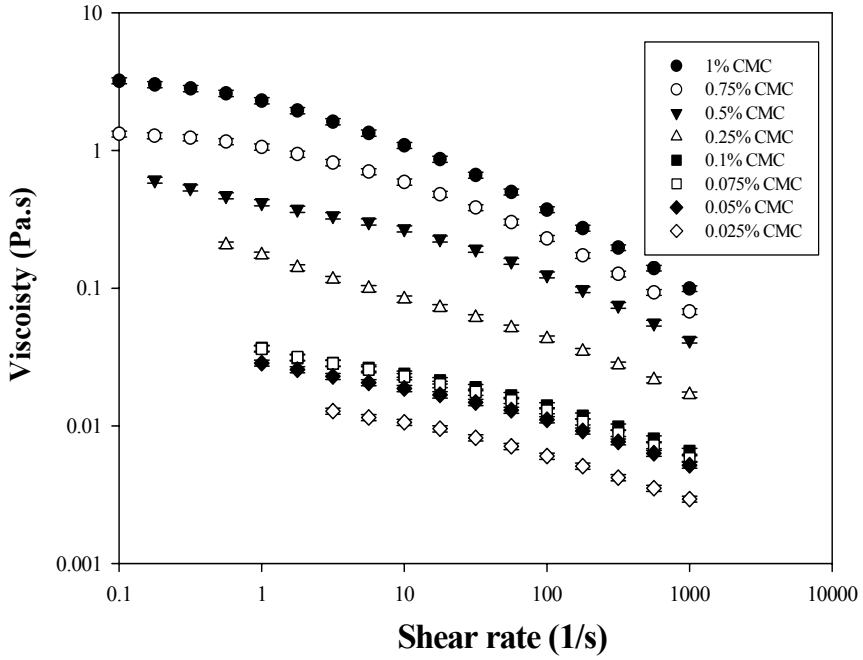

Figure 3.13 Viscosity versus shear rate profile of the CMC used. Error bars are for one standard deviation from the mean for 3 measurements.

Conc %	*k*	n	r^2
1	4.28	0.46	1.00
0.75	2.22	0.50	1.00
0.5	0.97	0.55	1.00
0.25	0.26	0.61	1.00
0.1	0.06	0.67	1.00
0.075	0.06	0.66	1.00
0.05	0.05	0.68	1.00
0.025	0.02	0.69	1.00

Table 3.3 A table of parameter fit of the measured shear stress versus shear rate to the power law model for CMC (Equation 3.7).

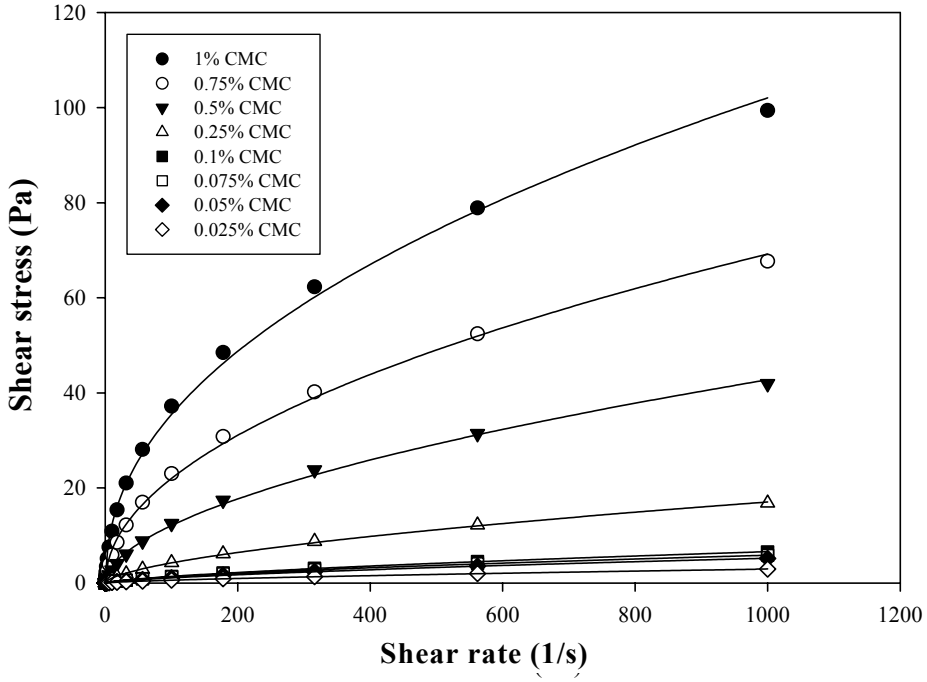

Figure 3.14 Shear stress versus shear rate profiles of CMC.

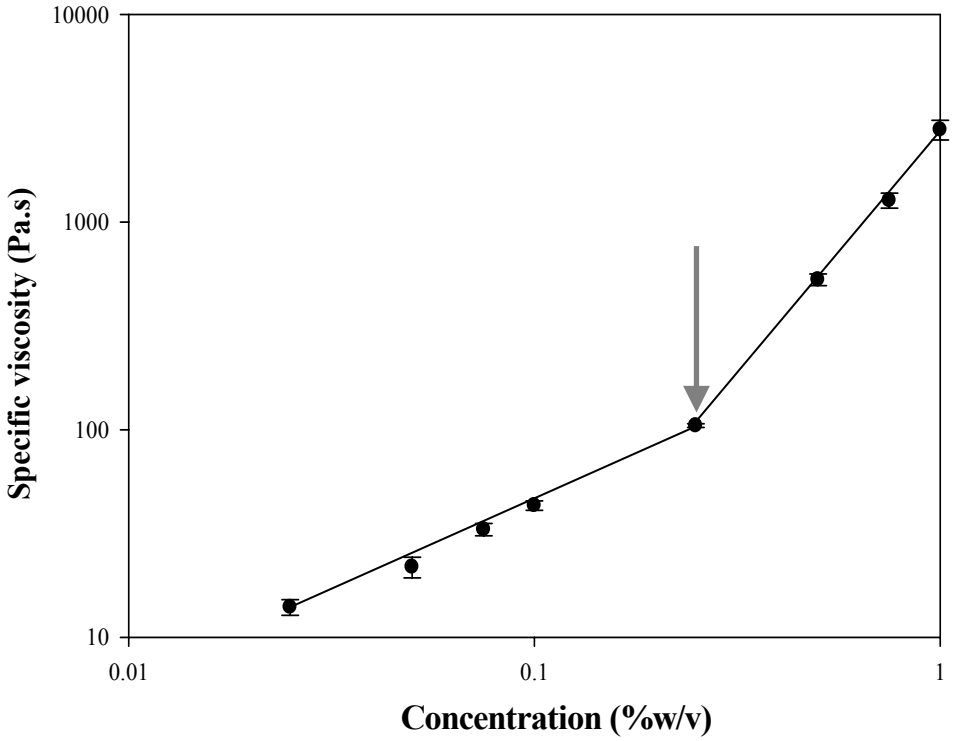

Figure 3.15 The specific viscosity versus the concentration of CMC. The point at which the two lines cross (indicated by the arrow) gives the concentration at which entanglement between the polymer chains begins. Error bars are for one standard deviation from the mean for 3 measurements.

3.5 Diffusion Through Biopolymer Networks Using FRAP

3.5.1 Introduction

Fluorescence recovery after photobleaching (FRAP) is a method for measuring the diffusion coefficient of tracer molecules within a solution (Kappel and Ellis, 2004). For the purposes of this body of work, FRAP has been used to measure the diffusion coefficient of riboflavin through various guar gum solutions. By determining any variation in the diffusion coefficient of riboflavin through guar gum solutions, the diffusive component of the molecular delivery (diffusion and convection) of experiments conducted in the Small Intestinal Model, can to be determined.

Photobleaching, also commonly referred to as fading, occurs when a fluorophore permanently loses the ability to fluoresce due to photon-induced chemical damage and covalent modification. Upon transition from an excited singlet state to the excited triplet state, fluorophores may interact with another molecule to produce irreversible covalent modifications. The triplet state is relatively long-lived with respect to the singlet state, thus allowing excited molecules a much longer timeframe to undergo chemical reactions with components in the environment. The average number of excitation and emission cycles that occur for a particular fluorophore before photobleaching is dependent upon the molecular structure and the local environment (Molecular Expression, 2008). The photobleaching effect can also be utilised to obtain specific information that would not otherwise be available. For example, in FRAP experiments, fluorophores within a target region are intentionally bleached with excessive levels of irradiation (Molecular Expressions, 2008).

FRAP employs irradiation of a fluorophore (Section 3.3.1), in this case riboflavin, in a 50 μm circular section of the overall sample (Figure 3.16), using a short laser pulse to photobleach it and thereby bleach the fluorescence in that area. This is followed by time-resolved image recording of the sample. As the fluorophore diffuses from outside the bleached area through the sample, a recovery of fluorescence can be observed as the unbleached riboflavin replaces the bleached riboflavin. The recovery of the fluorescence is measured over time. Photobleaching experiments are conducted with modern laser scanning microscopes, where the laser is used at high intensity for bleaching and low intensity for image recording (Kappel and Ellis, 2004). The original technique is described by Axlerod *et al.* (1976).

To perform the FRAP experiments, a TCS SP5 (Leica Microsystems, Germany) confocal microscope was used. An Argon laser with an excitation wavelength of 488 nm and an emission range of 500-650 nm was utilised. The settings were: x10 objective, numerical aperture 0.4 and pinhole 7. The scan speed was 1400 Hz and the image was converted into a digital output of 256 x 256 pixels, with each pixel size being 1.01μm. The scanning setting was bidirectional for the FRAP experiments and the bleached area's circular diameter was 50μm.

Figure 3.16 gives a diagrammatic representation of the recovery process after bleaching. Figure 3.17 shows the microscope images at 0, 2, 3 and 8 seconds after recovery. The intensity of the bleached area was monitored over the time of recovery and an example of this can be seen on Figure 3.18 for the normalised intensity.

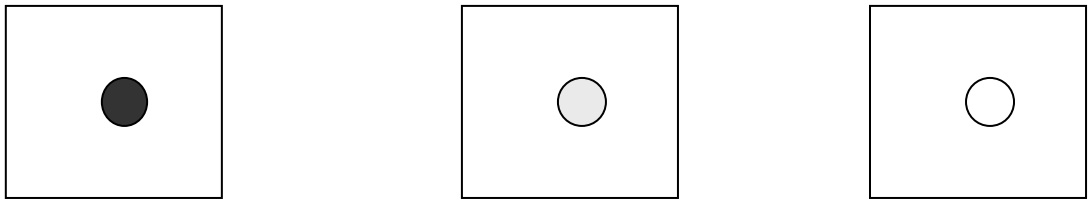

Time = immediately after bleaching

Time = during recovery

Time = infinity

Where ◯ is the bleached area

Figure 3.16 A diagrammatic representation of the recovery process by diffusion after bleaching

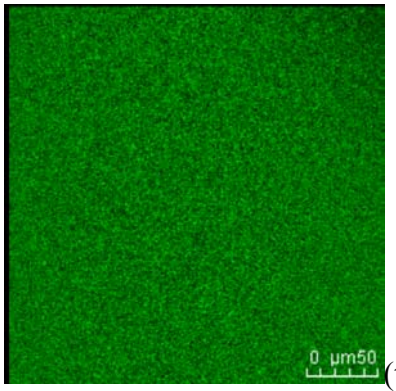

(t = 0)

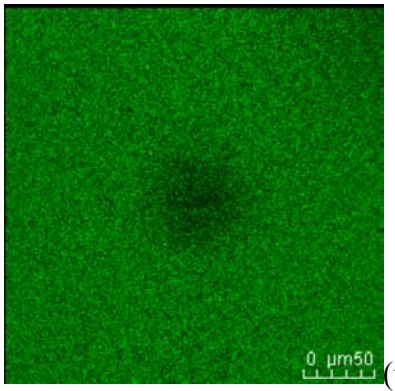

(t= 2s)

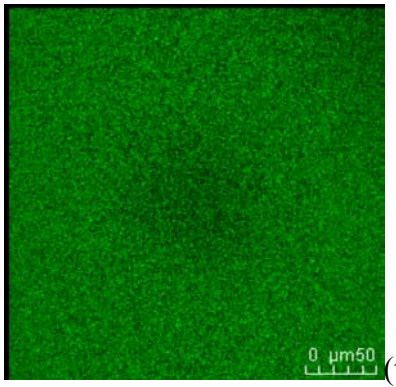

(t= 3s)

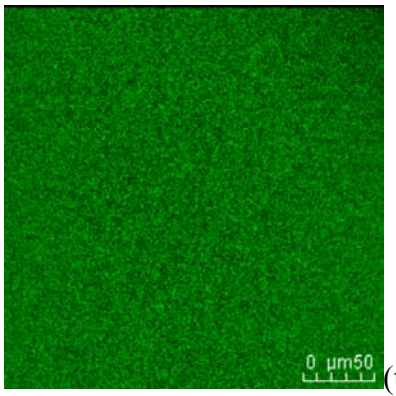

(t= 8s)

Figure 3.17 Digital output from the experiment for 0% guar at t = 0, 2, 3 and 8 seconds. The green indicates fluorescence and the black area shows the bleached section.

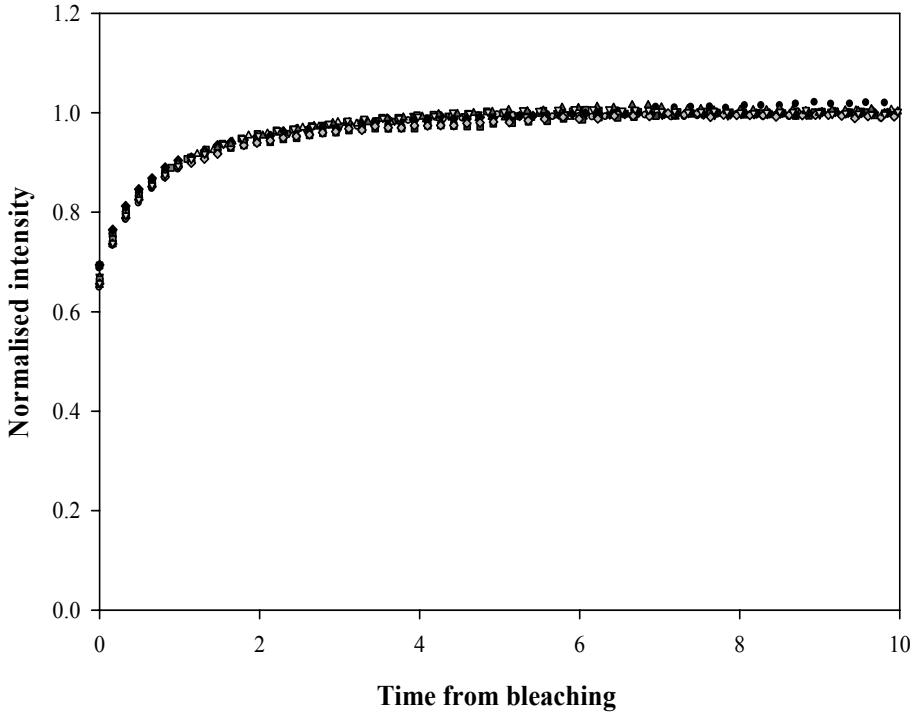

Figure 3.18 The intensity of the bleached area versus time, showing the post bleaching recovery.

3.5.2 Data Analysis

The data from the recovery of the bleached area, in the form of intensity and time was measured. This was then normalised (Figure 3.18) using the method introduced by Siggia *et al*. (2000) where the intensity at every frame (time point) is divided by the intensity of the first frame (time point) before bleaching. This method results in pre-bleach intensities being normalised to 1 as described by Equation 3.8.

$$NI = \frac{I}{PbI} \qquad \text{Equation 3.8}$$

Where NI is the normalised intensity, I is the measured intensity and PbI is the pre-bleach intensity.

The normalised data is then fitted to (Kappel, 2004):

$$y = y_o + a\left(1 - e^{-bt}\right) \qquad \text{Equation 3.9}$$

where y is the normalised intensity and t is the time after bleaching and a and b are constants. The parameter of interest b allows for the recovery half-time ($t_{1/2}$) to be determined from Equation 3.10.

$$t_{1/2} = \left(\frac{1}{b}\right) \times Ln(2) \qquad \text{Equation 3.10}$$

Axelrod *et al.* (1976) gave an expression for the temporal behaviour of fluorescence recovery. Where the transport is purely diffusive they suggest the use of Equation 3.11 to estimate the diffusion coefficient.

$$D = \frac{0.88 \times w^2}{4 \times t_{1/2}} \qquad \text{Equation 3.11}$$

where D is the diffusion coefficient in $\mu m^2/s$, w is the radius of the bleached area (μm) and $t_{1/2}$ is the recovery half-time (s).

3.6 The Diffusion Cell

3.6.1 Introduction

The diffusion cell was designed as a method to measure the mass transfer coefficient of molecules to a membrane, across the membrane and into the recipient side. The diffusion cell was fabricated at the workshops of the Chemical Engineering School at the University of Birmingham. The diffusion cell was designed to investigate the effect of variations in ingredients such as guar gum, on the mass transfer to the membrane and also to investigate the influence of shear on the mass transfer to the membrane. The purpose of the semi-permeable membrane (described in Section 3.6.2) was to contain the biopolymer on one side of the diffusion cell, by choosing a membrane pore size that was sufficiently small to restrict the movement of the biopolymer.

The concentration of the nutrient like molecule from the inner compartment to the recipient compartment was monitored by taking samples from the recipient side for analysis using a Perkin-Elmer Fluorimeter (Section 3.3.1) either on-line or off-line. For experiments where shearing of the sample was taking place, an overhead rheometer Physica Rheolab MC1 (Anton Paar, Germany) was used to stir the fluid and the torque measured for a given rotation speed. The design of the diffusion cell is shown in Figure 3.19 and the custom made impeller used for shearing is shown in Figure 3.20. The laboratory room temperature where the experiments were conducted was controlled at 20^{o}C; all experiments were conducted at this temperature.

The aim of the mixing experiments was to investigate the effect of convection on the rate of nutrient transfer to the membrane of the diffusion cell with different formulations.

3.6.2 Membrane Description

The membrane was a cellulose ester semi-permeable membrane (Spectra/Por 7, MWCO 8000 Daltons, size 8) purchased from Medicell International Ltd (London, UK). A non-active membrane was chosen for controlled investigation into the effect of biopolymer on the rate of nutrient transfer across the membrane.

The membrane was supplied wet (in 0.1% sodium azide solution) from Medicell UK and as instructed by the manufacturer, the membrane was soaked in 3 litres of water for 30 minutes prior to use to remove any sodium azide.

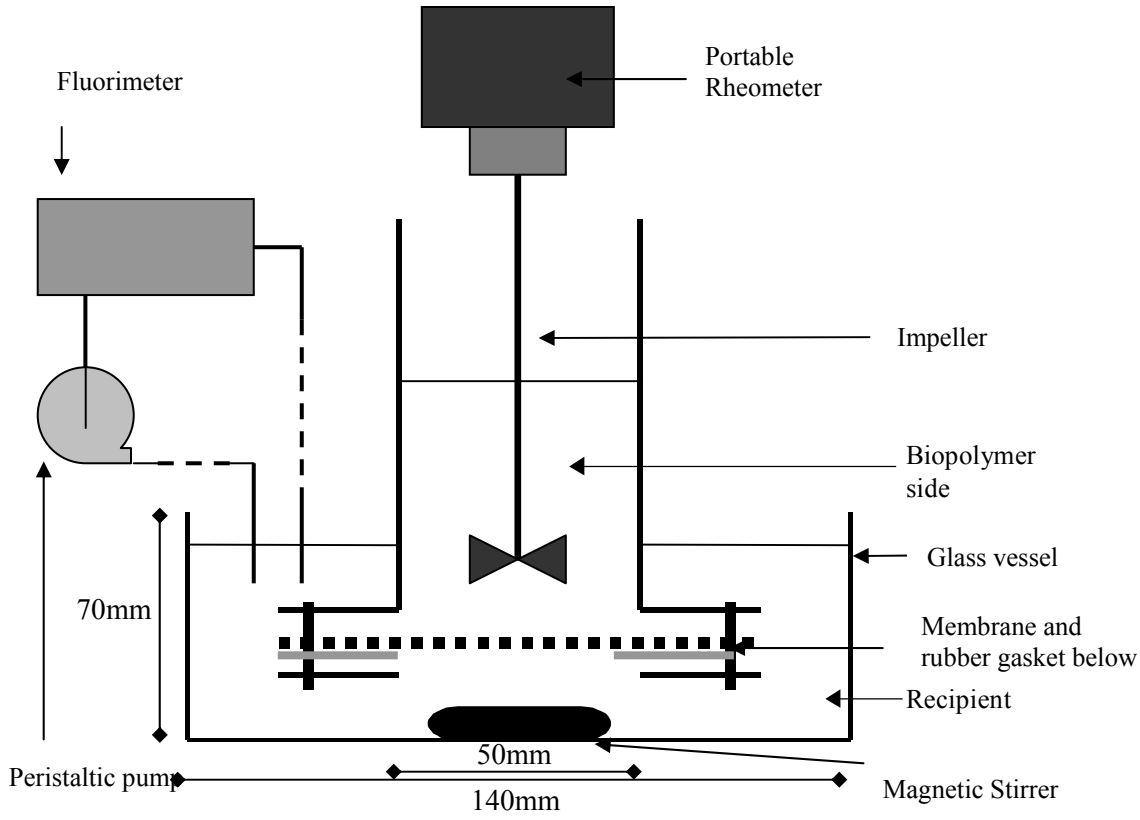

Figure 3.19 A diagram of the diffusion cell set up.

Figure 3.20 The impeller used as part of the diffusion cell set up.

3.6.3 Experiment Preparation

For the diffusion cell experiments the membrane was mounted in the diffusion cell. Six nuts and bolts were tightened to sandwich the membrane in place, with a rubber insert to act as a gasket. This prevented leakage from one side to the other.

The recipient side was filled with 500 ml of filtered water and the magnetic stirrer was set at setting 2 after having determined that this setting minimised the recipient side resistance using the stirrer plate (IKAMAG RCT, Germany) to ensure homogenous concentration in the recipient side. The biopolymer side was examined for leakage by adding water and checking for leaks. The water was then removed from the diffusion cell and 50 ml of the solution being investigated was placed into the cell. At this point, the cell and the glass vessel containing water were still separate. The cell was then placed immediately into the water in a manner that ensured there were no air bubbles remaining below the membrane. All experiments were carried out using fluids at the room temperature of 20^{o}C.

3.7 The Small Intestinal Model

The design of the Small Intestinal Model (SIM) required careful consideration to ensure that mechanical processing of the digesta in the human small intestine was accurately represented and that measurements of interest could be obtained. By being able to measure the parameters of interest whilst changing the properties of the food formulation (model digesta), the influence that the formulation variation has on the delivery of nutrient to the wall, the fluid dynamics and mixing profiles can be examined. Fluid dynamics and mixing profile measurements are presented in Chapter 6.

The SIM also allowed process parameters, such as the frequency of modelled segmentation action, the overall flow rate and the number of sections to which the segmentation was applied to be changed. Table 3.4 gives a comparative summary of the process conditions in the small intestine and the SIM.

Small Intestine	Model of the Small Intestine
Function - The small intestine is responsible for virtually all nutrient absorption in digestion. (Smith and Morton, 2001).	The model is a simplified representation of the real system that mimics the segmentation motion of the small intestine.
Dimensions - The small intestine is on average 6m in length and has a diameter ranging from 4cm at the stomach end to about 2.5cm at the junction with the large intestine (Martini, 2006).	The diameter of the membrane tubing that represents the food side is 3 cm and the length over which absorption takes place is 50cm.
Peristalsis - Propulsive contractions are responsible for propelling the digesta (peristalsis). Move analward at a velocity of 0.5 to 2.0 cm/sec, are normally very weak and die out after 3 to 5 centimetres (Guyton, 1996).	The overall flow in the system is generated from a variable peristaltic pump on both the food and recipient side.
Segmentation - The mixing contractions are known as segmentation contractions and are localised concentric contractions spaced at intervals along the intestine. The contractions are approximately 1cm in length (Guyton, 1996)	The segmentation is reproduced by the concentric constriction of the tube with the use of inflatable bladders.
Active Membrane - To be absorbed into the body, nutrient must pass through the epithelium which is a layer of cells that line the wall of the small intestine and are connected by tight junctions. The epithelium cell wall is made of a membrane with a lipid bi-layer containing phospholipids, steroids and proteins (Martini, 2006).	The membrane is made from cellulose ester and is a semi-permeable membrane. The purpose of the membrane is to form a barrier between the food and recipient side and allow for mass transfer and the delivery of nutrient to the inner side of the membrane to be measured which can be used to understand the delivery of nutrients or actives to the membrane of the small intestine.
Digesta: The digesta is an extremely heterogeneous system to investigate and previous approaches have used simple guar solutions as model systems to provide insight into effects of guar gum *in vivo* (Ellis,2000).	Biopolymer solutions have been used with a range of viscosities from 1 up to 7000 mPa.s, Covering the range found in *in vivo* studies; 0.01 – 10 Pa.s (Ellis *et al.,* 1996).
Temperature and pH – The temperature of the digesta can be assumed to be body temperature of 37^0C and the pH is 5.7–6.4 in the duodenum, up to 7.4 in the jejunum, up to 7.7 in the ileum. (Ekmekcioglu, 2001).	The temperature was maintained at the controlled temperature of laboratory of 20^0C and the pH of the water was 6.4.
Blood – Blood is a complex fluid which serves many functions, one of which is the transport of nutrients around the body.	The recipient side of the model allows for the detection of nutrients as it passes through the membrane and consists of filtered water.

Table 3.4 A comparison between the real small intestine and the SIM.

The SIM consisted of an inner porous flexible membrane and an outer flexible tube that is impermeable to water. As molecules diffused through the inner tube membrane into the fluid contained in the outer tube, they were detected by the fluorimeter (Section 3.3.1) using on-line sampling.

Segmentation is responsible for promoting mixing of the solid food particles with the secretions of the small intestine (Section 2.2.4). In the model this action was reproduced by the inflation and deflation of a rubber cuff around the tube by alternatively applying compressed air and a vacuum. The mechanical squeezing mechanism was controlled by a computer. The end result was a concentric mass exchanger that allowed for the mechanical deformation of both the inner and outer tubes in a physiologically representative manner.

The development of the SIM was a combination of design, fabrication and commissioning. The design was split into two stages: (i) an appropriate concentric tubular mass exchanger made from flexible material was designed and (ii) a means of inducing the correct mechanical motion was designed.

Two types of fluid flow are of interest using this model: the overall net fluid flow using the variable peristaltic pump; and also local flow from the dynamic annular radial contraction from squeezing of the tube. The fluid flows of interest are on the food side (biopolymer side) of the SIM; the experimental set up therefore ensured that food side mass transfer was measured, by minimising the recipient side resistance to mass transfer.

3.7.1 The Tubular Section

The aim was to develop a concentric mass exchanger from a flexible material to allow physiologically representative deformation to take place. The mass exchanger was made from two tubes as seen in Figure 3.21. The inner tube was a semi-permeable membrane made from cellulose ester (Spectra/Por 7, MWCO 8000 Daltons, size 8) (see Section 3.6.2). The same type of membrane was used in the diffusion cell studies described in Chapter 4. The outer tube was made from clear polyethylene tubing. A semi-permeable membrane was chosen as it is flexible and separates the two compartments being the biopolymer (food) side and the recipient side. The parameter of interest being the delivery of nutrient to the membrane on the food side (for different processing conditions and product formulations) and by measuring the concentration on the recipient side allows the delivery of the nutrient to the membrane to be investigated.

The flow rate on the recipient side must be sufficient to ensure that resistance to mass transfer on the recipient side is minimised, experiments describing the setting of these conditions are described in Section 5.2.2 and Table 5.3. There has been no attempt to model blood flow as this model investigates nutrient delivery to the wall of the intestine only and not across the intestine into the blood.

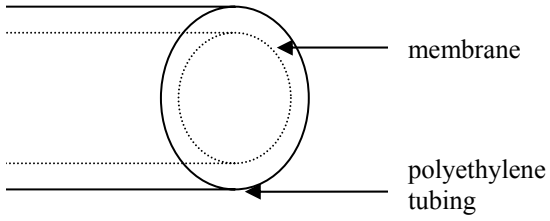

Figure 3.21 A diagram of the concentric tubes for the mass exchanger

To hold the inner semi-permeable membrane and outer tubing in place and to form separated compartments for the biopolymer side (food) and the recipient side, tube clamps were designed for each end of the tubes. The tubes clamps were fabricated from stainless steel and their design is shown in Figure 3.22. Two clamps were made, one for each end comprising of a collar each for the inner and outer tube. Fluid inlets/outlets for the inner and outer side were also incorporated into the tube design. The membrane and the tubing were held in place using two rubber gaskets on each end to form water tight seals.

The design used a length of 50 cm of tubing available for mass transfer. The flexibility in the tubing allowed for the tube to be deformed in a physiologically representative manner.

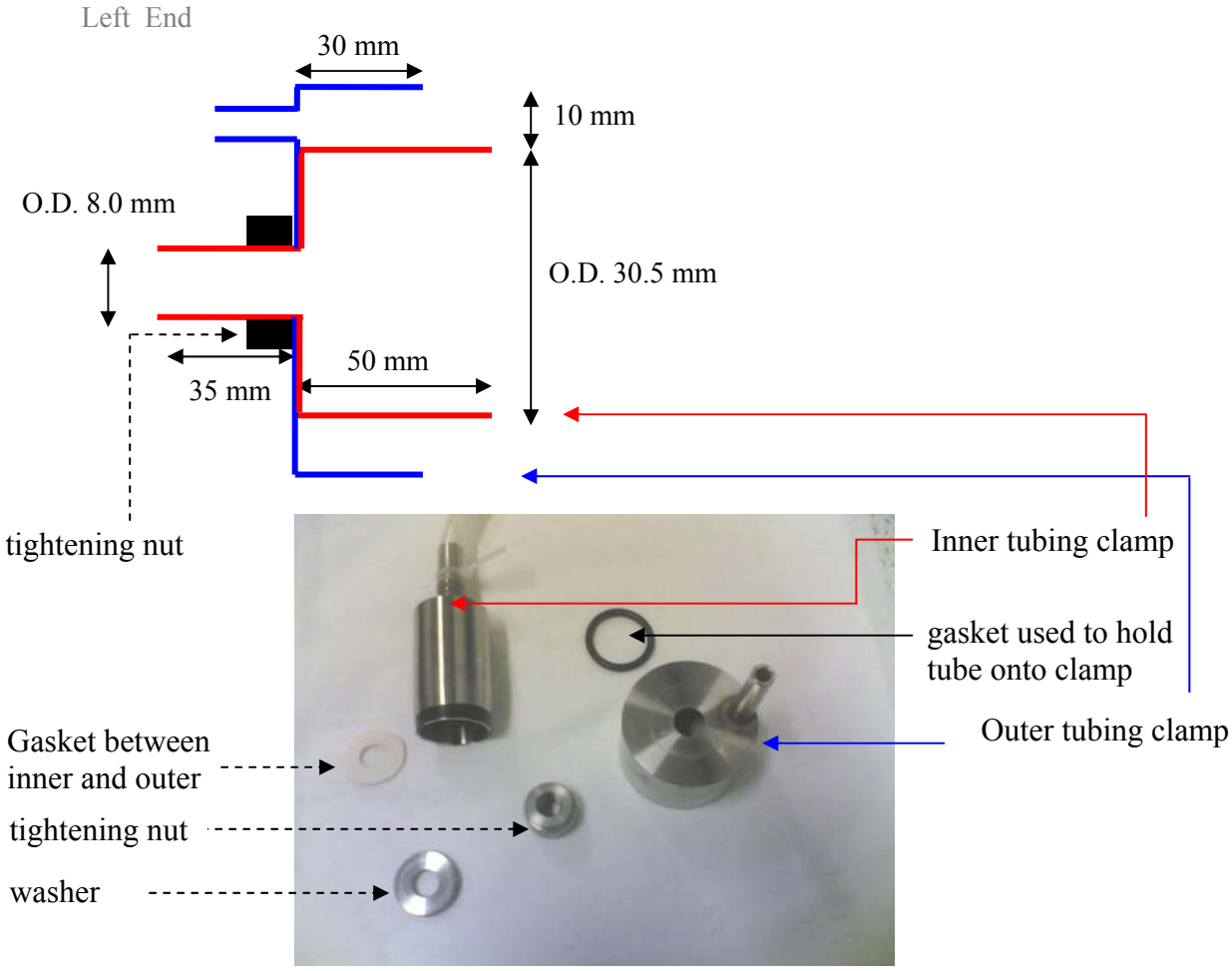

Figure 3.22 A diagram and picture of the left side tube clamp.

3.7.2 The Squeezing Mechanism

The second stage of the intestinal rig design and development was to design and make a mechanical squeezing mechanism. The squeezing was induced by a pneumatic method, using pressurised air for inflation and vacuum for deflation. The inflatable cuffs were from an Omron Blood Pressure machine. The cuffs were wrapped around the section of the tube to be squeezed. The inflation of the cuff was controlled by the opening and closing of solenoid valves (Burkert W2YLE, Germany) that control the opening and closing of the cuff (to the compressed air or the vacuum lines) at the correct time. The opening and closing of the solenoid valves was controlled from a programmable logic controller (National Instruments, NI USB-9162) that was connected to a computer running the control programme (National Instruments NI-DAQMAX). The computer contained a programme written by Derek Green (Birmingham University) that allowed for the timings and setting of the squeezing sequences to be set by controlling the inflation, deflation and delay times. The programmable logic controller (PLC) was powered by a 24V power supply (Power-one, 24VDC at 2.4A). The rate of inflation of the cuffs was monitored using a pressure indicator (Sunx: DP2-42E) for the compressed air. For safety reasons pressure relief valves (Norgen: 61B2) were also fitted to the compressed air lines.

The layout of the SIM is described schematically in Figure 3.23, showing the two compartments as the food side and the recipient side, separated by the semi permeable membrane. Each compartment had a surge tank to allow for the volume displaced by the squeezing of the tubes. Figure 3.24 shows a schematic of the tubing dimensions. Figure 3.25 is a photograph of the SIM for experiments with one cuff wrapped around the tubing for the set up. The tubes and individual parts are described by their allocated number.

Figure 3.26 is a photograph of the solenoid valves used to control the inflation and deflation of the cuffs that squeeze the tubes. The photograph also shows the pressure relief valves that are part of the safe design of the equipment. Figure 3.27 shows a picture of the control software panel used to set the timing sequences of the SIM.

The use of the blood-pressure cuffs to simulate the segmentation motion seen in the small intestine is a significant step toward modelling the wall motions. However, a limitation of the use of the blood pressure cuff is that the length of the cuff is approximately 12 cm (Figure 3.24) and the length of intestine which contracts during segmentation is 1 cm (Table 3.4). The blood-pressure cuff was used as it was a practical method of reproducing the segmentation motion and thus aids in the understanding of the effect that this motion has on the mass transfer and fluid dynamics in the small intestine. Chapter 7 address the further development of the small intestinal model (Section 7.2.2) and suggests development opportunities in this area.

Details of the experimental procedure for the experiments such as cuff inflation times, food and recipient side volumes, flow rates and formulations used are described in Chapter 5.

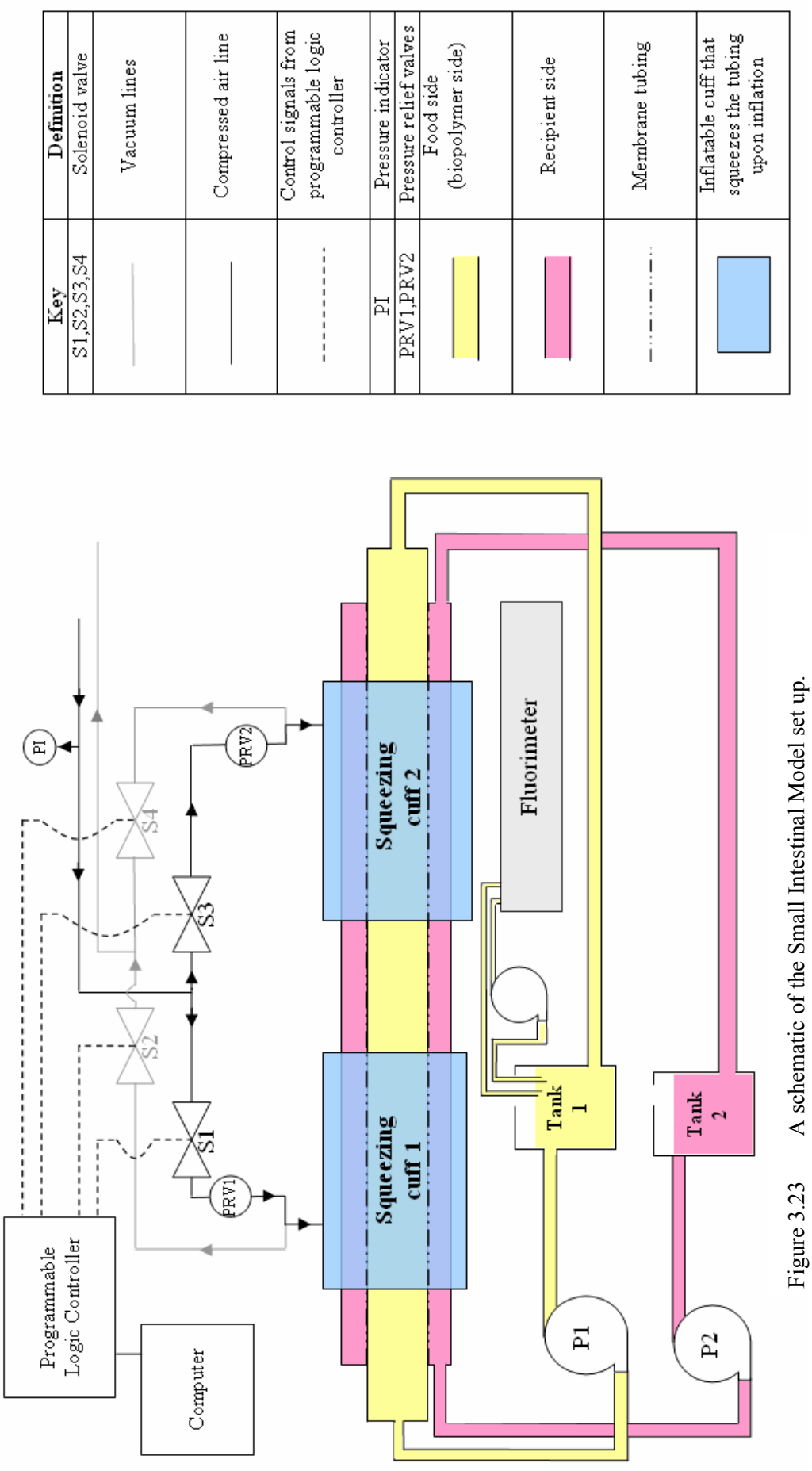

Figure 3.23 A schematic of the Small Intestinal Model set up.

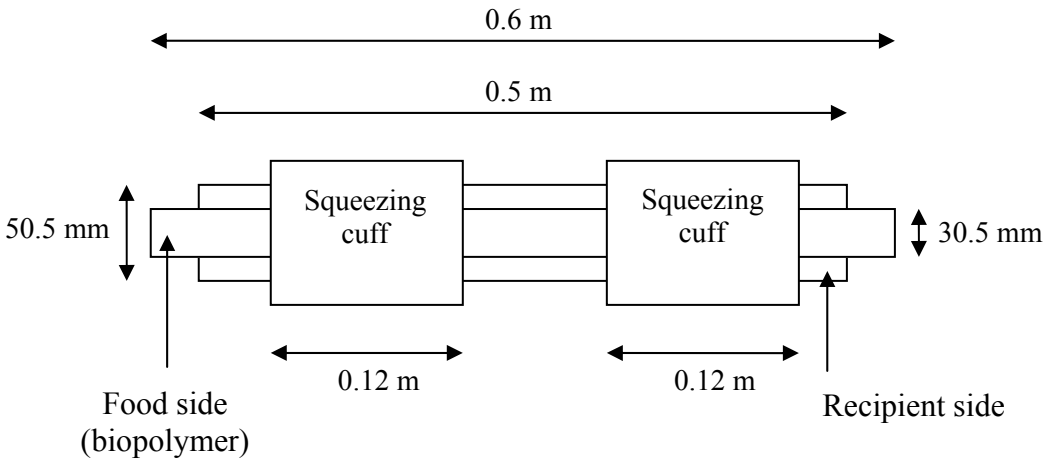

Figure 3.24 A schematic of the SIM with measurements.

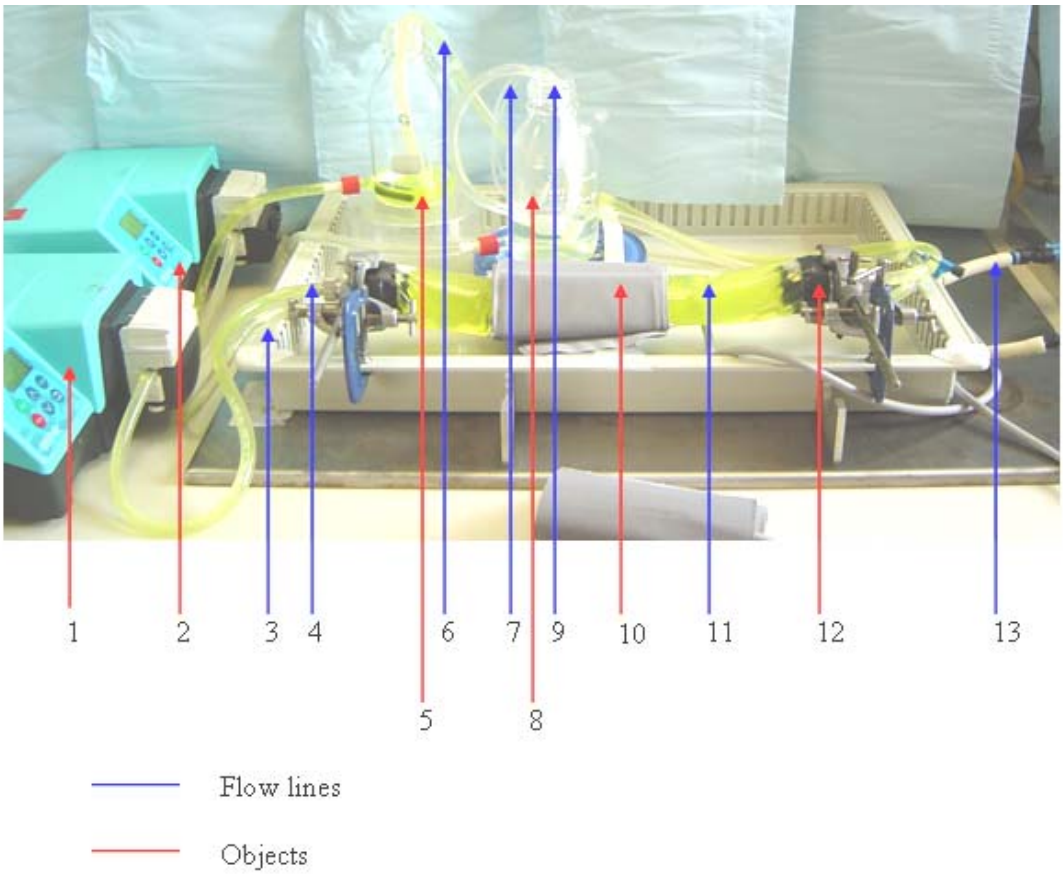

Figure 3.25 A photograph of the SIM set up for mass transfer experiments (for a single cuff experiment). A numerical description of the parts is as follows:

1. Peristaltic pump for inner (food) side (P1)
2. Peristaltic pump for outer (recipient) side (P2)
3. Inlet for the outer tube
4. Inlet for the inner tube
5. Feed and surge tank for the food side
6. Small intestine section outlet and feed tank inlet (food side)
7. Inflow and outflow to Fluorimeter (Perkin-Elmer LS 50B) for concentration analysis
8. Feed and surge tank for the recipient side
9. Recipient side section outlet and feed tank inlet
10. Inflatable cuff (Omron) to replicate the segmentation action
11. Small intestinal section
12. End of small intestinal section
13. Connections to gas lines (compressed/vacuum)

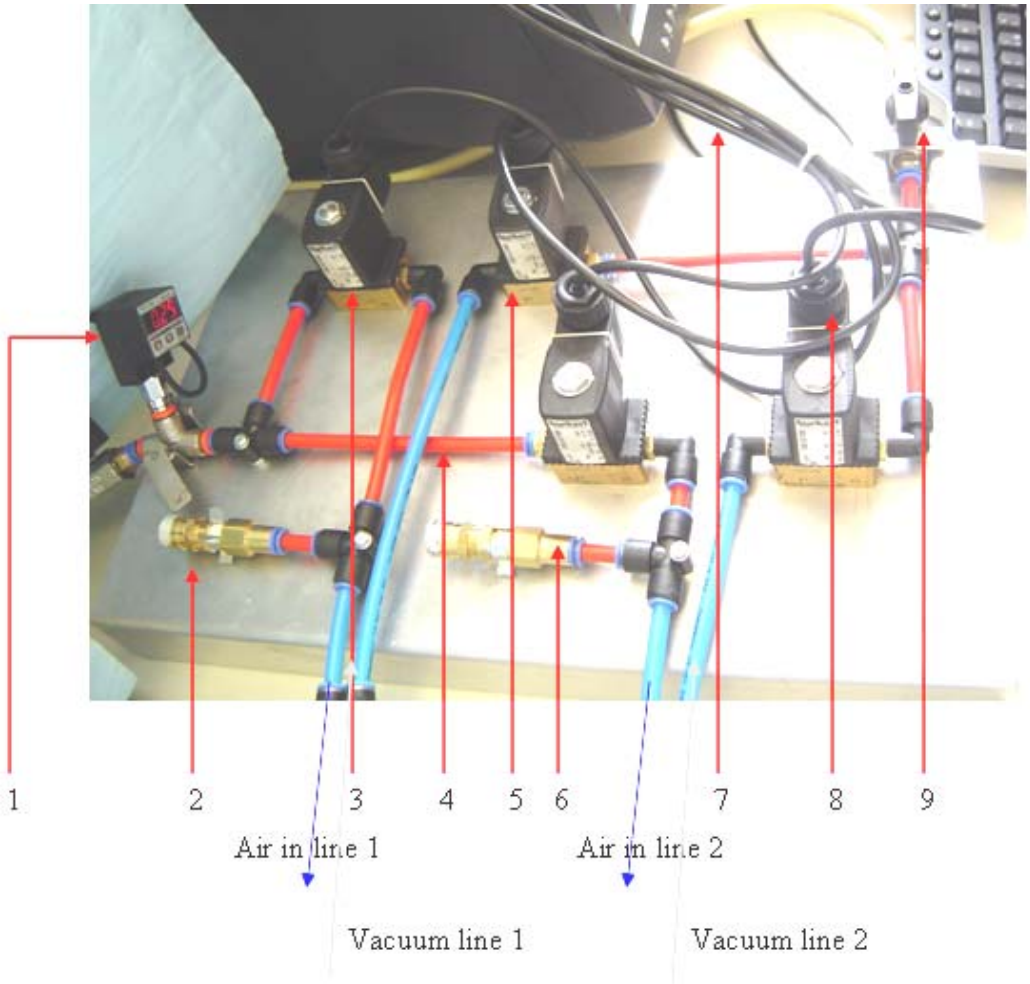

Figure 3.26 A photograph of the solenoid valve, compressed air, vacuum, pressure monitor and relief valves. A numerical description of parts is as follows:

1. Inlet pressure sensor connected to compressed air inlet line (Sunx: DP2-42E)
2. Pressure relief valve (Norgen: 61B2)
3. Solenoid valve (Burkert W2YLE)
4. Pressurised air tubing
5. Solenoid valve (Burkert W2YLE)
6. Pressure relief valve (Norgen: 61B2)
7. Connections for solenoid valves to programmable logic controller (PLC) for open and closed settings. PLC controlled by settable software on PC
8. Solenoid valve (Burkert W2YLE)
9. Main Vacuum

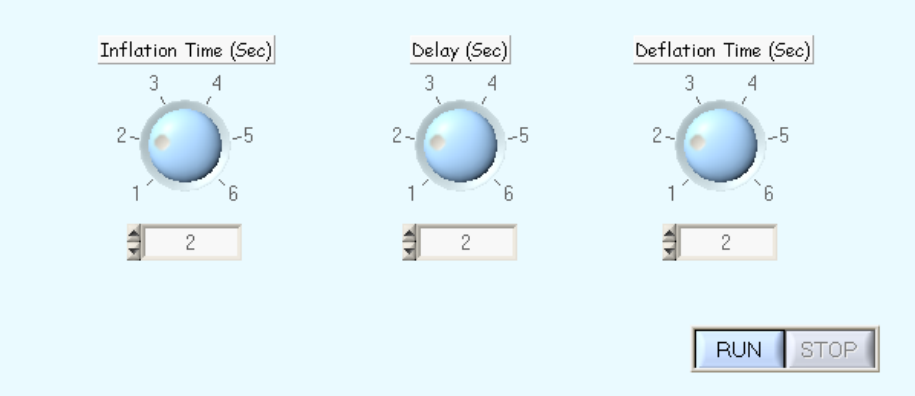

Figure 3.27 A screen capture of the control software for the SIM

3.8 Particle Image Velocimetry

Particle image velocimetry (PIV) is an experimental fluid dynamics technique used to study flow velocities within a process (Raffel *et al*., 1998). The dynamics of the flow velocities in the SIM were the area of interest here and PIV was chosen for its capability to perform instantaneous measurements across the entire plane of measurement simultaneously. Using the instantaneous velocity fields from PIV, it is possible to establish flow field velocities, shear rates and the Reynolds numbers of the process at a given point of time and space.

PIV is a non-intrusive technique that uses the interaction of laser radiation and tracer particles within the flow to determine instantaneous fluid velocities by measuring the change in the position of the small tracer particles at successive times.

A diagram of the 2-dimensional PIV setup is shown in Figure 3.28. The tracer particles in the fluid are illuminated by the plane of laser light twice in a short time interval and the

light scattered by the particles is recorded using a digital camera. The change of position of the particle in the image between the light pulses is used to calculate the particle velocity.

The tracer particles should follow the fluid motion exactly and it is therefore required that they are neutrally buoyant and small enough to follow the flow. The tracer particle should also scatter enough light to be detected and be of a high enough concentration to give reliable velocity measurements. Silver coated hollow glass spheres were used for these experiments as described in Section 3.8.2. A typical PIV image is shown in Figure 3.29 and portrays an image of 1000 x 1000 pixels and the tracer particles. The seeding density should result in approximately 10 pairs of particles present in a 32 x 32 pixels size interrogation window (Khan, 2005).

The basic components of digital PIV are:

1. Seeding particles;
2. Laser beam;
3. Charged Couple Device (CCD) cameras;
4. Synchroniser; and
5. Image Analysis.

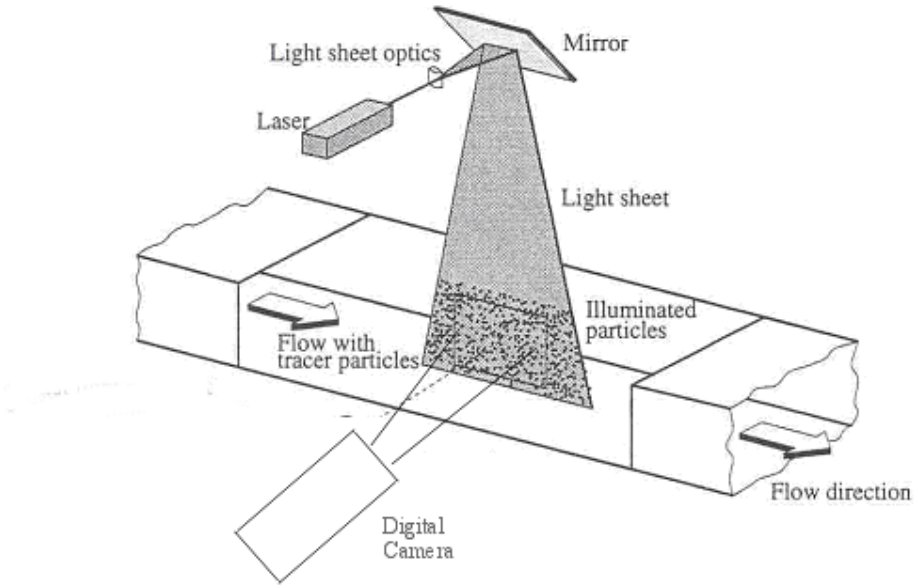

Figure 3.28 Schematic of the PIV system (Raffel *et al*., 1998)

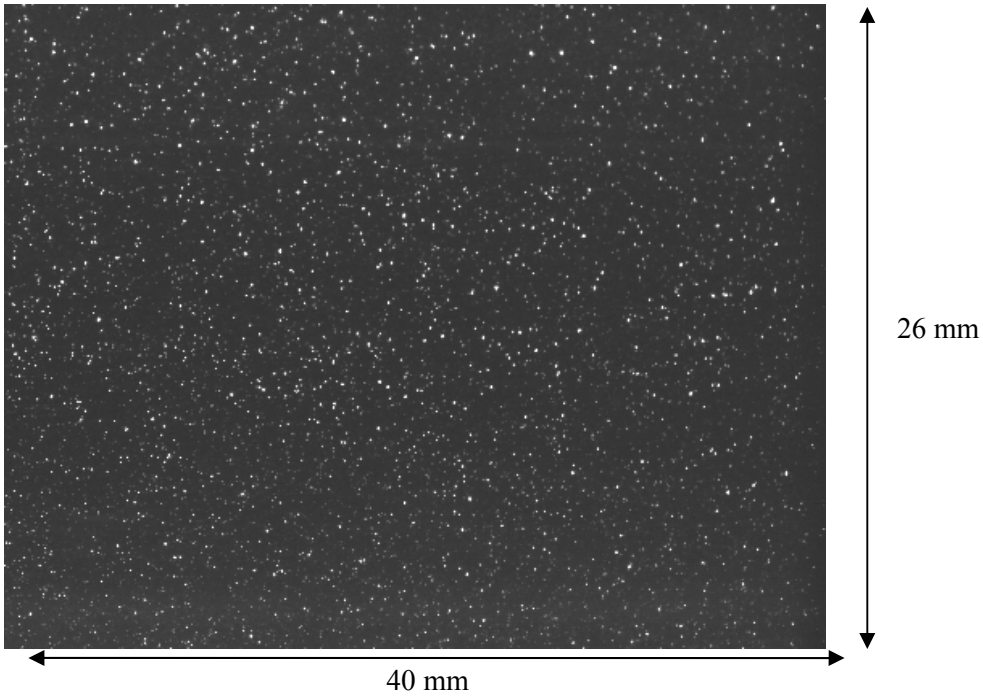

Figure 3.29 Typical seeded PIV image

3.8.1 Analysis

PIV systems measure velocity by determining particle displacement (Δx, Δy) in a flow over a known time Δt. For the coordinates used here, x is the horizontal direction and y the vertical direction. The pulsed laser sheet illuminates a plane in the flow and the position of the particles is recorded. A second laser pulse, Δt later, illuminates the same plane, creating the second set of particle images. As the particles in the flow field move by an amount Δx in the x-direction and Δy in the y-direction, in time Δt, the velocities of the particles in the x and y directions are given by:

$$u = \Delta x / \Delta t \text{ and } v = \Delta y / \Delta t \qquad \text{Equation 3.12}$$

The particle movements are captured by the image capture system (camera) and recorded as image displacements ΔX and ΔY. If M is the camera magnification, ΔX and ΔY are:

$$\Delta X = M^* \Delta x \text{ and } \Delta Y = M * \Delta y \qquad \text{Equation 3.13}$$

The particle images obtained from the two laser pulses are recorded on separate camera frames. The images in each of these frames are subdivided into a large number of interrogation regions.

To analyse the single-frame single-exposure images, a cross-correlation is carried out between the interrogation window of the first and second frames and is described by Equation 3.14.

$$R(x,y) = \iint I(x,y) I'(x + x_o, y + y_o) dxdy \qquad \text{Equation 3.14}$$

Where R is the spatial cross-correlation function of transmitted light intensity I for the first image and I' for the second image.

A Fast Fourier Transform (FFT) technique is used to solve Equation 3.14. The complex conjugate of each corresponding pair of Fourier coefficients is multiplied and then inverse FFT transformed to obtain the cross-correlation function. The spatial cross-correlation provides a statistical estimate of ΔX and ΔY for that region which is given by the peak of the cross-correlation function R. The peak of the cross-correlation function represents the most probable displacement of the group of particles between the sampled images. The distance of this maximum peak from the centre represents the displacement of a group of particles between the pair of interrogation windows (Khan, 2005). Since particle images are in separate frames, cross-correlation analysis also gives the direction of image displacement, and hence the velocity vector, described by Equation 3.15.

$$u = (\Delta X / M)/ \Delta t \text{ and } v = (\Delta Y / M)/ \Delta t \qquad \text{Equation 3.15}$$

3.8.2 Experimental Set Up

The experimental set up is shown diagrammatically in Figure 3.30 and is also shown as a photograph in Figure 3.31. The detailed description of the Small Intestinal Model (SIM) within which the flow was studied is given in Section 3.7. A modification was made to the SIM for the use of PIV by installation of viewing section fabricated from Perspex tubing, since rigid walls are required to prevent any movement interfering with the laser light. Around the Perspex tube was a square box housing that prevented the distortion of the laser as it entered the unit due to the tube curvature. The box was filled with the same fluid as in the tube to minimise refraction effects. A diagram of this is shown in Figure 3.32 with the visualisation box and the measurement area. The coordinates for the x and y directions are also given.

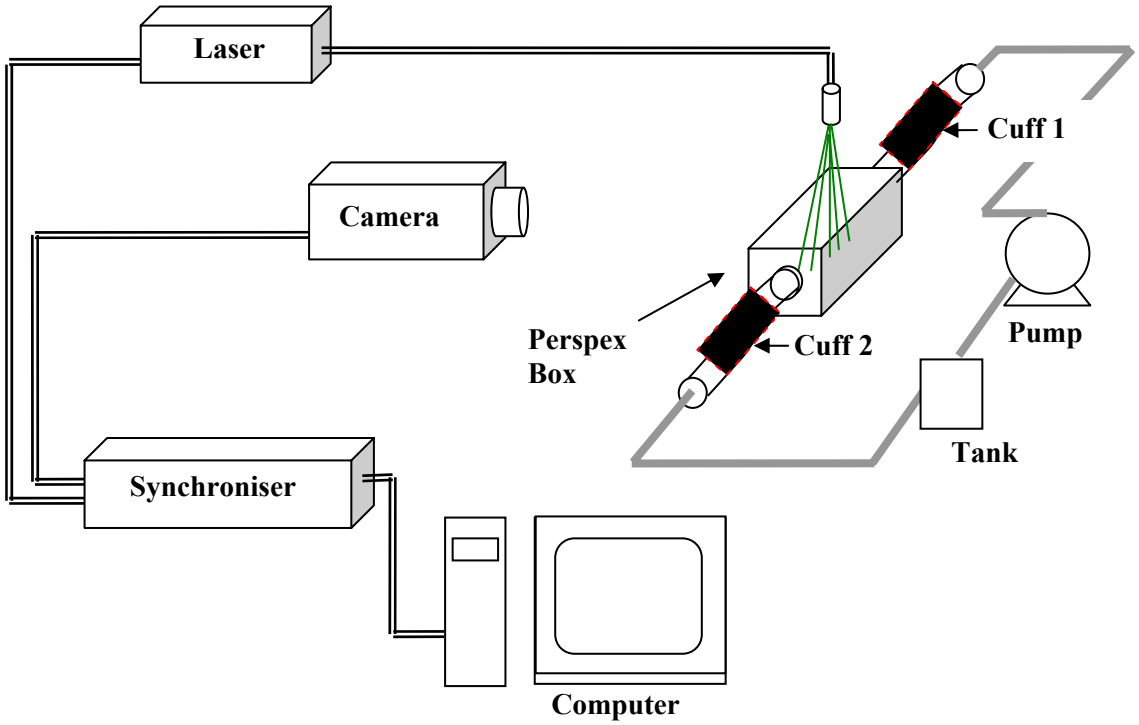

Figure 3.30 Schematic of the set up for PIV experiments.

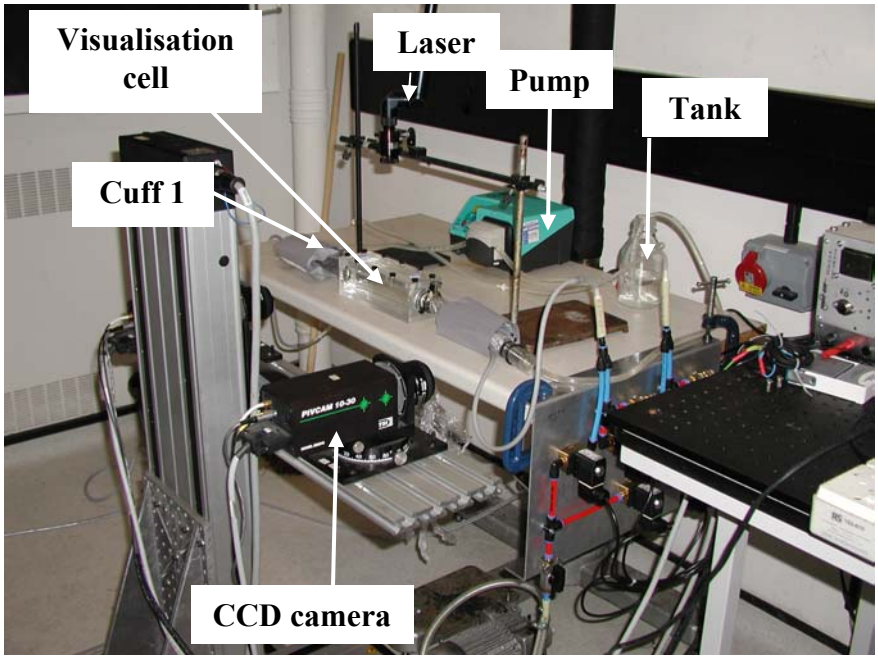

Figure 3.31 PIV Experimental Set up

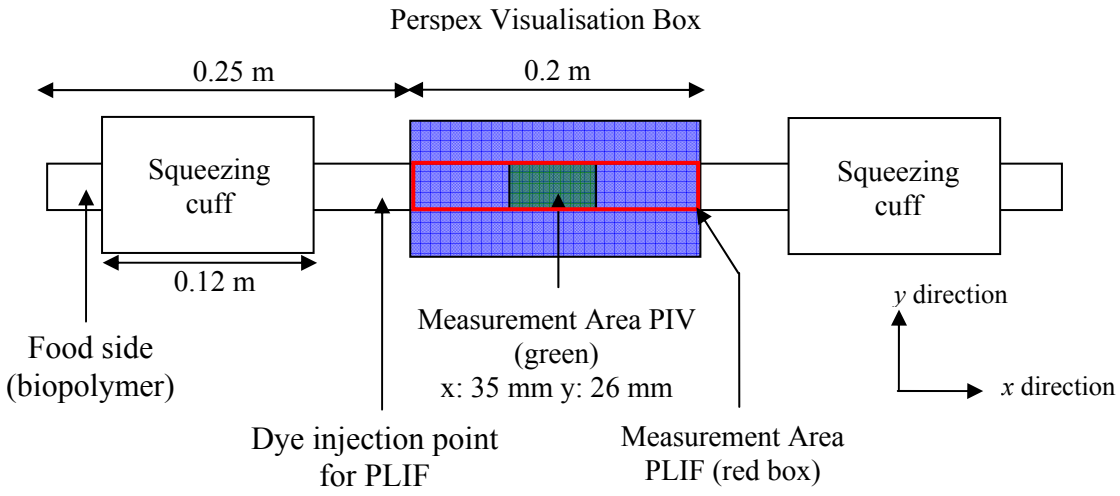

Figure 3.32 A schematic of the intestinal cell set up with dimensions and areas of measurement for PIV and PLIF.

The 2-D PIV system comprised of a TSI Powerview system (TSI Inc. USA) which is made from the following: a single 1000×1016 pixel; 8 bit Charged Coupled Device (CCD) camera (TSI PIVCAM 10-30, TSI Inc, USA); synchroniser; a dual head Nd-Yag laser emitting at 532 nm (New Wave Inc., USA); and laser sheet optics. The computer-controlled synchroniser performs the duty of triggering the laser pulse and camera with the correct sequence and timing. The CCD camera has the ability to capture PIV images with a very short time between them as a sequence. For these experiments, a -15 mm cylindrical lens and a 200 mm spherical lens were used, to give a minimum thickness of the laser sheet. The system was controlled using a Dell Precision 620 workstation (Dell Corp. USA) that was running the INSIGHT 6.0 software.

The particles used as a tracer were DANTEC (S-HGS-10) silver coated hollow glass spheres with a diameter of 10 μm. The particles were chosen as they were small enough to

follow the flow and able to scatter enough light to be detected. The effective flow following seeding particles should have a short relaxation time τ_s (Equation 3.16):

$$\tau_s = d_p^2 \frac{\rho_p}{18\mu} \qquad \text{Equation 3.16}$$

Where τ_s is a measure of the timescale required for the particles to attain velocity equilibrium with the fluid (Khan, 2005), d_p is particle diameter (m), ρ_p is the particle density (kg/m^3), and μ is the fluid dynamic viscosity (Nm^{-2}s). This work uses 10 μm particles; the relaxation time is 6 μs and the Stokes number (which is a ratio of particle and fluid response time) is small enough that the particles will follow the motion of the fluid. As the viscosity of the fluid increases the relaxation time decreases.

The images were captured at a rate of 4 Hertz and interrogated using the INSIGHT 6.0 software FFT cross correlation, which divides it into 32 x 32 pixel interrogation areas (IA) with 50% overlap between two neighbouring IA. The area of interest was a 26 mm x 35 mm box in the centre of the tube.

3.9 Planar Laser Induced Fluorescence

Planar laser induced fluorescence (PLIF) is a flow visualisation technique that can be used to give quantitative information on the shape and the spreading behaviour of tracer dye in a fluid. During these experiments PLIF has been used to determine the effect of variation of the concentration of viscosifying polymer (CMC), on the mixing effectiveness of a fluorescent dye into the bulk fluid. The PLIF technique and the information complement the velocity profiles from the PIV technique (Section 3.8). PLIF gives information on the

dispersion of the dye in the CMC fluids with varying concentrations of CMC, hence varying viscosities under the simulated small intestinal process conditions with the use of the SIM.

This work describes the development and application of a PLIF technique that measures the mixing performance in the SIM. The process is unsteady due to squeezing of the fluid upstream and downstream of the visualisation box.

3.9.1 PLIF Setting

The 2-D PIV system, comprising of a TSI Powerview system (TSI Inc. USA) as described in Section 3.8 and shown in Figure 3.30 was used for the PLIF experiments. For the purposes of PLIF a single frame was captured each time and a sharp cut-off high-pass wavelength filter (ALP545, TSI Inc.) was used on the camera to eliminate the light from the laser and only allow fluorescent light from the tracer fluid to pass through. Images were captured at a rate of 5 Hz and the experiments were conducted for 120 seconds.

1 ml of fluorescent dye (Rhodamine 6G, Sigma Aldrich) was introduced as the tracer (at a concentration of 0.5 mg l^{-1}) into the fluid flow immediately prior to the visualisation cell. The rhodamine dye solution was made using CMC at the same concentration as the fluid used in the experiment. A calibration was performed to be able to determine the dye concentration at any point of the image from the greyscale value from the black and white image. The calibration curve for the dye concentration to greyscale value for the set up used as part of these experiments is shown in Figure 3.33, showing that at low concentrations the concentration of the dye increases linearly to around 0.1 mg l^{-1} and then

becomes non-linear. This work used the decay of the area of the dye with a concentration of 50% and greater of the original concentration (i.e. 0.25-0.5 mg l^{-1}) as a measure of mixing. A change in greyscale value from 255 to 245 occurred as the concentration changed form 100% to 50% of the original concentration. Although within the non-linear region of the calibration; as high a concentration as possible was chosen as the initial concnetration to maximise the time period of the experiment.

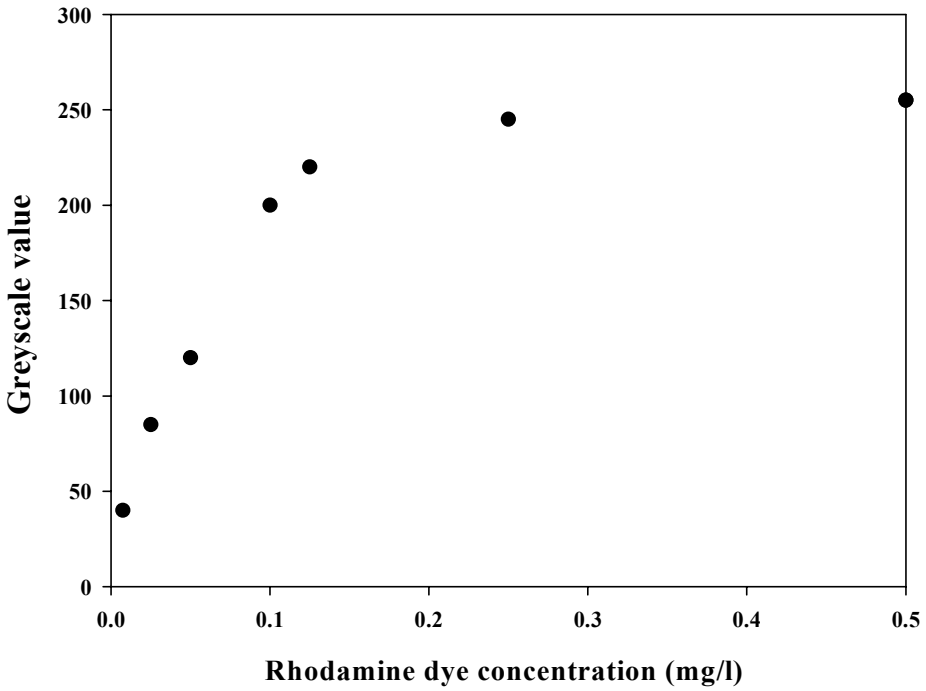

Figure 3.33 Calibration relating greyscale value to rhodamine dye concentration

3.10 Computational Fluid Dynamics

The technique of computational fluid dynamics (CFD) was used to create a computational model of the segmentation process in the SIM. The purpose of the CFD model was to complement the results found from the mass transfer experiments using the SIM and the results from the Experimental Fluid Dynamics (PIV and PLIF). Using the CFD technique it is possible to theoretically evaluate the fluid dynamic parameters as the fluid properties

change. The parameters of interest are: peak velocities, Reynolds numbers, flow profiles and shear rates.

CFD can be regarded as the analysis of systems involving fluid flow, heat transfer and associated phenomena such as chemical reactions, by means of computer-based simulations. CFD is a very powerful technique and spans a wide range of industrial and non-industrial application areas. Some examples are (Versteeg, 1995):

- Power plants - combustion in internal combustion engines, boilers and gas turbines;
- Environmental engineering - distribution of pollutants and effluents;
- Biomedical engineering - blood flow through arteries and veins;
- Hydrology and oceanography - flows in rivers and oceans;
- Aerodynamics - aircraft and vehicles, prediction of lift and drag; and
- Chemical process engineering - mixing and separation, such as polymer moulding.

A recent review on CFD as an effective and efficient design and analysis tool for the food industry by Norton and Sun (2006), discusses the fundamentals involved in developing a CFD solution and state-of-the-art review on various CFD applications in the food industry, such as ventilation, drying, sterilisation, refrigeration, cold display and storage, and mixing, and elucidates the physical models most commonly used in these applications. The CFD as part of this thesis expands the application of CFD in the food industry into the modelling of the segmentation motion seen in the small intestine to aid in product development.

The commercially available CFD code, FLUENT 6 (ANSYS, Inc., USA) was selected for this work as it has modelling capabilities in dynamic meshing. There is the benefit that once the segmentation motion and flow profiles have been validated using CFD for the real system, the transition to investigate different formulations and more complex and realistic geometries is easily possible.

To understand the influence that food formulation has on fluid flow profiles in the small intestine, a model of the process conditions (movement of the intestinal wall) in the small intestine was created using FLUENT. The model simulates the dynamic flow within the changing geometry of the tube. The fluid and mesh geometry inside the tube was assumed to be axisymmetric.

CFD codes are created around numerical algorithms that can tackle fluid flow problems. All commercial CFD packages include sophisticated user interfaces to input problem parameters and to examine the results (Versteeg, 1995).

FLUENT contains three main elements:

(i) Pre-processor: This consists of the input of a flow problem to a CFD programme by means of an operator-friendly interface and the subsequent transformation of this input into a form suitable for use by the solver. The user activities at the pre-processing stage involve:

- Definition of the geometry of the region of interest (the computational domain);
- Grid generation - A computational grid is the result of the sub-division of the computational domain into a number of finitely sized cells upon which the governing equations of the fluid flow are solved. Several types of meshes such

as orthogonal, body fitted and hybrid are available, each having their advantages and disadvantages;

- Definition of fluid properties; and
- Specification of appropriate boundary conditions.

The output is a mesh file that can be exported into the solver. The solution to the flow problem is defined at 'nodes' inside each cell. The accuracy of a CFD code is governed by the number of cells in a grid. In general, the larger the number of cells, the better the solution accuracy. Both accuracy of the solution and its cost in terms of necessary computer hardware and calculation time, are dependant on the fineness of the grid (Versteeg, 1995).

(ii) Solver: FLUENT solves the governing partial differential equations for the conservation of mass and momentum:

- Mass conservation equation

$$\frac{\partial \rho}{\partial t} + \nabla \cdot \left(\rho \vec{v} \right) = 0 \qquad \text{Equation 3.17}$$

Where ρ is the density, t is time, $\vec{v}$ is the velocity vector and ∇ is described in Equation 3.19. The first term on the left hand side is the rate of change of density (mass per unit volume) with time. The second term describes the net flow of mass out of the element across its boundaries and is called the convective term (Versteeg, 1995).

- Momentum conservation equations

$$\frac{\partial}{\partial t}\left(\rho \vec{v} \right) + \nabla \cdot \left(\rho \vec{v} \vec{v} \right) = -\nabla p + \nabla \cdot \left(\bar{\bar{\tau}} \right) + \rho \vec{g} \qquad \text{Equation 3.18}$$

Where p is the static pressure, $\bar{\bar{\tau}}$ is the stress tensor, ρ is the density, t is time, $\vec{v}$ is the velocity vector, $\rho\vec{g}$ is the gravitational body force and ∇ is described in Equation 3.19.

$$\nabla = \frac{\partial}{\partial x} + \frac{\partial}{\partial y} + \frac{\partial}{\partial z}. \qquad \text{Equation 3.19}$$

FLUENT uses a finite-difference numerical method known as the finite volume method to solve the partial differential equations, at a finite number of nodal points arranged in a grid pattern. The solution phase involves the initial approximation of all unknown variables, then discretisation by substitution of the approximation into the governing equations to give algebraic equations and finally the solution of the set of algebraic equations by an iterative technique.

(iii) Post processor: This is the analysis of the results generated by the solver and also includes any additional calculations performed on the solver results. FLUENT offers a wide range of user-friendly post-processing tools to enable visualisation of flow variables.

3.11 Summary

The materials and methods used as part of this work have been detailed within this chapter. The ingredients used have been described and characterised (guar gum, carboxymethyl cellulose sodium salt (CMC), riboflavin and starch). The methods section describes the use of rheometry to measure the shear dependant viscosity of the guar gums and CMC solutions. This information has been used to determine the critical concentration of the solutions and data to apply a power law model to the fluids, both of which have used to

design and analyse experiments and computational models. The origination and use of fluorescence to determine concentrations and in the use of FRAP to determine diffusion by concentration measurement has been described.

The design of the SIM, a novel piece of experimental equipment in the field of food technology and chemical engineering has been described; it is used in experiments in Chapters 5 and 6. The design of the Diffusion Cell has also been explained; this is used in experiments in Chapter 4.

The methods used for the two flow visualisation techniques, PIV and PLIF, are described within this chapter and the application of the techniques to investigate fluid flow and mixing are described in Chapter 6 with their findings.

CFD modelling has been described and it has been used to create a model of the segmentation motion seen in the small intestine that will theoretically determine the flow profiles of the characterised formulated fluids in the deforming areas (where visualisation techniques cannot be applied). The findings from this work are described in Chapter 6.

CHAPTER 4 – MOLECULAR MOVEMENT OF NUTRIENTS THROUGH BIOPOLYMER SOLUTIONS INVESTIGATED USING FRAP AND THE DIFFUSION CELL

4.1 Introduction

This chapter focuses on understanding the influence that structuring foods with a biopolymer such as guar gum has on the rate of nutrient delivery to the wall of the small intestine. The influence that certain biopolymers (such as guar gum) have on nutrient uptake rates in the human body has been extensively studied and described in Section 2.3.2.2 (Jenkins *et al.,* 1978; Blackburn *et al*., 1981; Edwards *et al*. 1987., 1988; Ellis *et al*., 1995). However the mechanism of the guar gum's effect on nutrient uptake has not been fully understood (Ellis *et al.*, 2000). This chapter will establish, within the diffusion cell:

i. the effect of shearing the fluid on nutrient delivery to the membrane;
ii. the influence of guar gum on diffusion;
iii. the possibility of surface layers forming on the membrane;
iv. the effect of guar gum concentration on delivery to the membrane;
v. the effect of viscosity for a constant guar concentration on resistance to mass transfer; and
vi. whether there is any permanent binding of riboflavin to the guar gum (i.e. are the results correct).

This knowledge and understanding will be important for analysing the riboflavin and guar gum experiments in the more physiologically representative models (Chapter 5).

A semi-permeable membrane in the diffusion cell separates two compartments (the recipient and biopolymer sides) and this has been used as a simple model to investigate the

influence of the biopolymer guar gum on nutrient delivery to the wall of the intestine in shear and with mixing. The surface area of the small intestine is estimated to be 2 million cm^2 (Ganong, 2005). This large area is due to the presence of surface folds, *villi* and *microvilli* (Section 2.2.4 and Figure 2.5). The flux per unit area described in Equation 2.6, N_1 (mol/m^2 s) will give an overall flux for a system that is proportional to the area and in the small intestine the large area is of benefit for absorption. This large surface area for absorption could make the rate limiting step for the total process of absorption into the blood to being the delivery of the nutrient to the wall of the intestine, as opposed to the transport of the nutrient across the membrane (depending on the nutrient and on the mechanism of transport across the membrane, described in Section 2.2.4.1).

The molecular delivery of the nutrients to the wall of the intestine is a result of two processes (i) diffusion and (ii) convection of the fluid. The convection of the fluid aids in the mixing. Detailed descriptions of diffusion and the combination of diffusion and convection for mass transfer studies are given in Section 2.4.4. This chapter describes the results from using two techniques: firstly the technique fluorescence recovery after photobleaching (FRAP) for diffusion coefficient measurement (Section 3.5); and secondly work using the diffusion cell with an overhead rheometer (Section 3.6).

Investigations using the diffusion cell are valuable when screening a large number of ingredients, prior to taking selected formulations forward for more detailed studies using the Small Intestinal Model (Chapter 5). This approach for screening the best performing samples to be used in further studies was adopted here to investigate the effect of guar gum on nutrient delivery. This is of industrial help for functional food development.

4.2 Investigation into the Influence of Guar Gum on Diffusion Using FRAP

FRAP was used to study both the diffusion coefficient of the model nutrient riboflavin through guar solutions and also the diffusion of a larger fluorescently labelled dextran through biopolymer solutions. A range of guar solutions were used to investigate the diffusion of riboflavin (Vidocrem A,B,C,D,E,F,G, Willy Benecke (WB)) all at a concentration of 1 % w/v and a control sample of 0 % w/v guar gum. The purpose of the experiments was to measure, using FRAP, the diffusion coefficient of a small and large model nutrient through biopolymer solutions and thus establish how the biopolymer guar affects the diffusion in the bulk of the fluid. Simple diffusion through the bulk of the fluid was chosen as a starting point for investigating the mechanisms responsible for the lowering effect of guar gum on postprandial hyperglycemia in diabetic humans described in Section 2.3.2.2.

The diffusion of riboflavin through a range of WB guar gum concentrations (0.025, 0.05, 0.75, 0.1, 0.25, 0.5, 0.75, 1 % w/v) was also studied. The diffusion of the fluorescently labelled dextran (FITC-dextran (FD150)) was investigated through the WB guar gum at various concentrations (0.025, 0.05, 0.75, 0.1, 0.25, 0.5, 0.75, 1 % w/v). Details of ingredients and solution preparation can be found in Section 3.2 of Chapter 3: Materials and Methods.

The experiments were carried out using a confocal microscope, at settings described in Section 3.5.1. Experiments were carried out with assistance of Han Blonk (Advanced Measurement and Imaging, Unilever R&D, Vlaardingen, Holland). An example of the

results for the fitted parameters from each of the five runs carried out on the different samples are presented in Table 4.1 and an example of time versus intensity and time versus normalised intensity are shown in Figures 4.1 and 4.2 respectively. The normalisation was carried out using the pre-bleached intensity (*PbI* from Equation 3.8) to give the normalised intensity *NI*. This does not return to 1 but ~0.98, due to degradation of the fluorescent activity of the bleached riboflavin. The diffusion coefficient was calculated for each sample using the method described in section 3.5.2. Equation 3.9 was used for fitting the data.

The results from the FRAP experiments have been plotted in Figures 4.3, 4.4 and 4.5 respectively for (i) riboflavin diffusion coefficient as a function of WB guar concentration, (ii) riboflavin diffusion coefficient for a range of samples of 1% w/v guar, and (iii) for the fluorescently labelled dextran, diffusion coefficient versus WB guar concentration.

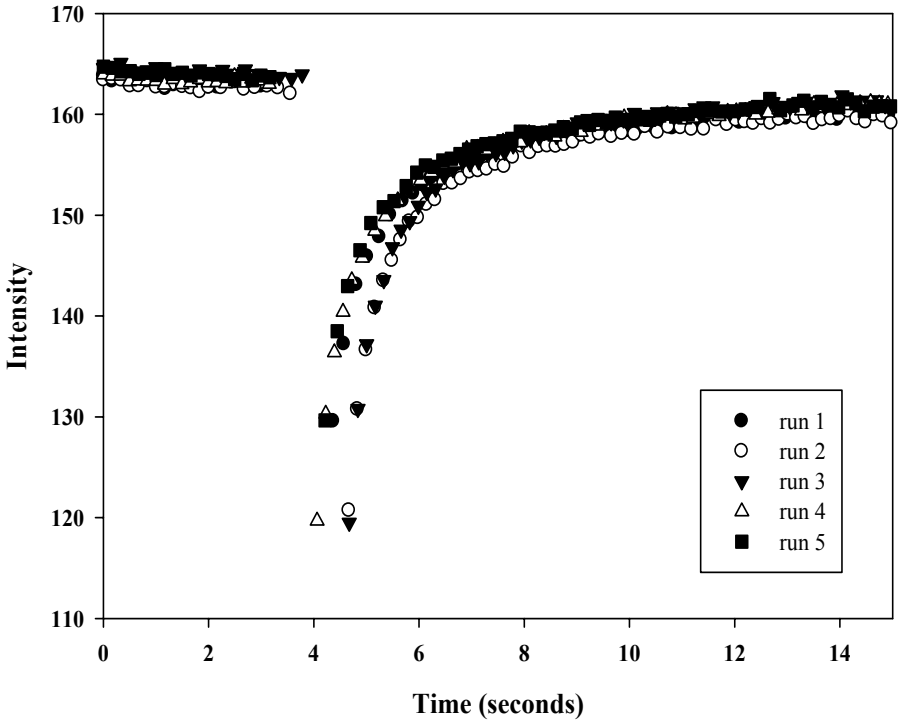

Figure 4.1 A plot of intensity versus time for the recovery of 1% WB guar solutions as an example of the non normalised recovery (data for 5 runs shown).

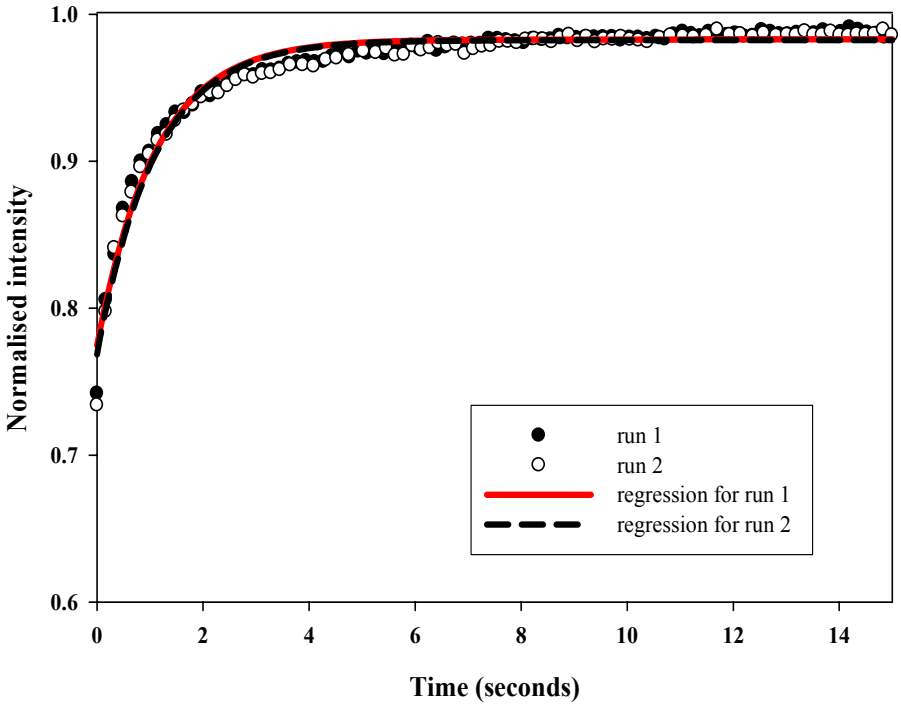

Figure 4.2 A plot of the normalised intensity versus time for the recovery of 1% WB guar solutions as an example of the normalised recovery. Data from the same experiments as those in Figure 4.1.

Experiment 0% Gum	b	$t^{1/2}$(seconds)	Diameter of bleached area (μm)	Diffusion Coefficient ($x10^{-10}$ m^2/s)
1	1.58	1.09	50	1.23
2	1.53	1.06	50	1.30
3	1.67	1.16	50	1.19
4	1.58	1.10	50	1.26
5	1.55	1.07	50	1.29

Mean	1.26
S.D.	0.04

Table 4.1 The parameter fitted values of 'b' for Equation 3.9 to the normalised data sets for the five runs carried out for 0% guar. The data for the average values and one standard deviation from the mean are tabulated. $t^{1/2}$ calculated using Equation 3.10 and Diffusion Coefficient calculated using Equation 3.11.

Figure 4.3 plots the riboflavin diffusion coefficient obtained using FRAP versus guar gum concentration, and shows that there is no measurable decrease in the riboflavin diffusion coefficient as guar concentration increased between 0 and 1% w/v. Similarly Figure 4.4 which plots riboflavin diffusion coefficient verses Vidocrem type (at 1 % concentration), shows that there is little variation in the diffusion coefficient of the riboflavin as the sample changed viscosity for a constant guar gum concentration. Figure 3.12 shows an 154 fold increase in viscosity between Vidocrem A and Vidocrem G: despite this there is no measurable change in the diffusion coefficient. Comparing the control of riboflavin in water and the 1% guar sample (Figures 4.3 and 4.4), there is clearly no decrease in the riboflavin diffusion coefficient. This suggests that the diffusion of the riboflavin is independent to the presence of the biopolymer network in the fluid: i.e. that the network is sufficiently diffuse to offer no obstacle to the molecule. Since the viscosity of the solvent water does not change with the presence of the biopolymer and the biopolymer itself is at low concentrations (~1% w/v), the diffusion of the riboflavin through the solution is equivalent to that of riboflavin through water.

Figure 4.5 shows the diffusion coefficient of a FD150 dextran molecule (MW=156,900) as a function of the concentration of the WB guar gum. The diffusion coefficient of the dextran is approximately six times smaller (0.25 x 10^{-10} m^2/s) in 0.25% w/v WB guar gum compared to 1.50 x 10^{-10} m^2/s for that of riboflavin at 20^oC. There is also a clear reduction of 34% in the diffusion coefficient for the FD150 dextran molecule between the 0.025% w/v WB guar sample and that of the 1% w/v WB guar sample. This suggests that there is an effect of structure on molecules of the size of the FD150 dextran molecule (MW=156,900), which is orders of magnitude larger than that of the riboflavin (MW= 376). The effect on diffusion will vary as a function of size.

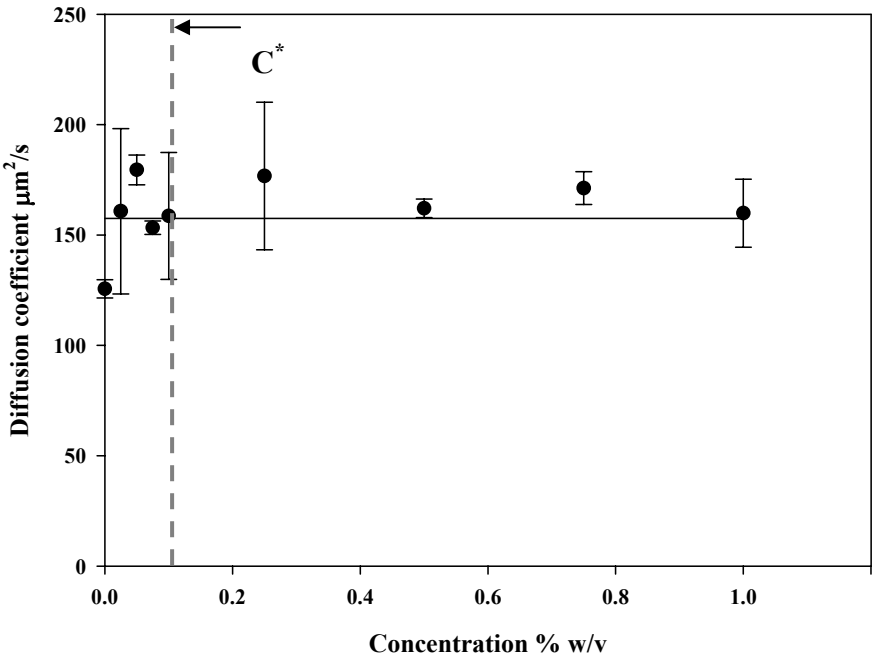

Figure 4.3 Plot of the riboflavin diffusion coefficient versus guar gum concentration for WB guar. The error bars show the standard deviation from a sample number of five.

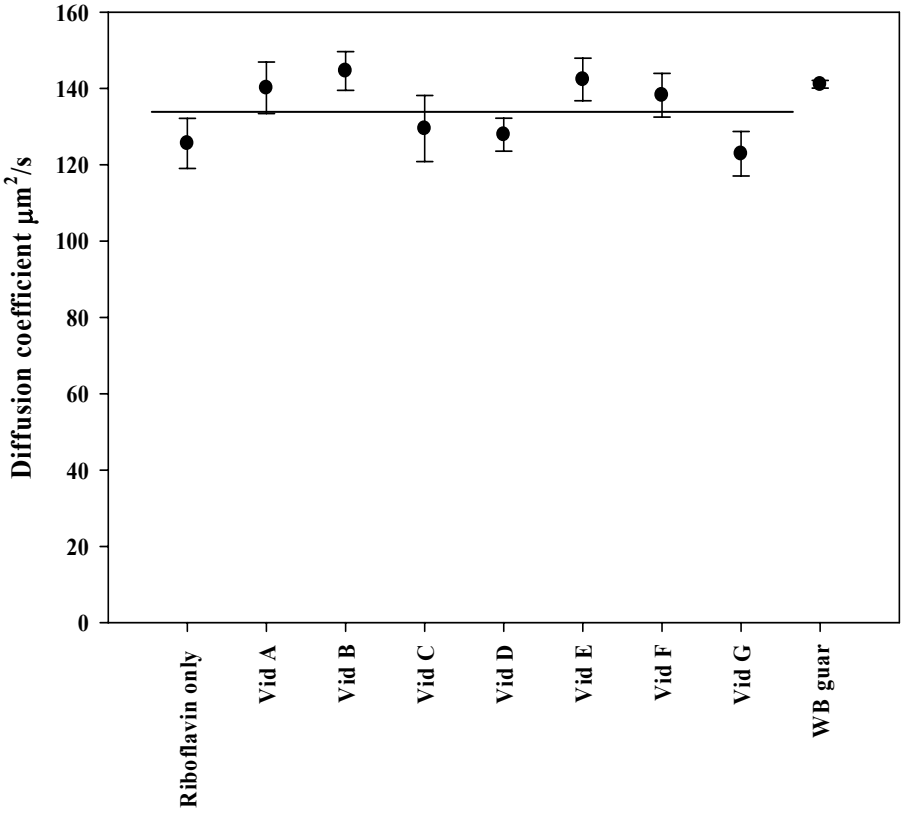

Figure 4.4 Plot of the riboflavin diffusion coefficient calculated from FRAP experiments for the samples of Vidocrem A-G, WB guar at 1% w/v and riboflavin only. The error bars show the standard deviation from a sample number of five.

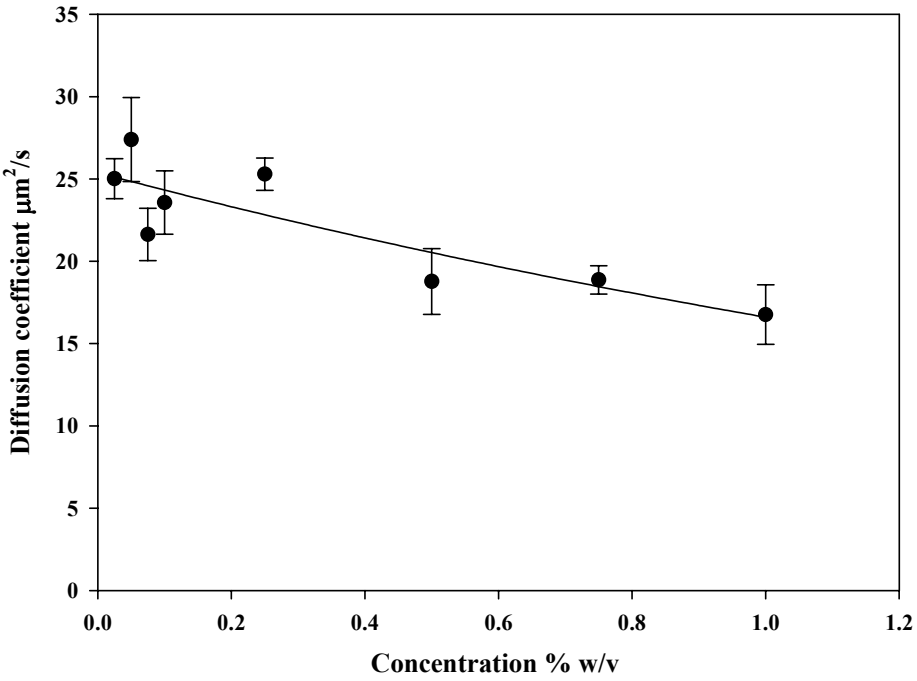

Figure 4.5 The diffusion coefficient of FITC dextran FD150 molecule versus concentration of WB guar gum. Fitted equation to y=a*exp(-b*x), where a = 25.4, b=0.4 and r^2=0.75

A common basis for estimating diffusion coefficients in liquids is the Stokes-Einstein (S-E) equation (Equation 2.5 in Section 2.4.4). Using the S-E relationship, the theoretical value for the diffusion coefficient in water is 4.90 x 10^{-10} m^2/s, using a value of 5A^o (Bajpai *et al*., 2005) for the hydrodynamic radius of riboflavin and 0.89 mPa.s as the viscosity for water, at 298 K. The S-E equation is derived by assuming a rigid solute sphere diffusing in a continuum of solvent, but where the solute size is less than five times that of the solvent the S-E equation breaks down (Cussler, 1997). The measured value for FRAP for riboflavin in water was 1.26 (+/- 0.04) x 10^{-10} m^2/s. The theoretical value is almost four times larger than the measured value although it has the same order of magnitude. This is a reasonable agreement. There was good reproducibility using the FRAP technique, with standard deviations ranging between 0.05 and 0.30 x 10^{-10} m^2/s; systematic experimental error is possible but the scatter in the data is small. The purpose of the FRAP studies was however to establish a qualitative understanding on the effect of the polymer guar gum on the diffusion of riboflavin.

The S-E equation is valid for diffusion through uniform mediums. As determined in Section 3.4, the zero shear viscosity of the 1% w/v WB guar gum solution is 7 Pa.s (~ 8000 times that of water). The S-E relationship describes the diffusion coefficient as being inversely proportional to the solvent viscosity. If the S-E relationship was valid for the biopolymer solution there would be a reduction in diffusion coefficient to ~ 4.8 x 10^{-14} m^2/s. Since the diffusion coefficient of the 7 Pa.s viscosity solution was measured to be 1.25 x 10^{-10} m^2/s, which is essentially identical to that of riboflavin in water, the S-E relationship does not to apply to diffusion through the biopolymer system. The reason that the S-E relationship is not applicable to these low concentration biopolymer

systems is that it uses the viscosity of the solvent to determine the diffusion coefficient. In this case, where a macromolecule is used at a concentration of 1% w/v (above the C^* concentration, implying that the polymer chains interact) to increase the viscosity of the bulk solution, the riboflavin behaves independently of the network and therefore water is still the solvent that the riboflavin passes through and the viscosity of the water must be used in the S-E relationship rather than that of the bulk fluid. For the dextran, being a larger molecule the biopolymer matrix is significant and the diffusion coefficient does change as the higher molecular weight dextran does not behave independently of the biopolymer network.

As noted in Chapter 2, Blackburn *et al*. (1984) investigated the time for glucose equilibrium to be reached between a dialysis bag containing guar and the surroundings. These experiments showed that as the guar concentration increased from 0 – 0.75 % w/v, the time taken for equilibrium also increased from ~ 30 min to ~ 70 min (as seen in Figure 2.16).

For the FRAP experiments used here, the change in viscosity was achieved by using different molecular weights of guar gum that allowed for differing viscosities for the same concentration of guar, as well as by varying the concentration of WB guar. Over a range of viscosities (8.9×10^{-4} – 7 Pa.s) negligible changes in diffusion coefficient were seen, whilst Blackburn *et al*. (1984) found that at a viscosity of ~ 0.27 Pa.s there was greater than a doubling in the half-time for equilibrium as compared to the control containing no guar (Figure 2.16). The results from the experiments conducted by Blackburn *et al*.(1984) are important in understanding the mode of action that guar gum has on the reduction on

postprandial hyperglycaemia. The FRAP experiments conducted as part of this work have showed that guar gum does not affect the diffusion coefficient through the bulk. This therefore suggests that the mechanism of the increased time for half the equilibrium concentration shown in Blackburn *et al*'s experiments (Figure 2.16) was not due to a change in bulk diffusion coefficient.

4.2.1 Conclusions

The method used in this investigation has allowed for the measurement of the diffusion coefficient in various guar samples. The understanding and knowledge of the diffusion coefficients are used later in this chapter and also in Chapters 5 and 6.

The FRAP experiments have shown that for a small molecule such as riboflavin, the diffusion coefficient is unaffected by the presence of guar at concentrations of up to 1% w/v; the resulting change in viscosity of the fluid from 8.9×10^{-4} – 7 Pa.s had no effect on the diffusion coefficient. However, for a large molecule such as dextran there is a reduction (32%) in the diffusion coefficient as the concentration of WB guar gum increases from 0.025% up to 1%. This indicates that the biopolymer network becomes more restrictive to the diffusion of the larger dextran molecule as the concentration of guar gum increases to 1% w/v.

4.3 Investigation into Delivery of Nutrient to a Membrane Surface Using the Diffusion Cell

As described in Section 2.4.4, nutrient delivery to the membrane surface must be influenced by diffusion and convection. By using the diffusion cell it has been possible to

determine the effects that biopolymer solutions of guar gum have on the delivery of nutrients to the membrane, under both static and mixed conditions on the donor side. By using the diffusion cell and measuring the recipient concentration, the flux across the membrane was measured; from this, the overall mass transfer coefficient (K) can then be calculated. By using the overhead rheometer (Section 3.6, Figure 3.19) it was possible to control the mixing within the donor side of the diffusion cell. The measured torque at the experimental stirrer speed for the non-Newtonian biopolymer solutions allowed the apparent Reynolds number to be determined from 0.1 to 5880. The overall mass transfer coefficient was determined while controlled mixing was taking place. At high Reynolds numbers the overall mass transfer resistance reached a plateau from which the membrane and the recipient side boundary layer could be determined as the system resistance. Using the system resistance it was then possible to calculate the biopolymer side mass transfer coefficient for different biopolymer concentrations and shear conditions, from the overall mass transfer coefficient.

The diffusion cell consists of two compartments separated by a semi-permeable membrane, as described in Section 3.6. The concentration of riboflavin on the recipient side (C_r) was measured using the fluorescence spectrophotometer. Using C_r, the volume on the recipient side (V_r), volume on the donor side (V_{dr}) and ($C_{st(d)}$) the initial concentration on the donor side, the donor side concentration (C_{dr}) could be calculated as:

$$C_{dr} = \frac{C_{st(d)}V_{dr} - C_r V_r}{V_{dr}} \qquad \text{Equation 4.2}$$

A set of experiments were carried out to confirm that the experiments gave correct results. One possibility was that there might be permanent binding of the model nutrient (riboflavin) to the guar gum; this was checked as described in Section 4.4. Concentration

versus time profiles were also used to investigate the possibility of surface fouling affecting the rate of mass transfer through the membrane; this is described in Section 4.5.

4.4 Concentration Profile to Equilibrium to Investigate the Binding of Riboflavin to Guar Gum

The possibility of permanent binding of the nutrient riboflavin (as model for glucose) to the biopolymer guar gum was investigated as this may be a possible mechanism of the reduction in the rate of riboflavin flux from one side of the diffusion cell to the other when guar gum is present as seen in Figure 4.6. The WB guar gum was used for these experiments as it results in the greatest viscosity (7 Pa.s) out of the guar samples (Vidocrem A-G, WB) at 1 % w/v concentration.

Two types of experiments were carried out to investigate the concentration profile of a 0.1 mM solution of riboflavin, with and without guar. The first set of experiments used 50 ml volumes of sample and the second set used 5 ml volumes of sample. For each set of experiments, comparisons were made between samples containing no guar and those containing 1% WB guar. The donor side was static for the equilibrium experiments. The recipient side was stirred sufficiently to ensure that the resistance on the recipient side was minimised as described in Section 3.6.

Figure 4.6 shows the results for the experiments using 50 ml samples and Figure 4.7 shows the results for experiments using 5 ml samples. In Figure 4.6 the final concentration for the solution containing no guar was 8.7 μM and the final concentration of the solution containing guar was 8.6 μM. Figure 4.7 shows that the final concentration of both solutions

(with and without guar) reached the equilibrium concentration of 1 μM. The concentration on the recipient side was measured and the concentration on the donor side was calculated using Equation 4.2. The riboflavin in the system was accounted for by comparing the experimental equilibrium concentration with the theoretical concentration. For the experiment using 5 ml of fluid on the donor side the theoretic equilibrium concentration is 1.0 μM and the solutions (with and without guar) reached the equilibrium concentration of 1 μM. For the experiments using 50 ml of fluid on the donor side the theoretic equilibrium concentration is 9.1 μM and the solutions reached the equilibrium concentration of 8.6 and 8.7 μM (with and without guar). Equilibrium experiments using 50 ml of sample were conducted over a time period of greater that 100 hours (i.e. more that 4 days) and accounted for 95% of the riboflavin, 5% is thought to have degraded over this period.

The plots also show a clear difference between the concentration versus time profiles of the solutions with and without the guar gum, implying that guar gum has an effect on the transport phenomena involved in the movement of riboflavin across the membrane. However there is no clear difference shown between the equilibrium concentration with and without guar gum and therefore no permanent binding is present.

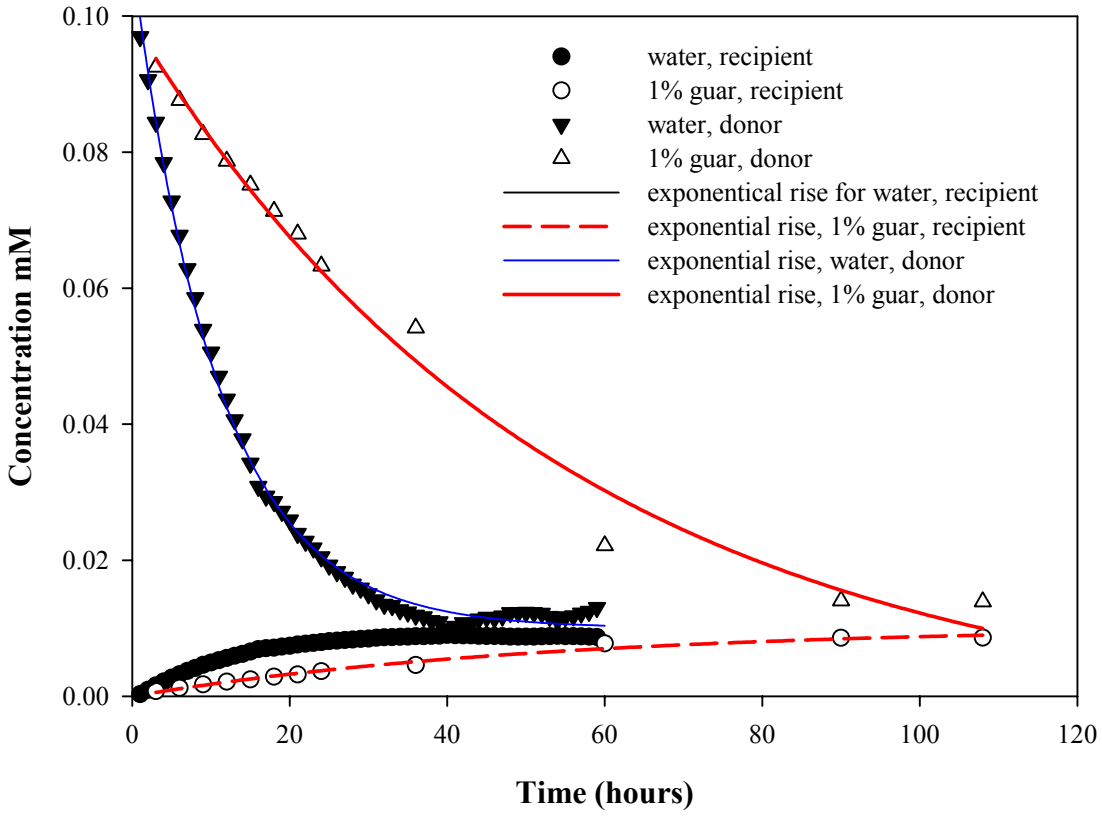

Figure 4.6 Concentration profile of riboflavin in the recipient side and donor side of the diffusion cell for 0% guar and 1% WB guar at volumes of 50ml. The circles are for recipient side concentrations (filled circle for water and hollow circle for 1% guar) and these values were measured. The donor side concentrations (triangles) were calculated from the recipient side concentration using the mole balance of equilibrium. The data was fitted to exponential rise ($y=a^*(1-e^{-b^*x})$) and exponential decay ($y=c^*e^{-d^*x}$) equations. For water recipient side, a*= 0.0091, b*= 0.081 and r^2= 0.99; for 1% guar recipient side, a*= 0.01, b*= 0.018 and r^2= 0.98; for water donor side, c*= 0.098, d*= 0.092 and r^2=0.99 and for 1% guar donor side, c*= 0.10 , d*= 0.018 and r^2= 0.98.

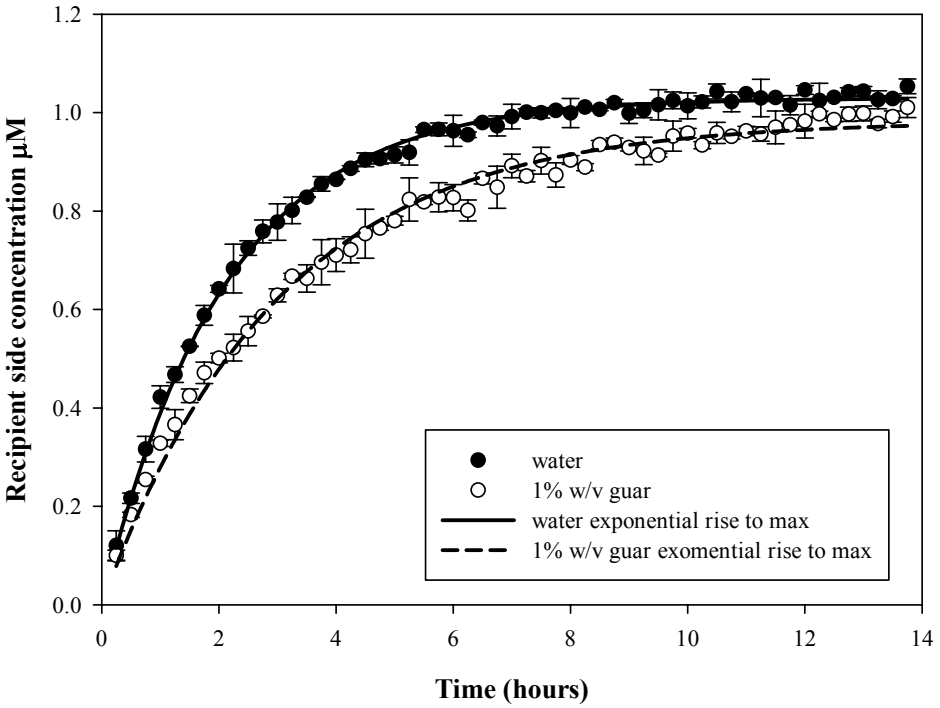

Figure 4.7 Concentration profile of the recipient side of the diffusion cell for 5ml sample volume with and without 1% guar gum. Error bars represent standard deviation from the mean of three experiments. Data fitted to y=a*(1-exp(-b*x)) where for water a= 0.0010, b= 0.47 and r^2= 0.99. For 1% guar a= 0.0010, b= 0.33 and r^2= 0.99.

4.4.1 Conclusions

The results show that the equilibrium concentration for systems with and without guar gum is the same, indicating that there is no permanent binding occurring. There is however a clear difference between the concentration versus time profile for samples with and without 1% w/v guar gum. This suggests that that the guar slows the transport phenomena involved in the movement of riboflavin from one compartment to another (i.e. when separated by a semi permeable membrane).

4.5 Investigation into Possible Fouling of the Membrane

The possibility that the difference in the concentration versus time profile seen in Section 4.4 (Figures 4.6 and 4.7) was caused by membrane fouling was investigated. If fouling of the membrane occurred, it could be due to:

- solid impurities from the guar gum depositing on the membrane;
- a concentrated biopolymer layer at the surface of the membrane; and/or
- the guar gum itself filling the pores of the membrane.

The experiments were carried out using the diffusion cell, described in Section 3.6 and WB guar gum was used for these experiments due to its high viscosity enhancement at 1% w/v concentration of 7 Pa.s. The recipient side was static for the fouling studies and the sample volume was 50 ml. The sequence of events for the experiments where the difference between the concentration versus time profile for samples with and without guar described in Section 4.4 were:

1. The diffusion cell was placed into the recipient side;
2. The sample was immediately placed into the diffusion cell and timing and concentration measurements began.

This method was used as part of these studies; in addition, a time delay was included in some experiments. The purpose of the time delay was to establish if the difference in the concentration versus time profile seen in Section 4.4 (Figures 4.6 and 4.7) was caused by membrane fouling. The time delay would allow for this membrane fouling process to take place. The time delay experiments followed the procedure:

1. The sample was placed into the diffusion cell;

2. The sample was left in the diffusion cell for one hour;
3. The diffusion cell was then placed into the recipient side and timing and concentration measurements began.

Introducing the time delay between introducing the guar gum solution on top of the membrane and inserting the diffusion equipment with the membrane and the guar gum solution into the recipient side allows fouling to take place if it were present. One hour was chosen as the hold time, as mass transfer experiments with and without guar take place over a one hour period. Figure 4.8 shows the results from the experiments as a concentration versus time plot. The graph shows a reduction in the amount of transfer of riboflavin with the guar gum as compared to without.

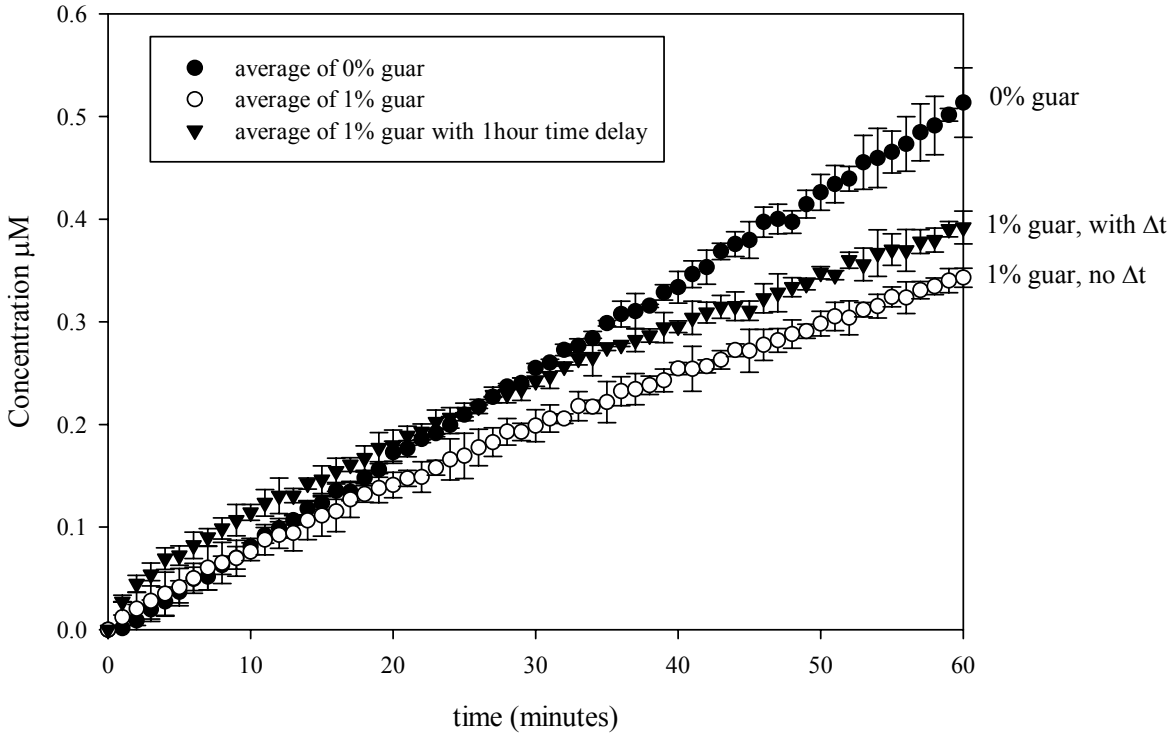

Figure 4.8 Concentration versus 0 and 1% guar gum and 1% guar gum with a 1 hour time delay. Experiments were carried out in triplicate and the error bars represent one standard deviation.

Data from the experiment in which there is a time delay show that by the end of the experiment the amount released is slightly greater (0.39 vs 0.35 μm) than when there was no time delay. This is likely to be due to diffusion of riboflavin into the membrane during the time delay prior to the diffusion cell being placed into the recipient side. If fouling occurred then it would be expected that the experiment with the time delay would result in a reduced level of release after one hour compared to without the time delay.

4.5.1 Conclusion

The fouling experiment suggests that the difference in the concentration versus time profile between samples with and without guar is not due to a fouling mechanism, but must be due to an alternative mechanism.

4.6 Controlled Mixing to Determine the Diffusion Cell Resistance to Mass Transfer

The aim of this investigation was to determine the resistance that the membrane and the recipient side water film contribute to the overall mass transfer coefficient (K). Equation 4.3 shows that K consists of three resistances, the biopolymer side (donor), the membrane and the water film (recipient side). The overall mass transfer coefficient has also been described in Section 2.4.4.2.

Investigations in (Section 3.6.3) have shown that the experimental conditions on the recipient side minimise the recipient side resistance to mass transfer. By finding the plateau of the overall resistance to mass transfer ($1/K$) on a plot of mixing velocities (represented by Reynolds numbers), the resistance from the system (membrane and recipient side film)

is determined. This is known as R_{system} (Equation 4.4). Using the R_{system} the biopolymer side mass transfer coefficient (k_{bp}) can then be calculated using Equation 4.5.

$$\frac{1}{K} = \frac{1}{k_{bp}} + \underbrace{\frac{l_{mem}}{D_{mem}} + \frac{1}{k_{rep}}}_{R_{system}} \qquad \text{Equation 4.3}$$

$$\frac{1}{K_{MAX}} = \frac{l_{mem}}{D_{mem}} + \frac{1}{k_{rep}} = R_{system} \qquad \text{Equation 4.4}$$

$$k_{bp} = \frac{1}{\left(\frac{1}{K}\right) - R_{system}} \qquad \text{Equation 4.5}$$

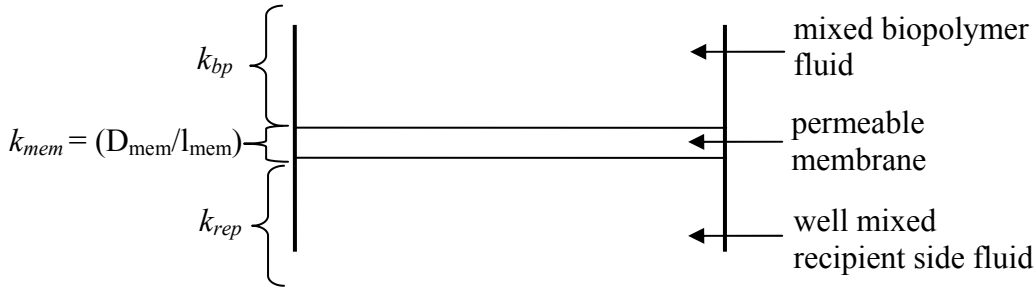

Figure 4.9 A diagram to show the biopolymer side mass transfer coefficient (k_{bp}), the membrane mass transfer coefficient (k_{mem}) and the recipient side mass transfer coefficient (k_{bp}), by using Equation 4.3 for the overall mass transfer coefficient (K).

To find K_{MAX} under controlled mixing conditions, a portable overhead rheometer (Physica Rheolab MC1, Paar Physica) was used for mixing. This allowed measurement of the torque at a given stirrer speed. In each experiment, the concentration on the recipient side was measured over 210 minutes and the flux of riboflavin from a 0.1 mM solution was measured. A series of experiments were carried out with varying amounts of WB guar and different stirring speeds. Since the guar gum solutions are shear thinning (Figure 3.8) the

method of calculating the (apparent) Reynolds number during mixing required more steps and is described below (Harnby, 1997).

The first step was to obtain the usual Newtonian power number-Reynolds number correlation (power curve) for the diffusion cell. This was determined using corn syrups of different dilutions and known viscosities over the range of mixing speeds. The mixing speeds used corresponded to the speeds suggested in the standard layout ISO/DIS 3219:1990. Measurements of torque at the range of stirrer speeds given in Table 4.2 were undertaken for the various fluids.

The power p was calculated from:

$$p = 2\pi N_a T \qquad \text{Equation 4.6}$$

The power number P_o was then calculated from:

$$P_o = \frac{p}{D_a^5 N_a^3 \rho} \qquad \text{Equation 4.7}$$

and the Reynolds number Re from:

$$\text{Re} = \frac{D_a^2 N_a \rho}{\mu} \qquad \text{Equation 4.8}$$

Where p is power (Js^{-1}), N_a is the agitator speed (s^{-1}), T is torque (Nm), D_a is agitator diameter (m) and ρ is the density (kg m^{-3}) and μ is the viscosity of the fluid (Pa.s).

Results for a viscous corn syrup solution that has Newtonian behaviour and a viscosity of 1 Pa.s are given in Table 4.2. From this data and from the other Newtonian viscosities, a plot of power number versus Reynolds number was made for the impeller (Figure 4.10).

STEP	Torque	Torque	N	p	Power no.	Re
(rpm)	%o	Nm	/s	w	-	-
25	8.9	0.00045	0.4	0.0012	481.0	0.21
50	17.8	0.00089	0.8	0.0047	240.5	0.41
75	26.9	0.0013	1.3	0.011	161.5	0.62
100	35.9	0.0018	1.7	0.019	121.3	0.83
200	72.5	0.0036	3.3	0.076	61.2	1.65
300	110.4	0.0055	5.0	0.17	41.4	2.48
400	149.6	0.0075	6.7	0.31	31.6	3.31
500	188.4	0.0094	8.3	0.49	25.5	4.13
600	229.1	0.011	10.0	0.72	21.5	4.96
700	270.7	0.014	11.7	0.99	18.7	5.79
800	313.4	0.016	13.3	1.3	16.5	6.61
900	358.5	0.018	15.0	1.7	14.9	7.44
1000	402.4	0.020	16.7	2.1	13.6	8.27

Table 4.2 An example of the data generated for a range of Power numbers for the fluid corn syrup at 1.17 Pa.s.

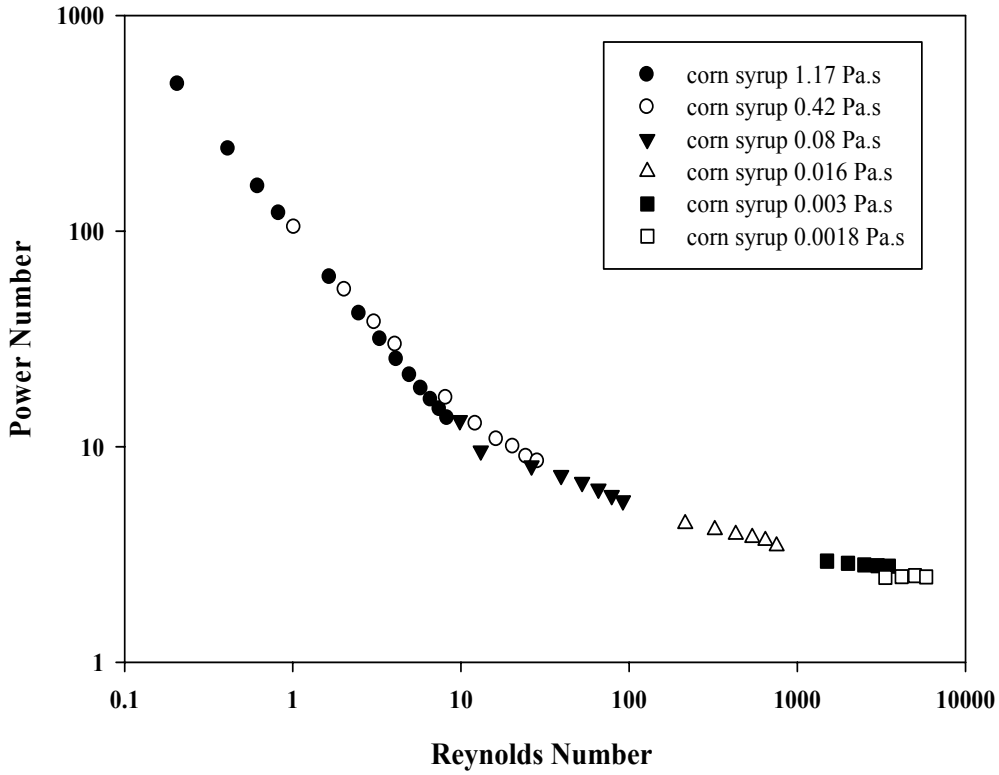

Figure 4.10 Power number vs Reynolds number for corn syrup of varying viscosities in the diffusion cell.

For non-Newtonian fluids, by using the measured value of power consumption to give a power number, the corresponding Reynolds number is determined from the Newtonian power curve (Harnby, 1997) as shown in Figure 4.10, this Reynolds number is known as the "apparent Reynolds number". The Reynolds number from the Newtonian power curve (apparent Reynolds number, Re_a) is then used to calculate the apparent viscosity (μ_a) for non-Newtonian fluids from Equation 4.9.

$$\mu_a = \frac{D_a^2 N_a \rho}{\mathrm{Re}_a} \qquad \text{Equation 4.9}$$

Equation 4.9 allows for the apparent viscosity to be calculated from the apparent Reynolds number (Re_a) where μ_a is the apparent viscosity (Pa.s), D_a is agitator diameter (m), N_a is the agitator speed (s^{-1}), ρ is the density (kg m^{-3}) and ρ is the density (kg m^{-3}) and Re_a is the apparent Reynolds number.

By using this method for the stirrer speed and the range of guar gum solutions used, the apparent Reynolds number and the apparent viscosity was determined, while also measuring the mass transfer coefficient for which the data is given in Section 4.7.

4.7 Measuring the Mass Transfer Coefficient Within the Mixed System

During the mixing experiment the concentration in the recipient side of the diffusion cell was measured over a period of 210 minutes. The volume of the sample was 50 ml and the experiments were carried out in the linear region of the concentration versus time equilibrium curve (Figure 4.6). Using the flux, membrane surface area, volume of recipient

side and the concentration difference, the mass transfer coefficient was calculated from Equation 4.3.

Figure 4.11 shows a typical plot of the riboflavin concentration versus time from which the overall mass transfer coefficient can be obtained. A good linear regression (R^2 of > 0.95) is obtained over the time period. An example of the calculation of the overall mass transfer coefficient calculated from Equation 2.6 is as follows; using a gradient of 1.07×10^{-5} mM/min, this is converted to 8.90×10^{-8} mmol/s from which N_i is determined using the membrane surface area (0.0020 m^2) to give 4.45×10^{-5} mmol/m^2s. The concentration difference is 100mmol/m^3 and therefore the overall mass transfer coefficient calculated to be 4.45×10^{-7} m/s.

Figure 4.12 is a plot of the inverse of the overall mass transfer coefficient (the resistance to mass transfer calculated from Equation 2.8) versus the apparent Reynolds number. Above a Reynolds number of 100 a clear plateau is reached. Once the mixing does not further improve the rate of mass transfer, a plateau in the mass transfer coefficient, which represents the resistance of the system. This can be used to extract values of the biopolymer side resistance from Equation 4.5. Values of 1/K for apparent Reynolds numbers of greater than 100 were averaged at 2.15×10^6 s/m and was determined as the resistance of the system, R_{system} in Equation 4.4.

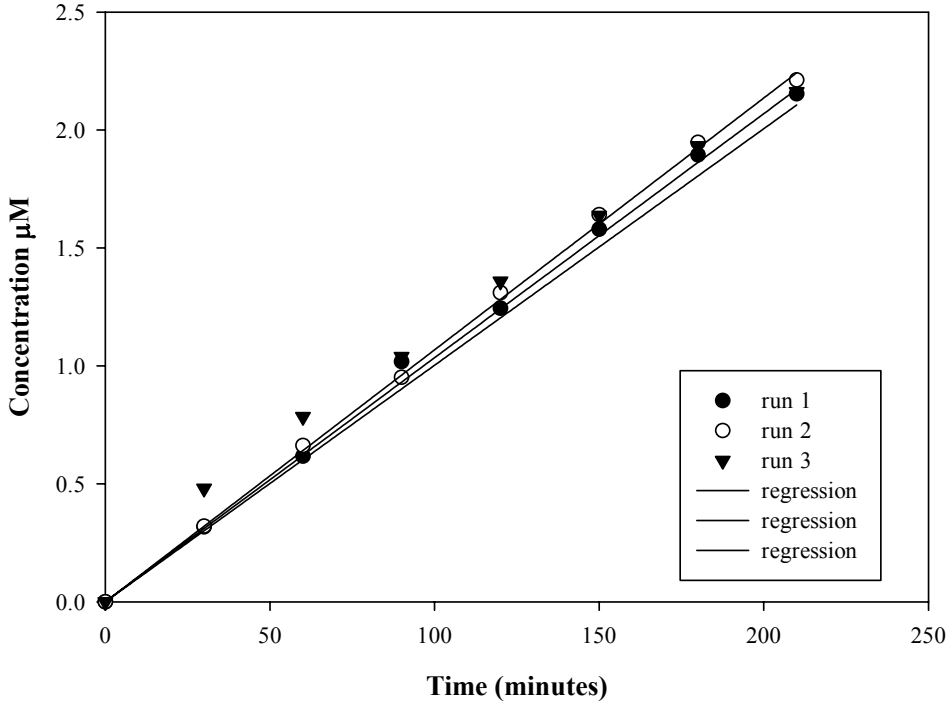

Figure 4.11 Recipient side concentration of riboflavin versus time for 0% guar gum, regression data, run 1,2,3 gives gradients of 1.0347 x10^{-5}, 1.0679 x10^{-5}, 1.0028 x10^{-5} mM/min, and R^2 values of 0.997, 0.999, 0.962 respectively.

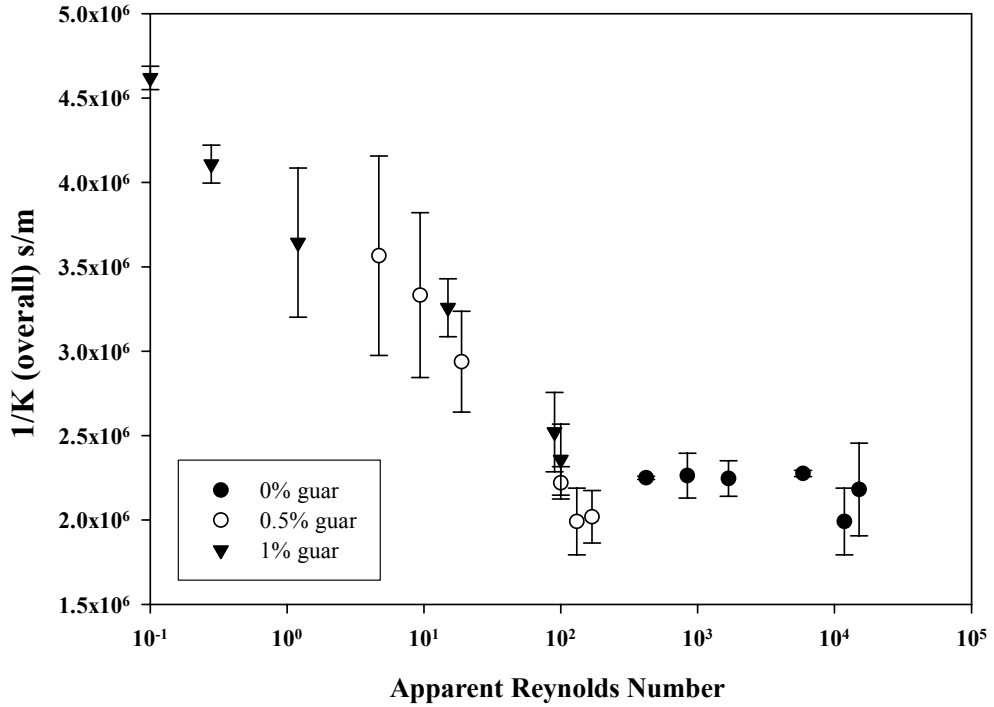

Figure 4.12 The reciprocal of the mass transfer coefficient, 1/K versus the apparent Reynolds Number. The apparent Reynolds numbers were achieved by varying the stirrer speed between 25 – 1000 rpm on the donor side and the recipient side was mixed using a magnetic stirrer plate at setting 2 (minimising the recipient side resistance).

4.7.1 Conclusion

The resistance of the system, i.e. the resistance from the membrane and minimised resistance on the recipient side (R_{system}), has been shown to be 2.15 x 10^6 s/m. This value is used to calculate the resistance from the biopolymer side from the overall mass transfer coefficient using this value.

4.8 The Effect of Guar Gum Concentration on the Biopolymer Side Mass Transfer Coefficient in the Diffusion Cell

Having established the resistance to mass transfer from the membrane and the water film on the recipient side of the diffusion cell (R_{system}) in Section 4.7, the next step was to investigate the effect of guar gum concentration on the guar-side mass transfer coefficient.

To investigate the effect of guar sample concentration, 50 ml of WB guar was used in the diffusion cell at concentrations of 0, 0.1, 0.25, 0.5, 0.75, 1, 1.5 and 2 % w/v and each experiment was carried out in triplicate. By measuring the recipient side concentration versus time profile for 210 minutes the overall mass transfer coefficient was calculated using Equation 4.3. From the overall mass transfer coefficient (K) the biopolymer side mass transfer coefficient was then determined using Equation 4.5.

Figure 4.13 shows typical recipient side concentration versus time profiles for guar gum solutions of various concentrations. Using the gradient from the plot from the regressions line, the overall mass transfer coefficient K was calculated. Table 4.3 shows the K value for each guar concentration with the standard deviation. The overall mass transfer coefficients have been plotted against the WB guar gum concentration in Figure 4.14.

Using the overall mass transfer coefficient (K) and the system resistance determined in Section 4.7, k_{bp} (the parameter of interest for the guar gum solution) was determined. The biopolymer side mass transfer coefficient k_{bp} was calculated using Equation 4.5 which is plotted against guar gum concentration in Figure 4.15.

The biopolymer side mass transfer coefficient k_{bp} has also been plotted against the zero shear viscosity (described and characterised in Section 3.4.1.1) of the sample (Figure 3.11) as the donor (biopolymer) side was static for these experiments.

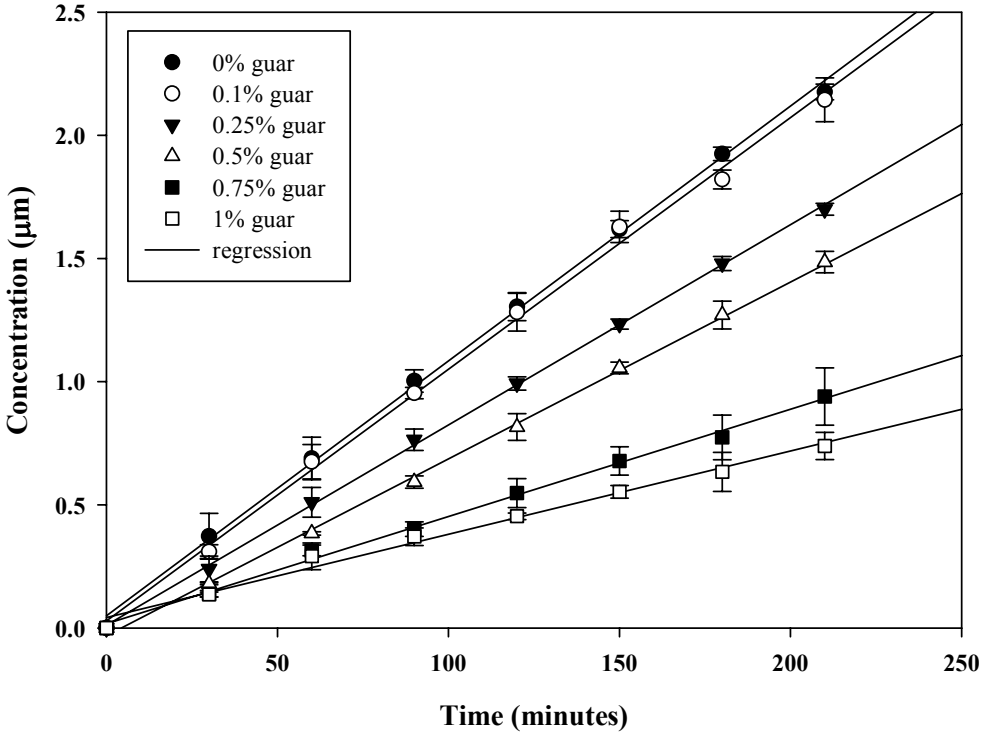

Figure 4.13 Recipient side concentration for a range of WB guar gum solutions (0, 0.1, 0.25, 0.5, 0.75, 1, 1.5 and 2%), the error bars are from the standard deviation of three experiments. The donor side was unstirred and the recipient side was mixed using a magnetic stirrer plate at setting 2 (minimising the recipient side resistance).

% w/v guar	Overall MTC m/s	st dev m/s
2	1.4×10^{-7}	1.1×10^{-8}
1.5	1.5×10^{-7}	4.3×10^{-9}
1	1.4×10^{-7}	1.1×10^{-8}
0.75	1.9×10^{-7}	2.2×10^{-8}
0.5	3.0×10^{-7}	1.2×10^{-8}
0.25	3.5×10^{-7}	4.1×10^{-9}
0.1	4.4×10^{-7}	1.2×10^{-8}
0	4.4×10^{-7}	1.4×10^{-8}

Table 4.3 The overall mass transfer coefficient at a range of guar concentrations and standard deviation; experiments in triplicate, standard deviations shown.

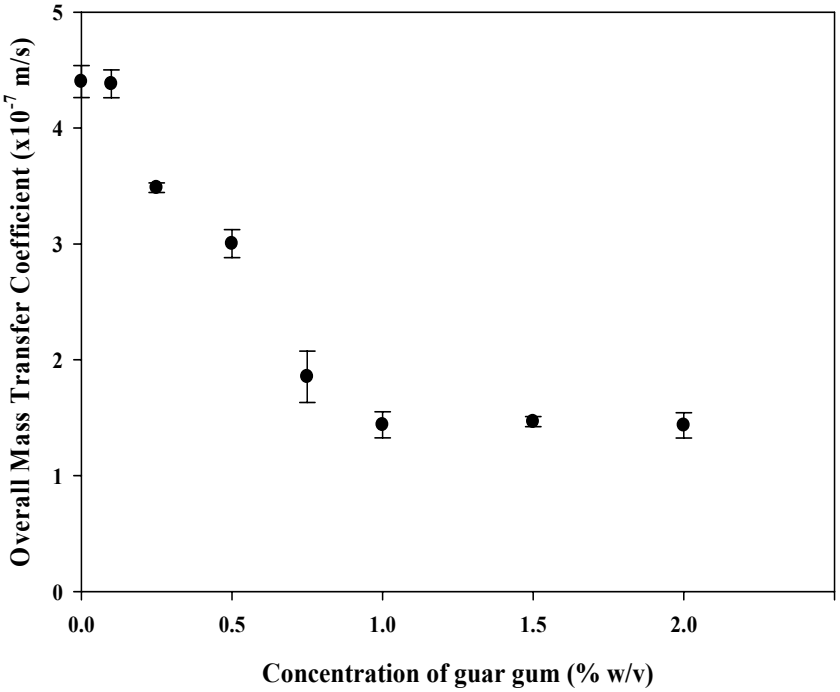

Figure 4.14 Overall mass transfer coefficient versus % guar for static conditions, where error bars represent one standard deviation from the mean of experiments carried out in triplicate. The donor side was unstirred and the recipient side was mixed using a magnetic stirrer plate at setting 2 (minimising the recipient side resistance). The guar concentrations correspond to viscosities given in Table 3.2.

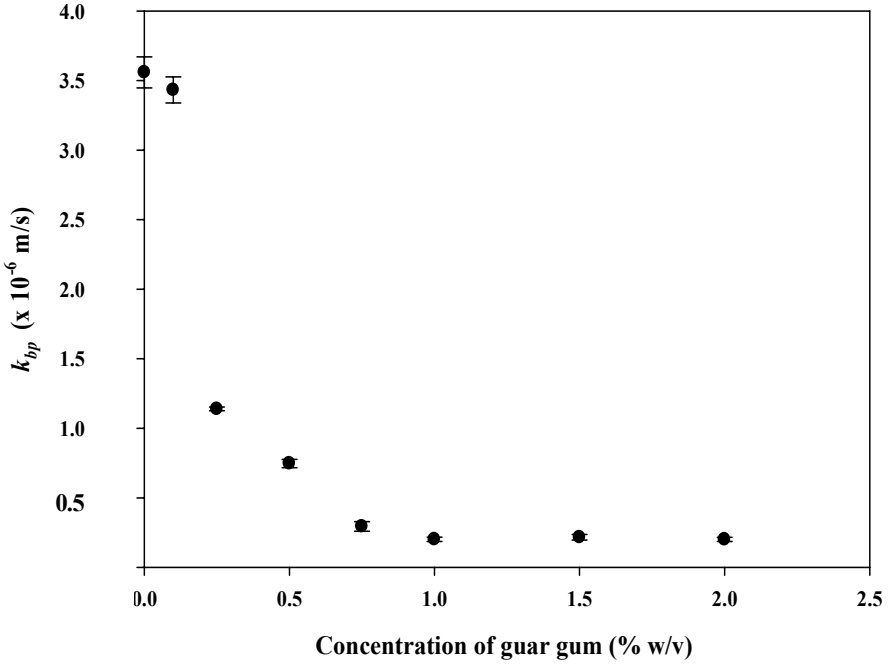

Figure 4.15 Mass transfer coefficient on the biopolymer side versus % guar for static conditions, where error bars represent one standard deviation from the mean of experiments carried out in triplicate.

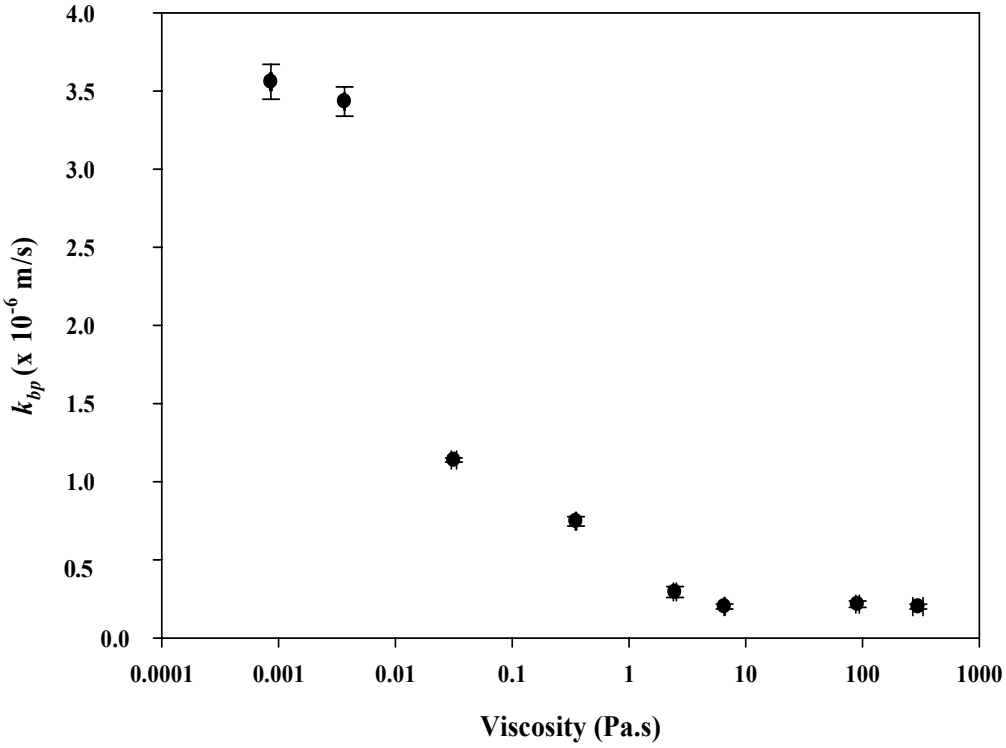

Figure 4.16 Mass transfer coefficient on the biopolymer side versus zero shear viscosity of the guar gum, where error bars represent one standard deviation from the mean of experiments carried out in triplicate.

Figure 4.15 shows that there is a clear decrease in the biopolymer side mass transfer coefficient which represents an increase in the resistance to mass transfer on the biopolymer side as the guar concentration rises to 1 % w/v. Mass transfer coefficient resistance decreases to a value of about 2 x 10^{-7} m/s, significantly below that of the rest of the system.

4.8.1 Conclusions

The conclusion from this investigation is that as the WB guar concentration is increased, the biopolymer side mass transfer coefficient decreases by 68% and then levels off. As the viscosity is raised to 7 Pa.s (Figure 4.16) as a result of increasing the guar concentration, the biopolymer side mass transfer coefficient decreases and then levels off. There is a clear reduction in the biopolymer side mass transfer coefficient as a consequence of increasing concentrations of guar gum up to 1 % w/v, after which a plateau is reached. However it is difficult to de-couple the effect of the concentration of guar gum in the fluid on the mass transfer from the effect of the viscosity of the fluid on mass transfer for a given type of guar gum. It is important to establish whether: (i) the concentration of guar gum or (ii) the viscosity of the solution is the critical parameter. Investigations into different guar gum types that give different viscosities for the same concentration of guar gum were required. This will determine if it was the presence of guar gum, or the viscosity increase, causing the change in mass transfer coefficient.

4.9 Investigation into the Effect of Viscosity Independently of the Concentration of Guar Gum

To de-couple the viscosity from the concentration, a range of guar gum samples were used that all generate different viscosities at a given concentration (w/v). Using the range of guar gums Vidocrem A – G with varying low shear viscosities (Figure 3.12) and WB guar at a concentration of 1% w/v, the fluids have a range of viscosities of 0.1-7 Pa.s, while all containing the same mass of guar gum. The sample was 50 ml in volume and the overall mass transfer coefficient was calculated from the concentration versus time profile for 210 minutes and experiments were carried out in triplicate.

Experiments were carried out to determine the overall mass transfer coefficient (K) from which the biopolymer side resistance was calculated using Equation 4.5. Figure 4.17 plots the results found from these experiments and shows that as the viscosity increases the resistance to mass transfer ($1/k_{bp}$) increases also. Since all the solutions have the same concentration of guar gum at 1% w/v, it thus suggests that the amount of guar gum in the system is not the cause of the increase in biopolymer side resistance.

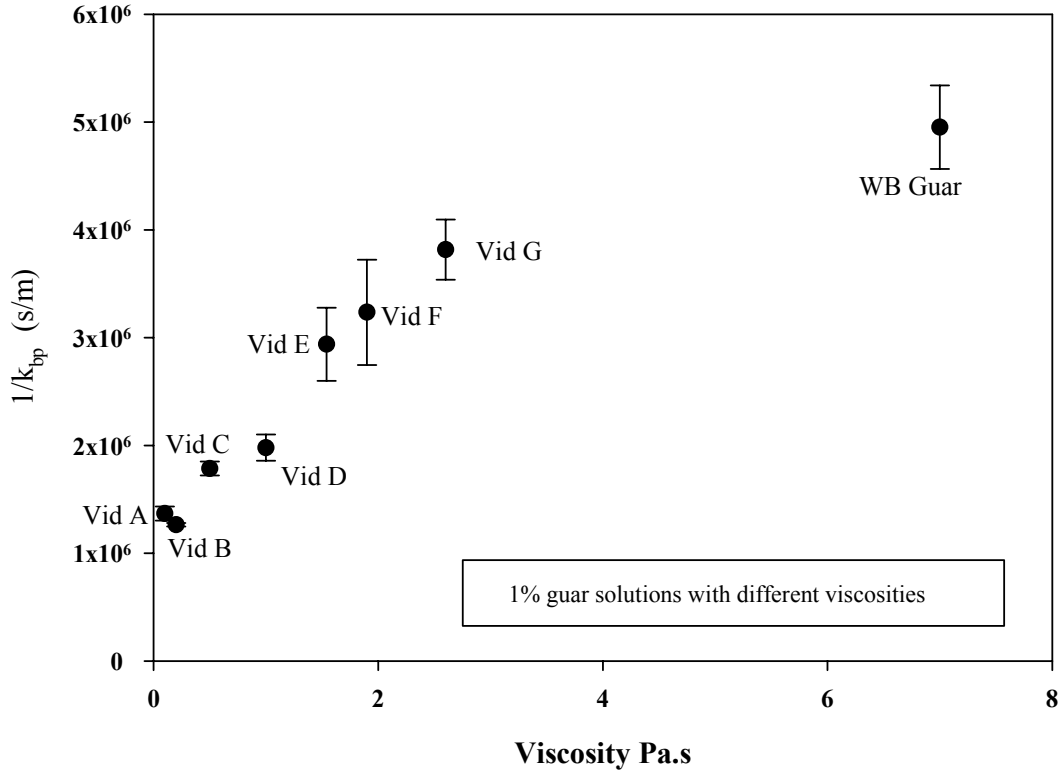

Figure 4.17 Mass transfer resistance on the biopolymer side versus viscosity guar for a range of 1% w/v guar solutions all under static conditions, where error bars represent one standard deviation from the mean of experiments carried out in triplicate.

The viscosity of the system has a clear effect on the resistance to mass transfer on the biopolymer side of the membrane. This has been shown by varying the concentration of the guar gum to change viscosity (Figure 4.16) and by changing the guar gum type at the same concentration (Figure 4.17). Since all the samples were at 1% w/v guar this indicated that as the configuration of the guar molecule changed to give a greater viscosity (by increasing the number of entanglements) the resistance to mass transfer increases.

4.10 Biopolymer Side Resistance While Shearing; Sh vs Re Analysis

By using data from Section 4.7 that was used to determine the resistance of the system, the biopolymer side resistance has been calculated using Equation 4.5. The biopolymer side resistances at a range of Reynolds numbers from 0.1 to greater than 5000 are plotted in Figure 4.18.

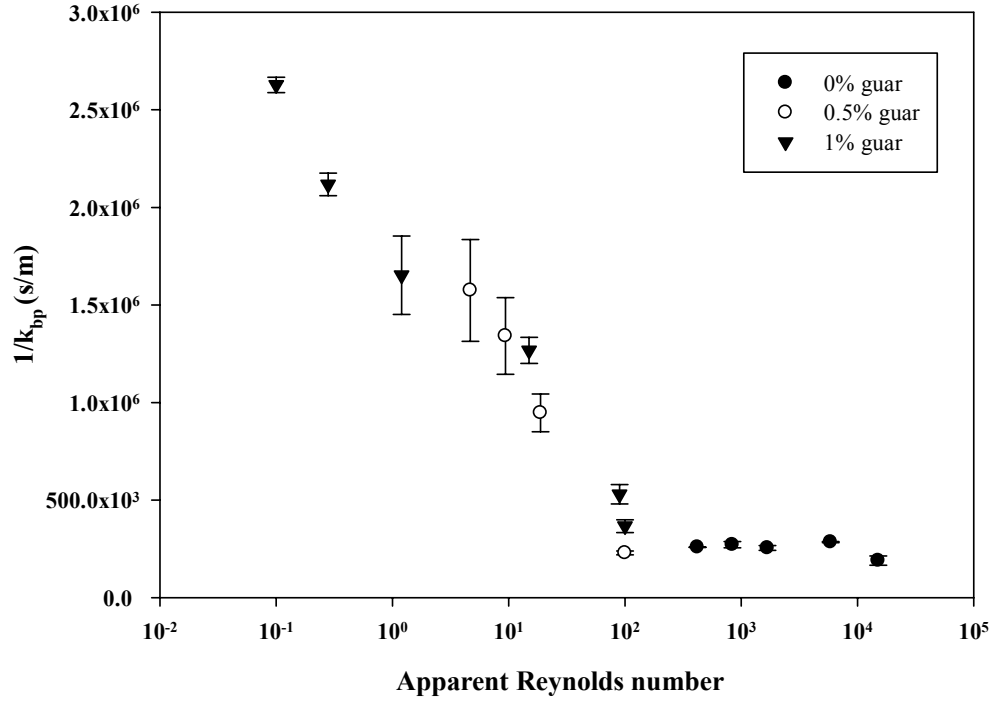

Figure 4.18 Mass transfer resistance on the biopolymer side versus Apparent Reynolds number for mixed conditions, where error bars represent one standard deviation from the mean of experiments carried out in triplicate.

To find the mass transfer enhancement from mixing it is important to calculate the Sherwood number using Equation 2.12. The Sherwood number is used to measure the mass transfer enhancement of systems with convection compared to diffusion alone, where k_{bp} is the biopolymer side mass transfer coefficient, L is the length scale and D is the diffusion coefficient.

Figure 4.18 shows that as the agitation in the diffusion cell increases (indicated by the increase in Reynolds number) there is a reduction in the resistance to mass transfer on the biopolymer side. Figure 4.19 plots the Sherwood number calculated from the biopolymer side mass transfer coefficient using Equation 2.12, showing a steady increase in the Sherwood number from apparent Reynolds numbers 0.1 to 20. Between 10 – 100 there is a significant increase from 100 to 300 in the Sherwood number after which the value is steady at approximately 300. The value of ~300 corresponds to being the region where there is no further enhancement of mass transfer with apparent Reynolds number.

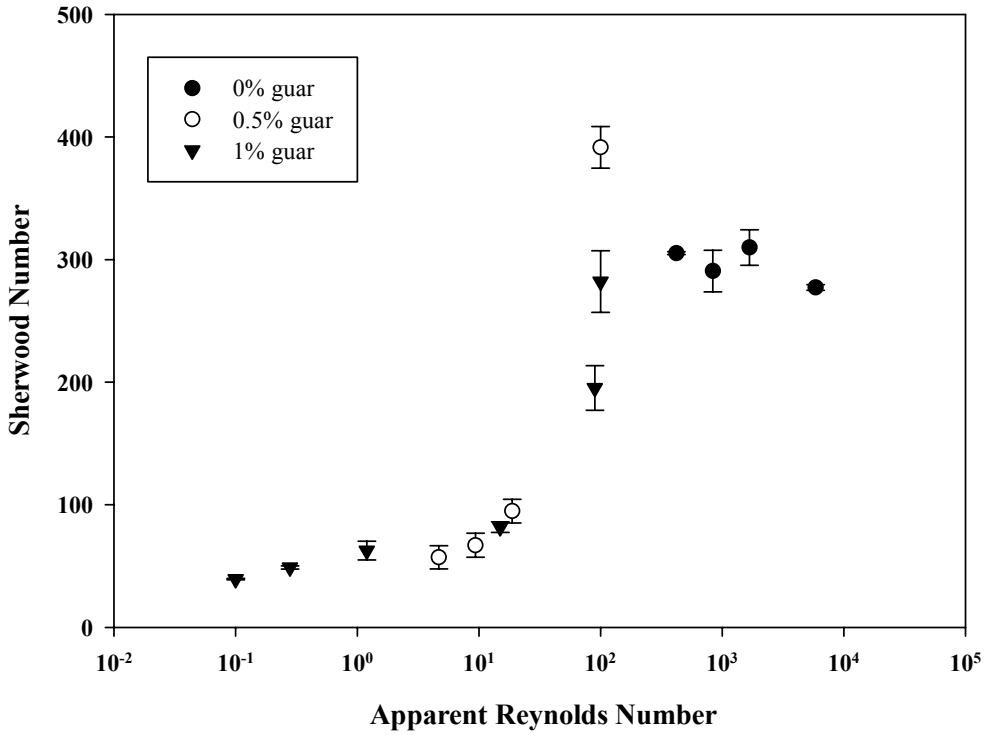

Figure 4.19 Mass transfer resistance on the biopolymer side versus apparent Reynolds number for mixed conditions, where error bars represent one standard deviation from the mean of experiments carried out in triplicate.

4.10.1 Conclusions

The envelope of resistance to mass transfer of the guar gum at different mixing conditions has been established. From the Sherwood number versus Reynolds number plot (Figure 4.19), the enhancement of mass transfer shown by the increase in Sherwood number from ~20 to ~ 300 from mixing, can be seen as the Reynolds number increases, although a plateau is reached at Reynolds numbers of greater than 100.

4.11 Overall Discussion and Conclusions for Diffusion and Mass Transfer Studies

To begin to understand the molecular delivery to the wall (absorptive surface) of the small intestine, diffusion and mass transfer has been investigated. Diffusion and mass transfer investigations have included the biopolymer (guar gum) in model food formulations to measure the effect that they have on nutrient delivery to the surface of the membrane. This is a model for the delivery to the surface of the intestine.

The surface area of the small intestine is very large due to the presence of *villi* and *microvilli*. This very large surface area for absorption suggests that the rate limiting step in absorption into the blood could be delivery of the nutrient to the wall of the intestine, as opposed to transport of the nutrient across the membrane (depending on the nutrient and on the mechanism of transport across the membrane). Therefore an investigation into the food side mass transfer coefficient was thought to be of value and has been carried out.

Studies using FRAP have shown that there is no reduction in the riboflavin diffusion coefficient by the addition of WB guar gum up to 1% w/v. Studies have also showed that for a range of guar gums of the same concentration but with varying viscosities, there is no

difference in the riboflavin diffusion coefficient. This indicates that the mechanism responsible for the lowering effect of guar gum on postprandial hyperglycemia described by Blackburn *et al.* (1984) is not a consequence of the guar gum changing diffusion of glucose in the bulk fluid. By using a larger molecule than riboflavin it has been shown that hindering of diffusion through the biopolymer network does take place for a large dextran molecule. This has implications for the delivery of material to the wall of the GI tract as well as the diffusion through the bulk of the digesta in cases of enzyme-substrate reactions; very large molecules will be retarded by reduced diffusion.

The concentration profiles in the diffusion cell over time (to equilibrium) were used to show that there is no permanent binding of the riboflavin to the guar gum. They also showed a distinct difference between the samples containing 1 % w/v WB guar and those that did not contain guar. Studies into fouling of the membrane showed that the reduction in the concentration versus time profile was not caused by a fouling mechanism.

Through application of controlled mixing in the diffusion cell whilst measuring mass transfer, the resistance of the system (R_{system}) to mass transfer was determined. This is important because it can calculate the resistance of the biopolymer side resistance from the overall mass transfer coefficient in other experiments.

Experiments investigating resistance to mass transfer on the biopolymer side under static conditions, at different concentrations, for the same type of guar sample, have shown that there is an increase until a maximum resistance is reached. This demonstrates that under static conditions the presence of the guar gum slows mass transfer.

The resistance to mass transfer on the biopolymer side was determined for mixing conditions and showed a reduction in resistance to a clear minimum at Re > 100. The Sherwood number versus Reynolds number plot showed that the mass transfer on the biopolymer side increased to a maximum, as mixing increased. This proves that mixing has an important role in the delivery of the nutrient to the membrane.

Overall, the diffusion cell gives a good understanding of the effect that an ingredient such as a biopolymer has on molecular delivery to the membrane surface. Establishing the ingredient side mass transfer coefficient from the overall mass transfer coefficient is useful to understand how the ingredient will affect molecular delivery to intestinal wall. The diffusion cell could therefore be used for investigating large numbers of ingredients prior to more detailed studies. The cell could investigate the effect that different ingredients i.e. the same polymer that give different physical properties of a solution, or of different polymers have on the delivery to the membrane of molecules with different molecular weights or other physicochemical properties such as charge. It is clear that the size of the diffusing species is critical; different size molecules will behave differently in the solution and at the interface within the GI tract.

While the diffusion cell makes a first estimate of the processes in the small intestine, mixing in the model is not representative of flow profiles in the human small intestine. Studies using the small intestinal model were then conducted to model the process conditions found in the human small intestine more closely and the results of these experiments are contained in the following chapter.

CHAPTER 5 - MASS TRANSFER STUDIES USING THE SMALL INTESTINAL MODEL

5.1 Introduction

The previous chapter studied molecular delivery of nutrients via biopolymer solutions to a membrane, as a model of delivery of nutrients to the intestinal wall. As discussed in Chapter 4, the mixing profiles within the diffusion cell do not accurately represent those found in the small intestine. In the small intestine the pumping and mixing of the digesta (the food and intestinal secretions in the small intestine) are produced by movements in the intestinal wall (Section 2.2.4.2). It is the objective of this chapter to understand how the structure and material properties of the digesta might influence delivery of nutrients to the intestinal wall. This has been achieved by using a physical model that mimics the segmentation movement found in the small intestine, which is thought to be responsible for mixing of the intestinal contents, as described fully in Section 2.2.4.2. The Small Intestinal Model (SIM) allows the fluid dynamics in the intestine be physically modelled and for nutrient delivery through the membrane surface to be measured. The SIM has also been used to study velocity profiles using flow visualisation techniques for which the results are described in Chapter 6.

The design, development and experimentation using the SIM were a major part of this Engineering Doctorate. The *in vitro* model that was developed is unique in its ability to combine a flow induced by a variable pump, with the important segmentation action created by an annular constriction, while being able to determine nutrient delivery to the membrane wall.

A series of experiments were carried out using the SIM with a range of WB guar gum concentrations 0-1% w/v. The guar gum solutions were used as a model fluid of the digesta and also as the ingredient, as at 6 g/litre (Blackburn *et al.*, 1984) guar has been shown to have positive effects on postprandial hyperglycaemia (Blackburn *et al.*, 1984). The fluids were investigated under the different processing conditions of 'with and without flow', coupled with experiments 'with and without segmentation' as outlined in Table 5.1.

		Flow induced by peristaltic pump	
		No Flow	*Flow*
Segmentation by squeezing motion	*No Squeeze*	No flow, No Squeeze	Flow, No Squeeze
	Squeeze	No Flow, Squeeze	Flow, Squeeze

Table 5.1 Experimental process conditions.

The variation in the process conditions allowed study into the effect of the overall flow and segmentation on the mass transfer coefficient on the biopolymer side (k_{bp}). The effect that fluid structuring has on k_{bp} under physiologically representative conditions was investigated. Biopolymer side mass transfer coefficient was chosen as the parameter of interest as this controls molecular delivery to the inner wall of the membrane by a combination of convection and diffusion.

The guar and riboflavin studies investigated the effect of fluid properties on delivery to the intestinal wall of physiologically representative nutrients. Simulating the flow of fluid in the small intestine was done by simulating wall motion and creating mixing conditions representative of the small intestine. Digestion in the SIM was then investigated with the

use of precooked starch (Section 3.2.4), digested under different process conditions, while the glucose concentration in the biopolymer (food) side and the recipient side was being measured (Section 3.3.5). Starch digestion experiments allowed the effect of the fluid properties on enzyme-substrate reaction and nutrient delivery to be investigated.

5.2 Mass Transfer Experiments Using Biopolymer Solutions and the SIM

5.2.1 Introduction

Investigations into mass transfer across the SIM using biopolymer solutions and varying process conditions were undertaken to establish the effect that processing and the influence of the product (guar gum solutions) have on molecular delivery to the membrane. Using these results it is possible to estimate the effect that would be found in the human small intestine.

A series of mass transfer experiments were carried out using the SIM. Formulations with differing Wille Benecke (WB) guar gum concentrations (Section 3.2.1) were used for the experiments. The formulations all contained riboflavin at 0.1 mM in addition to guar gum using the method of preparation given in Section 3.2.1. The volume of fluid used on both the food side and the recipient side was 1 litre (0.001 m^3) and was chosen to minimise the change in concentration on both sides over the period of the experiment while also using volumes of fluid that could be prepared and handled adequately. Figure 5.1 shows that using water with segmentation gave a final concentration after one hour of approximately 0.001 mM on the recipient side. Therefore the concentration on the food side would have reduced by 1% and the recipient side concentration could be considered negligible. This allowed for a constant concentration difference of 0.1mM to be used between the food side

and recipient side when determining the overall mass transfer coefficient using Equation 2.8. During the experiment the food side fluid was re-circulated to keep the volumes of fluids required for each experiment manageable and the recipient side fluid was re-circulated to establish a change in concentration in the recipient side concentration over time.

Mass transfer across the membrane was monitored by measuring the riboflavin concentration in the recipient compartment using a fluorescence spectrometer (Section 3.3.1.1).

For each concentration of guar gum, four processing conditions were investigated:

- No net flow induced by peristaltic pump *and* no squeezing by cuffs 1 and 2;
- Net flow induced by peristaltic pump *and* no squeezing by cuffs 1 and 2;
- No net flow induced by peristaltic pump *and* local flow from squeezing by cuffs 1 and 2 alternatively with a 2 second inflation time, 2 second deflation time, 2 second delay and 0.5 barg inlet air pressure; and
- Net flow induced by peristaltic pump *and* local flow from squeezing by cuffs 1 and 2 alternatively with a 2 second inflation time, 2 second deflation time, 2 second delay and 0.5 barg inlet air pressure.

These conditions were chosen to investigate the effect of (i) the flow induced by the peristaltic pump and (ii) squeezing to represent the segmentation action seen in the small intestine. Each experiment was carried out for one hour and repeated in triplicate for each

concentration and process condition. The guar gum concentrations used were 0, 0.1, 0.25, 0.5, 0.75 and 1% w/v.

The mass transfer coefficient was determined from the concentration time profiles, using Equation 2.8. An example of a concentration versus time profile is given in Figure 5.1 for an experiment with 0% w/v guar gum and with segmentation. Figure 5.1 shows that the concentration of riboflavin on the recipient side of the SIM increases with time and this allows for mass transfer coefficient to be calculated. The concentration was measured using a Perkin-Elmer Fluorimeter described in Section 3.3.2 and the samples were continually extracted and replaced into the recipient side tank (Tank 2 in Figure 3.23).

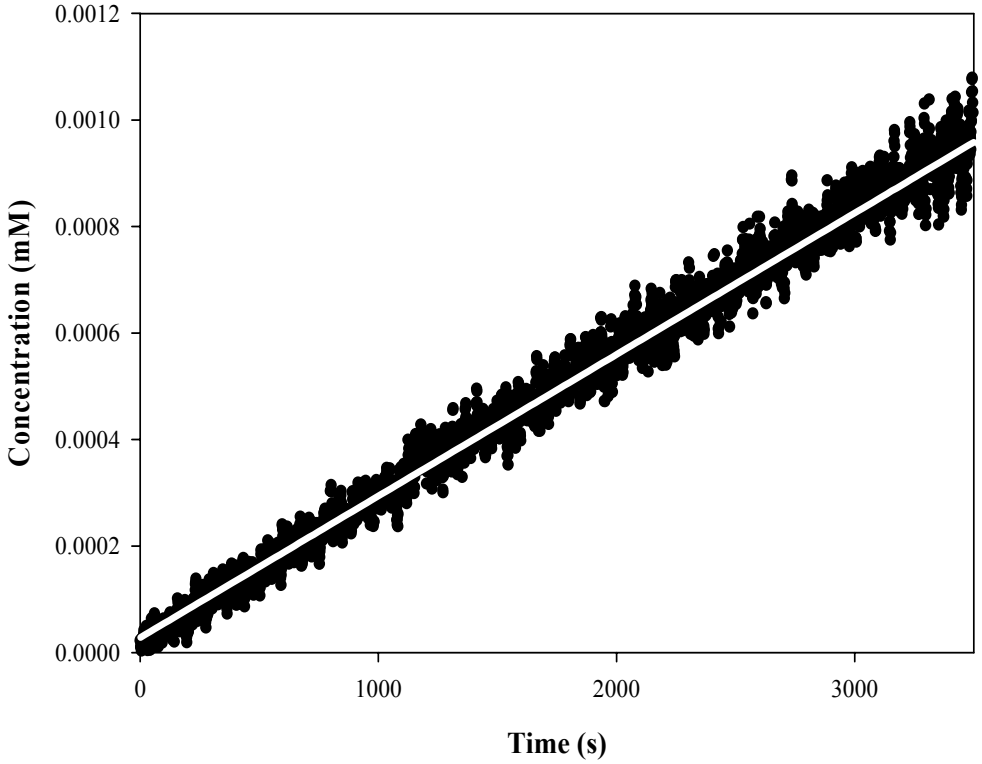

Figure 5.1 Example of trace of riboflavin obtained from experiment using water and with segmentation showing the change in concentration of riboflavin versus time. The white line is linear regression with an $R^2 = 0.99$.

5.2.2 Food Side Flow Conditions

Food side flow conditions were designed to represent as closely as possible the net flow velocity found in the small intestine of 0.01 m/min (Ganong, 2005). A peristaltic pump was used to give a volumetric flow of 1.2 x 10^{-5} m^3/min (a velocity of 0.016 m/min) through an unsqueezed tube; this flow was the minimum flow rate of the pump.

The flow Reynolds number (i.e. without squeeze) was calculated using the zero shear viscosity of the guar gum solution. To quantify the mass transfer enhancement of the system due to convection compared to diffusion alone it was important to calculate the Sherwood number (Equation 2.12). The biopolymer side mass transfer coefficient (m/s) k_{bp} was determined from the experiments. *L,* the characteristic length (m), was taken as 3.05 x 10^{-2} m, the diameter of the tube and *D* was taken as (1.25 $^{+}/_{-}$ 0.04) x 10^{-10} m^2/s from the measured values from viscosity matched solutions using FRAP (Section 4.2).

Table 5.2 shows the range of flow Reynolds numbers (1.2 x 10^{-3} - 9) for the overall flow conditions of the experiment. The change is due to the variation in the zero shear viscosity from 8.9 x 10^{-4} to 7 Pa.s; the flow velocity is 1.6 cm/min and tube diameter are constant.

Concentration of Guar % w/v	Zero Shear viscosity Pa.s	Density kg/m^3	Re
0	0.00089	1000	9
0.1	0.004	1001	2
0.25	0.03	1002.5	0.3
0.5	0.35	1005	0.02
0.75	3	1007.5	0.0028
1	7	1010	0.0012

Table 5.2 Flow Reynolds numbers of the system with a flow velocity of 0.274 mm/s and diameter of 30.5 mm.

In Figure 5.1 typical data of concentration versus time is shown, for water under squeezed conditions. A good linear regression (R^2 of 0.99) is obtained over a 1 hour period giving a gradient ($2.66 \pm 0.13 \times 10^{-6}$) from which N_i is determined using the recipient side total volume (0.001 m^3) and the membrane surface area (0.05 m^2). This gives a flux of $5.32 \pm 0.27 \times 10^{-5}$ mmol/m^2s. By dividing the molar flux (mmol/m^2.s) by the concentration difference in mmol/m^3 an overall mass transfer coefficient K, was obtained as $5.32 \pm 0.27 \times 10^{-7}$ m/s. The set up in the SIM results in a cyclical forward and backward flow, as the tube wall moves in the SIM to create a local flow. The particle image velocimetry results from Chapter 6 show that at the point in-between the two cuffs used for squeezing there is an oscillation in the flow velocities and direction.

The overall mass transfer coefficient K, was found for the full range of guar concentrations and results are shown in Figure 5.2. This graph shows the effect of changing the formulation guar concentration on the overall mass transfer coefficient for the four processing conditions investigated.

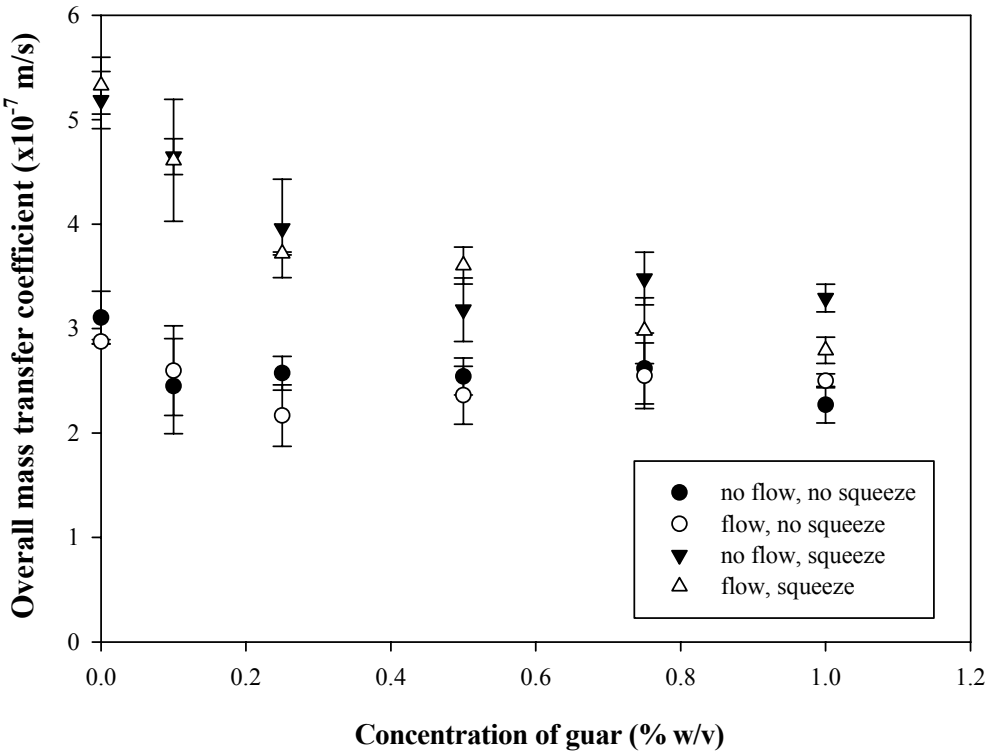

Figure 5.2 A plot of the overall mass transfer coefficient *K* versus concentration of guar for the four processing conditions: (i) no flow, no squeeze, (ii) flow, no squeeze, (iii) no flow, squeeze, (iv) flow, squeeze. The experiments were carried out in triplicate and the error bars show one standard deviation from the mean.

The maximum overall mass transfer coefficient K_{MAX} (as described by Equation 4.4), was estimated using water on the tube side under process conditions that minimised the biopolymer side film resistance close to the membrane by running high flow experiments. Experiments carried out consisted of varying flows on both the recipient side and then on the food side (0.1 mM solution of riboflavin) and recipient side (water), and are described in Table 5.3. By increasing the recipient side fluid flow rate and establishing that there was no significant change in the overall mass transfer it was shown that the recipient side was not controlling mass transfer i.e. experiments (1-3) in Table 5.3 show that doubling the flow keeps the mean *K* constant. In experiments (4-6) the food side fluid flow rate was then increased for constant recipient flow rate and three sets of experiments were carried

out at increasing flow rates (50, 100 and 150 ml/min). Since there was no significant increase in the overall mass transfer coefficient, this established that the overall mass transfer coefficient was at its maximum (K_{MAX}) of 5.32 $^{+}/_{-}$ 0.42 x 10^{-7} m/s for flows greater than around 4.0 x 10^{-4} m^3/min. Each experimental condition was repeated three times to obtain an mean of the overall mass transfer coefficient and the standard deviation.

	Recipient side flow M^3/min	**Food side flow m^3/min**	**Mean *K* (m/s)**	**Standard deviation (m/s)**
1	4.0 x 10^{-4}	1.2 x 10^{-5}	2.97 x 10^{-7}	2.4 x 10^{-8}
2	6.0 x 10^{-4}	1.2 x 10^{-5}	2.88 x 10^{-7}	1.8 x 10^{-8}
3	8.0 x 10^{-4}	1.2 x 10^{-5}	2.92 x 10^{-7}	2.1 x 10^{-8}
4	4.0 x 10^{-4}	2.0 x 10^{-4}	5.32 x 10^{-7}	4.2 x 10^{-8}
5	4.0 x 10^{-4}	4.0 x 10^{-4}	5.18 x 10^{-7}	3.9 x 10^{-8}
6	4.0 x 10^{-4}	6.0 x 10^{-4}	5.29 x 10^{-7}	4.8 x 10^{-8}

Table 5.3 Mean overall mass transfer coefficient (*K*) for experiments using water with varying recipient and food side flow rate to establish the maximum overall mass transfer coefficient.

Using the K_{max} value of 5.32 $^{+}/_{-}$ 0.42 x 10^{-7} m/s it was possible to establish the system resistance (R_{system}), i.e. the combined resistances of the membrane (l_{mem} / D_{mem}) and the recipient side resistance ($1/k_{rep}$) assuming k_{bp} is then negligible (see Equations 4.3, 4.4 and 4.5).

R_{system} was found to be 1.89 $^{+}/_{-}$ 0.17 x10^6 s/m which compared to 2.15 $^{+}/_{-}$ 0.20 x10^6 s/m found for the R_{system} in the diffusion cell. The parameter of interest (k_{bp}) for the fluids containing guar was then determined using Equation 4.5. with experiments at different biopolymer concentrations and process conditions. From a simple resistance model the k_{bp} can be considered to be made up of two components:

$$k_{bp} = \frac{D}{l} \qquad \text{Equation 5.1}$$

Where D is the diffusion coefficient (m^2/s) and l is the film thickness (m). In the SIM it can be assumed that the diffusion coefficient is constant at a given guar concentration. Using Equation 4.5 the biopolymer side mass transfer coefficient k_{bp} was then determined and plotted on Figure 5.3 for the four different types of experiments.

Using the data from Figure 5.2 the overall mass transfer coefficient and R_{system}, the food-side mass transfer coefficient (k_{bp}) was calculated from Equation 4.5 for experiments at different biopolymer concentrations and process conditions. Figure 5.3 shows the following:

(i) that the primary effects of mixing are due to squeezing; the tube side mass transfer coefficient k_{bp} is essentially independent of the guar concentration, and therefore the viscosity of the system, without squeezing occurring. Also, there is no real difference between the k_{bp} (without squeezing) with and without flow induced by the peristaltic pump; the data lie within the experimental variation. The low flow velocity of 16 mm/min gives biopolymer mass transfer coefficients that are basically the same as with no flow, showing that the resistance to mass transfer with and without this low flow velocity are very similar. This suggests that the segmentation/ peristaltic effects are controlling under conditions similar to those found in the GI tract.

(ii) when squeezing was carried out using 0.1% w/v guar, k_{bp} increased from 5.0 $x10^{-7}$ to 34 $x10^{-7}$ m/s (a factor of approximately 7). As the guar concentration increased, and therefore viscosity increased, the effect of squeezing is reduced. At guar concentrations above ~0.5% there is little difference between the squeezed and un-squeezed systems. It is thought that the reason for the reduced mass transfer enhancement under squeezed conditions at guar concentrations above 0.5% w/v is caused by these changes in viscosity which reduces mixing at the wall.

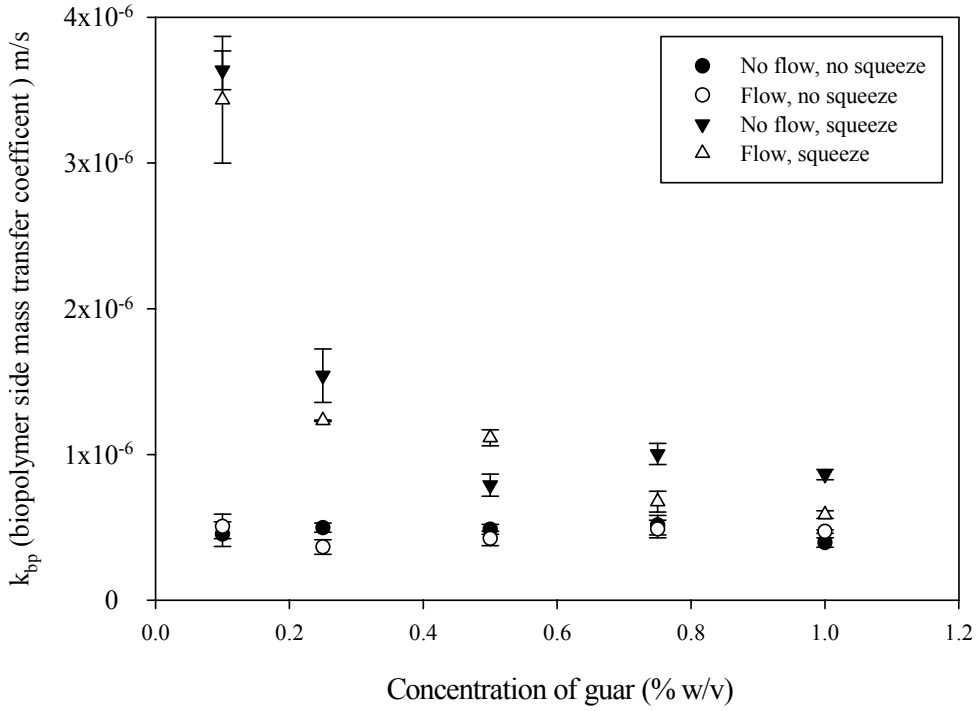

Figure 5.3 Plot of the guar side mass transfer coefficient at different guar concentrations in the intestinal cell under four processing conditions: (i) no flow, no squeeze, (ii) flow, no squeeze, (iii) no flow, squeeze, (iv) flow, squeeze. The experiments were carried out in triplicate and the error bars show one standard deviation from the mean. The data is tabulated in Table 5.4.

Conc of guar gum (% w/v)	Zero shear viscosity (Pa.s)	No flow no squeeze		Flow no squeeze		No flow, squeeze		Flow, squeeze	
		$k_{bp}x10^{-7}$ (m/s)	s.d.x10^{-7}(m/s)	$k_{bp}x10^{-7}$ (m/s)	s.d.x10^{-7}(m/s)	$k_{bp}x10^{-7}$(m/s)	s.d.x10^{-7}(m/s)	$k_{bp}x10^{-7}$ (m/s)	s.d.x10^{-7}(m/s)
0.1	0.004	4.53	0.84	5.07	0.84	36.36	1.33	34.34	4.35
0.25	0.03	4.98	0.31	3.65	0.50	15.41	1.84	12.32	0.05
0.5	0.35	4.86	0.34	4.24	0.50	7.89	0.75	11.15	0.55
0.75	3	5.15	0.67	4.89	0.60	10.03	0.73	6.76	0.72
1	7	3.96	0.33	4.71	0.12	8.62	0.35	5.87	0.26

Table 5.4 Table of the data of the guar side mass transfer coefficient at different guar concentrations in the intestinal cell under four processing conditions: (i) no flow, no squeeze, (ii) flow, no squeeze, (iii) no flow, squeeze, (iv) flow, squeeze. The experiments were carried out in triplicate and the error bars show one standard deviation from the mean.

Figure 5.4 shows the enhancement of the biopolymer side mass transfer coefficient with squeezing; k_{sq} is the biopolymer side mass transfer coefficient with squeezing and $k_{no\ sq}$ is the biopolymer side mass transfer coefficient without squeezing so that $k_{sq}/k_{no\ sq}$ represents enhancement due to squeezing. For 0.1 w/v guar gum the k_{sq} is 36.36 ($^{+}$/- 1.33) x 10^{-7} m/s and $k_{no\ sq}$ is 4.53 ($^{+}$/- 0.84) x 10^{-7} m/s which gives a $k_{sq}/k_{no\ sq}$ 8.02.

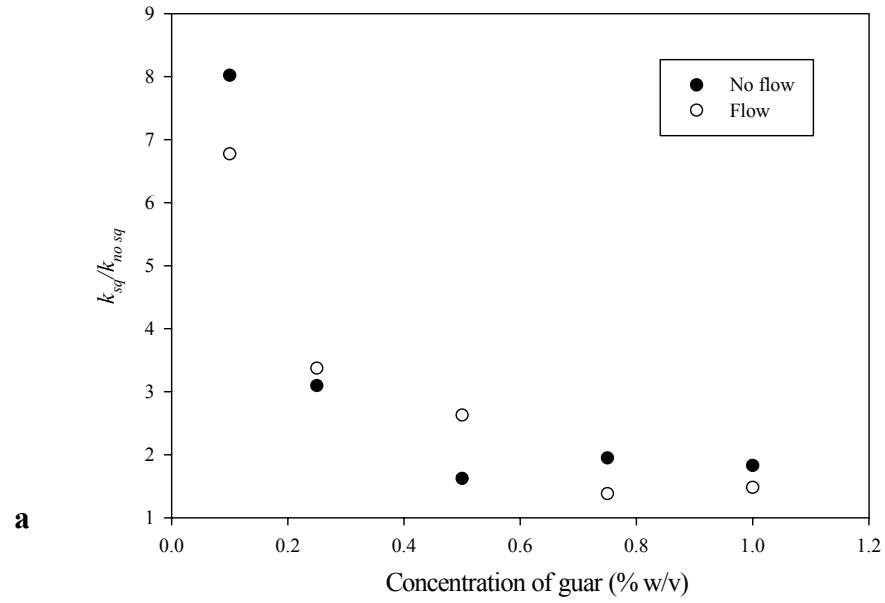

a

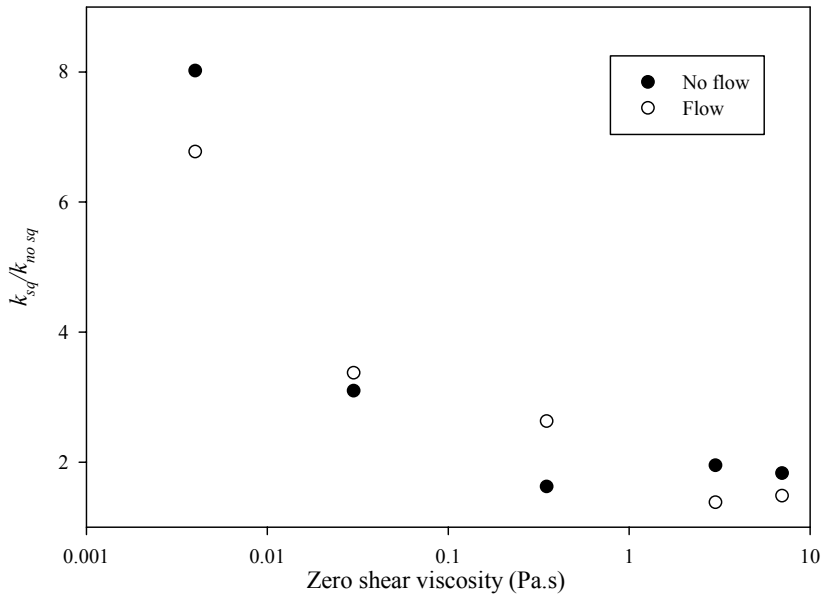

b

Figure 5.4(a&b)Plots of the guar side mass transfer coefficient with squeezing divided by the guar side mass transfer coefficient without squeezing against (a) the concentration of guar % w/v and (b) the viscosity of the guar. The data used is the same as that for Figure 5.3 tabulated in Table 5.5

Zero shear viscosity (Pa.s)	No flow $k_{sq}/k_{no\ sq}$	Flow $k_{sq}/k_{no\ sq}$
0.004	8.02	6.77
0.03	3.10	3.37
0.35	1.62	2.63
3	1.95	1.38
7	2.18	1.25

Table 5.5 Table of data showing the ratio k_{sq} to $k_{no\ sq}$ for conditions with flow and no flow from the data given in Table 5.4.

As the diffusion coefficient is unchanged by the presence of guar gum, any change in k_{bp} between squeezed and un-squeezed conditions can be described in terms of a change in the concentration boundary layer (Figure 2.23). At concentrations above 0.5% w/v there is negligible reduction in the film thickness due to the squeezing motion (Figure 5.3) which is due to the increased viscosity of the fluid. Figure 5.4 shows that the enhancement of segmentation falls significantly from 0.1 – 0.5% w/v guar gum.

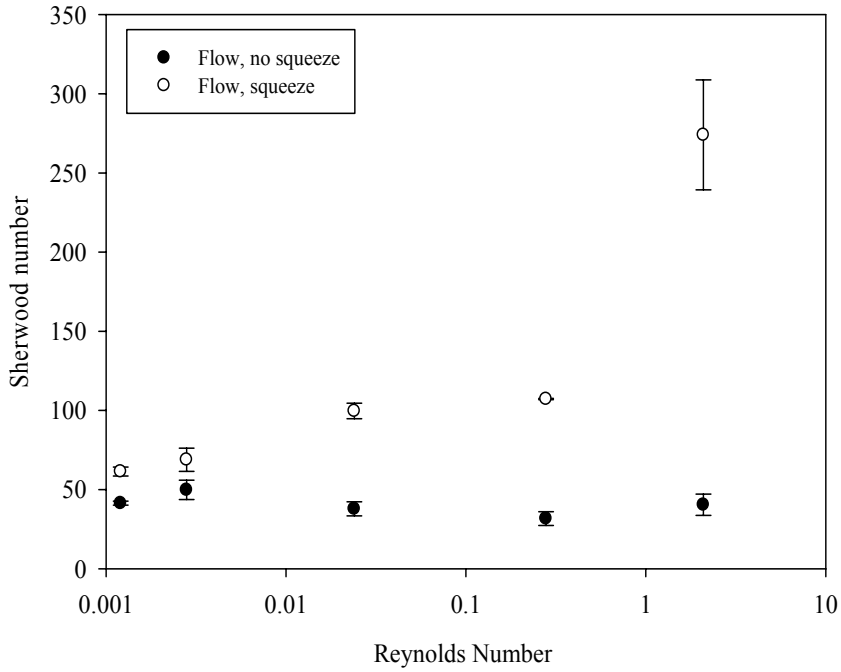

Figure 5.5 Plot of Sherwood number vs overall Reynolds number of the system (Table 5.2) for experiments where there was squeezing by the two cuffs alternatively (2 second inflation, 2 second deflation and 2 second delay) and no squeezing. The Reynolds number was changed by manipulating the viscosity as the flow rate was kept constant.

Figure 5.5 plots Sherwood number of the guar gum solutions determined from biopolymer side mass transfer coefficient of the guar gum solutions (Equation 2.12) against the overall flow Reynolds number (Table 5.2). The plot shows that the Sherwood number is largely independent of the Reynolds number when there is no squeezing flow. However, the Sherwood number increases with the Reynolds number as squeezing takes place, showing mass transfer enhancement by reducing fluid viscosity.

These results show that transport to the membrane can be affected by the fluid properties under physiologically representative process conditions. Delivery of molecules to the membrane is largely unaffected by the net flow from the peristaltic pump, but the squeezing process causes more mixing and flow close to the membrane surface. As the concentration of the guar is increased under squeezed conditions, then mixing and flow at the membrane surface is decreased. The effect of segmentation as mimicked by the squeezing action has been demonstrated in a physiologically representative system that suggests that the effect the biopolymer guar gum could have in the actual small intestine.

5.2.3 Conclusions

Experiments using the SIM (a representative model of a section of the human small intestine) with simulated flow profiles, as described in Section 2.2.4. Segmentation motion has a significant effect on nutrient delivery to the intestinal wall reflected in changes in the mass transfer coefficient on the biopolymer side, k_{bp}. This is most likely due to the increased mixing at the membrane surface. Where flow is induced by the peristaltic pump alone, increasing the bulk viscosity using guar had no direct consequence on the mass transfer across the membrane. The experiments conducted with segmentation showed significant enhancement to mass transfer showing that the segmentation motion is the controlling factor for mass transfer to the membrane.

This novel model of the small intestine has been used to understand how structuring model foods can impact on nutrient delivery to the intestinal wall. The results are in a agreement with the observations found by Blackburn *et al.* (1984), who showed reduction in the rate

of glucose absorption (Figure 2.14) in humans given model foods containing guar gum. Blackburn *et al.* (1984) concluded that guar improves glucose tolerance predominantly by reducing glucose absorption in the small intestine. They also speculated that this is probably done by inhibiting the effect of intestinal motility on fluid convection. This work has been able to take the hypothesis given by Blackburn *et al.* (1984) and show that it is the case. This has been shown by conducting experiments using the SIM and the results given in Figure 5.4(a&b) show that as the concentration of guar gum and the viscosity of the fluid increases, the enhancement seen in the biopolymer side mass transfer coefficient from segmentation is inhibited, probably due to reduced fluid convection.

The advantage of the SIM is that is a useful tool for the future to further understand the effect that food ingredients such as guar gum could have on mass transfer of nutrient to the membrane, as demonstrated here while reproducing the types of flow profiles expected in the small intestine. The limitation of the SIM is that it models molecular delivery to the intestinal wall (including the mucus layer) only, and however does not model the transport of nutrients across the membrane into the blood which can be a result of active transport mechanisms as discussed in Section 2.2.4.1. The model focuses on reproducing the flow profiles of the small intestine and since the guar gum is non-ionic it is therefore not affected by ionic strength or pH (Chaplin M, 2008) and the physiological pH and ionic strength has not been modelled here. However if investigating ionic polymers then care must be taken to reproduce physiological pH and ionic strength.

5.3 Starch Digestion Investigations Using the SIM

In Section 5.2 the effect of guar gum and the segmentation motion on molecular delivery to the inner wall of the membrane in the SIM has been established. This section describes experiments using the SIM to investigate the effect of structuring a model food formulation containing guar gum on the digestion of starch and subsequent release of glucose. The concentration of the glucose produced was monitored both on the food side and the recipient side of the SIM.

As the starch is digested the appearance of glucose in the food side would be expected and so after a period of time glucose would be expected to be seen in the recipient side as it moves across the membrane. The purpose of these experiments is to understand what effect that guar gum and segmentation have both on the rate of appearance of glucose and on mass transfer to the recipient side.

A model of the system is proposed. The rate of change of glucose concentration on the food side is equal to the rate of generation of glucose (rate of reaction) minus the rate of mass transfer across the membrane. This has been described as an equation in Equations 5.2 and 5.3.

(Rate of change of glucose concentration)$_{\text{on "food" side}}$ = (Rate of generation of glucose) - (Rate of mass transfer through tube)

(Rate of generation of glucose) = rate of reaction; (Rate of mass transfer through tube) = mass transfer

$$V\frac{d[c]}{dt} = VK_{react}[starch] - K_m A[c - c_{recipient}] \qquad \text{Equation 5.2}$$

$$\frac{d[c]}{dt} = K_{react}[starch] - \frac{K_m A}{V}[c - c_{recipient}] \qquad \text{Equation 5.3}$$

Where V is the volume of the food side (0.001 m^3), c is the concentration of glucose (mM), K_{react} is the rate of starch digestion (s^{-1}), [starch] is the concentration of starch (mM), K_m is the overall mass transfer coefficient (m s^{-1}), A is the area for mass transfer (m^2) and $c_{recipient}$ the concentration of glucose (mM) on the recipient side. The SIM was used as the equipment for the experiments (Section 5.2). The fluids used during the investigations were 5% w/v starch (precooked) solutions (Section 3.2.4) that were either formulated with (i) no guar gum or (ii) 0.5% w/v WB guar gum (Section 3.2.1). At the start of each experiment a digestion assay (Section 3.3.5) was mixed into the starch solution (Section 3.3.5) to give physiological concentrations of enzyme and then placed into the SIM.

The digestive enzyme hydrolyses the starch into glucose as described by Equations 5.4 (a & b). The two different enzymes in the starch digestion assay serve two different purposes. The pancreatic α-amylase randomly cleaves the α(1-4) glycosidic linkages of amylose to yield dextrin, maltose or maltotriose. The second enzyme amyloglucosidase further breaks the glucosidic bonds in the dextrins, maltose and maltotriose to form glucose.

$$(C_6H_{10}O_5)_x + H_2O \xrightarrow{\text{α-amylase}} (C_6H_{10}O_5)_y \qquad \text{Equation 5.4 (a)}$$

starch polymer dextrin, maltose, maltotriose

$$(C_6H_{10}O_5)_y + H_2O \xrightarrow{\text{amyloglucosidase}} C_6H_{12}O_6 \qquad \text{Equation 5.4 (b)}$$

dextrin maltose, maltotriose glucose

For the experiments one litre of fluid was used on the recipient side and one litre of fluid on the food (biopolymer) side. The circulation time for the food side was 80 minutes. Once the digestion assay had been added, the concentration of glucose was measured in the food side of the SIM and in the recipient side of the SIM every 15 minutes. The samples were taken from the outlet points of the SIM (Figure 3.23) using a needle (to penetrate the tubing) and syringe. The method of the fluid preparation and digestion assay are described in Section 3.3.5. The glucose concentration was measured using an Accu-Chek Aviva glucose monitor that was calibrated for the glucose concentrations in the fluids that were being used. For each experimental condition experiments were carried out in triplicate.

Figures 5.6(a) and Figure 5.6(b) show the results from investigations carried out into the effects of intestinal flow conditions and the presence of guar gum on the digestion of starch and the delivery of glucose to the membrane wall. Figure 5.6(a) shows the appearance of glucose on the food side (side containing the starch solution i.e. the inner tube) of the SIM as a product of the digestion of starch. Figure 5.6(b) shows the concentration of glucose on the recipient side of the SIM over time for the same experiments as those in Figure 5.6(a). As the glucose is transferred from the food side into the recipient side it is measured. The concentration of the glucose on the food side of the model increases over time due to the digestion of the starch (as shown in Figure 5.6(a)). The rate of flux from the food side to the recipient side is dependant on the mass transfer coefficient and the concentration difference between the food and recipient side (Equation 2.6). For starch digestion experiments shown in Figure 5.6 the flux from the food side to the recipient side increases in all cases (Figure 5.6(b)) since the concentration difference between the food and recipient side increases due to starch digestion. Further to this there are changes in the

mass transfer coefficient due to different processing condition (with and without squeezing) and different formulation (with and without guar).

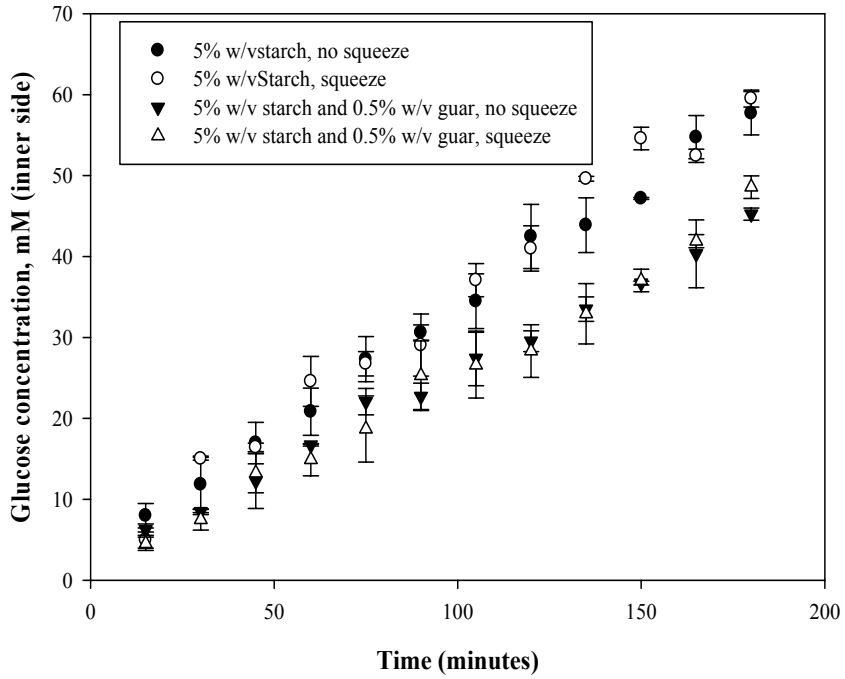

Figure 5.6(a) Glucose concentration versus time on the food side of the SIM. The error bars represent the average of three experiments.

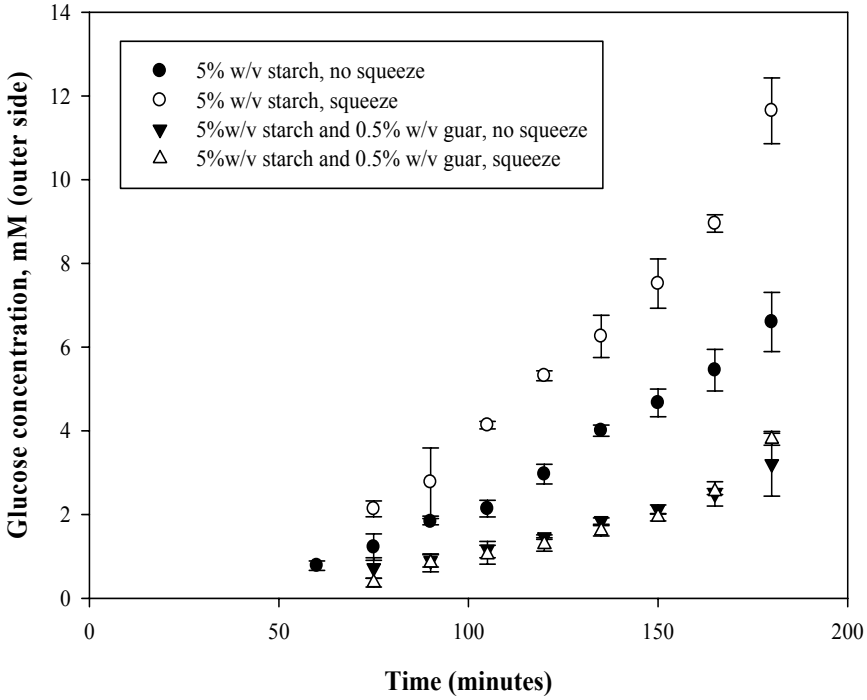

Figure 5.6(b) Glucose concentration versus time on the recipient side of the SIM. The error bars represent the average of three experiments.

By carrying out experiments with and without guar gum has allowed for the investigation into whether the guar gum interacts with the starch and the amylase/ amyloglucosidase at a physical level. The effect of the increase in viscosity resulting from the addition of guar gum on the rate of starch hydrolysis as well as mass transfer of glucose to the membrane wall have been investigated.

The proposed kinetics of the reaction is that of the Michaelis-Menton equation (Perry, 1998):

$$\frac{d(P)}{dt} = \frac{V_{\max}(S)}{K_M + (S)} \qquad \text{Equation 5.5}$$

where (P) is the product, glucose in this case, $V_{\max}$ is the maximum rate of reaction, (S) is the substrate (starch) concentration and K_M is the Michaelis constant. The Michaelis-Menton equation is frequently used to describe the kinetic behaviour of enzyme reactions. Over the course of this experiment a maximum of 25% of the starch has been converted into glucose. The forward reactions ultimately of starch to glucose are enzyme catalysed reactions and no enzymes are present for the reverse reaction of glucose polymerisation to starch. Since only 25% of the total starch was reacted and no enzyme was present for the reverse reaction the system will be far from equilibrium and therefore the recycling of the food side material was acceptable. The maximum of 25% of the starch has been converted can be estimated readily; 5% w/v in 1 litre is 50g, the molecular weight of the starch monomer $(C_6H_{10}O_5)_x$ is 162 g/mol resulting in 309 mM solution of glucose for full starch digestion. Since the maximum concentration achieved was ~ 70 mM (Figure 5.7), this equates to less than 25%. Since the glucose released versus time profile in this region is linear (Figure 5.7), one can assume zero order kinetics (Equation 5.6) over this region, the

rate of reaction is independent of the starch concentration, since the concentration is so high that [S] >> K_M

$$\frac{d(P)}{dt} = V_{\max} \qquad \text{Equation 5.6}$$

where (P) is the product concentration (glucose) where the volume is 1 litre (hence the product molar concentration is the same as the number of moles) and k the reaction rate is equal to V_{max} with units of mmol/time (mmol/s).

Figure 5.7 shows the kinetics more clearly. This data has been generated by calculating the total number of moles of glucose present in both the food and recipient sides and dividing this by the volume on the food side to obtain the concentration that would have been obtained with no transfer through the membrane. Linear regression has been applied to the data for each experimental condition and the gradient used to determine the rate of reaction given in Table 5.6.

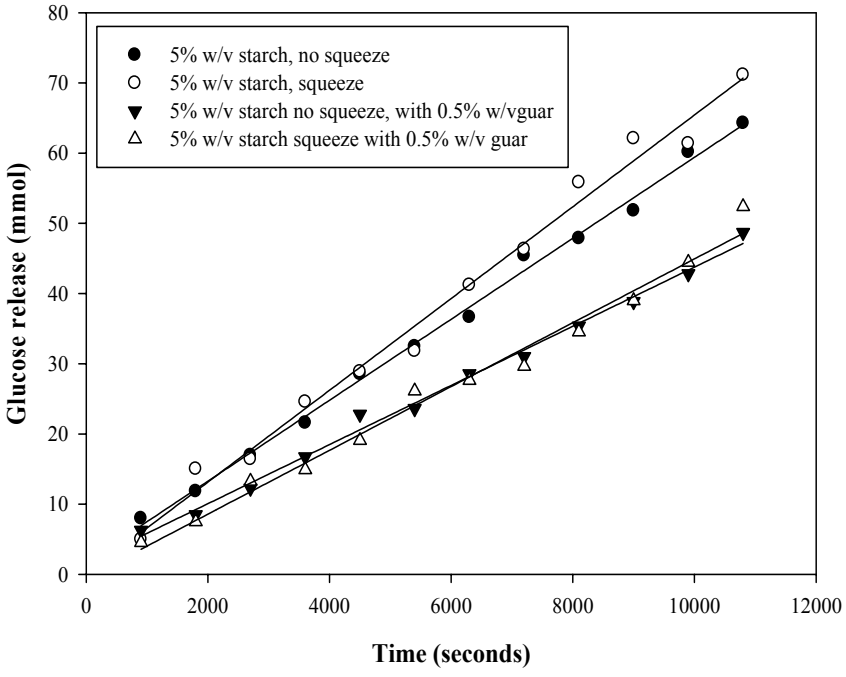

Figure 5.7 Glucose release, equivalent concentration on the food side versus time on the recipient side of the SIM. Used to determine rate of reaction.

Experimental Conditions	k x 10^{-3} (mmol/s)	+/- s.d. x 10^{-3} (mmol/s)	R^2
Starch with No Squeeze	5.8	0.31	0.99
Starch with Squeeze	6.4	0.21	0.98
Starch and Guar with No Squeeze	4.2	0.17	0.99
Starch and Guar with Squeeze	4.5	0.29	0.97

Table 5.6 The rate of digestion of glucose production from starch digestion for experiments with and without guar gum and with and without squeezing.

Table 5.6 shows that squeezing has a very small effect (less than 10%) on the rate of digestion for both systems with and without guar gum. However, the presence of guar gum reduces the rate of the starch digestion to the final product of glucose by about 30% (28% when there is no squeezing and by 30% when there is squeezing).

Guar gum will also affect mass transfer. Experiments investigated the effect of the presence of guar on the overall mass transfer coefficient of glucose from the food side to the recipient side with and without squeezing. Figure 5.6(b) shows the glucose on the recipient side of the SIM as the glucose passes through the membrane and appears on the recipient side. There is a time delay of one hour for the appearance of the glucose; this is required first for glucose to be present on the food side and then for sufficient glucose to pass through the membrane to be measured.

To calculate the overall mass transfer coefficient for each experimental condition the approach adopted was to: (i) use the concentration difference at each measurement time and (ii) calculate the average flux of glucose from the food compartment into the recipient

side (N_1 (mol/m^2 s)) as described in Equation 2.6. This allowed calculation of a mass transfer coefficient over the period of the experiment.

The results from calculating the overall mass transfer coefficient have been tabulated in Table 5.7 and show that for experiments with guar gum present there is no difference between the mass transfer coefficient for the two cases (as seen for high guar gum values in the experiments of Section 5.2). For the fluids that did not contain guar, there is a clear difference between the mass transfer coefficient for conditions with and without squeezing.

Experimental Conditions	**Overall Mass Transfer Coefficient (x 10^{-7} m/s)**	**+/- s.d. (x 10^{-8} m/s)**
Starch with No Squeeze	2.20	3.1
Starch with Squeeze	3.29	3.1
Starch and Guar with No Squeeze	1.38	3.1
Starch and Guar with Squeeze	1.40	2.3

Table 5.7 The mass transfer coefficient for the four experimental conditions.

Table 5.7 gives the mass transfer coefficients for the four different experimental conditions. The effect of squeezing on the mass transfer coefficient is to give a 50% increase compared to no squeeze when no guar is present. This reduces to a 1% increase when guar is present; this is within the error of the experiment. The presence of guar reduces the mass transfer coefficient by 37% when there is no squeezing taking place, compared to a 57% reduction when squeezing takes place. The relative magnitude of the overall mass transfer coefficient is shown in Figure 5.8, with the condition ‘starch + no squeeze’ normalised to 100% as this would be considered the control case.

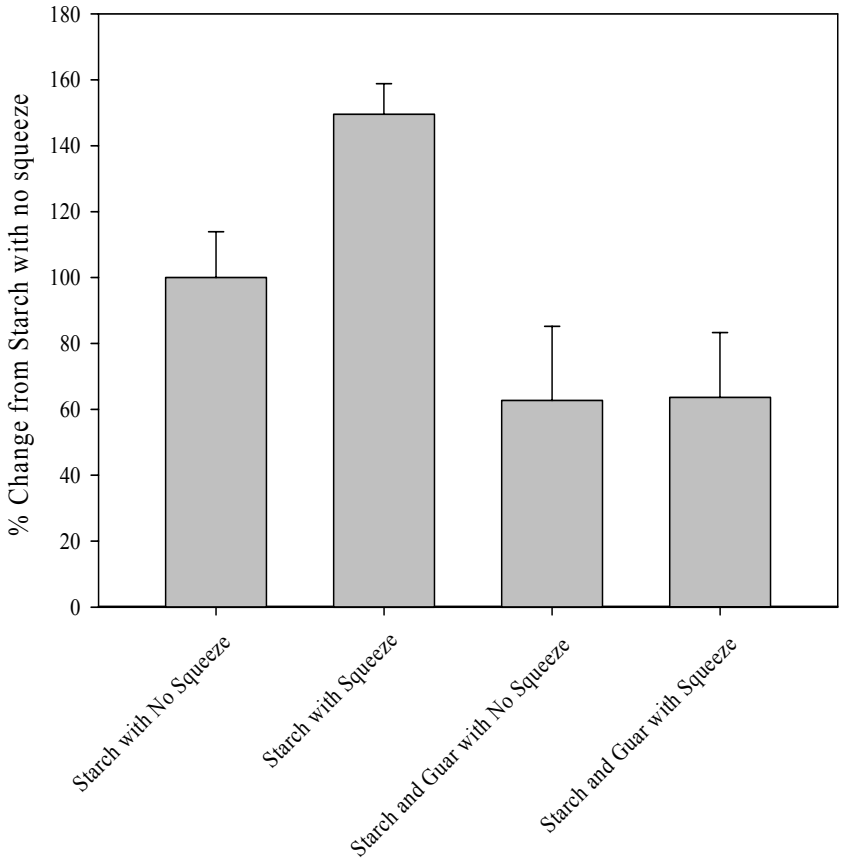

Figure 5.8 Shows the % deviation of the average mass transfer coefficient for the 4 experimental conditions (i) starch no squeeze, (ii) starch with squeeze, (iii) starch and guar no squeeze and (iv) starch and guar with squeeze. Error bars represent the one standard deviation from the mean.

For comparison, the overall mass transfer coefficients between the riboflavin experiments and the starch digestion experiments have been compared in Table 5.8. Although they are not the same in absolute terms they are in the same order of magnitude and the qualitative effects of the squeezing and the addition of guar gum are similar. By scaling the overall mass transfer coefficients with the square root of the molecular weight, the scaled overall mass transfer coefficients are similar.

Experimental Conditions	Riboflavin Overall Mass Transfer Coefficient (K) (x 10^{-7} m/s)	Glucose Overall Mass Transfer Coefficient (K) (x 10^{-7} m/s)	Riboflavin $K/(M_r)^{0.5}$ (x 10^{-7})	Glucose $K/(M_r)^{0.5}$ (x 10^{-7})
Flow with No Squeeze	2.87	2.20	0.15	0.16
Flow with Squeeze	5.19	3.29	0.27	0.25
Flow and Guar with No Squeeze	2.27	1.38	0.12	0.10
Flow and Guar with Squeeze	2.79	1.40	0.14	0.10

Table 5.8 A table to compare the overall mass transfer coefficient (K) determined for the riboflavin (M_r 376 g/mol) experiments and glucose (M_r 180 g/mol) from the starch experiments. The overall mass transfer coefficient (K) has also been scaled by dividing by $(M_r)^{1/2}$.

The physiological implication of this work is to show that in a system where the enzyme has been mixed with the substrate, further mixing by segmentation does not significantly enhance the rate of digestion. However the presence of 0.5% w/v of guar gum reduces the rate of glucose generation (starch digestion) by ~ 30% for process conditions with and with out squeezing. This reduction in starch digestion would have significant implications on the time that it takes to break starch down into glucose and therefore could potentially have positive effects on the controlled delivery glucose in the small intestine.

Further to this the presence of the guar gum has significantly reduced the overall mass transfer coefficient for the transport of glucose from the food side to the recipient side of the SIM. This also indicates that guar gum could aid in reduction of the postprandial hyperglycaemia by reducing the rate of delivery of glucose to the wall of the small intestine.

5.3.1 Conclusions

The first conclusion to be drawn from these experiments is that the presence of guar gum in relatively low concentrations (0.5 % w/v) has a significant reduction (~30%) on the rate of glucose release from starch digestion for process conditions with and without squeezing. One can conclude that the reduction in the rate of starch digestion is due to the reduction in the diffusion of the enzyme through the fluid containing guar gum since segmentation had no real effect on for systems containing guar (Table 5.7) .

The second conclusion from the investigation is that the presence of guar reduces the mass transfer coefficient by 37% when there is no squeezing taking place and by 57% when squeezing takes place. This shows that guar reduces both the rate of digestion of starch and the rate of mass transfer from the food side to the recipient side of the SIM.

5.4 Overall Discussion and Conclusions

This chapter has described experimental results generated using the novel design of the SIM with the segmentation motion, which has allowed for investigation into the effect of structuring formulated foods and the effect of segmentation itself. Experiments have shown the significant effect that the segmentation motion has on nutrient delivery to the intestinal wall as a consequence of changes in the mass transfer coefficient on the biopolymer side, k_{bp} as a result of increased mixing.

Since the SIM models the fluid flow as a consequence of segmentation in the small intestine and the measures the delivery of nutrient to the membrane wall and thereby models the effect of segmentation on delivery of the nutrient to the intestinal wall; an understanding of the importance of this segmentation motion on molecular delivery in the intestine has been demonstrated.

Segmentation enhances mass transfer to the membrane but the addition of guar gum reduced the enhancement caused by the segmentation motion. This therefore shows that the effect guar gum has on reducing the peak value of postprandial hyperglycaemia, described in Section 2.3.2.2 and shown in Figure 2.14, may be attributable to the reduced mass transfer to the membrane.

Experiments using a starch digestion assay and the SIM, with and without the presence of guar gum have shown that guar gum reduces the rate of starch digestion. Results from absorption experiments showed that the presence of guar gum reduced the delivery of glucose to the membrane for both squeezed and non-squeezed conditions. Therefore foods

containing starch with guar used as an additional ingredient, would be expected to have a reduced peak value of postprandial hyperglycaemia. This might be achieved in the small intestine by: (i) reducing the rate of starch digestion into glucose as a consequence of restricted diffusion (as seen for FD150 dextran molecule in Figure 4.5); (ii) reducing the mass transfer enhancement seen due to the mixing of the fluid.

The fluid dynamics clearly have a large influence on the molecular delivery to the membrane. This work has used an empirical approach to date to represent segmentation and it is now necessary to quantify the flow within the SIM to give an estimate of the flow patterns due to physiology. To further understand this, experimental and computational fluid dynamics have been used to obtain further detail on fluid velocities in the axial and radial directions with different fluid properties. This is expanded on in Chapter 6.

CHAPTER 6 - EXPERIMENTAL FLUID DYNAMICS TECHNIQUES APPLIED TO THE SMALL INTESTINAL MODEL

6.1 Introduction

In Chapter 4, the diffusion and mass transfer through model food formulations were investigated using the diffusion cell. The purpose of the this experiment was to understand the impact that the addition of guar gum has on the molecular delivery of a model nutrient while being processed. Chapter 5 described the development of a model system to investigate the effect that guar gum has on molecular delivery under more realistic process conditions. The process conditions of interest were those of the small intestine and in particular the segmentation motion. This chapter report the results from the use of the SIM for fluid dynamics investigations and computational modelling. The methods used to investigate fluid dynamics in the SIM have been:

(i) Particle Image Velocimetry (PIV), used to investigate the velocities generated in the SIM;

(ii) Planar Laser Induced Fluorescence (PLIF), used to investigate the mixing performance of the SIM;

(iii) Computational Fluid Dynamics (CFD), used to model the system to give a theoretical understanding of the process in the region of segmentation where flow visualisation techniques are ineffective.

The PIV and PLIF techniques have been described in detail in Chapter 3 (Section 3.8 and 3.9) as has the CFD (Section 3.10).

6.2 Particle Image Velocimetry (PIV)

6.2.1 Rig Set up

Two-dimensional PIV was used to measure the radial and axial fluid velocity components for different formulations being processed through the SIM (described in Section 3.7). A detailed experimental description of PIV can be found in Section 3.8. The radial direction is defined as the y direction and the axial direction is defined as the x direction, as shown in Figure 3.32. The velocity vectors in the x and y direction (shown in Figure 3.32) were recorded for each point on an x-y grid for a given time and saved as .vec files for reading in INSIGHT 6.0. Using a Vector Plotting Tool written in MATLAB by Kenneth Chung of Birmingham University (see Appendix 1), the .vec files were read into MATLAB to give a matrix that contained all the relevant data from the experiment. It was then possible to carry out analysis of the data in MATLAB and also to import the velocity data into the PIV software Tecplot 9.

6.2.2 Experimental Set Up

Using the rig described in detail in Section 3.8 a series of experiments were carried out to investigate the effect of the incorporation of a viscosifying polymer upon the fluid dynamics of the SIM. The polymer used was carboxymethyl cellulose (CMC) which is fully described and characterised in Chapter 3 (Section 3.4). CMC was used since the opacity of the guar gum solutions rendered them unsuitable.

The CMC used gave a good rheological match (compare Figures 3.8 and 3.13) to the guar gum and was visually transparent, thus allowing for its use in these flow visualisation experiments. Experiments were carried out using CMC at concentrations 0.5, 0.25, 0.1,

0.05 and 0 % w/v CMC. This gave a range of zero shear viscosities between 0.54 and 0.001 Pa.s. The SIM was used as described in Chapter 5 with the addition of the flow visualisation cell (as shown in Figures 3.31 and 3.32). The operating settings were the same as experiments described in Chapter 5 (Section 5.2.2). The inflation of the cuffs produced the segmentation motion as described in Section 2.2.4.2. The outflow from the SIM would discharge into a tank and the tubing was always kept below the fluid level in the tank to allow for backflow. The tank would also act as the feed tank to the SIM, thus maintaining the tracer concentration. Once the correct amount of tracer particles was added, the fluid was pumped around the flow circuit until the tracer particles had become fully dispersed in the fluid. A four second time delay was given between the start of the PIV measurements and the beginning of the SIM segmentation time cycle.

The experiment ran for 120 seconds for each trial and therefore resulted in observations for 10 cycles. At an image capture frequency of 4 Hertz this led to 480 sample points for each experiment.

6.2.3 Results

Using the PIV technique it was possible to establish the change in velocity at the centre point of the visualisation tube over the duration of each experiment. Figure 6.1 (a-g) shows schematically the movement of the tube over the course of a squeezing cycle.

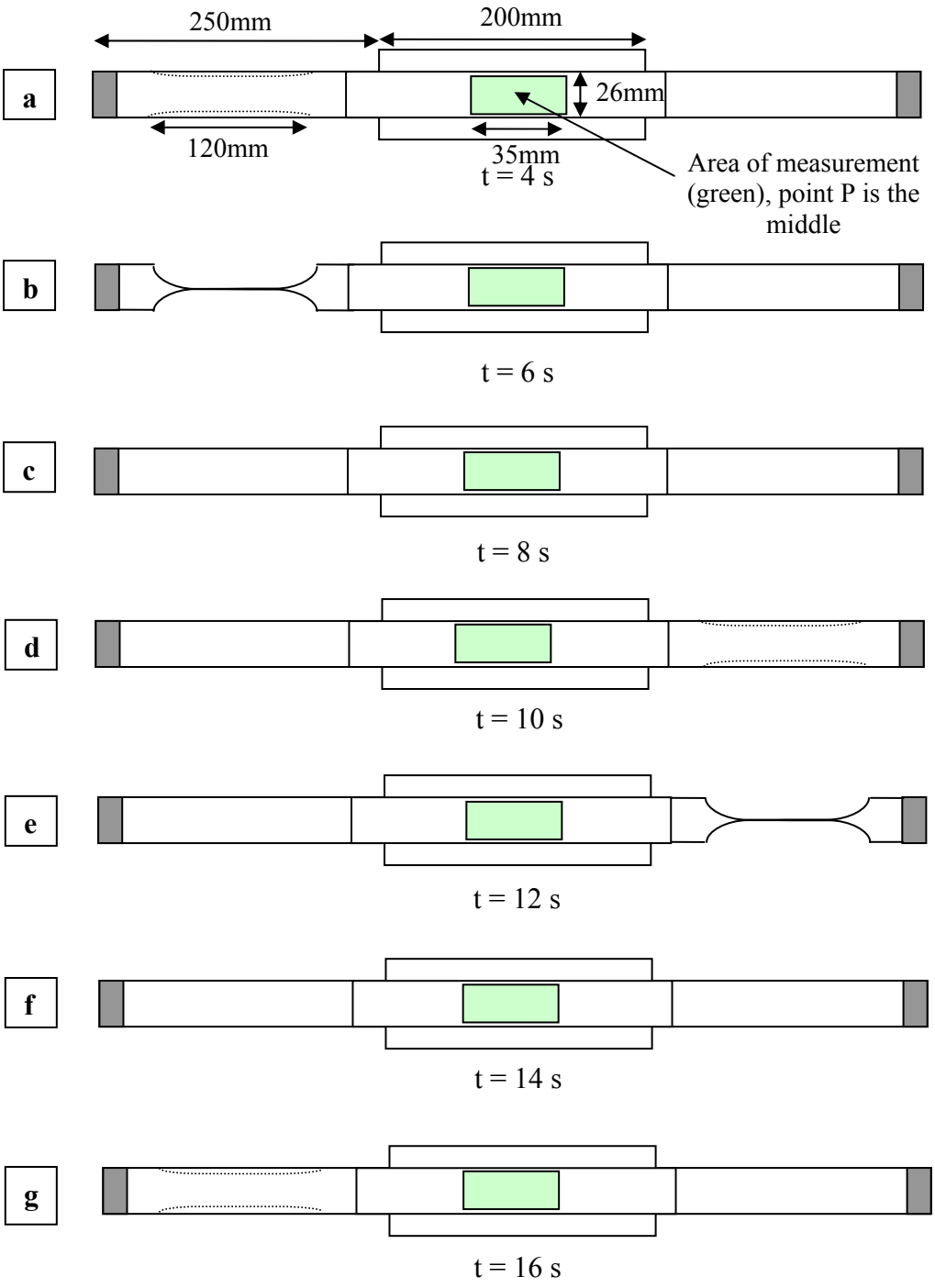

Figure 6.1 Diagram showing the sequence of events for the wall movement of one cycle from (a) time 4 seconds at which time (b) the squeezing on cuff 1 begins for 2 seconds after which (c) there is a deflation for 2 seconds and then (d) a delay for 2 seconds and then (e-g) the sequence begins for cuff 2. The green box represents the area of measurement. Total length of cycle time is 12 seconds.

For each velocity measurement a pair of images is taken 500 μs apart from each other. The velocity is determined by the displacement of particles over that time, as is described in Section 3.8. A pair of images was captured four times per second and the change in velocity within the field of measurement field could be measured over the period of the experiment (120 seconds). The field over which the measurement was taken is shown in Figure 3.32 and Figure 6.1.a and the velocity vector measurement was determined as described in Section 3.8 and Section 6.2.1. Each time frame for the 480 measurements of each experiment gave a vector plot as shown in Figure 6.2 plotted using Techplot.

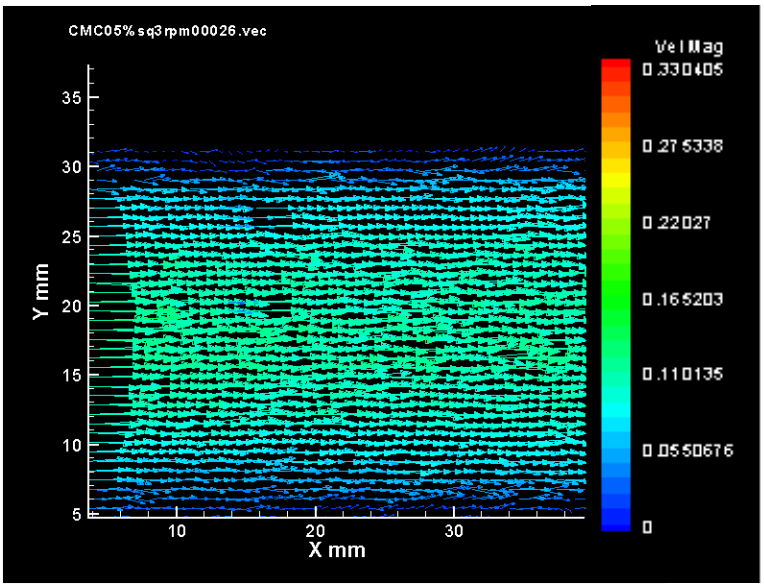

Figure 6.2 The velocity vector plot for 1 of the 480 time measurements taken over a 120 second period for the fluid 0.5% CMC (an example for illustrative purposes).

For each fluid (CMC concentrations 0.5, 0.25, 0.1, 0.05 and 0% w/v) using the PIV, a velocity profile was obtained over the 120 second period at the mid point of the cell shown in Figure 6.1.a for one of the twelve second sequences. By taking the middle point (Point P in Figure 6.1.a) within the frame, the axial and radial velocity components could be plotted and are shown in Figure 6.3 for 0.5% w/v CMC. The velocity component for point P was

used to determine the axial and radial velocity to determine how these change over time for the different fluids. Figure 6.3.a shows the axial velocity at the middle point within the measurement frame and shows the cyclical increase and decrease of both the positive X (forward) and negative X (backwards) velocity. Figure 6.3.b shows more closely the axial velocity for one full cycle, with a forward stroke and a backward stroke; peak velocities are on the order of 0.3 m/s, several orders of magnitude greater than the 0.27×10^{-3} m/s considered as the mean flow in the experiments. Figure 6.3.c shows the radial velocity shown in the frame of measurement and reveals that there is no real change from zero in the radial velocity component during the experiment.

The axial velocity across the radius at the middle length of the field has been profiled for the forward stroke and the backward stroke in Figure 6.4 for 0.5% w/v CMC. The three parts of Figure 6.4 (a-c) show various points of time in the forward and backward stroke. The small graphs in the corner of the plots in Figure 6.4 (a-c) relate the point of time for the radial profile with the mid point axial velocity which is Figure 6.3.b. The development of the velocity profile can be seen in Figure 6.4.a and the decay of the forward velocity profile is shown in the Figure 6.4.b. The development and decay of the reverse velocity is shown in Figure 6.4.c. Figure 6.4 thus shows the development and decay of velocity profiles in the forward and backward direction for one cycle period.

The velocity contours for the flow field have been plotted using the Techplot 9.0 software and are shown in Figures 6.5 a-d respectively for certain times in the cycle. This shows the overall velocity contours for the measurement field as the flow develops and this corresponds to Figure 6.5 e-g showing times 12.25, 12.5, and 12.75 seconds respectively.

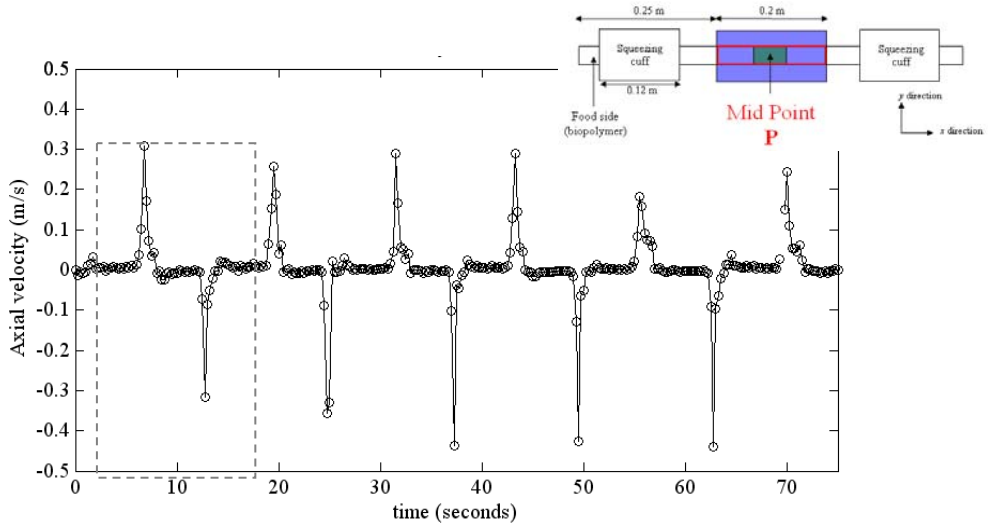

(a)

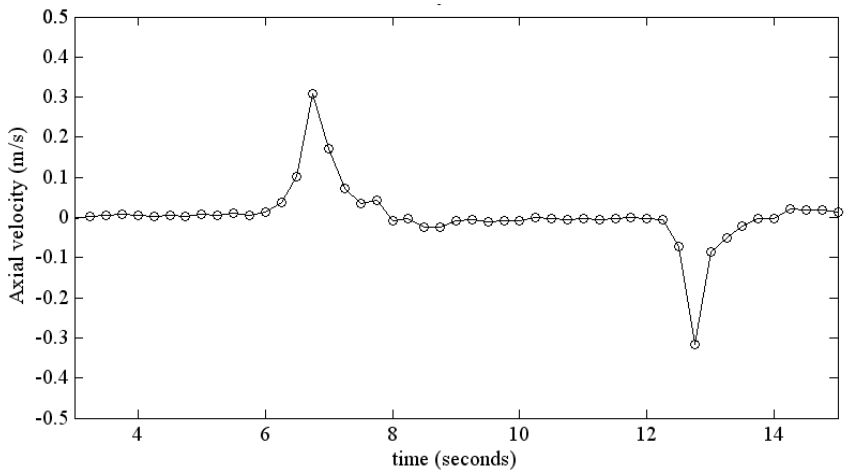

(b)

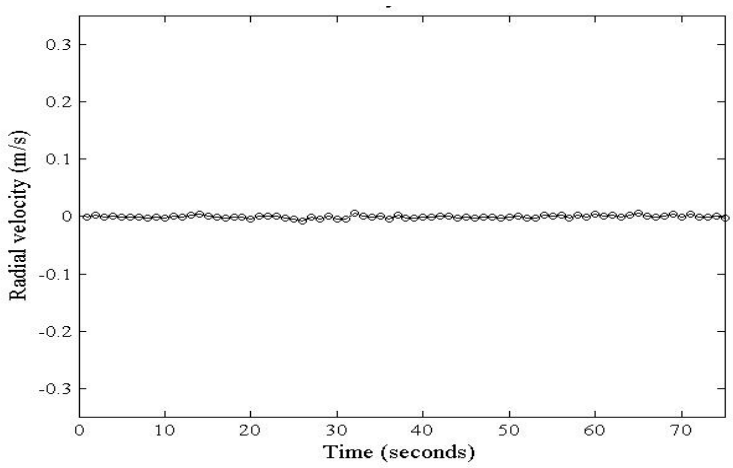

(c)

Figure 6.3 Plots of the results from a 0.5% w/v CMC experiment at the mid point P both for axial and radial position (x and y) of the visualisation cell: (a) shows the axial velocity where the box (--) shows 1 cycle; (b) axial velocity for one cycle as shown in Figure 6.1; (c) the radial velocity over 75 seconds.

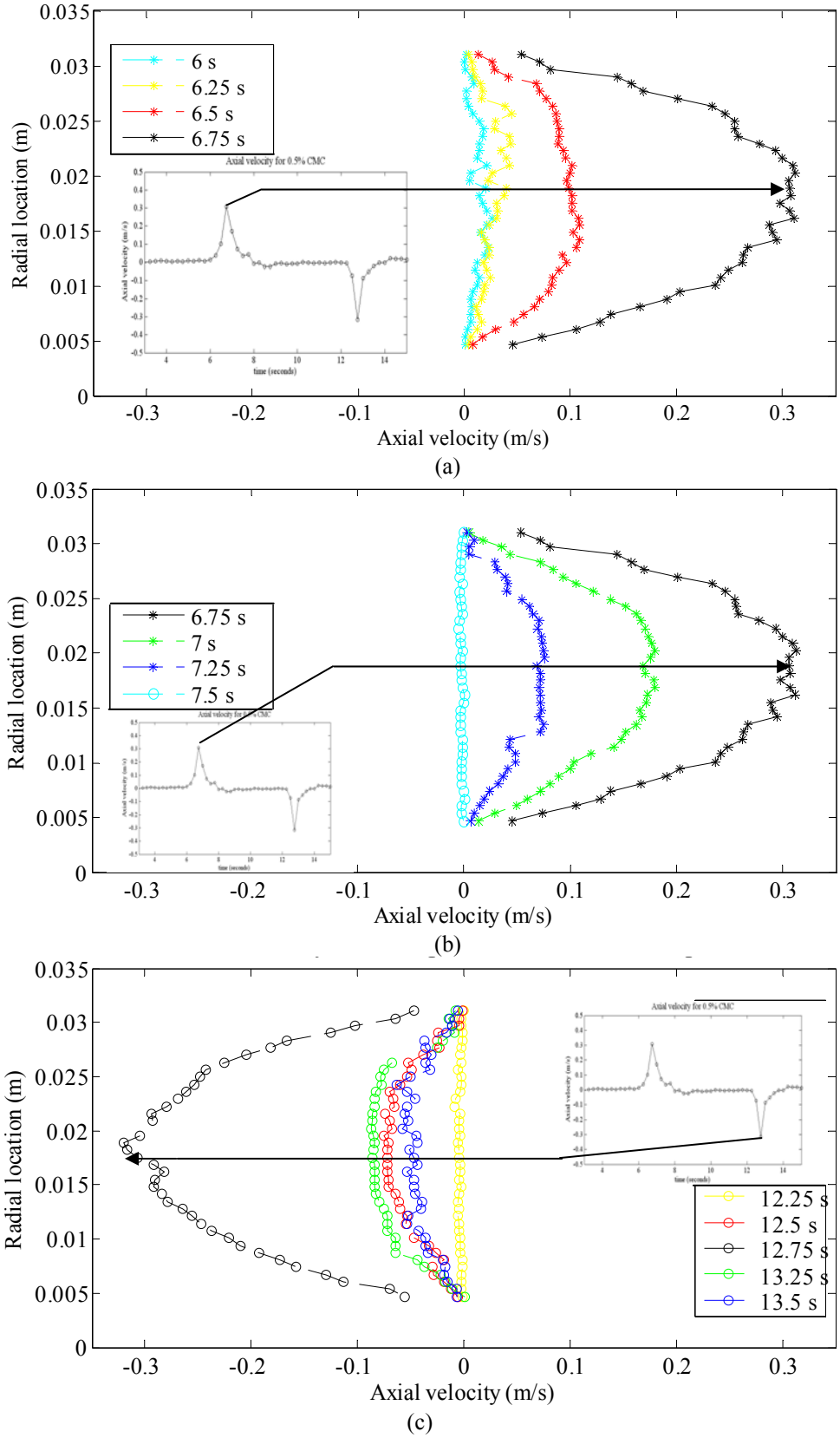

Figure 6.4 (a-c) The axial velocity across the radial position for a forward and backward squeeze for 0.5% CMC at the middle length of the field of view. A small graph is placed in the corner showing the point corresponding to the velocity profile. The time in the legend correspond to the time from Figure 6.1

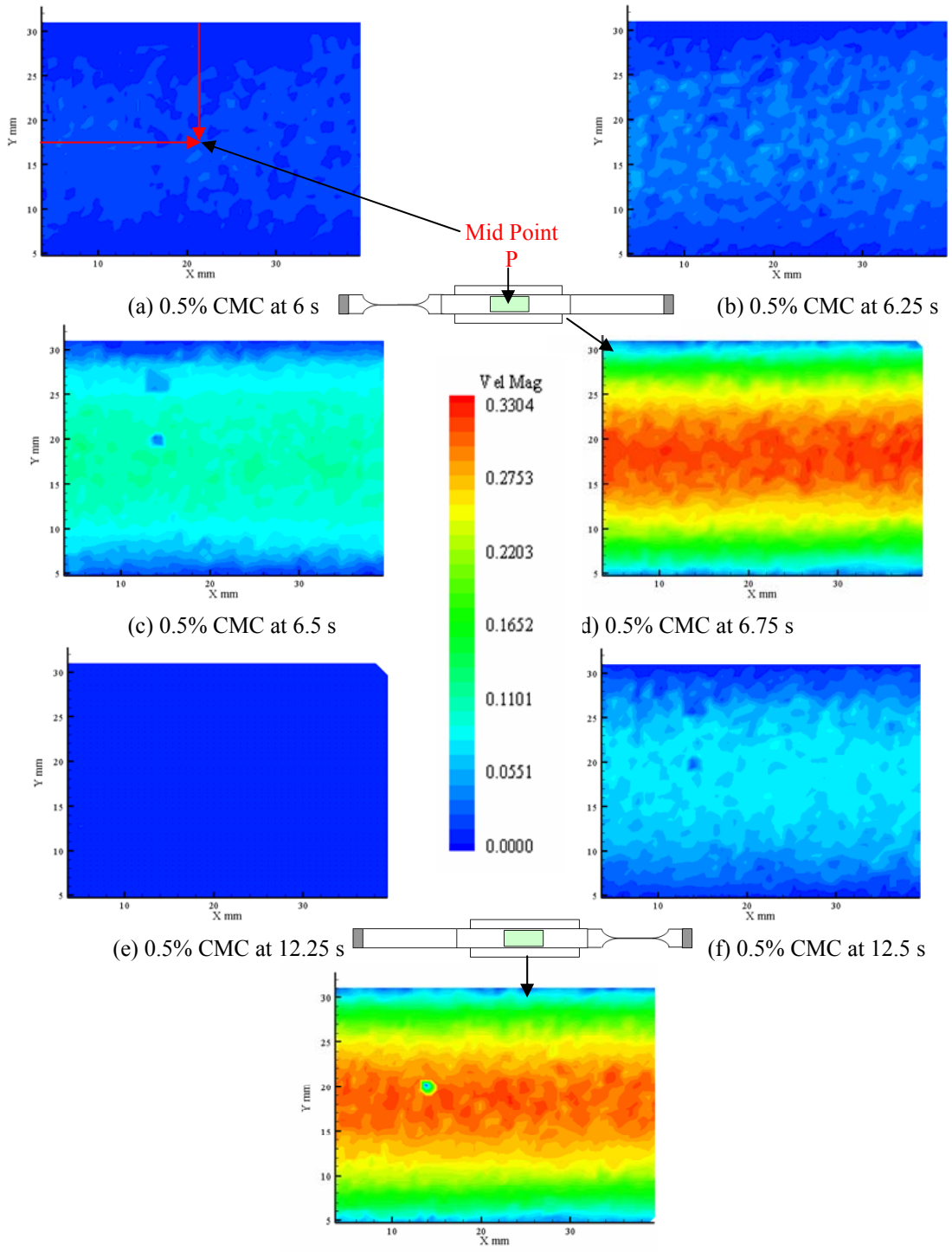

(a) 0.5% CMC at 6 s (b) 0.5% CMC at 6.25 s

(c) 0.5% CMC at 6.5 s d) 0.5% CMC at 6.75 s

(e) 0.5% CMC at 12.25 s (f) 0.5% CMC at 12.5 s

(g) 0.5% CMC at 12.75 s

Figure 6.5 (a-g) The contour plots from the velocity measurements at various time points (a – 6 seconds, b – 6.25 seconds, c – 6.5 seconds, d – 6.75 seconds, e – 12.25 seconds, f – 12.5 seconds, g – 12.75 seconds) that correspond to the forward and backward stroke shown in Figure 6.4. Data were post processed using Techplot. Point P in Figure 6.5(a) x=20 mm, y = 17.5 mm is the centre point in the channel, Point P in Figure 6.1.

6.2.4 Overall Results from PIV

For each of the five fluids (0, 0.05, 0.1, 0.25 and 0.5 % CMC) further analysis of the data was carried out and the results are described and presented below. The parameters of interest were the peak volumetric flow rate, the peak Reynolds Number during segmentation (Re_{seg}), the velocity profiles and the shear rates.

6.2.4.1 Volumetric Flow and Reynolds Number During Segmentation (Re_{seg})

The volumetric flow rate was determined by the summation of the individual annular volumetric flows determined from the velocity at a given radial location for each fluid using Equation 6.1.

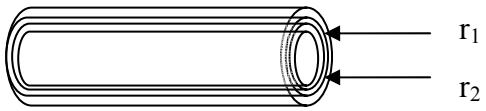

Cross sectional area of cylinder (A) = $\pi r_1^2 - r_2^2$

Volumetric flow ($Q_{segment}$) = A x velocity of segment

Overall Volumetric flow ($Q_{overall}$)= $\Sigma Q_{segment}$ (Equation 6.1)

The volumetric flow rate at the time of the peak velocity has been plotted in Figure 6.6. Table 6.1 shows the data measured for each of the fluids using the PIV technique and gives the values measured for the average volumetric flow, from which the average velocity was determined by dividing by the area of total flow. The averages of five data points are presented with their standard deviation. Figure 6.6 gives a graphical representation of the data and indicates that as the concentration of CMC is increased from 0 to 0.5% and the viscosity increases, the peak volumetric flow rate decreased by the order of one third. The peak volumetric flow (for water 1.6 x 10^{-4} m^3/s) of the fluid is several orders of magnitude

greater than the overall volumetric flow of the system (3.3 x 10^{-9} m^3/s). This suggests that within the small intestine for short periods of time and over short lengths of the intestine there are volumetric flow rates that are several orders of magnitude greater than the overall flow rate.

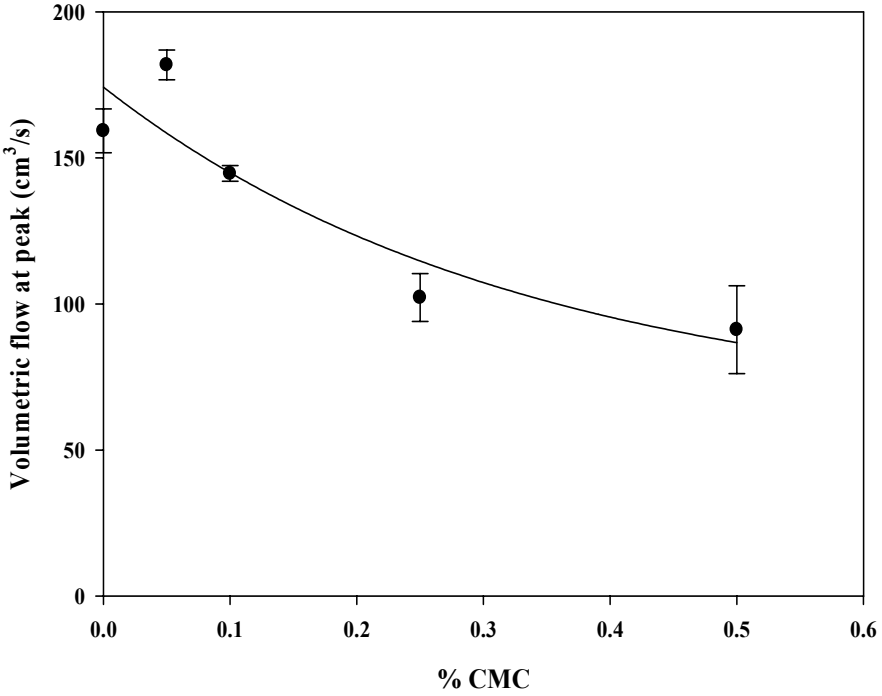

Figure 6.6 Plot of the volumetric flow at peak velocities for CMC concentrations 0.5, 0.25, 0.1, 0.05 and 0 %. The error bars represents one standard deviation from the mean from five data points. The fitted equation is an exponential decay (y=y0+a*exp(-b*x)), where y0 is 6.2 x 10^{-5}, a = 0.0001, b= 3 and r^2= 0.84.

Fluid	peak velocity (m/s)		average velocity (m/s)		peak volumetric flow (x 10^{-4} m^3/s)	
% CMC	ave	s.d.	ave	s.d.	ave	s.d.
0.5	0.31	0.08	0.17	0.028	0.91	0.15
0.25	0.43	0.09	0.26	0.006	1.02	0.08
0.1	0.37	0.07	0.27	0.005	1.45	0.03
0.05	0.34	0.09	0.34	0.010	1.82	0.05
0	0.36	0.08	0.30	0.014	1.59	0.08

Table 6.1 Table to show the data measured for the peak velocities, average velocities and the volumetric flow rates for the five fluids investigated.

When fluid with a uniform velocity enters a pipe, a boundary layer forms at the side of the walls which gradually thickens as the distance from the entry point increases. Since the fluid in the boundary layer is retarded and the total flow remains constant, the fluid in the central stream will be accelerated. At a certain distance from the inlet, boundary layers, which have formed in contact with walls, join at the axis of the pipe, and, from that point onwards, occupy the whole cross-section and consequently remain of constant thickness. *Fully developed flow* then exists (Coulson, 1998). If the boundary layers are still streamlined when fully developed flow commences, the flow in the pipe remains streamlined. This analysis has been carried out to establish the cases where flow would be expected to be fully developed, although unsteady laminar flow may also develop. If the boundary layers are already turbulent, turbulent flow will persist. The PIV will aid in establishing the Reynolds numbers and the axial and radial velocity components to further our understanding of this dynamic system.

An approximate experimental expression for the inlet length L_e for laminar flow is given by Equation 6.2:

$$\frac{L_e}{d} = 0.0575 \times \mathrm{Re} \qquad \text{Equation 6.2}$$

Where d is the diameter of the pipe and Re is the Reynolds number with respect to the pipe diameter (Coulson, 1998).

Using the average velocity of the flow across the 26 mm inner diameter Perspex tube (given in Table 6.1), the peak Reynolds number during segmentation (Re_{seg}) was calculated using Equation 2.2 and the inlet length to establish laminar flow, L_e determined. This data has been presented in Table 6.2 and the peak Reynolds number during segmentation

against the viscosity of the fluids has been plotted in Figure 6.7. The Figure shows that the Reynolds number (segmentation) using the diameter of the unsqueezed tube of 0.026 m, dramatically reduces from 7800 to 390 with the addition of 0.05% CMC and is further reduced with increasing concentrations of CMC. The addition of CMC moves the fluid from the near turbulent range to the laminar range of Reynolds numbers. Note that an estimation of the Reynolds number in the constriction is made in Section 6.4.

Table 6.2 also shows the inlet length for laminar flow L_e which indicates that as the Reynolds number (segmentation) increases the inlet length for laminar flow increases also. For the 0.5 % CMC fluid the inlet length for laminar flow is short (0.013 m) and when there is no CMC the inlet length for laminar flow is long (12 m). The length from the midpoint of the segmentation to the midpoint of the measurement is 0.225 m, hence fully developed flow would only be expected for the 0.5 and 0.25 % CMC solution. This is discussed in further detail in the Section 6.2.4.2 in context of velocity profiles.

Fluid	**visocisty**	**average velocity (m/s)**		**Re_{seg}**		**L_e**
% CMC	**Pa.s**	**ave**	**s.d.**	**ave**	**s.d.**	**m**
0.5	0.529	0.17	0.028	8	1	0.013
0.25	0.106	0.26	0.006	63	5	0.094
0.10	0.044	0.27	0.005	160	3	0.24
0.05	0.023	0.34	0.010	390	11	0.58
0	0.001	0.30	0.014	7800	368	12

Table 6.2 A table of the viscosity, the segmentation Reynolds Number measured using PIV and the inlet length for developing laminar flow. Given for five fluids of varying CMC concentration and the standard deviation is determined from five data points.

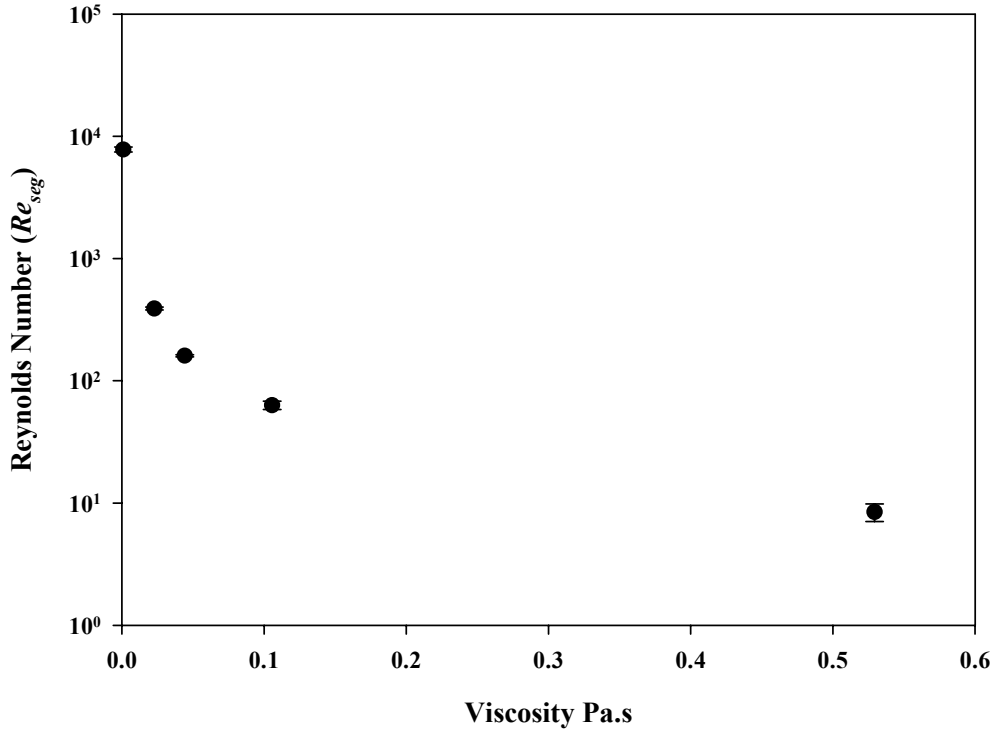

Figure 6.7 Plot of the peak segmentation Reynolds Number versus viscosity for CMC concentrations 0.5, 0.25, 0.1, 0.05 and 0 %. The error bars represents one standard deviation from the mean from five data points.

6.2.4.2 Velocity Profiles

By taking the velocity profiles across the radius of the tube and normalising the velocities by dividing by the average velocity (calculated from the volumetric flow rate) for each experiment, the velocity profiles can be compared. The velocity profiles are shown in Figure 6.8 (a-e) where U_x is the axial velocity and U is the average velocity.

The results for the velocity profiles can be compared to those of fully developed velocity flow profiles for power law fluids with the same rheology using Equation 6.3 (Coulson, 1998).

$$\frac{U_x}{U} = \frac{3n+1}{n+1}\left[1-\left(\frac{s}{r}\right)^{\frac{(n+1)}{n}}\right] \qquad \text{Equation 6.3}$$

Where U is the mean velocity, U_x is the velocity at point s (radial position), r is the overall radius and n is the power law exponent (Equation 3.6), where n is given in Table 3.3 for the fluids used, as shown in Figure 6.9.

It can be observed from Figures 6.8 a-e that for the low CMC concentration solutions (0, 0.05, 0.1 % CMC) there is a large discrepancy between the theoretical and measured velocity profiles with the measured profiles being flatter. The discrepancy reduces as the concentration of CMC is increased and the flow profile is as would be expected for continuous flow for 0.25 and 0.5% CMC solutions. This can be explained by the fact that only the flow of 0.25 and 0.5 % CMC solutions would have been fully developed as determined in Section 6.2.4.1 from Table 2.2. The context of this situation to that in the human intestine is made in (Section 6.2.5).

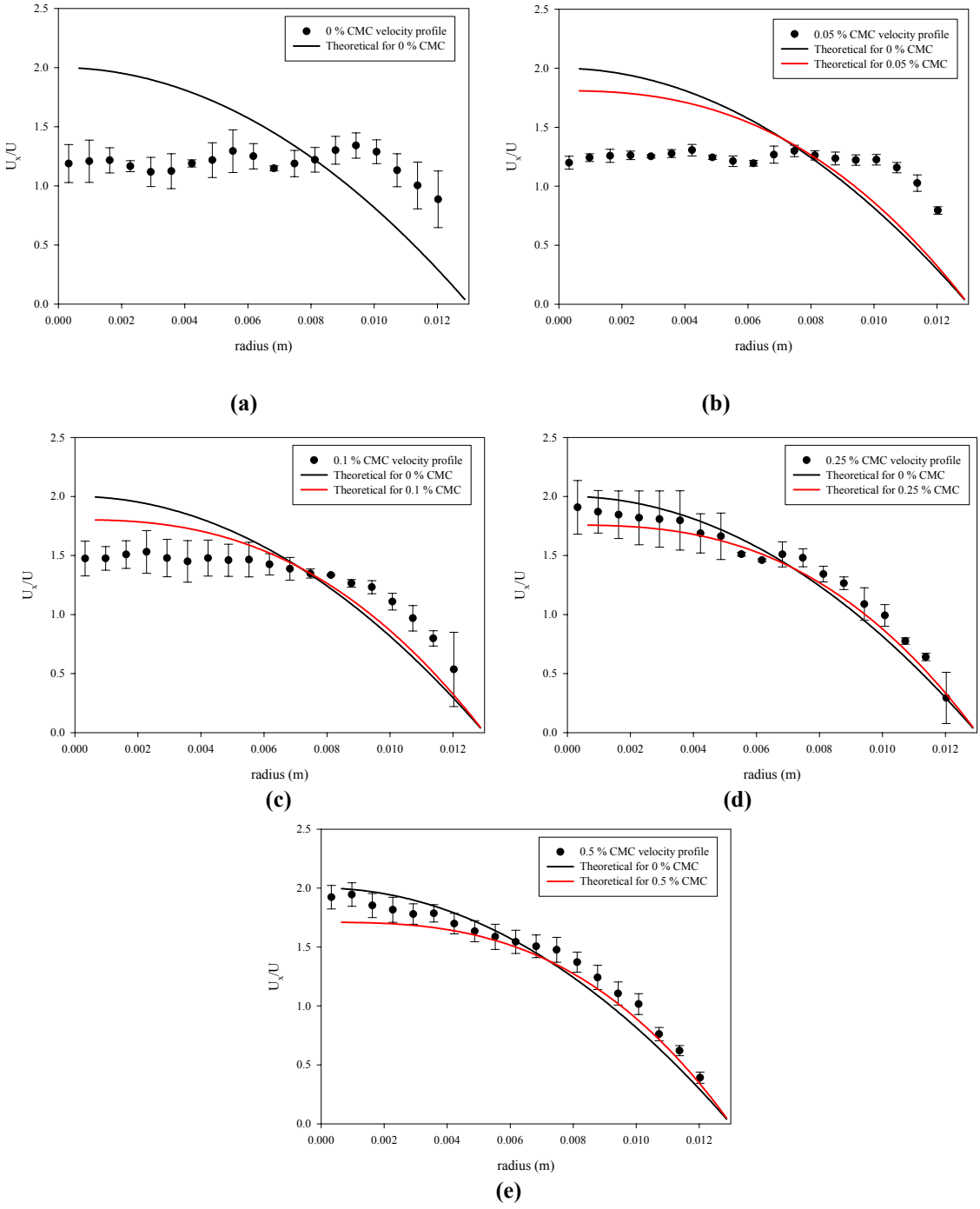

Figure 6.8.a-e The radial velocity profile across the radius of the middle length of the measurement for CMC solutions 0% (Figure a), 0.05% (Figure b), 0.01% (Figure c), 0.25% (Figure d), 0.5% (Figure e) at the time of peak flow and SIM geometry of Figure 6.1.b for 5 cycles. U_x is the axial velocity and U average velocity. Error bars represent one standard deviation for five peak flow data points. Theoretical velocity profiles are also plotted for comparison using Equation 6.3 and data from Table 3.3.

6.2.4.3 Shear Rate

The shear rate from the PIV experiments at a given time can be plotted using the software Techplot 9. The change in the axial velocity (dU_x) divided by change in radial position (dr) (i.e. dU_x/dr), was used by Techplot to determine the shear rate. The contour plots of the shear rate at the peak axial velocities are shown on Figures 6.9 (a-e) for fluids 0.5, 0.25, 0.1, 0.05 and 0% CMC. For water, there appears to be very little shear not only for the bulk fluid but also close to the wall. However, fluids containing CMC, the shear is maximum near the walls. From the velocity profiles given in Figure 6.8, the shear profiles are as expected as the water has a flat profile and the 0.5 % CMC is approaching a parabolic profile.

The average of the peak shear rates (at peak volumetric flow) have been plotted in Figure 6.10 which shows that the peak shear rate increased from 31 to 117 s^{-1} as the concentration of CMC was increased from 0 to 0.5% CMC. This gives an indication of the range of shear rates that would be expected in the small intestine upstream and downstream of a segmentation contraction. A shear thinning material such as the model digesta formulated with guar gum (Figure 3.8) and CMC (Figure 3.13) would behave as a fluid with a lower viscosity to itself in the regions of high shear which are the areas close to the wall. In the real situation this would reduce the resistance to flow near the wall and aid in the passage of material through the small intestine and to the wall of the small intestine during the squeezing motion.

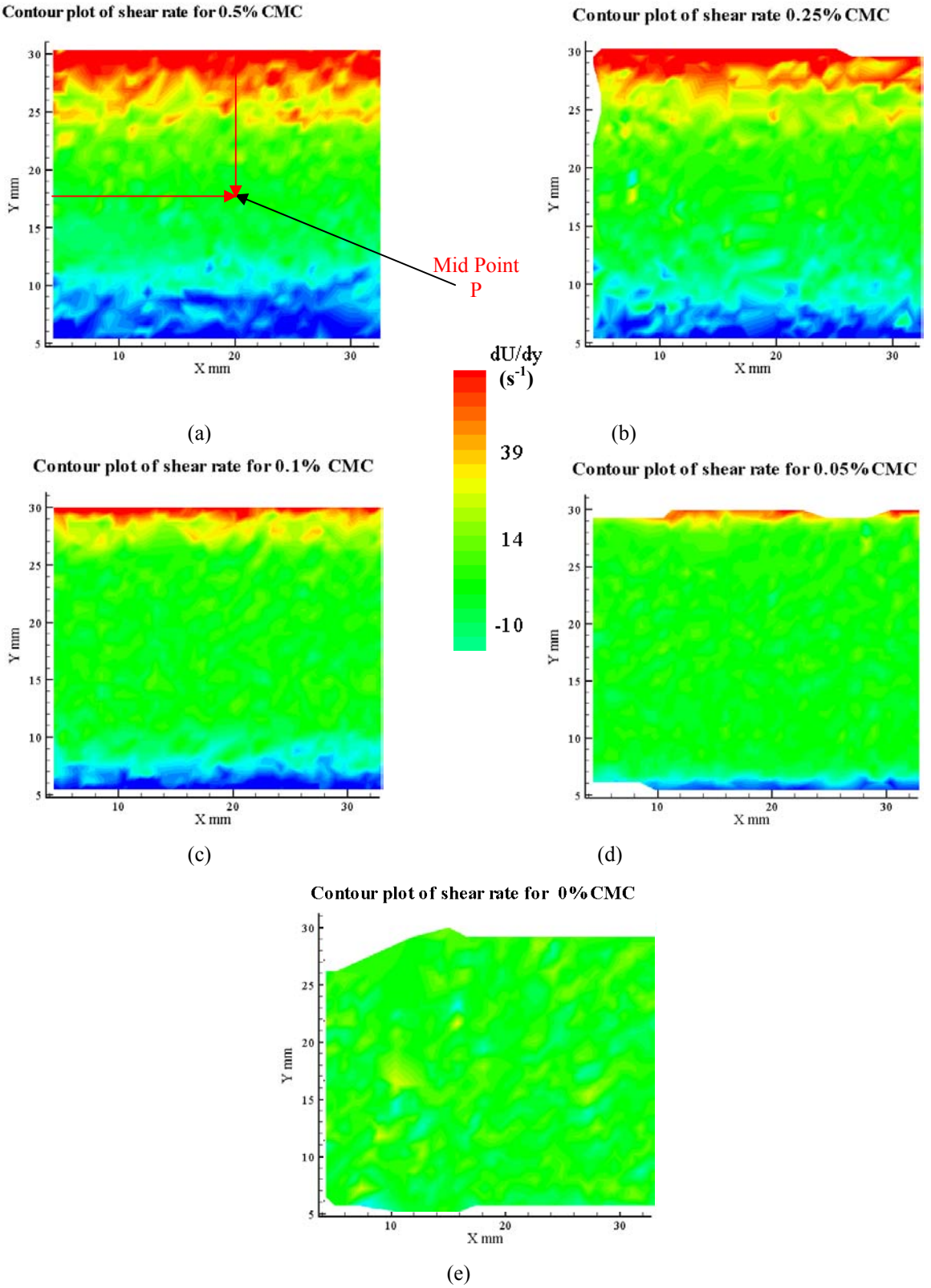

Figure 6.9 Contour plots of the shear rate for (a) 0.5% CMC, (b) 0.25% CMC, (c) 0.1% CMC, (e) 0% CMC shown for position in the cycle shown in Figure 6.1.b and using the apparatus shown in Figure 3.31. Data were post processed using Techplot. Point P in (a) is x=20 mm, y = 17.5 mm, the centre point in the channel, Point P in Figure 6.1, units of scale are s^{-1}.

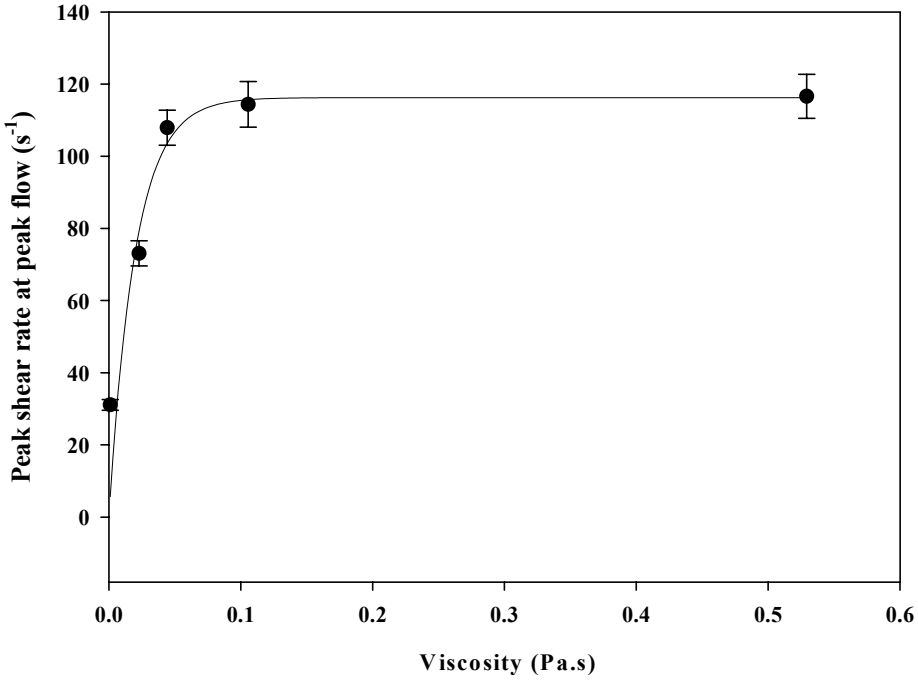

Figure 6.10 Plot of the peak shear rate at peak flow versus viscosity for CMC concentrations 0.5, 0.25, 0.1, 0.05 and 0 %. The error bars represent one standard deviation from the mean from five data points. The fitted equation is an exponential rise to a maximum y=a*(1-exp(-b*x)), where a = 116, b= 50 and r^2= 0.87.

6.2.5 PIV Conclusions

This work has shown that it is possible to study the flow profiles in the SIM using PIV, demonstrating that the PIV technique can be used to study the effect of structuring food formulation with biopolymers on the fluid dynamics in a model of the small intestine.

The PIV experiments have shown that the radial velocity component measured at the centre point of the measurement cell is very small relative to the axial velocity for all the fluids studied over the course of several squeezing cycles. Using the PIV technique it has been shown that the volumetric flow at peak axial velocity for a squeeze decreases as the viscosity of the fluid is increased. The pressure exerted during squeezing was kept constant during the experiment as the pressure on squeezing in the small intestine appears to remain

constant (within a range) during the periods of motility, as described by Imam *et al.* (2003).

The flow profiles under these non-steady state conditions do not mimic those expected for continuous laminar flow for the power law fluids at the low concentration (0, 0.05, 0.1 % CMC), although they do match the theoretical profiles for continuous flow at higher concentrations (0.25, 0.5% CMC) as they are then fully developed. The velocity profiles were used to determine the peak volumetric flow rate and peak Reynolds numbers which have been used in mixing studies in subsequent work (Section 6.3).

Using this PIV technique it has also been possible to understand the shear profile downstream of a segmentation contraction. It has been determined that the maximum shear rate changes from 31 to 117 s^{-1} as the concentration of CMC was increased from 0 to 0.5% CMC.

The technique is valuable to determine the velocity profiles, peak Reynolds numbers and shear rates in the SIM used as a model of the motility and mass transfer in the human small intestine. This will allow for researches to use a shear rate range representative to those expected in the human small intestine to evaluate the viscosity of digesta. The use the shear rates for viscosity measurement of digesta has been variable in the past, for example, in twelve separate studies conducted to measure digesta viscosity in hamsters, rats, chicks, salmon, humans and pigs, different shear rates were used, ranging from 0.005 to 90 s^{-1} (Dikeman *et al.*, 2006).

This PIV technique in combination with the SIM is currently limited to use in sections upstream/downstream of the segmentation contraction, as the movement of the wall renders the technique ineffective in a section with a moving wall. Computational fluid dynamics (Section 6.4) was used to investigate the theoretical fluid dynamics in the SIM in the area of the segmentation motion.

6.3 Planar Laser Induced Fluorescence (PLIF)

6.3.1 Use of PLIF

The use of PLIF has been described in Section 3.9. PLIF was used to determine the effect of variation of the concentration of viscosifying polymer (CMC) on the mixing effectiveness of a fluorescent dye into the bulk fluid. PLIF is a visualisation technique which can be applied to give quantitative information on the shape and the spreading behaviour of the tracer (1 ml of Rhodamine dye) in the SIM. To complement the velocity profiles from PIV in Section 6.2, PLIF gives information on the dispersion of dye in CMC fluids with different concentrations, under the simulated small intestinal process conditions (i.e. using the SIM).

6.3.2 SIM Settings

The SIM has been described in Section 3.7 with the modification made for flow visualisation studies described in Section 6.2.2. The outflow from the SIM was placed in a separate vessel from the inflow. The tubing was always kept below the fluid level in the outflow reservoir to allow for backflow. The experiments used a two cuff set up that had an inflation time of two seconds and deflation time of two seconds and a delay of two seconds. The air pressure used for the inflation was 0.5 barg. The inflation of the cuffs produced segmentation motion as described in Section 2.2.4.2 and the overall flow is as close as possible to the net flow rate found in the small intestine (Guyton, 1996) (i.e. 1 cm/min). This was achieved using a peristaltic pump to give a volumetric flow of 1.2 x 10^{-5} m^3/min (a velocity of 2.3 cm/min), which was again the minimum flow rate of the pump.

6.3.3 Fluids

The fluids used for the experiments were the CMC solutions described in Section 3.4. CMC was chosen as the solutions are clear and thus can be used in flow visualisation techniques and it has similar rheological properties to the guar gum (compare Figures 3.8 and 3.13). Guar gum did not give a visually clear solution and was therefore unsuitable for this technique. CMC solutions were used for these experiments at 0.5, 0.25, 0.1, 0.05 and 0% w/v.

6.3.4 Imaging

The images taken were in the form of a digital picture (as seen in Figure 6.11 (a)) and all the images for each experiment were taken from time 0 (when full injection had taken place) until time 120 seconds, at an image acquisition rate of 5 Hz. This provided 600 images that were analysed for each experiment using the QUIPS software (licensed by Leica) for image analysis and further processing using MATLAB.

The first stage of image analysis was to designate the region of interest (ROI) depicted by the red box in Figure 6.11 and this is shown in the context of the rest of the system in Figure 3.32. The image was analysed for the greyscale range selected as a minimum of 245 and a maximum pixel intensity of 255. The threshold value of the greyscale was chosen to be 245 as this corresponds to the 0.25 g/ml (Figure 3.33) which is half the initial concentration of the dye (which was 0.5 g/ml with a greyscale value of 255). Therefore the software would value the pixels with greyscale values of 255 – 245 as 1, for example, and the 244 - 0 values as 0. The dye was injected immediately upstream of the flow visualisation box (as shown in Figure 3.32).

The calibration of the dye concentration versus the greyscale value is detailed in Section 3.9, Figure 3.33. The parameter being measured during the experiments was the area of the largest feature that corresponded to a concentration greater than half of the original concentration.

For each image taken during the experiment by the QUIPS software, the features that had a greyscale value greater than 245 were identified and an example of these features is shown in blue in Figure 6.11 (b).

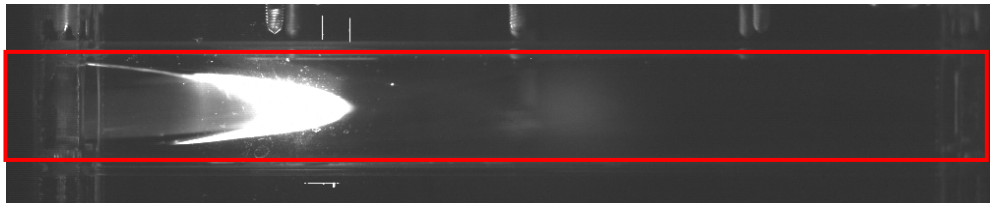

Figure 6.11 (a) An example of an image that was taken for further analysis, showing the region of interest within the red box and the dye is shown in white. The fluid was 0.5% CMC and taken time 0.6 second of the experiment. The fluid was flowing from left to right in the geometry of the picture.

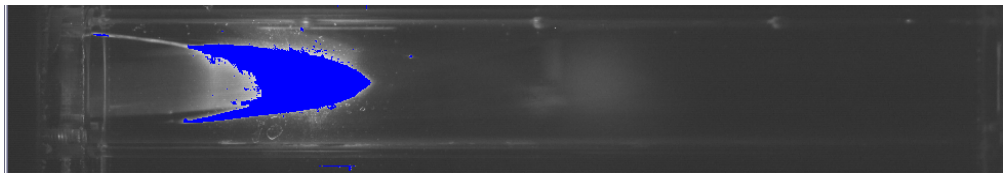

Figure 6.11 (b) A picture of the feature that is measured using QUIPS from the picture shown in Figure 6.11 (b). The blue represents the areas that are of a greyscale 245-255 and of a concentration between 0.5 - 0.25 mg l^{-1}.

6.3.5 Experimental Approach

The experimental approach was to measure the change in area of the feature (0.5 - 0.25 mg l^{-1} in concentration) corresponding to the region of the flow which is half the original concentration or greater.

PLIF has been used to measure and obtain the global averaged mixing time for 95% homogeneity (τ_{95}) (Simmons *et al*., 2004), which is used to quantify the mixing efficiency in changing process systems. However, in this experimental set up, the time taken to achieve the equilibrium concentration would not be a representative measure of the effect of segmentation on mixing as it is an open system (fluid that has the system is not recycled to be the feed fluid in the SIM). Even with a closed system, due to the presence of the peristaltic pump upstream and the buffer tank downstream of the SIM, the time taken for the equilibrium concentration to be achieved would not be a real measure of the effect of segmentation on mixing. The approach of examining the effect that the incorporation of the CMC polymer has on the mixing while being processed under representative physiological conditions using the SIM, was therefore taken by measuring the decay of the dye to less than half of the original concentration. The measurement of the area of dye that is greater than half the original concentration (the feature) over time shows the time dependence of the mixing process between the fluid containing the dye and the fluid without the dye.

Figure 6.12 shows the motion that the SIM goes through over one cycle time of the experiment. Figure 6.13 shows examples of images taken by the camera in the field of measurement through the fluorescence screening filter for the first 5.8 seconds of the 0.5% CMC experiment (i.e. Figure 6.13 (a-d)). Figure 6.15 illustrates the measurements taken in

the experiments; Figure 6.15(a) shows the spread of the dye with diffusion and diffusion and mixing and Figure 6.15(b) shows the movement of the dye into and out the field of view and the resulting cyclical increase and decrease in area.

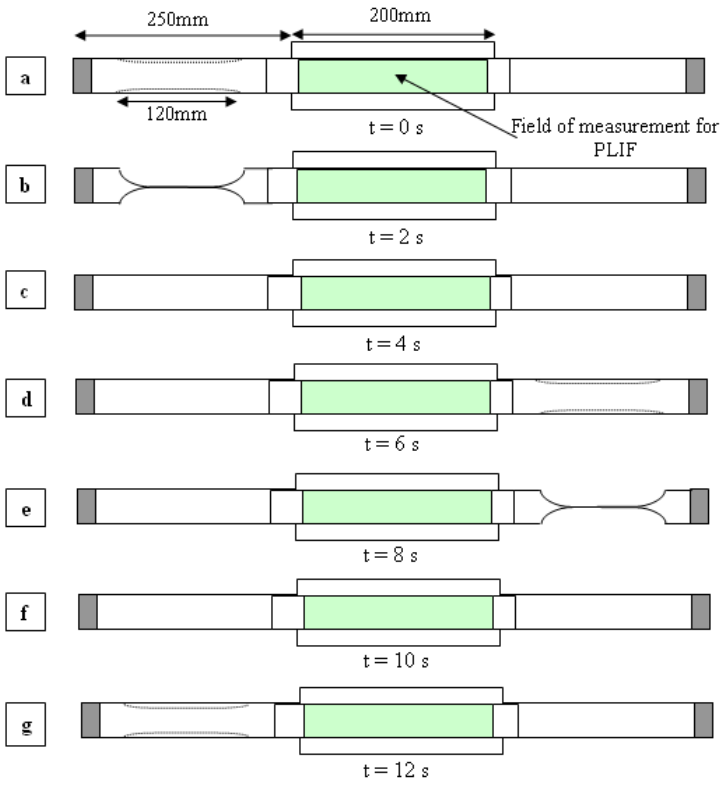

Figure 6.12 (a-g) A figure to show the motion of the SIM during the PLIF experiments at different times in the cycle; the PLIF cycle starts at t=0.

Figure 6.13 is an example of the raw data that is obtained from the PLIF from the start of an experiment (0 -5.8 seconds) when the duration of the experiment is 120 seconds. The times given in Figure 6.13 of 0 to 5.8 seconds correspond to the position of the contraction in the SIM as shown in Figure 6.12 at that particular time. From Figure 6.13 it is possible to observe the forward stretching of the dye-containing fluid between 0 and 2.0 seconds, as well as the retraction of the dye-containing fluid back into the tube between 2.0 and 4.0 seconds once the segmentation motion has ceased. Figure 6.13 shows typical data

generated from PLIF experiments prior to analysis. Having shown images at the start of an experiment in Figure 6.13 as an example, an image at the end of each experiment (time = 120seconds) for each fluid is given in Figure 6.14. Figures 6.13 and 6.14 are examples of the images taken during experiments prior to analysis.

The analysis of each of the 600 pictures taken per experiment was automated using the QUIPS software, to give an output in the form of a text file. This gave the area of the features (between 50-100% of the original concentration) for each image at a given time. The code used to automate the image analysis using QUIPS is given in Appendix 1.

The text files containing the data from the experiment were then read into MATLAB and the area of the largest feature at each time was identified using a programme (Appendix 1). The area of the largest feature area at each time point was normalised with the largest feature area during the experiment and plotted against time using MATLAB. The Figures have been plotted for each of the CMC concentrations 0.5, 0.25, 0.1, 0.05 and water and are shown on Figures 6.16 (a-e).

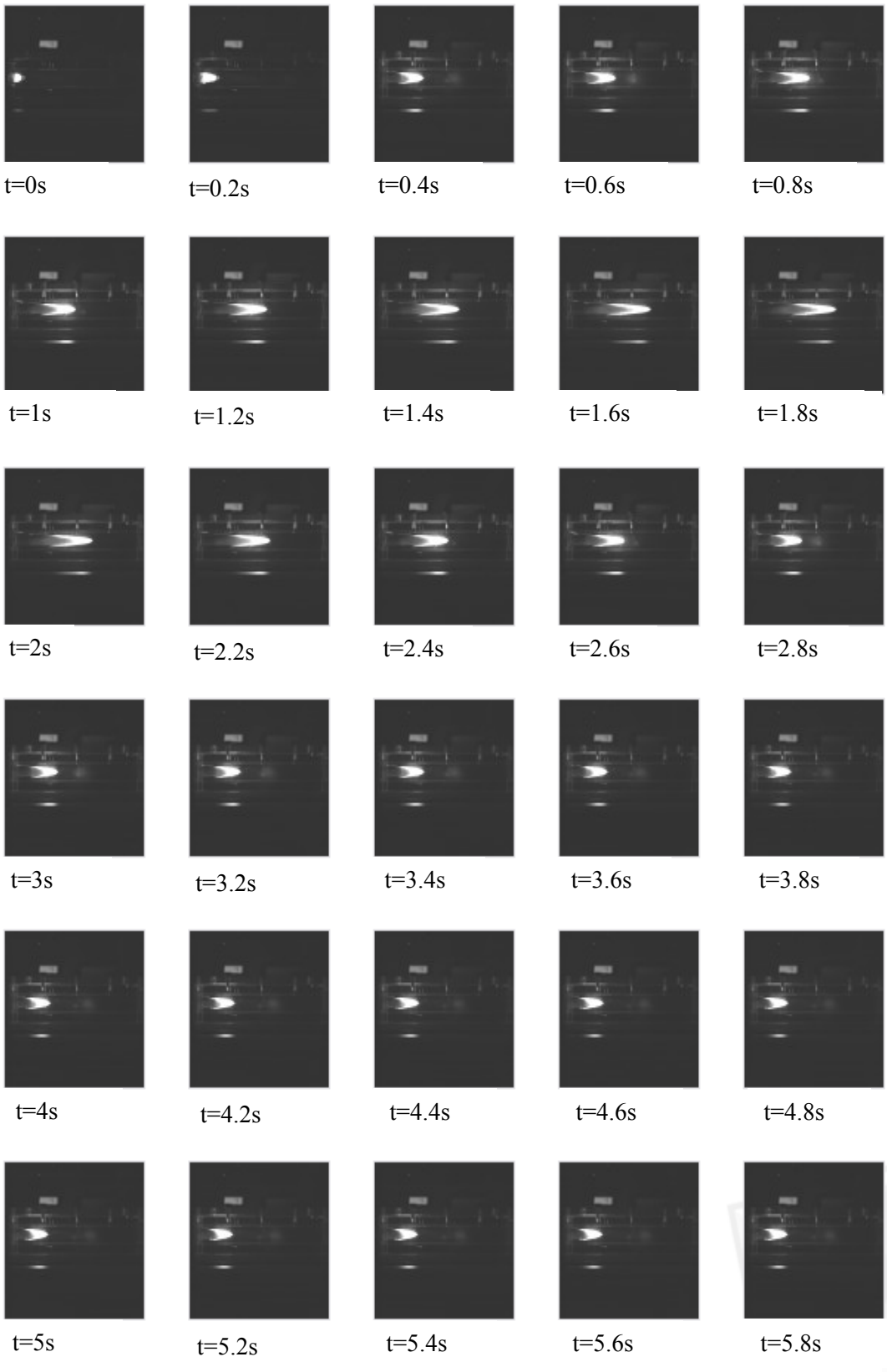

Figure 6.13 Figure showing the digital images taken by the camera at various time sequences, a short exert from an experiment lasting 120 seconds for 0.5% CMC.

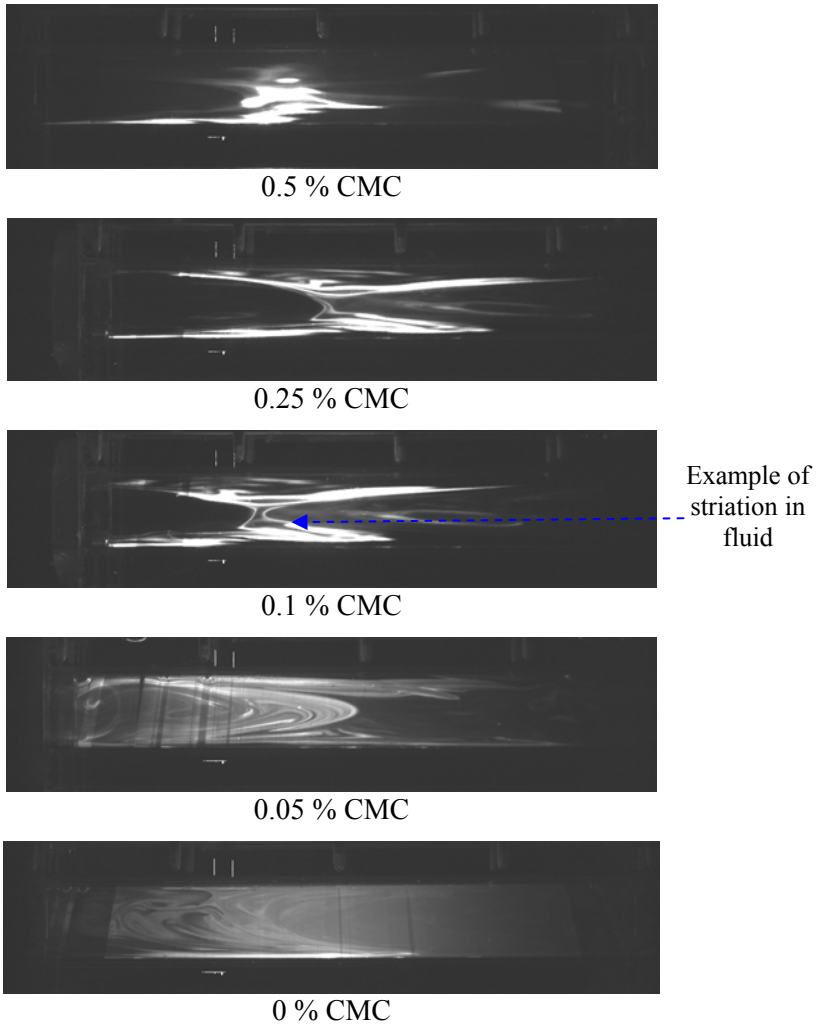

Figure 6.14 Pictures of the visualisation frame at time 120 seconds of the experiment for the fluids 0, 0.05, 0.1, 0.25 and 0.5 % CMC.

6.3.6 Results

Each experiment consisted of 10 cycles of each cuff squeezing and lasted for 120 seconds in total. Due to the dynamic nature of this flow, as seen by velocity vectors in Figure 6.2 (for water), the fluorescent area of interest changes for two reasons:

1. The dye concentration falls below 0.25 mg/l due to the dye diffusion into less concentrated areas. The processing of the fluid causes the stretching of fluid which increases the contact area between fluid with and without the dye and this leads to an increased amount of diffusion. The diffusion of the dye can be represented by Equation 6.4:

$$\lambda = \sqrt{D_m t}$$ Equation 6.4

Where λ is the diffusion length scale (μm), D_m is the molecular diffusivity (μm^2 s^{-1}) and t is the time in seconds (s). Using the diffusion coefficient of the riboflavin measured in Chapter 4 (Table 4.1) of 126 μm^2 s^{-1}, as an estimate of the Rhodamine diffusion coefficient and the time of the experiment as 120 seconds, gives a diffusion length scale of 123 μm (indicating that an increase of 123 μm in the length of the edge to the centre of the oval in Figure 6.15(a) would take place over the course of the experiment.)

2. The fluid moves in and out of the flow visualisation box as the bulk fluid moves forwards and backwards. It is for this reason that the peak normalised areas throughout the experiment are used. This has been described in a diagram in Figure 6.15 and the results from experiments show this in Figures 6.16 (a-e).

The fluorescent area, also called the "feature area" (area with a concentration between 1 and 0.5 times the original dye concentration) for each time point was normalised with the maximum fluorescent area (and maximum feature area) for the experiment. Since the movement of the bulk fluid which had the "feature" as part of it moved out of the flow visualisation box and then back into it cyclically throughout the experiment, the peak value of the normalised feature area for each cycle were chosen. Figures 6.17.(a-e) show the normalised area of the largest feature. The cyclical increase and decrease in the area is due to the "feature" leaving and re-entering the visualisation cell. The reduction in the peak area is due to the enhanced diffusion from mixing.

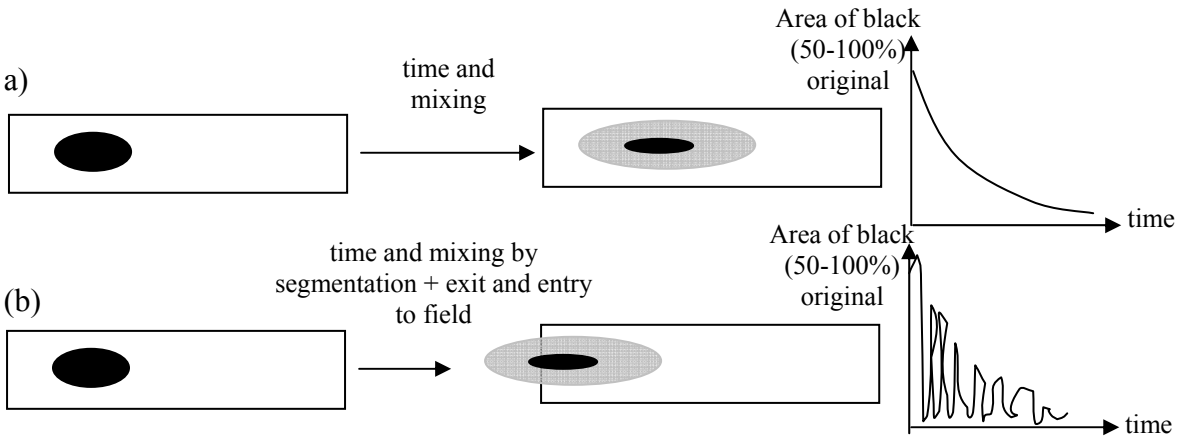

Figure 6.15 A diagram to explain the measurement in the experiment: (a) diffusion and mixing; (b) the movement of the dye into and out of the field of view and the cyclical increase and decrease in the area shown on the graph.

The peak data points for each time series were plotted against time and are shown in Figure 6.17. The data was then fitted to an exponential decay equation given in Equation 6.5 using the SigmaPlot 10 software. The reason for using the exponential decay equation to fit the data was to investigate the possibility of chaotic flow as described by Ottino *et al.* (1990). Ottino (1990) states that one of the manifestations of chaotic mixing is the exponential divergence of initial conditions.

$$y' = a' e^{-b'x'} \qquad \text{Equation 6.5}$$

Where y' is the normalised area, x' is the time and a', b' are the fitted parameters. The results of the fitting are shown in Table 6.3 where b' is the exponential exponent of interest which has been plotted against CMC concentration in Figure 6.18.

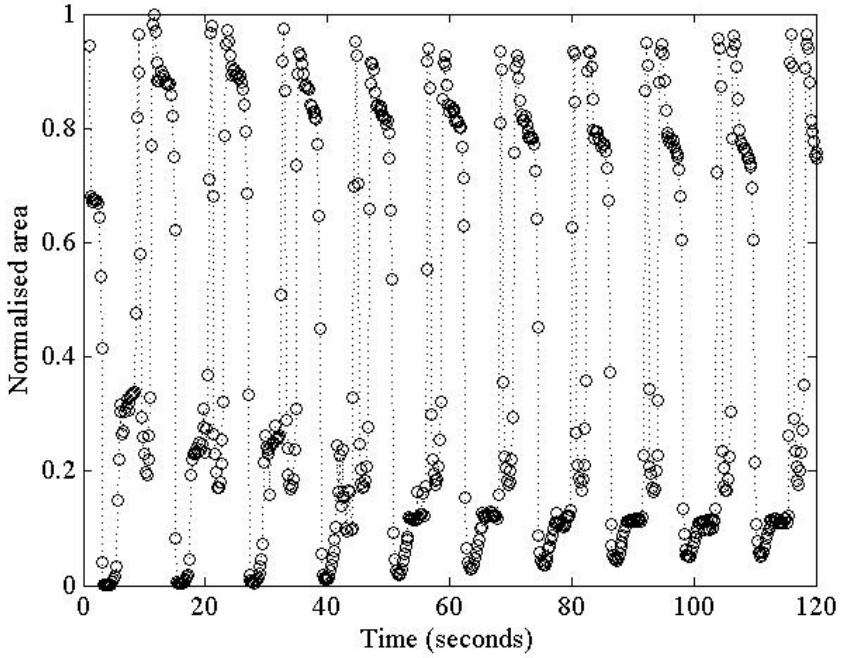

Figure 6.16 (a) The normalised area of the "feature" between 50-100% of the original concentration for 0.5% w/v CMC. The cyclical increase and decrease is due to the exit of the feature and re-entry from the field of view on full squeezing of the SIM.

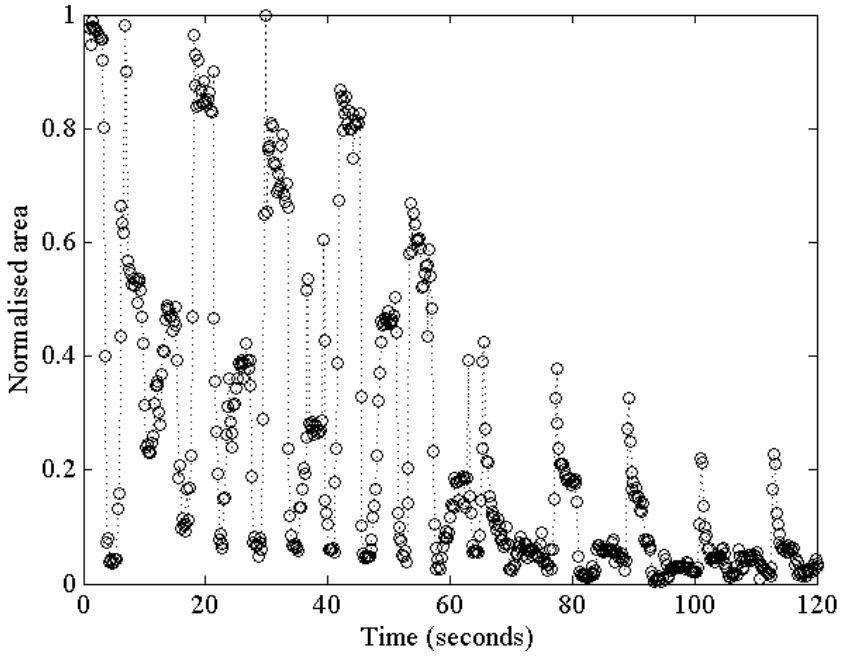

Figure 6.16 (b) The normalised area of the "feature" between 50-100% of the original concentration for 0.25% w/v CMC. The cyclical increase and decrease is due to the exit of the feature and re-entry from the field of view on full squeezing of the SIM. The decrease in the peak values is due to the reduction in the area of the feature with a concentration between 50-100% as a consequence of mixing.

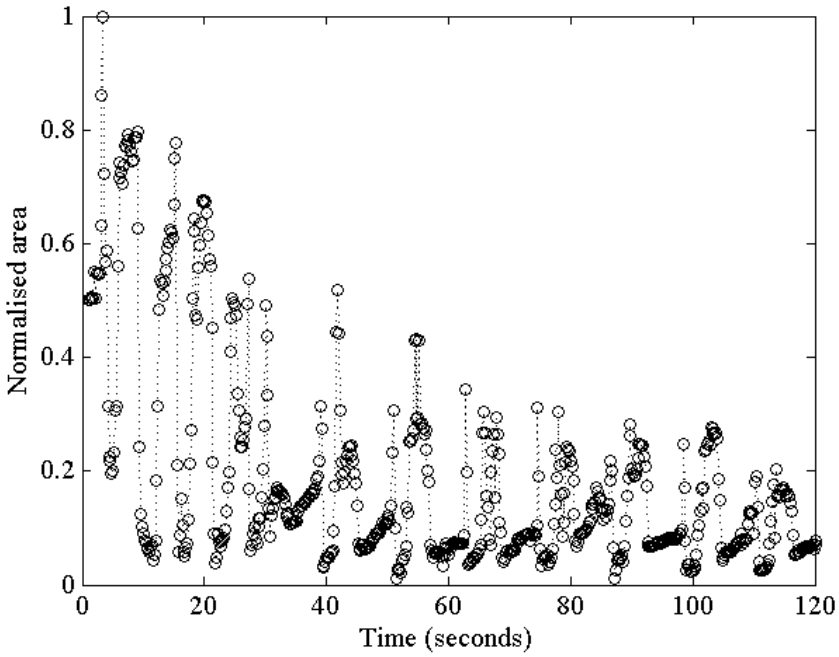

Figure 6.16 (c) The normalised area of the "feature" between 50-100% of the original concentration for 0.1% w/v CMC. The cyclical increase and decrease is due to the exit of the feature and re-entry from the field of view on full squeezing of the SIM. The decrease in the peak values is due to the reduction in the area of the feature with a concentration between 50-100% as a consequence of mixing.

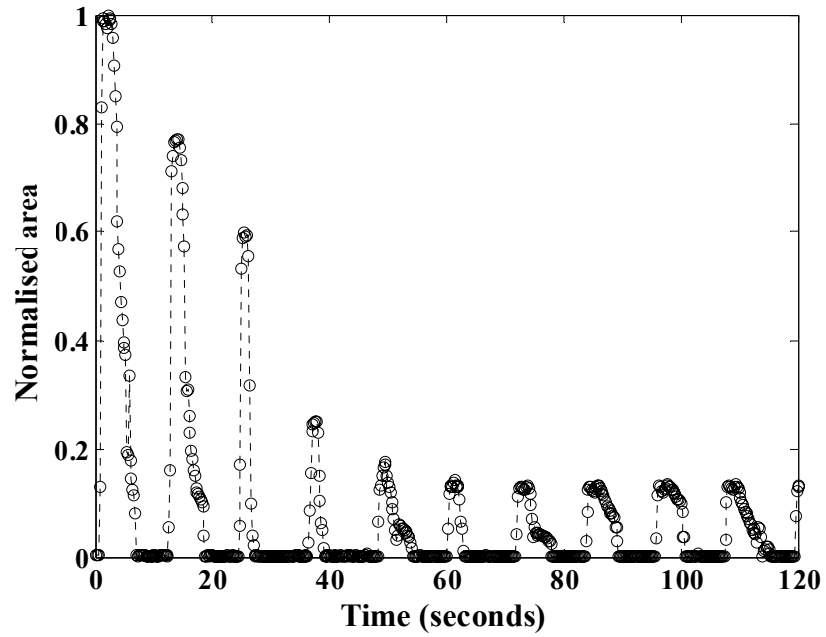

Figure 6.16 (d) The normalised area of the "feature" between 50-100% of the original concentration for 0.01% w/v CMC. The cyclical increase and decrease is due to the exit of the feature and re-entry from the field of view on full squeezing of the SIM. The decrease in the peak values is due to the reduction in the area of the feature with a concentration between 50-100% as a consequence of mixing.

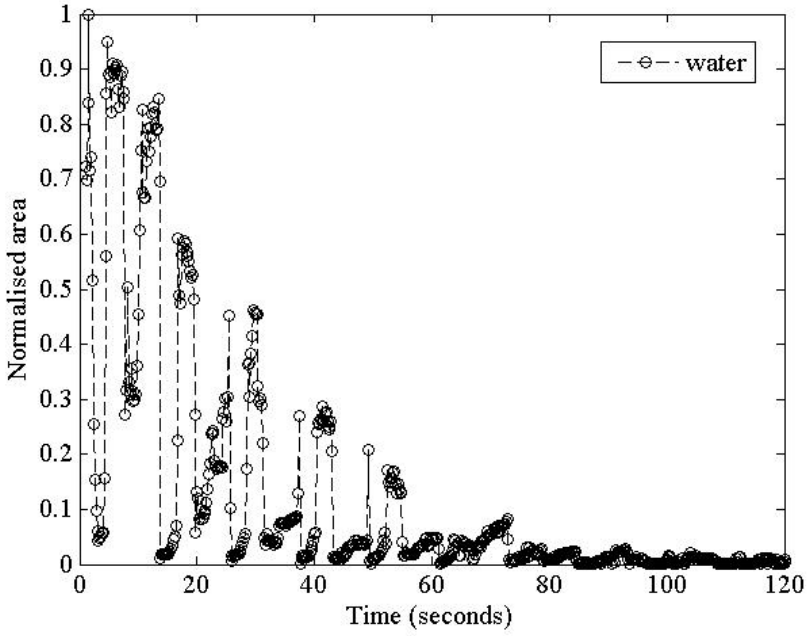

Figure 6.16 (e) The normalised area of the "feature" between 50-100% of the original concentration for water. The cyclical increase and decrease is due to the exit of the feature and re-entry from the field of view on full squeezing of the SIM. The decrease in the peak values is due to the reduction in the area of the feature with a concentration between 50-100% as a consequence of mixing.

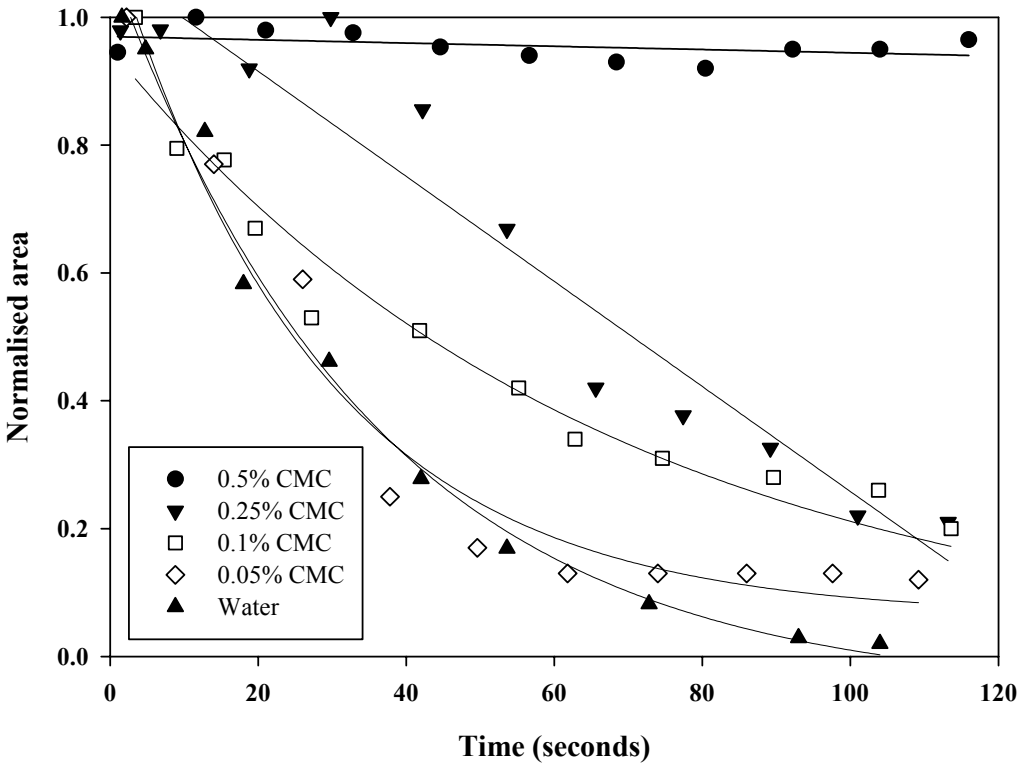

Figure 6.17 A plot of peak normalised values versus time for 0.5%, 0.25% 0.1%, 0 and water over time. (- solid lines represent the fitted exponential equations to the data).

% CMC	a'	b'	r^2	Viscosity Pa.s	Re (segmentation) From Table 6.2
0	1.10	0.032	0.99	0.001	7800
0.05	1.10	0.030	0.95	0.023	390
0.1	0.95	0.015	0.96	0.044	160
0.25	1.13	0.012	0.87	0.106	63
0.5	0.97	0.001	0.18	0.529	8

Table 6.3 Table showing the parameters a' and b' and r^2 for the equation $y = a' \exp(-b' x')$ (Equation 6.5) fitted to the experimental data.

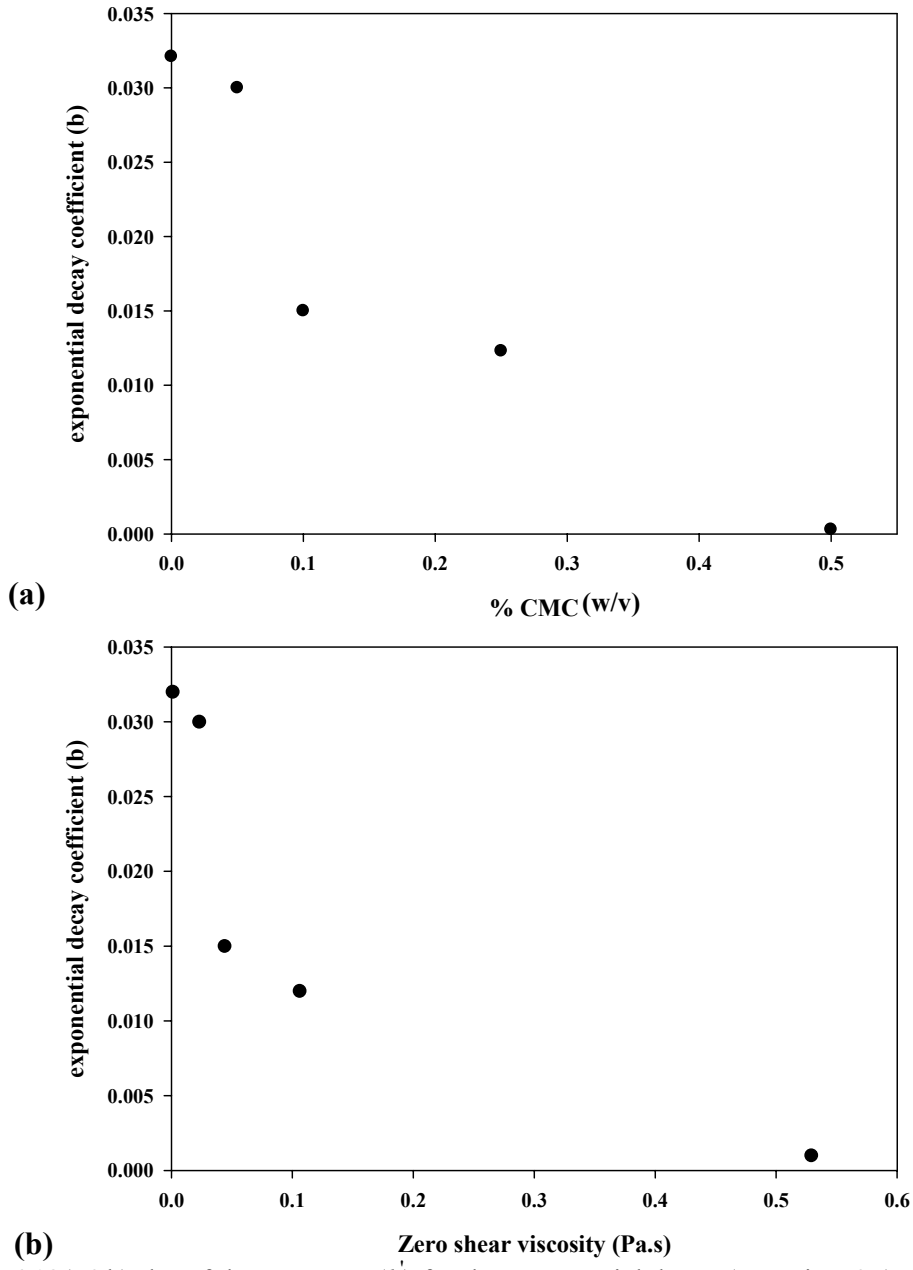

Figure 6.18(a&b)Plot of the exponent (b') for the exponential decay (Equation 6.5)of the feature area for fluids against **(a)** concentration of CMC **(b)** zero shear viscosity (Pa.s).

Plotting the peak values for each cycle has allowed a quantitative measure of the decay in the feature area where the original concentration changed from 0.5 mg/l to 0.25 mg/l. The effectiveness of mixing within the system can be related to the exponential decay coefficient. A high exponential decay coefficient indicates that the size of the area with a high concentration (50-100% of the original dye concentration) reduced fast as a consequence of effective mixing, while a low exponential decay coefficient indicates that the area with a high concentration reduces slowly as a consequence of ineffective mixing.

For low viscosities (concentrations up to 0.1% w/v CMC) the exponential behaviour is clear, and mixing is seen clearly over time. The two highest concentrations have more linear behaviour, and at the highest concentration (0.5% w/v CMC) little mixing is seen.

Figure 6.18 clearly shows that there is a change in the decay profile as the concentration and viscosity of the CMC solution is increased and that the decay takes a longer period of time as the concentration and viscosity of CMC solution is increased. This indicates that the mixing time as the concentration and viscosity of CMC solution is increased the mixing time also increases.

Using the Reynolds numbers established from the PIV experiments in Section 6.2 shows that as the concentration changes from 0.5 to 0 % w/v CMC, the peak Reynolds numbers range from 8 - 7800 as the viscosity changes with varying CMC concentrations (Table 6.2).

Previous work by Alvarez (2002) using the PLIF technique investigated the mechanisms of mixing and creation of structure in laminar stirred tanks. Alvarez (2002) used a 1% CMC solutions as a non-Newtonian model fluid and Rhodamine G as a fluorescent dye and states that no exchange of material other than by diffusion was possible between the chaotic and regular regions (Alvarez *et al*., 2002).

The existence of the striations in the dye at the end of the experiment (time = 120 seconds) seen in Figure 6.14 is characteristic of a predominantly laminar mixing process (Ottino, 1989) and is also seen in the modelling of Howes and Mackley (1991). The reason for striations being characteristic of laminar mixing is that eddy diffusion would eliminate them in turbulent flow. Since Ottino (1990) states that one of the manifestations of chaotic mixing is the exponential divergence of initial conditions, the data has been fitted to the exponential decay equation (Equation 6.5) and some good fits to this equation are seen in Figure 6.18.

The results from the PLIF fitting to the exponential equation are shown in Figure 6.18 which shows that the exponent of the exponential decay decreases by a factor of 100 from 0.032 to 0.0003 as the concentration of CMC increases from 0 to 0.5%. This indicates that the mixing in the 0.5% CMC solution is very poor and that over the 120 second period there was very little dilution in the dye concentration by mixing mechanisms. At lower concentrations of CMC the mixing parameter (the exponent of the exponential decay) increases, showing improved mixing. This indicates that the incorporation of polymeric material into food formulations can be used to control mixing in the small intestine.

The use of the PLIF technique combined with the SIM has allowed the effect of incorporating the viscosity increasing polymer CMC on the mixing effectiveness of the process conditions within the small intestines to be studied. The reduction in the area that has a concentration of between 50-100% of the original dye concentration indicates the amount of mixing that has taken place. The reduction of the area (between 50-100% of the original concentration) has been fitted to an exponential decay function (Equation 6.5), that quantifies the rate of the decay of the area and hence quantifies the mixing effectiveness of the system. Results have shown that as the concentration of CMC increases from 0 to 0.5% the exponential decay coefficient decreases from 0.032 to 0.0003, indicating less effective mixing as the concentration of CMC increases.

Mixing is an important function of the small intestine where food digestion takes place due to enzyme-to-food substrate interaction. This work has indicated that the rate of digestion could be controlled by influencing the mixing of enzymes introduced into the small intestine. Also, the mixing would influence the dispersion and dissolution of controlled release actives within the intestine.

6.3.7 PLIF Conclusions

The use of PLIF and the measurement of decay of the area which is greater than 50% of the original dye concentration is an effective measure of mixing effectiveness. The results obtained have allowed for the conclusion to be drawn that the addition of CMC at low concentrations (0.5% w/v) greatly impairs laminar mixing (from Reynolds numbers of 8 at peak velocity given in Table 6.2) within the SIM and concentrations of 0.1 w/v half the exponential decay coefficient. This understanding could be used to aid the design of food formulations that intend to influence enzyme - substrate mixing, molecular delivery, or containing encapsulated particles where dispersion and dissolution are relevant.

6.4 Computational Fluid Dynamics Model (CFD) of the SIM

6.4.1 Introduction

The computational modelling of the physical processes that take place within the small intestine is the focus of this section. Previous work has shown that the incorporation of certain ingredients such as guar gum into food that passes through the intestine have an influence on the rate of glucose absorption and cause a reduction in postprandial hyperglycaemia (Ellis *et al.,* 2000).

The use of Magnetic Resonance Imaging (MRI) of food within the stomach has revealed important process parameters for example the grinding forces in the antrum are of the order of 0.6 N (Marciani *et al*., 2001). MRI images of the stomach have also been used to develop computational models of the stomach (Pal *et al.,* 2004). The technique of imaging foods in the small intestine may be possible in the future and will give valuable data for creating computational models upon availability of the data.

Jeffery *et al.* (2003) modelled the flow fields generated by peristaltic reflex in isolated guinea pig ileum by using a numerical method to solve for the flow generated by the moving walls using visual parameters for the wall movements that had been previously published. The findings were that downstream and reverse flow regimes were present as well as vortical flow patterns (as seen in Figure 2.19.b) that redistributed particles and mixed liquids. The wall movements generated pressures and shear stresses, particularly along the moving section of the wall. Their analysis showed that contractions produce not only laminar flow, but also downstream and reverse flow as well as vortical flow patterns likely to promote digestion and absorption (Jeffery *et al*., 2003).

The computational model developed as part of this work is based on simulating the SIM described in detail in Chapter 3. The primary reason for basing the computational model on the physical model was that experimental data exists for the model system. The understanding that has been developed over the course of this body of work extends from the influence of the guar gum on diffusion (Chapter 4), modelling of the effect that guar gum has on molecular delivery and starch digestion within the SIM (Chapter 5) and also experimental fluid dynamics within the SIM (Sections 6.2 and 6.3). By modelling the SIM computationally it has been possible to compare the data from the SIM experiments with the CFD results for validation purposes.

Since the experimental fluid dynamic techniques within the SIM (Sections 6.2 and 6.3) could not investigate the fluid dynamics in the deforming segment as the deformation of the wall would interfere with the technique a computational approach was adopted to investigate this area.

The computational model development was also intended to be a step towards being able to rapidly predict the influence that a change in food formulation would have on molecular delivery and also further the understanding of the process.

6.4.2 Development of the CFD Model of the SIM

The CFD model that has been developed replicates closely the segmentation motion that occurs in the small intestine and that is simulated by the SIM. The CFD pre-processing software GAMBIT 2 was used to construct the geometry and FLUENT 6.2.16 was used for

processing and post-processing of the model. The method of CFD has been described in Section 3.10.

The length of the section modelled was 0.25 m with a radius of 0.015m. The mesh was constructed as a 2-D axisymetric problem (having symmetry around the axis shown in yellow in Figure 6.19). The mesh consists of 682 triangular cells and 700 quadrilateral cells as seen in Figure 6.19.

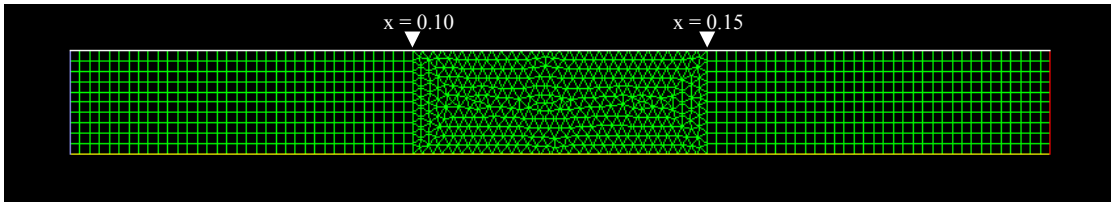

Figure 6.19 A picture of the mesh used for the FLUENT model, the axis is shown in yellow on the base.

6.4.3 Model Set-up and Processing

The model was set up in two parts, (i) the static part and (ii) the dynamic part:

(i) The static part consisted of defining the model for the solver, the materials, the operating conditions and boundary conditions. The solver type used was the segregated option, the formulation was implicit, the time was unsteady, the velocity formulation was absolute, the unsteady formulation was 1st-order implicit and the gradient option was cell-based. The material properties used for the fluids were water and 0.05, 0.1, 0.25, 0.5% carboxymethyl cellulose (CMC) and the material properties used were those measured in Chapter 3 (Table 3.3). The fluids are modelled as non-Newtonian power law fluids as described by Equation 3.6. The boundary conditions were set to give an overall flow

resulting in an Reynolds number of 10, using an inlet mass flow of 7.84 x 10^{-4} kg/s with a uniform velocity profile at the inlet. The outlet (red line in Figure 6.19) was a pressure outlet to atmospheric pressure.

(ii) The dynamic part consisted of the movement of the middle section of the wall which was prescribed using a User Defined Function (UDF) given in Appendix 1. As the wall moves, the mesh that the wall is moving into becomes distorted and therefore updates to an acceptable quality mesh again. This was done by using the dynamic mesh parameters 'smoothing' and 'remeshing' (FLUENT, 2005). For smoothing, the Spring Constant Factor used was 0.3, boundary node relaxation 1, convergence tolerance 0.001 and number of iterations 1. For remeshing, the size function and 'must improve skewness' options were used with the settings of 0.004 as the minimum length scale, 0.0128 as maximum length scale, maximum cell skewness of 0.65, a size remeshing interval of 1, size function resolution of 3, size function variation of 0.5 and a size function rate of 0.99. The motion of the wall was controlled by a User Defined Function (UDF) and is described in Section 6.6.4 as sin function. The wall movement was not modelled to force fit the CFD data to the PIV data.

The control of the solution used the following settings, under relaxation factors: pressure at 0.3, density of 1, body forces of 1, momentum of 0.7. The pressure-velocity coupling solution setting used was 'simple' and the discrimination settings were pressure as 'standard' and momentum as 'second order upwind'. A convergence criteria was assigned of 0.0001, x-continuity, y-continuity and momentum.

The solutions were carried out using the computing facilities at Birmingham University on the Central Applications Service, CAPPS (cluster of 6 dual processor HP J6700 workstations running at 750 MHz utilising the Hewlett Packard HP-UX operating system).

6.4.4 Mesh Motion

The motion was controlled by a User Defined Function (UDF) where the midpoint was controlled by the function described in the UDF and is a sin function. The points on either side were prescribed by the function given in UDF and is also a *sin* function. These functions give the overall UDF shown in Appendix 1 and is written in C code. The movement of the wall can be seen in Figure 6.20 and the location of the movement between x=0.10 and x=0.15 can be related to the mesh shown in Figure 6.19. The wall returns to the original flat position along the same path as seen in Figure 6.20. The moving mesh deformed by the movement of the wall is shown in Figure 6.21, depicting the movement of the wall as time progresses from 0.5 seconds to 4.0 seconds with 0.5 second intervals. This wall motion is however not an exact model of the wall motion profile of the PIV experiments but is an approximation of the physical system.

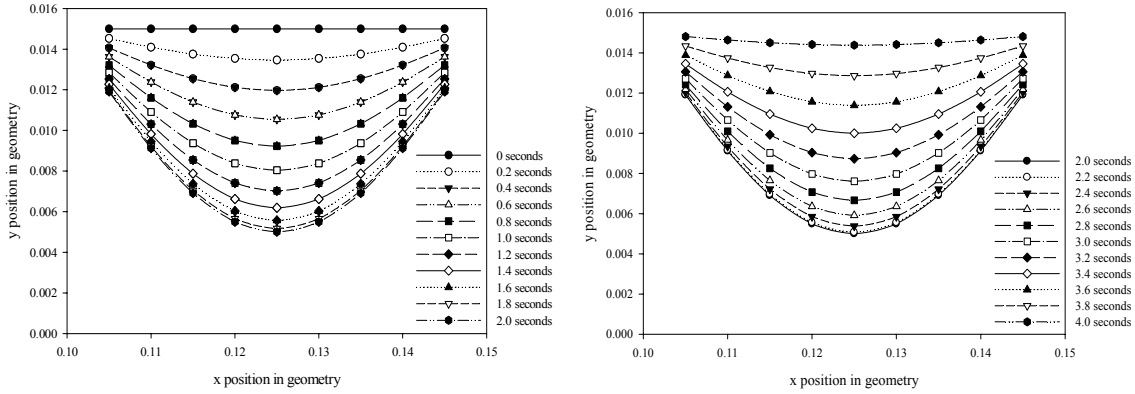

Figure 6.20 A plot of the movement of the wall of the mesh with time, left plot shows the downward motion, right plot shows the upward recovery.

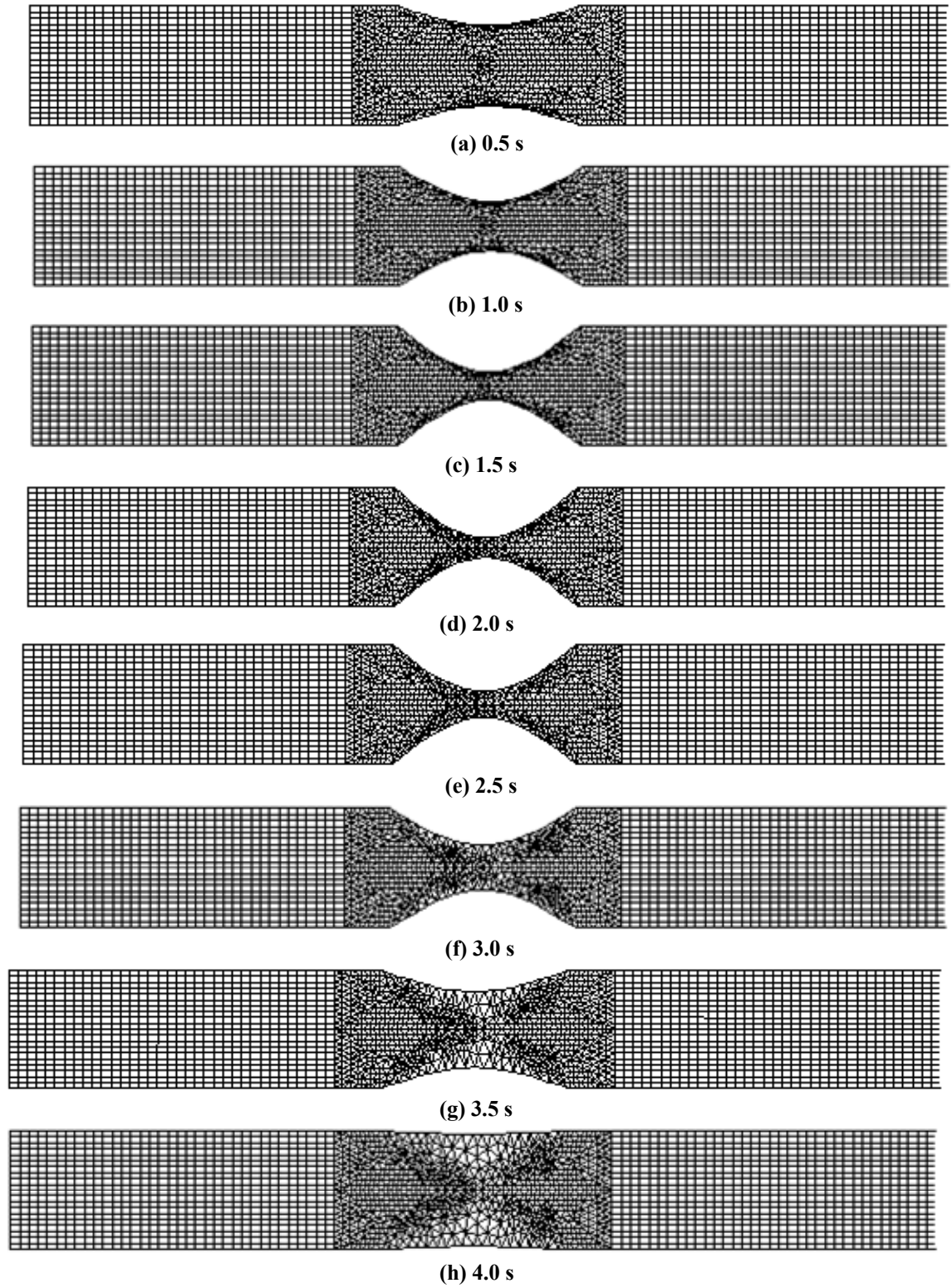

Figure 6.21(a-h)Figures of the mesh at sequential time points (a) 0.5 s, (b) 1.0 s, (c) 1.5 s, (d) 2.0 s, (e) 2.5 s, (f) 3.0 s, (g) 3.5 s, (h) 4.0 s showing the motion of the wall and the reorientation of the mesh. The wall moves in the sequence shown in Figure 6.21.

6.4.5 Results

Simulations were undertaken for water, 0.05, 0.1, 0.25, and 0.5 % CMC and the material properties used were those measured in Chapter 3 (Table 3.3). The fluids were modelled as non-Newtonian power law fluids as described by Equation 3.6 and with the fluid properties given in Table 3.3. The boundary conditions used for the inlet were to give an overall net flow resulting in a Reynolds number of 10, using an inlet mass flow of 7.84×10^{-4} kg/s with a uniform velocity profile at the inlet. The outlet (red line in Figure 6.19) was a pressure outlet to atmospheric pressure.

A plot of the velocity at the midpoint of the geometry (x:0.125, y:0) is shown against time in Figure 6.22. Figure 6.22 shows the increase and decrease of the midpoint velocity over the four seconds.

Contour plots of the velocity are shown in Figure 6.23 for water for the times 0.5, 1.0, 1.5, 2.0, 2.5, 3.0, 3.5 and 4.0 seconds. Figure 6.23 shows the change in the velocity over the geometry as the time changes and the wall motion takes place. The colour gradient shows the velocity contours for the solution. The velocity contour plots show the areas in which significant changes in velocity are occurring for a given time frame. The boundary conditions used were such that there was a constant inlet mass flow and the exit was a pressure outlet to atmospheric pressure, hence when the wall moved inward there was not a symmetrical displacement of fluid to both sides.

Velocity vector plots show the direction and magnitude of the flow at a given point in the geometry and are presented for water in Figure 6.24 for time 1 s (where ‘a’ is an overall

view and ‘b’ a close up), time 2 s (where ‘c’ is and overall view and ‘d’ a close up), time 3 s (where ‘e’ is an overall view and ‘f’ a close up) and time 4 s (where ‘g’ is an overall view and ‘h’ a close up). Figure 6.24.b shows that at time 1 second there are no recirculation flow patterns. As the segmentation motion continues there is the appearance of recirculation flow pattern as seen in Figure 6.24.d at time 2 seconds. The recirculation continues as shown in Figure 6.24.e and Figure 6.24.f at time 3 seconds and is then followed by full reverse flow at time 4 seconds, as shown in Figure 6.24.g and Figure 6.24.h.

As discussed by Jeffery *et al.* (2003) the mixing of liquids and redistribution of particles is critically dependent on the occurrence of vortical flow patterns, due to changes in flow direction. This has been shown in Figure 6.24 as part of these studies are for water, the same fluid as modelled by Jeffery *et al.* (2003). The vortices are transient in nature and disappear over time as seen between Figure 6.24 (g) and Figure 6.24 (h), where the vortices are replaced with complete reverse flow.

A comparison of the velocity vectors adjacent to the moving wall at time 2 seconds (maximum segmentation depth) between the five fluids is shown in Figure 6.25. Vortex flow is only present in Figure 6.25.a and b, the fluids containing 0% and 0.05% guar; all fluids greater than 0.05% in concentration of guar cease to show vortices, due to the increase in viscosity of the fluid. This therefore shows that the incorporation of concentrations of 0.1% viscosifying polymer (CMC) and greater has the effect of mitigating the vortices by increasing the resistance to flow.

Figure 6.26 (a-h) shows the shear profile of water over the period of the segmentation motion. Figure 6.26.e shows that at the time 2.5 seconds there is largest change in the shear seen. The change in the shear rates is seen to be in the region of segmentation.

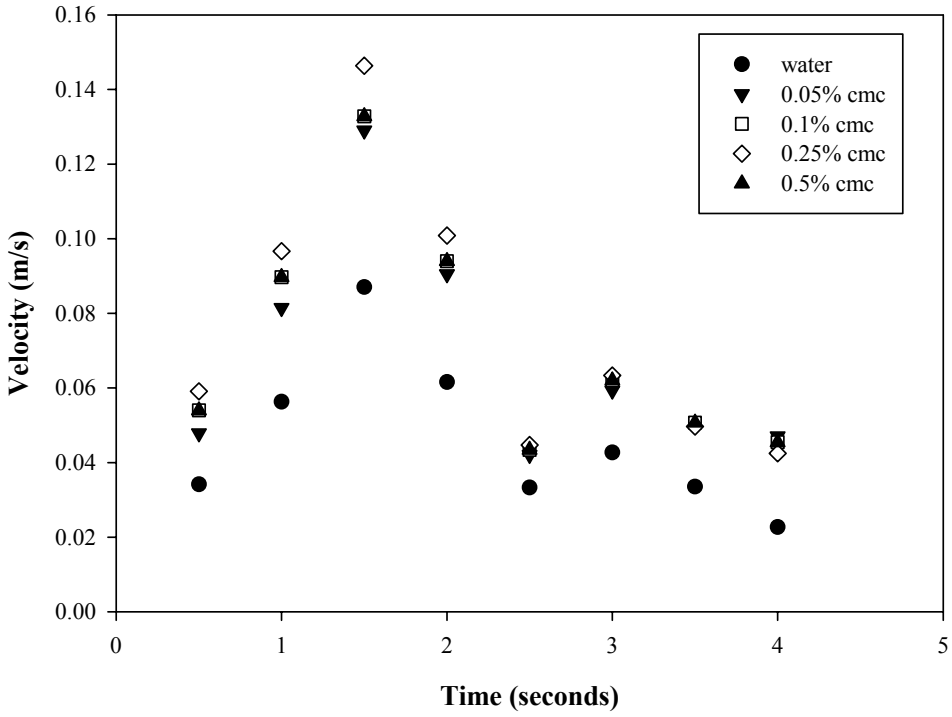

Figure 6.22 Plot of the velocity at the centre point of the mesh (x:0.125, y:0) against time.

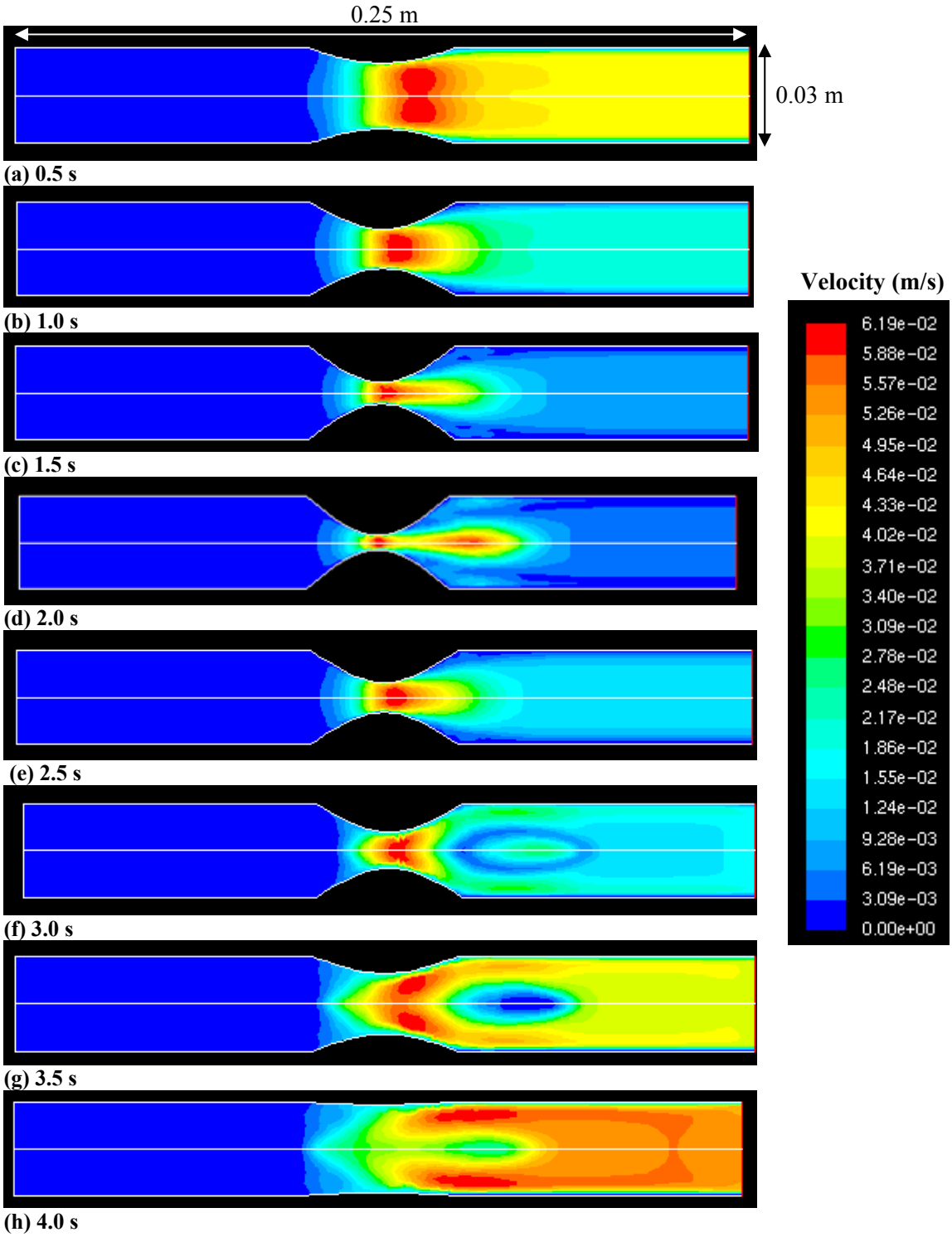

Figure 6.23 (a-h)Figures of the modelled velocity contours for water at sequential time points (a) 0.5 s, (b) 1.0 s, (c) 1.5 s, (d) 2.0 s, (e) 2.5 s, (f) 3.0 s, (g) 3.5 s and (h) 4.0. Scale is in m/s.

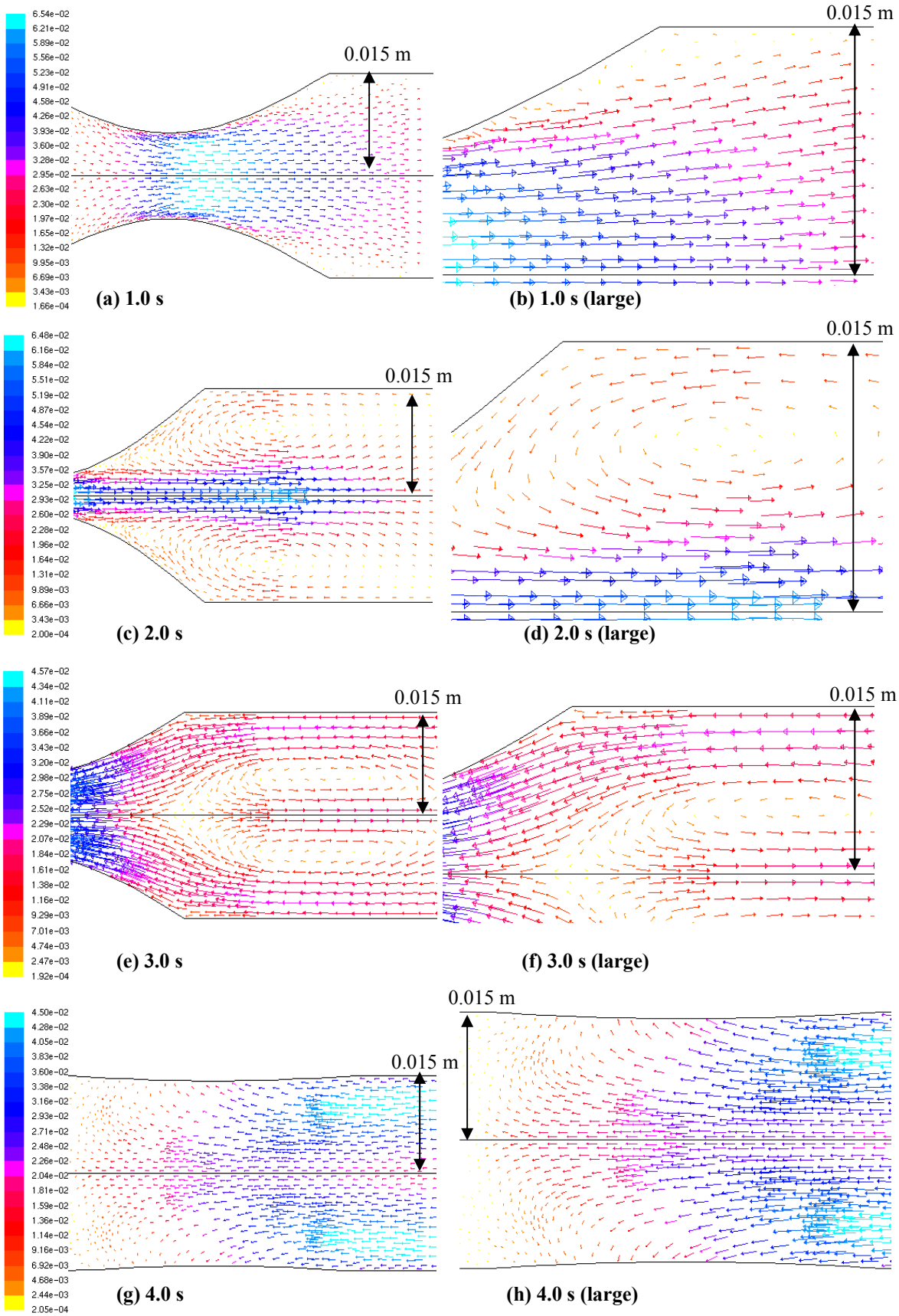

Figure 6.24 (a-h)Figures of the modelled velocity vectors for water at time 1 s (a & b), time 2 s (c & d), 3 s (e & f), 4 s (g & h). Scale is in m/s.

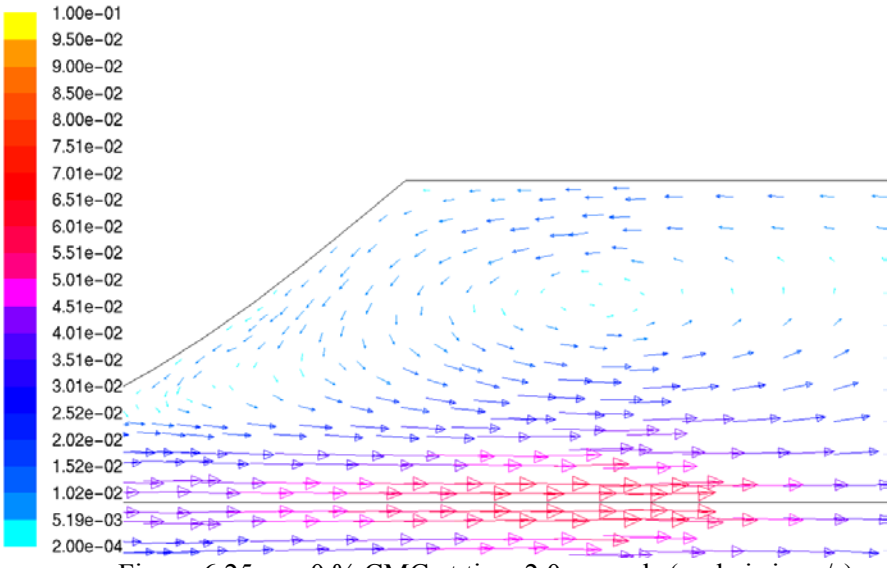

Figure 6.25.a 0 % CMC at time 2.0 seconds (scale is in m/s).

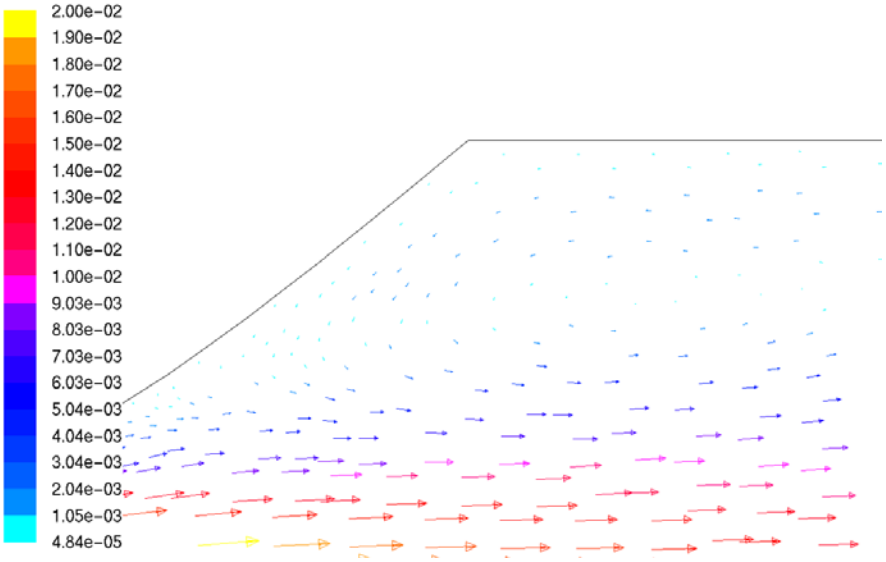

Figure 6.25.b 0.05 % CMC at time 2.0 seconds (scale is in m/s).

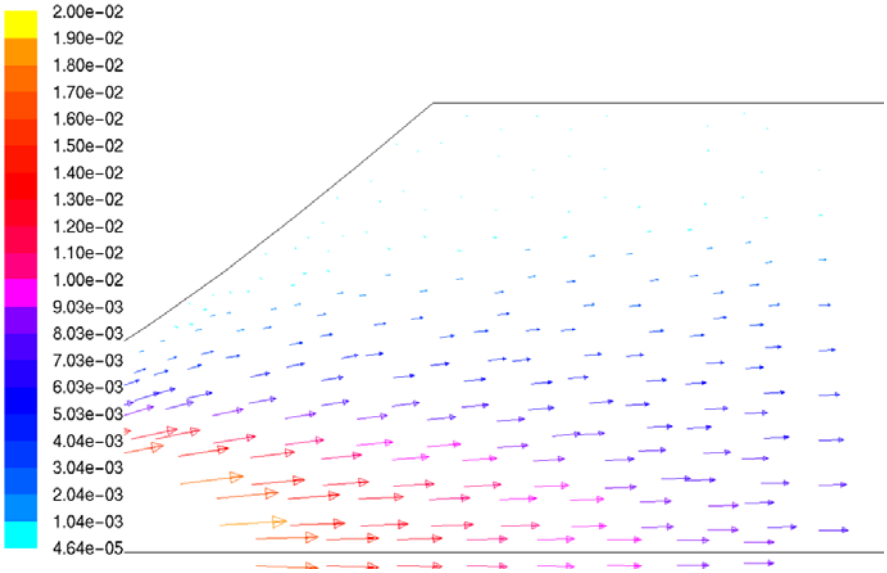

Figure 6.25.c 0.1 % CMC at time 2.0 seconds (scale is in m/s).

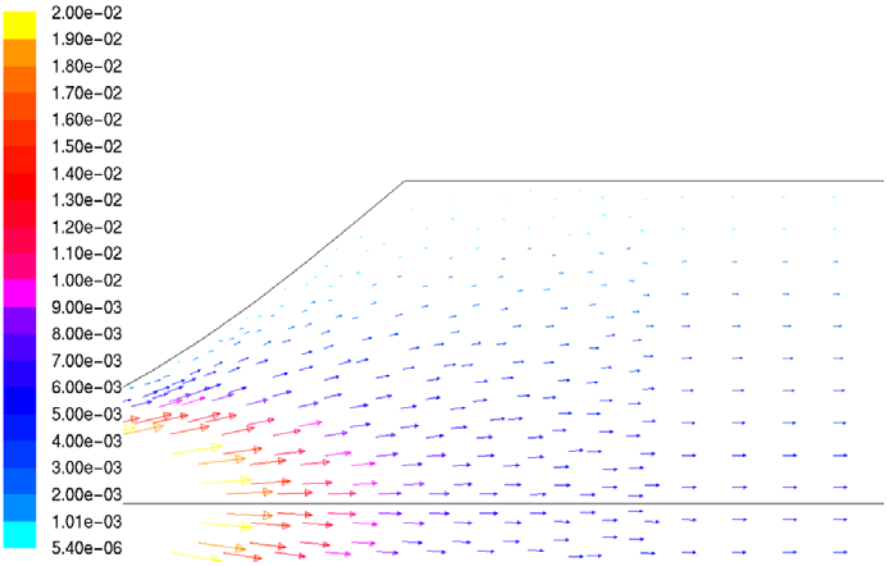

Figure 6.25.d 0.25 % CMC at time 2.0 seconds (scale is in m/s).

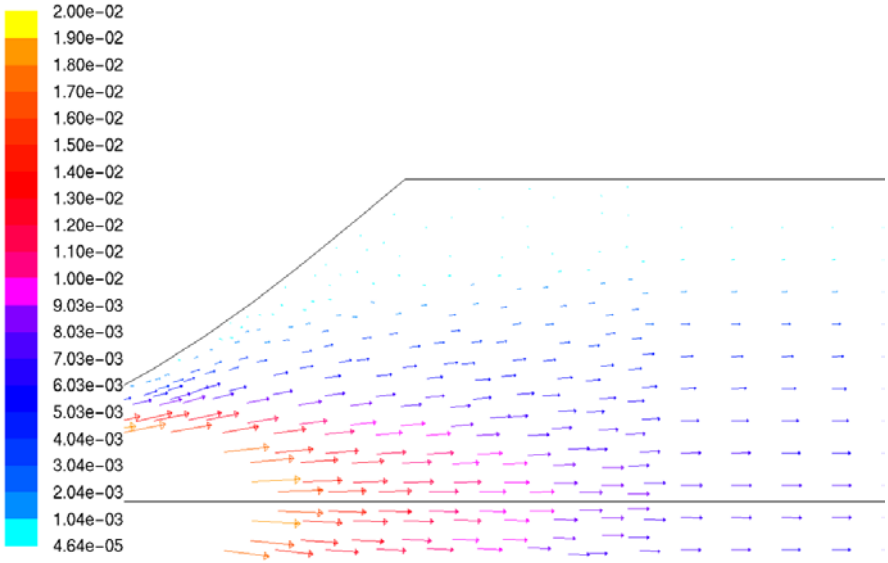

Figure 6.25.e 0.5 % CMC at time 2.0 seconds (scale is in m/s).

Figure 6.25 (a-e)Comparison of the velocity vectors adjacent to the moving wall at time 2 seconds (maximum segmentation depth) between the five fluids (0, 0.05, 0.1, 0.25, 0.5% CMC).

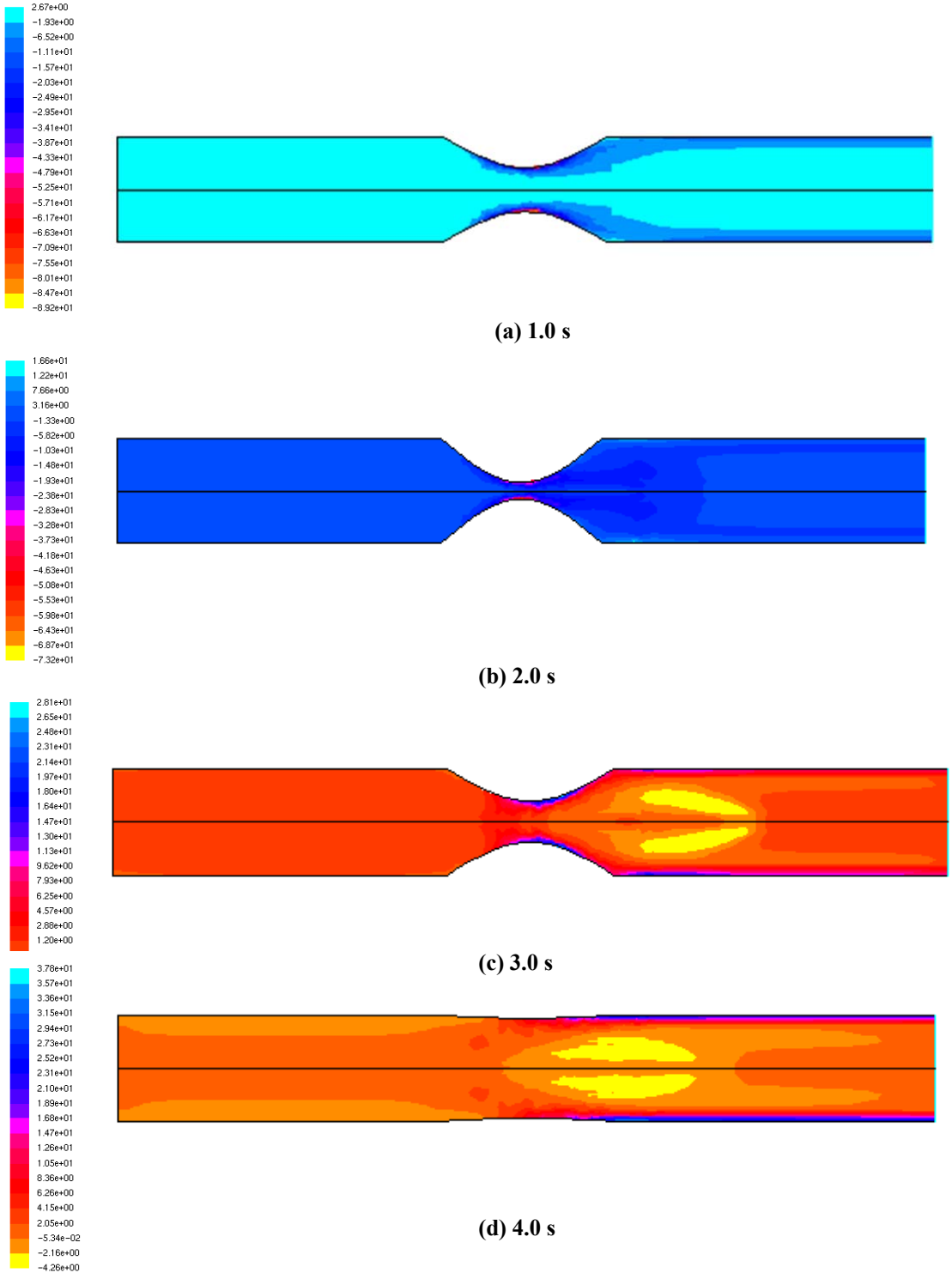

Figure 6.26 (a-d)Figures of the shear profile (1/s) for water at sequential time points (a) 1.0 s, (b) 2.0 s, (c) 3.0 s and (d) 4.0 s (scale is in s^{-1}).

A comparison between the flow velocities at the midpoint of the flow visualisation cell (at point P in Figure 6.3) and the theoretical flow velocities from the CFD model (x:0.125, y:0 in Figure 6.19) has been plotted in Figure 6.27 for a series of different times (CFD times taken as in Figure 6.21 corresponding to PIV times for the same condition as in Figure 6.1). The peak velocity flow profiles (i.e. at the maximum squeeze position in Figure 6.1.b and Figure 6.21.d) at the exit at time 2.0 seconds are shown in Figures 6.28.a-e for the five fluids (0, 0.05, 0.1, 0.25 and 0.5% CMC) in their normalised form, with the average flow velocity from the volumetric flow rate. Each plot has been shown with the velocity profile modelled using FLUENT, the theoretical velocity profile for fully developed flow for the power law fluid (Equation 6.2) and for 0% CMC. The profile measured using the particle image velocimetry (PIV) technique in Section 6.2 has been included for comparison.

Figure 6.27 shows (i) good agreement in the shapes of the simulated and measured curves and, (ii) differences in the magnitudes however arise across the range. The differences in magnitude will result both from measurement error from the fact that the compression in the SIM will not be the idealised shape assumed using the CFD model. It can be noted from Figure 6.27 that the CFD tends to under predict the peak velocity during the squeeze cycle. An explanation of this is that the CFD assumes an idealised wall movement that displaces the fluid steadily over the 2 second period; while in practice in the SIM this would not necessarily be the case. It would be useful to quantify the shape of the squeezed profile, but the results seem similar. Figure 6.28 shows excellent agreement between the measured and calculated profiles at the peak velocity when the velocity profiles are normalised. The difference between the experiment, CFD and theoretical (steady-state) velocity can clearly be seen to decrease as the viscosity increases.

The peak velocity profiles modelled using the computational model compared with the experimentally determined profiles from PIV, showed that the measured profiles are similar to the computationally determined profile expected (Figures 6.28 (a-e)). The transient flow profiles determined as a result of the segmentation motion are different to the theoretical velocity profiles for fully developed flow for the given fluid properties. The difference between the transient flow profiles measured and predicted (using FLUENT), to the theoretical fully developed flow velocity profile, reduces as the amount of CMC in the solution increases.

The peak Reynolds number has been plotted against the viscosity of the fluid in Figure 6.29 which were determined from both computational modelling (using FLUENT) and the PIV measurements (Section 6.2). There is good agreement in the trends seen in the values between those simulated and measured. However, there are differences in the magnitude of the values which is once again will result from measurement error and from the fact that the compression of the SIM will not be the idealised shape assumed by the CFD model.

The peak shear rates have been plotted against the viscosity of the fluid for the five fluids modelled in the process and also their results from the PIV experiments (Section 6.2). The results shown in Figure 6.30 indicate that there is good correlation between the peak shear rates predicted (using FLUENT) and those measured using PIV in Section 6.2.

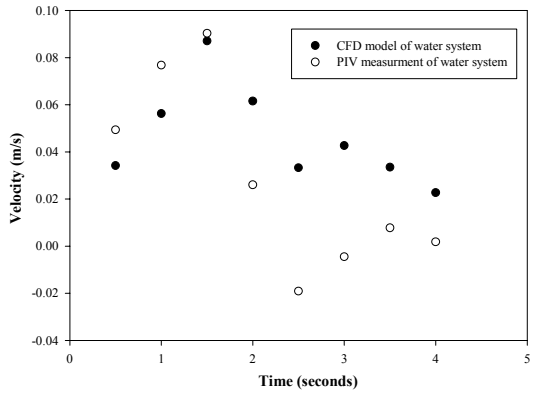

(a) 0 % CMC

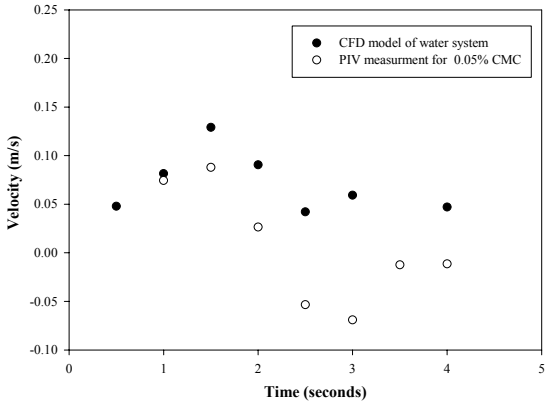

(b) 0.05 % CMC

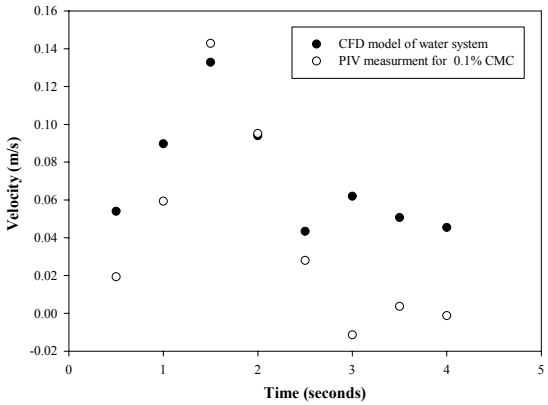

(c) 0.1 % CMC

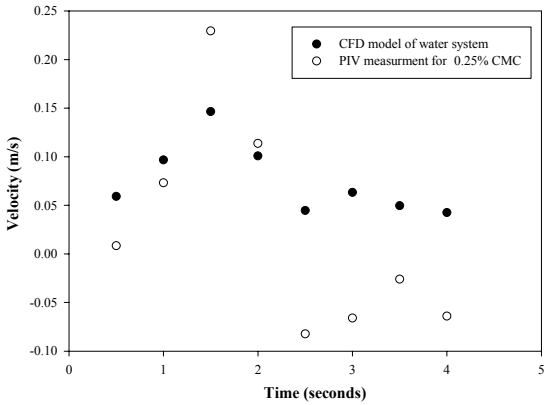

(d) 0.25 % CMC

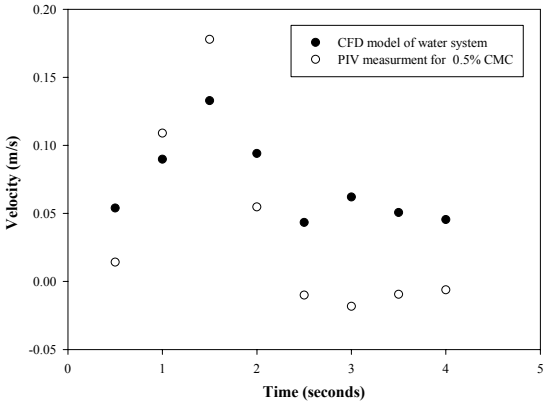

(e) 0.5 % CMC

Figure 6.27(a-e)A series of axial velocity plots (at point P in Figure 6.3 and x:0.125, y:0 for the CFD mesh in Figure 6.19) for five different fluids: (a) water, (b) 0.05% CMC, (c) 0.1% CMC, (d) 0.25% CMC, (e) 0.5% CMC. Each plot shows the axial velocity at the midpoint modelled using FLUENT and measured using the PIV technique in Section 6.2.

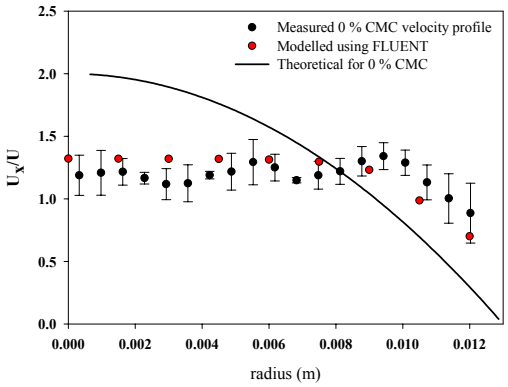

(a) 0 % CMC

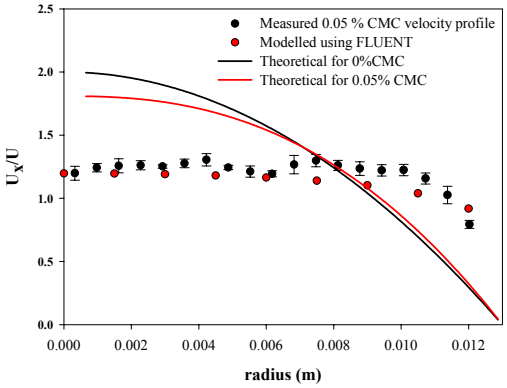

(b) 0.05 % CMC

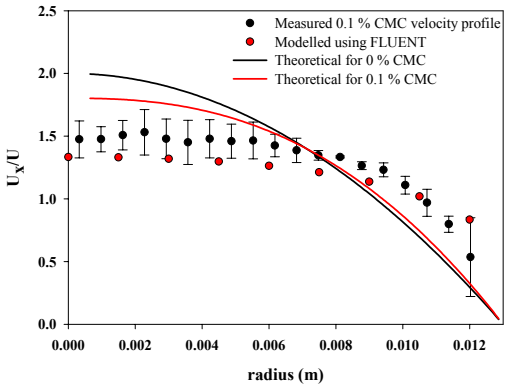

(c) 0.1 % CMC

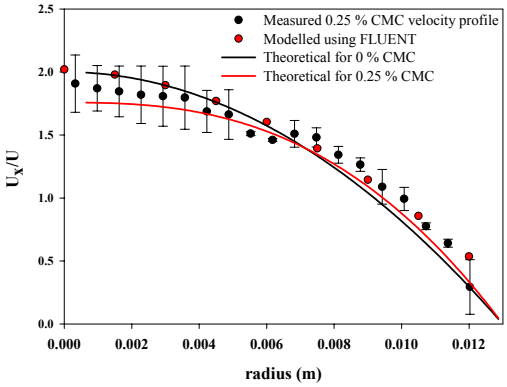

(d) 0.25 % CMC

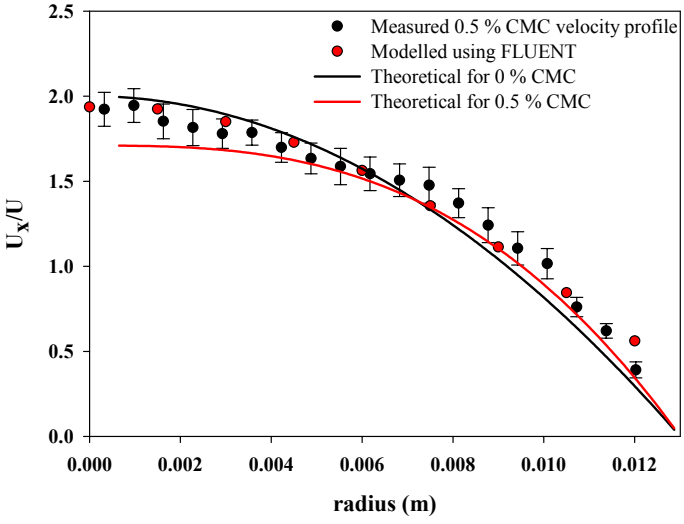

(e) 0.5 % CMC

Figure 6.28(a-e)A series of velocity profile plots for five different fluids: (a) water, (b) 0.05% CMC, (c) 0.1% CMC, (d) 0.25% CMC, (e) 0.5% CMC. Each plot shows the velocity profile modelled using FLUENT, the theoretical velocity profile for fully developed flow for the power law fluid (Equation 6.2) and for 0% CMC, and the profile measured using the PIV technique in Chapter 6.

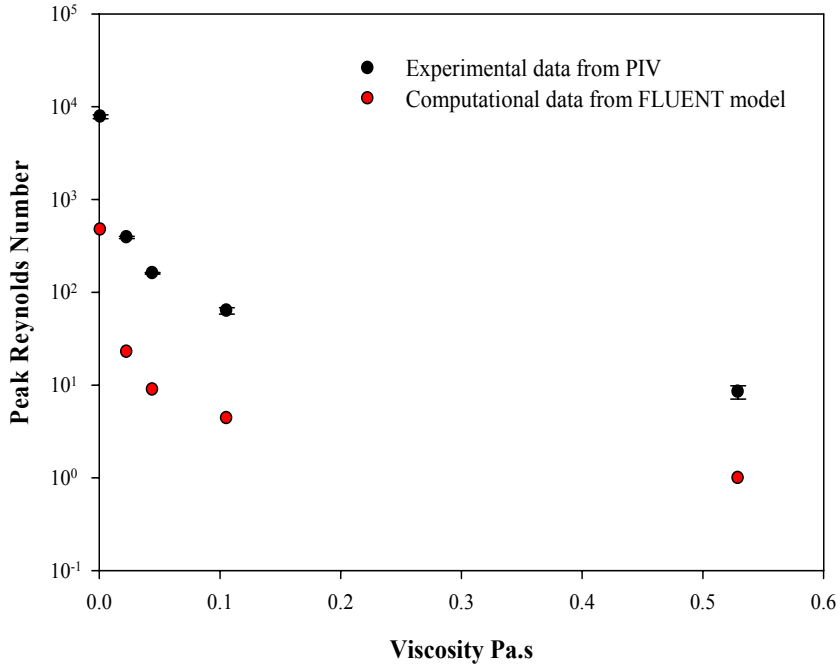

Figure 6.29 Plot of Peak Reynolds number versus viscosity for both the experimental values from PIV studies (Section 6.2) and the theoretical data from the FLUENT model.

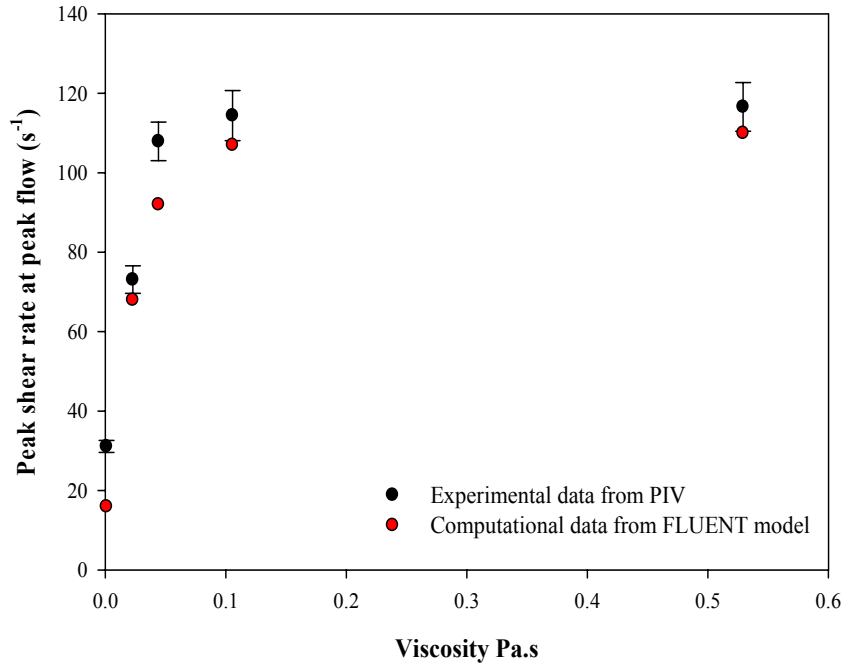

Figure 6.30 Plot of peak shear rate versus viscosity for both the experimental values from PIV studies (Section 6.2) and the theoretical data from the FLUENT model.

6.4.6 Conclusions

The purpose of the computational modelling was to model the flow profiles that would be expected in the region of segmentation, since this was not possible experimentally due to the movement of the wall distorting the measurement technique.

The CFD model has been shown to predict: the axial velocities at the midpoint of visualisation cell over time, velocity profiles at the peak velocity and the peak shear rates as compared to those determined using experimental fluid dynamics techniques. This gives confidence into the calculated velocity vectors in the deforming region determined using the CFD model.

The CFD model shows that vortex flows can form in some formulations of the model food, with the viscosifying polymer CMC that was used to represent guar gum (shown in Figures 2.25 a-e). This suggests that under some situations vortex flows can form in the GI tract. This reduction in vortical flow patterns would be expected to reduce the surface renewal at the membrane and thus reduce the overall mass transfer coefficient as seen in previous SIM experiments (Chapter 5).

The design of this model of the small intestine to predict the fluid dynamics in the small intestine using a computational method and based on an experimental model (Chapter 5), is the first step towards modelling of complex food structures being processed in the small intestine and their influence on nutrient delivery.

6.5 Overall Conclusions

The fluid dynamics within the SIM have been the area of interest of this chapter. The PIV experiments investigated the fluid dynamics from the segmentation in the small intestine and the effect that the incorporation of CMC had on this. By using this technique, it has been possible to determine that the radial velocity component is negligible compared to axial velocity upstream and downstream of the segmentation contraction in SIM and would be expected to be the case within the small intestine also. The peak shear rates measured in the SIM give an indication of the shear rates expected in the actual human small intestine and were found to increase from 31 to 117 s^{-1} as the concentration of CMC was increased from 0 to 0.5% CMC. The PIV technique has been shown to be a practical and viable method for studying the effect that structuring food formulations with biopolymers has on the fluid dynamics in the SIM.

PLIF has been used to show that the addition of CMC at low concentrations (0.5% w/v) greatly impairs mixing within the SIM (which models the time dependant process conditions seen in the small intestine). This is a realistic fluid model of a structured food/beverage formulation that has been studied within a realistic process model of the small intestine and has shown significant effects on mixing within the system. This understanding is important for the design of food formulations that could potentially alter enzyme - substrate mixing and molecular delivery, and also for formulations that contain encapsulated particles where dispersion and dissolution are relevant. Since the Rhodamine was dissolved within a CMC solution prior to injection this gives an insight into mixing within the luminal flow of a polymer containing beverage.

Although the pH and ionic strength of the environment in the small intestine has not been modelled within the SIM as part of these experimental fluid dynamics studies; an understanding has been developed of the significance that segmentation has on mixing within the lumen of the small intestine and also the effect that rheology modifying food ingredients such as CMC can have on these processes.

Since it was not possible to experimentally investigate the fluid dynamics in the deforming region of the segmentation action, due to the laser light distortion from the wall movement, computational fluid dynamics was used to investigate this further. The CFD model predicts the velocity profiles and shear rates that were determined using the experimental fluid dynamics techniques, thus partially validating the model and giving further confidence in the calculated velocity vectors in the deforming region. The CFD model showed a reduction in vortical flow while using fluid properties of CMC solution of 0.1% w/v and greater. The flow profiles of the fluid in the GI tract can be predicted from this result. Reduction in vortical flow patterns that develop and disappear would reduce the surface renewal at the membrane and lead to a reduction in the overall mass transfer coefficient which has been seen in previous SIM experiments (Chapter 5). Therefore the CFD model developed has shown to predict results comparable to those measured from experimental fluid dynamics techniques using the SIM. More complete agreement would be expected if the experimental segmentation profile of the tube were controlled more accurately.

CHAPTER 7 - CONCLUSIONS AND FUTURE WORK

This thesis has described work which attempts to understand the chemical engineering processes that occur within the small intestine. The processes of fluid flow of molecular delivery, mixing and enzyme – substrate reactions have been investigated with the aid of physical and computational models developed as part of this work. The context of the work has been to understand the influence that food ingredients such as guar gum may have on the processes that occur in the small intestine. This has been carried out to improve the design of foods that are intended to control molecular delivery of nutrients or actives in the small intestine. All the work as part of this thesis has this underlying theme as the basis of investigation, from the diffusion studies work at the μm length scale to the fluid dynamics work at the cm length scale. The conclusions from this work are given in Section 7.1 and recommendations for future work are described in Section 7.2.

7.1 Main Conclusions

7.1.1 Development of a Physical Model of the Small Intestine

This work has shown the development of an *in-vitro* small intestinal model that is capable of mimicking the segmentation motion that is thought to be responsible for the majority of the mixing that takes place within the small intestine. The model was designed, and has demonstrated capability in determining, the concentration of a nutrient or active on the inner wall of a moving membrane which represents the inner wall of the small intestine. This allows for the molecular delivery to the intestinal wall to be evaluated for different product formulations while simulating the physical processing conditions of the small intestine.

7.1.2 Development of the Computational Model

The development of the computational model using the commercially available software FLUENT has been a step towards modelling of complex food structures being processed in the small intestine and their influence of nutrient delivery. This model has given an insight into the fluid dynamics in the region of deformation from the segmentation motion.

7.1.3 Influence of Guar Gum on Delivery and Digestion Within the Small Intestine

The influence of guar gum on diffusion using fluorescence recovery after photobleaching (FRAP) showed that guar gum had no effect on the riboflavin diffusion coefficient. Using a range of guar gum types at the same concentration with varying viscosities showed that guar gum had no effect on the riboflavin diffusion coefficient. Further FRAP studies using a fluorescently labelled dextran that was a larger molecule than riboflavin, concluded that there was a hindering of diffusion through the biopolymer network above a certain concentration of guar gum.

Using the diffusion cell experiments it was possible to conclude that there is no permanent binding of the riboflavin to the guar gum. Studies into fouling of the membrane showed that the reduction in the concentration versus time profile that had been seen during experiments was not caused by a fouling mechanism.

The Sherwood number versus Reynolds number plot for the diffusion cell experiments showed that the enhancement of the mass transfer on the biopolymer side to the maximum point was reached as mixing increased. The diffusion cell gives an understanding of the effect that the ingredient has on the molecular delivery to the membrane surface, from

which the molecular delivery to intestinal wall can be further understood (although representative fluid dynamics to those found in the small intestine are not included in the diffusion cell model). The advantage of the diffusion cell model is that it can be used for screening large numbers of ingredients prior to more detailed studies using the SIM (which more accurately represents the fluid dynamics seen in the human small intestine).

Experiments using the SIM have shown the significant effect that the segmentation motion has on nutrient delivery to the intestinal wall as a consequence of changes in the mass transfer coefficient on the biopolymer side mass transfer coefficient. This is due to the increased mixing that occurs which has been shown using experimental fluid dynamics. The SIM experiments have shown that the addition of guar gum reduced the mass transfer enhancement to the membrane generated by the segmentation motion. This shows that in the physiological situation the guar gum would reduce the mass transfer to the membrane i.e. the wall of the intestine and therefore potentially reduce the postprandial hyperglycaemia of the guar containing food.

Starch digestion experiments concluded that guar gum reduces the rate of starch digestion by reducing diffusion of the enzyme within the fluid. Absorption experiments showed that guar gum reduced the delivery of glucose to the membrane for both squeezed and non-squeezed conditions.

7.1.4 Conclusions from Experimental and Computational Fluid Dynamics of the SIM

The conclusion from the first experimental fluid dynamics technique particle image velocimetry (PIV) used with the SIM, was that the radial velocity component is very small

relative to the axial velocity at the mid-point between two squeezing sections. The volumetric flow at peak axial velocity as a result of the segmentation action, decreases as the viscosity of the fluid is increased. Using the PIV technique, the shear profile downstream of a segmentation contraction was determined and the maximum shear rate was shown to change from 31 to 117 s^{-1} as the concentration of CMC was increased from 0 to 0.5%.

The main conclusion from the second experimental fluid dynamics technique planar laser induced fluorescence (PLIF) is that the addition of CMC at low concentrations (0.5% w/v) greatly impairs mixing within the SIM. This understanding is important for the design of food formulations intended to alter enzyme - substrate mixing or molecular delivery. This is also important information for formulations that contain encapsulated particles where dispersion and dissolution are relevant.

The fluid dynamics in the deforming region of the segmentation action was inaccessible to experimental fluid dynamics techniques due to laser light distortion from the wall movement. This was partially overcome by the development of the computational fluid dynamics of the SIM. The computational model developed of the SIM has been shown to predict velocity profiles, peak Reynolds numbers and shear rates, comparable to those measured from experimental fluid dynamics techniques.

The computational model showed that there is a reduction in transient vortical flow due to the formulation of the model food with the viscosifying polymer CMC at 0.1% w/v and

above. The CMC was used to represent guar gum which has previously been shown to reduce postprandial hyperglycaemia (Blackburn *et al.*, 1984).

7.1.5 Conclusions Relevant to Food Digesta

The conclusions that are relevant to food digesta have been listed below:

- Investigation into the influence of guar gum on diffusion through a model digesta, using FRAP showed that guar gum had no effect on the riboflavin diffusion coefficient.

- Further FRAP studies showed that the diffusion of larger dextran molecules through a model digesta was hindered by guar gum.

- The diffusion cell model can be used to screen the influence of large numbers of ingredients on model digesta.

- Experiments using the SIM have shown that the segmentation motion has a significant effect on nutrient delivery to the intestinal wall. This has been shown to be due to increased mixing, using experimental fluid dynamics.

- The SIM experiments have shown that the addition of guar gum to a model digesta reduced the mass transfer enhancement to the membrane generated by the segmentation motion.

- Starch digestion experiments concluded that guar gum reduces the rate of starch digestion in the digesta by reducing diffusion of the enzyme within the fluid. Absorption studies as part of the starch digestion experiments showed that guar gum reduced the delivery of glucose to the membrane for both squeezed and non-squeezed conditions.

- Using the experimental fluid dynamics technique PLIF has shown that the addition of CMC at low concentrations (0.5% w/v) greatly impairs mixing of a model digesta within the SIM. This is of particular relevance to the design of food formulations intended to alter enzyme – substrate mixing or molecular delivery.

- The computational model showed that there is a reduction in transient vortical flow directly adjacent to the segmentation region due to formulation of the model food with the viscosifying polymer CMC at 0.1% w/v and above.

- Agreement between experimental and computational fluid dynamics was good but would be improved by more accurate representation of the squeezing motion in the CFD code.

7.2 Future Work

To gain a more complete understanding of the processes that foods go through in the small intestine and the influence that food formulation has on digestion and absorption, further work is still required. The future work could potentially be in five areas:

i. investigations into other formulations;

ii. further development of the small intestinal model (SIM);

iii. further development of the computational model; and

iv. collaborative research work with other research groups in the area of gastrointestinal modelling and food design.

v. Model validation

7.2.1 Investigations into Other Food Formulations

There is extensive potential to use the techniques developed as part of this body of work in the future for the study of other formulated food systems. The studies carried out as part of this work used relatively simple model food systems to investigate the influence on biopolymer incorporation into foods on molecular delivery. In the future, the SIM could be used to study the controlled delivery of ingredients that have been encapsulated in food matrices such as gelled networks, or in novel emulsions. Further investigations using enzyme substrate interactions would be of value.

7.2.2 Further Development of the Small Intestinal Model (SIM)

There is potential for further development of the SIM. One option is that the number of segmentation points could be increased from the current set up where two squeezes take place to four (for example). This would involve attaching two further cuffs that induce the segmentation motion and the length of the membrane segment could be increased also to

accommodate further segmentation points. The addition of pH and ionic concentration control of the fluid within the SIM would be a good additional feature for the study into the effects of ionic polymers within the small intestine.

The use of the experimental fluid dynamics technique PLIF in conjunction with the SIM demonstrated in this thesis could be further developed to measure and investigate the change in striation thickness from chaotic mixing in the SIM as a function of time.

7.2.3 Further Development of the Computational Model

The computational model could be developed further in a number of ways: (i) the geometry could be modified further to include a second segmentation motion; (ii) the segmentation motion itself could be manipulated to give different motions and for a longer time sequence; (iii) the properties of the fluid and the model set up could be enhanced to include diffusion, reaction of species and multiphase flow. With the power of the CFD techniques and the initial validation conducted as part of this work, there is large potential for future work in this area. Also as further information on the processing of food in the small intestine emerges it may be possible to use MRI images to construct more realistic geometries and prescribe actual motion for the small intestine in a similar way to the work by Pal *et al*. 2004 for the modelling of the stomach.

7.2.4 Collaborative Research Work with Other Research in the Area of Gastrointestinal Modelling and Food Design

This research work has built models for the GI tract; models currently exist of various other sections of the intestine such as the IFR model of the stomach and the model of the human large intestine developed by Spratt *et al.* (2005). There would be great value in

collaborative research work with these groups, with many of the studies having the same ultimate aim to commercialise the knowledge and modelling capability for novel food and pharmaceutical formulation design and development. Careful negotiation would however be required in the collaborative research vision where the protection of the intellectual property generated will allow for a robust technology platform that could be commercialised. At an industrial level, an understanding of digestion from a fluid mechanical / engineering standpoint would enable much better understanding of how digestion is affected by these flows, and what contribution this makes to the whole digestive process.

Along with potential collaboration opportunities between research groups looking at different areas of the gastrointestinal tract, the potential also exists for interdisciplinary research between Food Technologists, Medical Professionals, Nutritionists and Engineers to further develop the understanding in this field of study.

7.2.5 Model validation

A significant part of the future work required is the validation of the experimental and computational models against a human. The most likely method of this is with the use of MRI techniques which are beginning to be applied to the small intestine (Hoad *et al*., 2007) study the processing of foods. This is an essential step in the SIM's development to add further benefit in understanding food behaviour in humans in relation to health.

APPENDIX 1

Code (C programme) used for User Defined Function in CFD for segmentation action

```
#include "udf.h"

DEFINE_GRID_MOTION(peristalsis_simple,domain,dt,time,dtime)
{
 Thread *tf = DT_THREAD(dt);
 face_t f;
 Node *v;

 real Y0=0.015;
 real dY=2.5e-3;
 real omega=0.77;
 real Xmin=0.1;
 real Xmax=0.15;
 real sign;


 int n;

 /* set deforming flag on adjacent cell zone */
 SET_DEFORMING_THREAD_FLAG(THREAD_T0(tf));

 sign = (Y0-dY)*sin (omega * time);

 Message ("\n\ntime = %f, sign = %f", time, sign);

 begin_f_loop(f,tf)
   {
    f_node_loop(f,tf,n)
      {
       v = F_NODE(f,tf,n);

       /* update node if x position is greater than 0.02
          and that the current node has not been previously
          visited when looping through previous faces */

       if (NODE_X(v) > Xmin && NODE_X(v) < Xmax && NODE_POS_NEED_UPDATE (v))
         {
          /* indicate that node position has been update
             so that it's not updated more than once -AND nodes at the
                    interface stay where the pipe is */

               NODE_POS_UPDATED(v);

          NODE_Y(v)=Y0-sign*sin(M_PI/(Xmax-Xmin)*(NODE_X(v)-Xmin));
               Message("\n%f it loops", NODE_Y(v));
         }
      }
   }

 end_f_loop(f,tf);
}
```

Matlab Vector Plotting tool provided by Kenneth Chung for PIV

```
clear
clf
display ('-----------------------------------------------')
display ('------------Vector Plotting Tool---------------')
display ('--------------------V1-m/s---------------------')
display ('----------------------by-----------------------')
display ('---------------Kenneth Chung-------------------')
display ('-----------------June 2007--------------------')
display ('-----------------------------------------------')

fname1 = ('F:\PIV experiments\PIV experiments 110507\HD2\Ajay');%input
('Folder directory? e.g. (C:) >> ','s')
fname2 = ('CMC05%sq3rpm');%input ('Folder name? (e.g. TRIAL) >> ','s')
nfiles = 999;%input ('Last Frame? (e.g. 499) >> ')
fname3 = [fname1,'\',fname2,'\Vector\',fname2,'00000.vec']

s=csvread([fname3],1,0);
xt=find(s(:,5)<1);
s(xt,3:4)=NaN;
s(:,5)=[];
format short e;
s(:,1:2)=s(:,1:2)/1000;
x = s(:,1);
y = s(:,2);
z = s(:,3);
b = find (y == s (1,2));
b1 = max (size (b));
a = find (x == s (1,1));
a1 = max (size (a));
U =reshape(z,b1,a1);
U = U;
z = s(:,4);
V =reshape(z,b1,a1);
V = V;
X=reshape(x,b1,a1);
Y=reshape(y,b1,a1);

%%%%%%%%%%%%%%%%%%%%%%%%%%%%%%%%%%%%%%%%%%%%%%%%%%%%%%%%%%%%%%%%%%%%%%%%%%%%%%%

for i = 1 : nfiles;

if i < 10
fname3 = [fname1,'\',fname2,'\Vector\',fname2,'0000',int2str(i),'.vec']
elseif 100 > i & i > 9
fname3 = [fname1,'\',fname2,'\Vector\',fname2,'000',int2str(i),'.vec']
elseif 1000 > i & i > 99
fname3 = [fname1,'\',fname2,'\Vector\',fname2,'00',int2str(i),'.vec']
else
fname3 = [fname1,'\',fname2,'\Vector\',fname2,'0',int2str(i),'.vec']
end

if exist (fname3)>0

s=csvread([fname3],1,0);
xt=find(s(:,5)<1);
```

```
s(xt,3:4)=NaN;
s(:,5)=[];
z = s(:,3);
U2 =reshape(z,b1,a1);
z = s(:,4);
V2 =reshape(z,b1,a1);
U=cat(3,U,U2);
V=cat(3,V,V2);
end
end
clear U2 V2;
display ('Data Loading Completed')
%%%%%%%%%%%%%%%%%%%%%%%%%%%%%%%%%%%%%%%%%%%%%%%%%%%%%%%%%%%%%%%%%%%%%%%%%%%%%%%

sz=size(U);
c1=sz(1,3);
for i=1:b1
    for j=1:a1
        clear  ru rv
       ru=find (~isnan(U(i,j,:)));
rv=find (~isnan(V(i,j,:)));
UA(i,j) = mean(U(i,j,ru));
VA(i,j) = mean(V(i,j,rv));
    end
end

%%%%%%%%%%%%%%%%%%%%%%%%%%%%%%%%%%%%%%%%%%%%%%%%%%%%%%%%%%%%%%%%%%%%%%%%%%%%%%%
quiver (X,Y,UA,VA,8);
set(gca,'DataAspectRatio',[1 1 1])
%%%%%%ip=total no. of instant... image nsep=separation btw images

nsep=1;
for ip=1:300;
    NU(:,:,ip)=U(:,:,(1+(ip-1)*nsep));
        NV(:,:,ip)=V(:,:,(1+(ip-1)*nsep));
end
```

Matlab programme for recording the largest feature from processed PLIF images where the data read as a text output from the QUIPS software analysis.

```
for i=2:length(numones)
frame=s(numones(i-1):numones(i)-1,:);
frame(:,1)=[];

dummy=sort(frame);
num=size(frame,1);
A(i-1,:)=dummy(end,:);

if num>1
less_A(i-1,:)=dummy(end-1,:);
else
less_A(i-1)=NaN;
end
%save files related to each frame
file_name=[num2str(i-1) '.dat'];
save(file_name,'i','-ASCII')

clear temp num dummy;
end
```

REFERENCES

Abrahamsson B., Pal A., Sjöberg M., Carlsson M., Laurell E. and Brasseur J.G. (2005) A novel *in vitro* and numerical analysis of shear-induced drug release from extended release tablets in the fed stomach, *Pharmaceutical Research,* **22**(8), 1215–26.

Alvarez M. M., Zalc J. M., Shinbrot T., Arratia P. E., and Muzzio F. J. (2002) Mechanisms of Mixing and Creation of Structure in Laminar Stirred Tanks, *American Institute of Chemical Engineering Journal*, 48(10), 2135-2148.

Arnoldi, A. (2004) Functional Foods, Cardiovascular Disease and Diabetes, Woodhead Publishing, Cambridge, England.

Appelqvist I.A.M., Malone M.E., Goff T.C., Heinrich E. and Nandi A. (2002) Controlled deposition and release of flavours to control aftertaste. In: Williams P.A., Phillips GO. (2002) *Mouth*, *Gums and Stabilisers for the Food Industry*, Cambridge, U.K, Published RSC; **11**, 43-53.

Artursson P. and Karlsson J. (1991) Correlation Between Oral-Drug Absorption in Humans and Apparent Drug Permeability Coefficients in Human Intestinal Epithelial (Caco-2) Cells, *Biochemical and Biophysical Research Communications,* **175**, 880-885.

Axelrod D., Koppel D.E., Schlessinger J., Elson E. and Webb W.W. (1976) Mobility measurement by analysis of fluorescence photobleaching recovery kinetics, *Biophysical Journal,* **16,** 1055-1069.

Bajpai S.K. and Sharma S. (2005) Dynamic Release of Riboflavin from Ethyl Cellulose Coated Barium Alginate Beads for Gastrointestinal Drug Delivery: An in vitro Study, *Journal of Macromolecular Science, Part A: Pure and Applied Chemistry,* **42**, 649–661.

Banker G.S. and Rohodes C.T. (2002) Modern Pharmaceutics, Informa Health Care, London.

Barbosa-Cánovas, Gustavo V. and Fito P. (2000) Food Engineering, Springer - Verlag.

Behall K. (1997) Dietary fiber: nutritional lessons for macronutrient substitutes, *Annals of the New York Academy of Sciences*, **819**, 142–154.

BBC website (2006) Scientists create artificial gut [online] http://news.bbc.co.uk/1/hi/health/6136546.stm [Accessed July 2008]

Blackburn N.A. and Johnson I.T. (1981) The Effect of Guar Gum on the Viscosity of the Gastrointestinal Contents and on Glucose-Uptake from the Perfused Jejunum in the Rat 2, *British Journal of Nutrition*, **46**(2), 239-246.

Blackburn N.A., Holgate A.M. and Read N.W. (1984) Does Guar Gum Improve Post-Prandial Hyperglycemia in Humans by Reducing Small Intestinal Contact Area 4, *British Journal of Nutrition*, **52**(2), 197-204.

Blanquet S., Marol-Bonnin S., Beyssac E., Pompon D., Renaud M. and Alric M. (2001) The 'Biodrug' Concept: an Innovative Approach to Therapy, *Trends in Biotechnology,* **19,** 393-400.

Boyer J. and Liu R.H. (2004) Apple phytochemicals and their health benefits, *Nutrition Journal,* **3**, 5.

British Standards Institute. (1975) British Standards Glossary of Terms Relating to the Sensory Analysis of Food, British Standards Institute, London.

Buettner A., Beer A. and Hannig C. and Settles M. (2001) Observation of the Swallowing Process by Application of Videofluoroscopy and Realtime Magnetic Resonance Imaging—Consequences for Retronasal Aroma Stimulation, *Chemical Senses*, **26**, 1211–1219.

Businessweek (2006) Nestlé: Fattening Up On Skinnier Foods, Matlack C. [online]. www.businessweek.com/globalbiz/content/jun2006/gb20060622_479192.htm [Accessed June 2008]

Cancer Research UK (2008) The Stomach [online] www.cancerhelp.org.uk/help/default.asp?page=3905 [Accessed July 2008]

Chaplin M (2008) Water Structure and Science – Guar Gum www.lsbu.ac.uk/water/hygua.html [Accessed July 2009]

Christensen J., Macagno E.O. and Melville J.G. (1978) Motility and Flow in Small-Intestine 1, *Journal of the Engineering Mechanics Division-Asce,* **104,** 11-29.

Coulson J.M. and Richardson J.F. (1998) Chemical Engineering Volume 1: Fluid Flow, Heat Transfer and Mass Transfer, Oxford: Butterworth-Heinemann.

Cross M.M. (1965) Rheology of Non-Newtonian Fluids: A New Flow Equation for Pseudoplastic Systems, *Journal of Colloid Science,* **20**, 417.

Cussler E.L. (1997) Diffusion Mass Transfer in Fluid Systems, 2nd Edition, Cambridge: University Press.

Dean J.R and Ma R. (2007) Approaches to Assess the Oral Bioaccessibility of Persistent Organic Pollutants: A Critical Review, *Chemosphere*, **68**(8), 1399-1407.

DeSesso J.M. and Jacobson C.F. (2001) Anatomical and Physiological Parameters Affecting Gastrointestinal Absorption in Humans and Rats, *Food and Chemical Toxicology,* **39,** 209-228.

Dias V.C. and Yatscoff R.W. (1994) Investigation of Rapamycin Transport and Uptake Across Absorptive Human Intestinal-Cell Monolayers, *Clinical Biochemistry,* **27**, 31-36.

Dikeman C.L. and Fahey G.C. Jr. (2006) Viscosity as Related to Dietary Fiber: A Review, *Critical Reviews in Food Science and Nutrition,* **46**(8), 649–63.

Doll R. and Peto R. (1981) The Causes of Cancer: Quantitative Estimates of Avoidable Risks of Cancer in the United States Today, *Journal of the National Cancer Institute,* **66,** 1191-308.

Edwards C.A., Blackburn N.A., Craigen L., Davison P., Tomlin J. and Sugden K. (1987) Viscosity of Food Gums Determined Invitro Related to Their Hypoglycemic Actions 1, *American Journal of Clinical Nutrition,* **46**(1), 72-77.

Edwards C.A., Johnson I.T. and Read N.W. (1988) Do Viscous Polysaccharides Slow Absorption by Inhibiting Diffusion Or Convection?, *European Journal of Clinical Nutrition*, **42**(4), 307- 312.

Ellis P.R., Rayment P. and Wang Q. (1996) A physico-chemical perspective of plant polysaccharides in relation to glucose absorption, insulin secretion and the entero-insular axis, *Proceedings of the Nutrition Society,* **55**(3), 881-898.

Ellis P.R., Roberts F.G., Low A.G. and Morgan L.M. (1995) The Effect of High-Molecular-Weight Guar Gum on Net Apparent Glucose-Absorption and Net Apparent Insulin and Gastric-Inhibitory Polypeptide Production in the Growing Pig - Relationship to Rheological Changes in Jejunal Digesta 1, *British Journal of Nutrition,* **74**(4), 539-556.

Ellis P.R., Wang Q., Rayment P., Ren Y., and Ross-Murphy S B. Guar Gum: Agricultural and Botanical Aspects, Physicochemical and Nutritional Properties and Its Use in the Development of Functional Foods. In: Cho S.S. and Dreher M. (2000) Handbook of Dietary Fibre*,* New York: Marcel Dekker.

Ekmekcioglu C. (2000) Intestinal bioavailability of minerals and trace elements from milk and beverages in humans, *Nahrung/Food*, **44,** 390.

Faas H., Steingoetter A., Feinle C., Lengsfeld H., Boesiger P., Fried M. and Schwizer W. (2002) Effects of meal consistency and ingested fluid volume on the intragastric distribution of a drug model in humans—a magnetic resonance imaging study, *Alimentary Pharmacology and Theraputics,* **16**(2), 217–24.

Farenbach M.J., Riccardi A. and Saunders J.C. (1965) Comparative Effects of Guar Gum and Pectin on Human Serum Cholesterol Level, *Circulation,* **11**, 31-32.

Faulks R.M. and Southon S. (2005) Challenges to Understanding and Measuring Carotenoid Bioavailability, *Biochimica et Biophysica Acta,* **1740**, 95–100.

FDA, Bioavailability and Bioequivalence Studies for Orally Administered Drug Products, General Considerations (Issued 7/2002, Posted 7/2002), U.S. Food and Drug Administration/Center for Drug Evaluation and Research

Finkelstein E.A., Fiebelkorn I.C. and Wang G. (2003) National medical spending attributable to overweight and obesity: how much, and who's paying? *Health Affairs,* Supplement **W3**, 219-226.

Flora Professional (2008) Flora pro.active – your questions answered [online] www.flora-professional.co.uk/whichfloraisrightforyou/proactivproductrange/flora-proactiv-questions.aspx?style=1 [Accessed June 2008]

FLUENT 6.2 User's Guide (2005), ANSYS Inc. USA

Fluorin B.E. The influence of dietary fibre on carbohydrate digestion and absorption. In: Schweizer T.G. and Edwards C.A. (1992) Dietary Fibre – A Component of Food. Nutritional Function in Health and Disease, London: Springer Verlag.

Food Business Review (2008) Healthy Growth in functional food market despite drop in consumer trust [online] www.food-business-review.com/article_feature.asp?guid=790A5689-9454-4AB4-93EF-E449853628E1 [Accessed June 08]

Fryer P.J., Pyle D.L., and Rielly C.D. (1997) *Chemical Engineering for the Food Industry*, Blackie Academic and Professional, London ISBN 0 412 495 007.

Ganong W. (2005) Review of Medical Physiology, U.S.: The McGraw-Hill Companies.

Gallaher D.D. and Hassel C.A. The role of viscosity in the cholesterol-lowering effect of dietary fiber. In: Kritchevsky D. and Bonfield C. (1995) Dietary Fiber - Health and Disease, St. Paul: Eagan Press.

Gentilcore D., Chaikomin R., Jones K.L., Russo A., Feinle-Bisset C., Wishart J.M., Rayner C.K. and Horowitz M. (2006) Effects of Fat on Gastric Emptying of and the Glycemic, Insulin, and Incretin Responses to a Carbohydratemeal in Type 2 Diabetes*, The Journal of Clinical Endocrinology and Metabolism,* **91**, 2062–2067.

Gibson G.R. and Williams C.M. (2002) Functional Foods, UK: Woodhead Publishing, Cambridge, England.

Gregersen H. (2002) Biomechanics of the Gastrointestinal Tract, London: Springer.

Gray H. (1918) Anatomy of the human body, 20th Edition, Philadelphia: Lea & Febiger.

Guillon F. and Champ M. (2000) Structural and Physical Properties of Dietary Fibres, and Consequences of Processing on Human Physiology 1, *Food Research International,* **33**, 233-245.

Guyton A.C. and Hall J.E. (1996) Textbook of Medical Physiology, 9th Edition, London: W.B. Saunders.

Harnby N., Edwards M.F. and Nienow A.W. (1997) Mixing in the Process Industries, 2nd Edition, Oxford: Butterworth-Heinemann.

Hedren E., Mulokozi G. and Svanberg U. (2002) *In vitro* accessibility of carotenes from green leafy vegetables cooked with sunflower oil or red palm oil, *International Journal of Food Sciences and Nutrition,* **53**, 445–453.

Henry C.J.K. and Chapman C. (2002) Nutrition Handbook for Food Processors, Cambridge: Woodhead Publishing.

Hoad C.L., Marciani L., Foley S., Totman J.J., Wright J, Bush D., Cox E.F., Campbell E., Spiller R.C. and Gowland P.A. (2007) Non-invasive quantification of small bowel water content by MRI: a validation study, *Physics in Medicine and Biology,* **52**(23), 6909-6922.

Holland F.A. and Bragg R. (1995) Fluid Flow for Chemical Engineers, 2nd Edition, London: Elsevier.

Howes T. and Mackley M.R. (1990) Experimental Axial-Dispersion for Oscillatory Flow Through A Baffled Tube, *Chemical Engineering Science,* **45**, 1349-1358.

Howes T., Mackley M.R. and Roberts E.P.L. (1991) The Simulation of Chaotic Mixing and Dispersion for Periodic Flows in Baffled Channels, *Chemical Engineering Science,* **46**, 1669-1677.

Idkaidek N.M. and Abdel-Jabbar N. (2001) A Novel Approach to Increase Oral Drug Absorption, *Pharmaceutical Development and Technology,* **6,** 167-171.

Imam H., Sanmiguel C., Larive B., Bhat Y., and Soffer E., (2003) Study of intestinal flow by combined videofluoroscopy, *American Journal of Physiology, Gastrointestinal and Liver Physiology,* **286**, 263-270.

International Food Information Council Foundation (2006) Functional Foods [online] http://ific.org/nutrition/functional/index.cfm [Accessed June 08]

Insel P., Turner E. and Ross D. (2004) Nutrition, 2nd Edition, Sudbury USA: Jones and Bartlett.

Jeffrey B., Udaykumar H.S. and Schulze K.S. (2003) Flow fields generated by peristaltic reflex in isolated guinea pig ileum: impact of contraction depth and shoulders, *American Journal of Physiology, Gastrointestinal and Liver Physiology,* **285**, 907-918.

Jenkins D.J., Wolever T.M., Leeds A.R., Gassull M.A., Haisman P., Dilawari J., Goff D.V., Metz G.L. and Alberti K.G. (1978) Dietary Fibres, Fibre Analogues, and Glucose Tolerance: Importance of Viscosity, *British Medical Journal,* **1,** 1392-1394.

Johnson I.T. and Gee J.M. (1981) Effect of Gel-Forming Gums on the Intestinal Unstirred Layer and Sugar-Transport Invitro, *Gut,* **22,** 398-403.

Kappel C. and Ellis R. (August 2004) *Confocal Application* Letter, No.18.

Khan F. (2005) Investigation of Turbulent Flows and Instabilities In a Stirred Vessel Using Particle Image Velocimetry, PhD thesis, Loughborough University.

Kong F. and Singh R.P. (2008.a) Disintegration of Solid Foods in Human Stomach, *Journal of Food Science*, **73(**5), 67-80.

Kong F. and Singh R.P. (2008.b) A Model Stomach System to Investigate Disintegration Kinetics of Solid Foods during Gastric Digestion, *Journal of Food Science*, **73(**5), E202-E210.

Krul C., Luiten-Schuite A., Baan R., Verhagen H., Mohn G., Feron V. and Havenaar R. (2000) Application of a Dynamic in Vitro Gastrointestinal Tract Model to Study the Availability of Food Mutagens, Using Heterocyclic Aromatic Amines As Model Compounds, *Food and Chemical Toxicology,* **38,** 783-792.

Leclere C.J., Champ M., Boillot J., Guille G., Lecannu G., Molis C., Bornet F., Krempf M., Delort-Laval J. and Galmiche J.P. (1994) Role of viscous guar gums in lowering the glycemic response after a solid meal, *American Journal of Clinical Nutrition* **59**, 914-921.

Leger A.J. (2005) Mathematical and Numerical Modelling of Peristaltic Flow and Absorption in the Small Intestine, PhD thesis, Bath University.

Livny O., Reifen R., Levy I., Madar Z., Faulks R., Southon S. and Schwartz B. (2003) ß-carotene bioavailability from differently processed carrot meals in human ileostomy volunteers, *European Journal of Nutrition*, **42,** 338–345.

Macagno E.O., Christensen J. and Lee C.L. (1982) Modeling the Effect of Wall Movement on Absorption in the Intestine, *American Journal of Physiology* **243,** 541-550.

Macagno E.O. and Christensen J. (1980) Fluid-Mechanics of the Duodenum, *Annual Review of Fluid Mechanics,* **12**, 139-158.

Mackley M.R., Tweddle G.M. and Wyatt D. (1990) Experimental heat transfer measurements for pulsatile flow in baffled tubes, *Chemical Engineering Science,* **45**, 1237-1242.

Mackley M.R. and Stonestreet P. (1995) Heat-Transfer and Associated Energy-Dissipation for Oscillatory Flow in Baffled Tubes, *Chemical Engineering Science,* **50**, 2211-2224.

Marciani L., Gowland P.A., Spiller R.C., Manoj P., Moore R.J., Young P., Al-Sahab S., Bush D., Wright J. and Fillery-Travis A.J. (2000) Gastric response to increased meal viscosity assessed by echo-planar magnetic resonance imaging in humans, *Journal of Nutrition*, **130**, 122–127.

Marciani L., Gowland P.A., Fillery-Travis A., Manoj P., Wright J., Smith A., Young P., Moore R. and Spiller R.C. (2001) Assessment of Antral Grinding of a Model Solid Meal With Echo-Planar Imaging 1, *American Journal of Physiology-Gastrointestinal and Liver Physiology,* **280,** 844-849.

Marciani L., Wickham M.S.J. and Singh G. (2007) Enhancement of intragastric acid stability of a fat emulsion meal delays gastric emptying and increases cholecystokinin release and gall bladder contraction, *American Journal of Physiology, Gastrointestinal and Liver Physiology*, **292**, 1607–1613.

Martini F.H. (2006) Fundamentals of Anatomy & Physiology, 7th Edition, London: Pearson/Benjamin Cummings.

Matont A., Hopkins J. and William McLaughlin C. (1993) Human Biology and Health, Englewood Cliffs, New Jersey, USA: Prentice Hall.

McQueen D.M. and Peskin C.S. (2001) Heart simulation by an immersed boundary method with formal second-order accuracy and reduced numerical viscosity: *Mechanics for a New Millennium, Proceedings of the International Conference on Theoretical andApplied Mechanics* (ICTAM) 2000, (H. Aref and J.W. Phillips, eds.) Kluwer Academic Publishers.

Minekus M., Marteau P., Havenaar R. and Huisintveld, J.H.J. (1995) A Multicompartmental Dynamic Computer-Controlled Model Simulating the Stomach and Small-Intestine, *Atla-Alternatives to Laboratory Animals,* **23,** 197-209.

Molecular Expression (2008) Photobleaching [online]
http://micro.magnet.fsu.edu/primer/java/fluorescence/photobleaching/
[Accessed August 2008]

Moog F. (1981) The Lining of the Small-Intestine 1, *Scientific American,* **245,** 154.

Morris E.R. and Ross-Murphy S.B. (1981) Chain flexibility of polysaccharides and glycoproteins from viscosity measurements, *Techniques in Carbohydrate Metabolism*, **310**, 1-46.

National Enzyme Company (2004) The First Quantitative Evidence Proving
The Efficacy Of Supplemental Enzymes [online]
www.hacres.com/diet/research/Enzyme_TNO_Brochure.pdf [Accessed July 2008]

Norton I.T., Fryer P.J. and Moore S. (2006) Product/process integration in food manufacture: Engineering sustained health, *American Institute of Chemical Engineering Journal*, **52**(5), 1632-1640.

Norton T. and Sun D.W., (2006) Computational fluid dynamics (CFD) - an effective and efficient design and analysis tool for the food industry: A review, *Trends in Food Science and Technology*, **17**, 600-620.

Omoni A.O. and Aluko R.E. (2005) The anti-carcinogenic and anti-atherogenic effects of lycopene: a review, *Trends in Food Science and Technology*, **16**, 344–50.

Ottino, J.M. (1989) The Kinematics of Mixing: Stretching, Chaos and Transport, Cambridge: Cambridge University Press.

Ottino J.M. (1990) Mixing, Chaotic Advection, and Turbulence, *Annual Review of Fluid Mechanics*, **22**, 207-253.

Pal A., Indireshkumar K., Schwizer W., Abrahamsson B., Fried M. and Brasseur J.G. (2004) Gastric flow and mixing studied using computer simulation, *Proceedings of the Royal Society of London Series B-Biological Sciences,* **271,** 2587-2594.

Parada J. and Aguilera J.M. (2007) Food Microstructure Affects the Bioavailability of Several Nutrients, *Journal of Food Science,* **72**(2), 21-32.

Patent WO/2003/055331, Food Product With High Viscosity, 10.07.2003, Wuersch, P, (Societes des Products NESTLE S.A.).

Patent WO/2004/10550, Satiety enhancing food products, 09.12.2004, Van Benthum, W.,A.,J. (UNILEVER N.V.).

Perkin Elmer (2006) An Introduction to Fluorescence Spectroscopy [online]. http://las.perkinelmer.com/content/manuals/gde_fluorescencespectroscopy.pdf [Accessed July 2008]

Perry R.H. and Green D.W. (1997) Perry's Chemical Engineers' Handbook, 7th Edition, McGraw-Hill.

Phillips G.O. and Williams P.A. (2000) Handbook of Hydrocolloids**,** UK: Woodhead Publishing.

Purves W.K., Orians, G.H. and Heller, H.C. (1998) Life: The Science of Biology, 5th Edition, Sunderland USA: Sinauer Associates.

Rabe S., Linforth R.S.T., Krings U., Taylor A.J. and Berger R.G. (2004) Volatile release from liquids: A comparison of in vivo APCI-MS, in-mouth headspace trapping and in vitro mouth model data, *Chemical Senses and Flavor,* **29**, 163-173.

Raffel M., Willert C. and Kompenhans J. (1998) Particle Image Velocimetry - A Practical Guide, Berlin: Springer-Verlag.

Reis N., Vincente A.A., Teixeira J.A. and Mackley, M.R. (2004) Residence times and mixing of a novel continuous oscillatory flow screening reactor, *Chemical Engineering Science*, **59**, 4967-4974.

Riversideonline (2008) [online] www.riversideonline.com/source/images/image_popup/d7_digestivesystem.jpg [Accessed July 2008]

Roberts F.G., Smith H.A., Low A.G. and Ellis P.R., Influence of wheat breads containing guar flour supplements of high and low molecular weights on viscosity of jejunal digesta in the pig. In: Southgate D.A.T., Waldron K., Johnson I.T. and Fenwick G.R. (1990) Dietary Fibre: Chemical and Biological Aspects, UK: Institute of Food Research.

Ross-Murphy S.B. (1984) Rheological Methods. Physical Techniques for the Study of Food Biopolymers**,** London: Blackie Academic & Professional.

RT Answers (2008) Treatment for Head and Neck Cancer **[**online] www.rtanswers.org/treatment/disease/head_neck.htm [Accessed July 2008]

Siggia E.D., Lippincott-Schwartz J. and Bekiranov S. (2000) Diffusion in inhomogenous media: theory and simulations applied to a whole cell photobleach recovery, *Biophysical Journal.,* **79**, 1761-1770.

Simmons M.J.H., Zhu H., Bujalski W., Hewitt C.J. and Nienow A.W., (2007) Mixing in a Model Bioreactor Using Agitators with a High Solidity Ratio and Deep Blades, *Chemical Engineering Research and Design,* **85** (5), 551-559

Simulations-plus (2008) What Is GastroPlus™ ? [online]. http://www.simulations-plus.com/Products.aspx?grpID=3&cID=16&pID=11 [Accessed June 2008]

Slaughter S.L., Ellis P.R., Butterworth P.J., (2001) An investigation of the action of porcine pancreatic K-amylase on native and gelatinised starches, *Biochimica et Biophysica Acta* 1525 (2001) 29-36

Smith M.E. and Morton D.E. (2001) The Digestive System, Livingstone: Churchill.

Spiller R.C., Trotman I.F., Higgins B.E., Ghatei M.A.**,** Grimble G.K.**,** Lee Y.C.**,** Bloom S.R.**,** Misiewicz J.J. and Silk D.B. (1984) The Ileal Brake—Inhibition of Jejunal Motility After Ileal Fat Perfusion in Man, *Gut,* **25**, 365-374.

Spratt P., Nicolella C. and Pyle D.L. (2005) An Engineering Model of the Human Colon, *Trans IChemE C,* **83**, 147-157.

Spratt P. (2003) Development of a System for Modelling of the Human Large Intestine, PhD thesis, University of Reading.

Stewart B.H., Chan O.H., Lu R.H., Reyner E.L., Schmid H.L., Hamilton H.L., Steinbaugh B.A. and Taylor M.D. (1995) Comparison of Intestinal Permeabilities Determined in Multiple In-Vitro and In-Situ Models - Relationship to Absorption in Humans, *Pharmaceutical Research,* **12,** 693-699.

Stoll B.R., Batycky R.P., Leipold H.R., Milstein S. and Edwards D.A. (2000) A Theory of Molecular Absorption From the Small Intestine, *Chemical Engineering Science,* **55,** 473-489.

Taylor A.J. (1996) Volatile Flavor Release From Foods During Eating, *Critical Reviews in Food Science and Nutrition*, **36**, 765–784.

Taylor A.J. and Linforth R.S.T. (1996) Flavour release in the mouth, *Trends in Food Science and Technology,* **7**(12), 444-448.

Torsdottir I., Alpsten M., Andersson H. and Einarsson S. (1989) Dietary Guar Gum Effects on Postprandial Blood Glucose, Insulin and Hydroxyproline in Humans, *Journal of Nutrition,* **119** (12), 1925-1931.

Tharakan A., Rayment P., Fryer P.J. and Norton I.T. (2007) Modelling of physical and chemical processes in the small intestine, *Proceedings of European Congress of Chemical Engineering (ECCE-6)*, Copenhagen, 16-20 September, 2007.

Thomas A. (2006) Gut Motility, Sphincters and Reflex Control, *Anaesthesia and Intensive Care Medicine*, **7**(2), 57–58.

Unilever. (2006) Unilever Annual Report, Unilever. [online] www.unilever.com/ourcompany/investorcentre/annual_reports/ [Accessed July 2008]

Unipektin product literature, 2008, Unipektin AG, Eschenz

Urbain J.C., Siegel J.A., Charkes N.D., Cutsem E., Maegdenbergh V. and Roo M. (1989) The two component stomach: effects of meal particle size on fundal and antral emptying, *European Journal of Nuclear Medicine*, **15**, 254–259.

U.S. National Library of Medicine (2008) [online] www.nlm.nih.gov [Accessed July 2008]

US 2006/0105093, Satiety emulsions and food compositions, Bialek J M, Melnikov S M, Winter I, Publication date (15.11.05).

Versteeg H.K. and Malalasekera W. (1995) An Introduction to Computational Fluid Dynamics The Finite Volume Method, UK: Addison–Wesley Longman Higher Education.

Versantvoort C.H., Van de Kamp E. and Rompelberg C.J.M. (2004) Development and applicability of an *in vitro* digestion model in assessing the bioaccessibility of contaminants from food, RIVM report 320102002/2004 [online]. Available from: www.rivm.nl/en/ [Accessed March 2008]

Wickham M., Faulks R. and Mills C. (2006) Joint HESI / ILSI Research Foundation / ILSI International Food Biotechnology Committee (IFBiC) Workshop on Assessing the Effects of Food Processing on Allergenicity, 19-21 June, 2006, Estoril Portugal.

Wildman R.E.C (2001) Handbook of Nutraceuticals and Functional Foods, Boca Raton: CRC Press.

Willett W. (1995) Diet, Nutrition and Avoidable Cancer, *Environmental Health Perspectives,* **103**, 165-170.

WO/2003/055331, Food Product with High Viscosity, Wuersch P, Ballevre O, Milton H, Sievert B, Publication date (10.07.2003).

Wright J., Wulfert F. Hort J. and Taylor A.J. (2007) Effect of Preparation Conditions on Release of Selected Volatiles in Tea Headspace, *Journal of Agricultural and. Food Chemistry*, **55**, 1445-1453.

Yu L.X. and Amidon G.L. (1999) A Compartmental Absorption and Transit Model for Estimating Oral Drug Absorption, *International Journal of Pharmaceutics,* **186,** 119-125.

Yu L.X., Crison J.R. and Amidon G.L. (1996) Compartmental Transit and Dispersion Model Analysis of Small Intestinal Transit Flow in Humans, *International Journal of Pharmaceutics,* **140,** 111-118.